

A Thesis Submitted for the Degree of PhD at the University of Warwick

Permanent WRAP URL:

<http://wrap.warwick.ac.uk/131791>

Copyright and reuse:

This thesis is made available online and is protected by original copyright.

Please scroll down to view the document itself.

Please refer to the repository record for this item for information to help you to cite it.

Our policy information is available from the repository home page.

For more information, please contact the WRAP Team at: wrap@warwick.ac.uk

234

*

D 71420/87.

HEATH G. R.

plates

234

WARWICK.

THE MICROSTRUCTURAL STABILITY
OF Si-AL-O-N CERAMICS IN
SEVERE THERMAL ENVIRONMENTS
by
GARY ROBERT HEATH

A thesis submitted to the University of Warwick
for the Degree of Doctor of Philosophy

Department of Physics
University of Warwick
Coventry CV4 7AL

November 1985

ACKNOWLEDGEMENTS

Thanks are due to Professor A.J.Forty for the provision of laboratory facilities and to the S.E.R.C. for financial assistance. I also wish to thank Joseph Lucas Ltd. for additional financial support and in particular Dr.R.J.Lumby, Dr.A.Sweda and Dr.E.Butler (of Lucas-Cookson-Syalon, Monkspath, Solihull) for their valuable technical co-operation and supply of the materials studied.

I am indebted to my supervisor, Dr.M.H.Lewis, for his guidance, support and enthusiasm throughout this work and in the preparation of this thesis.

I wish also to thank the technical staff of the department for their assistance, with special mention to Mr.G.Smith for his general technical support and for maintaining the electron microscopes in their optimal condition and Mr.D.Lee for assistance in specimen preparation.

Finally I would like to thank all the colleagues and friends in the department who provided both humour and wisdom during this work.

SUMMARY

The work described in this thesis is broadly a study of the stability of the microstructure of a range of pressureless sintered Y-Si-Al-O-N ceramics in various high temperature environments. More specifically, the stability is assessed with respect to resistance to; oxidation, fracture, annealing and laser irradiation. The techniques used for microstructural assessment are; Transmission and Scanning Electron Microscopy, Energy Dispersive X-ray Analysis together with Electron and X-ray Diffraction.

Microstructural modifications are facilitated by changing the content of the phase 21R in the initial composition. The as-sintered material has a glass matrix and 21R is demonstrated to alter the glass Nitrogen level. Nitrogen is concluded to be a critical factor influencing the observed mechanical properties. The matrix can be crystallised to Yttrium Disilicate (Y2S) or Yttrium Aluminium Garnet (YAG) and their relative merits are assessed.

Oxidation behaviour for all the Y-Si-Al-O-Ns is presented, with emphasis on sub-oxide modifications. Material with a Y2S matrix exhibits excellent oxidation resistance, comparable to Hot-Pressed (H.P.) material, whilst YAG-containing material catastrophically oxidises above a threshold temperature of 1300°C. The degradation mechanism is a reaction between YAG and SiO₂ (the oxide) producing a ternary eutectic liquid. This degradation was overcome by a novel modification of the surface matrix to the Silicon Oxynitride phase.

The fracture toughness (K_{IC}) together with slow crack growth rates and mechanisms are studied at high temperatures using Notched Beam and Double Torsion specimens respectively. A critical dependence on the presence of any residual glass was demonstrated and an exceptionally high K_{IC} level recorded.

Laser-cut surfaces are studied and identify the material loss mechanisms. This work is the first such study and identifies H.P. material as highly suitable for laser machining.

CONTENTS

Summary	Page
<u>CHAPTER 1 - INTRODUCTORY REVIEW AND OBJECTIVES</u>	1
1.1 Engineering with Ceramics	
1.2 Silicon Nitride Ceramics	4
1.2.1 Crystal chemistry of Si_3N_4	4
1.2.2 Si_3N_4 Fabrication	5
1.2.3 Improvement in grain boundary phase properties	9
1.3 Si-Al-O-N Ceramics	10
1.4 Objectives	13
<u>CHAPTER 2 - STABILITY OF CERAMIC MICROSTRUCTURE IN OXIDISING ENVIRONMENTS: A REVIEW</u>	14
2.1 Oxidation Mechanisms	14
2.2 Oxidation of Si_3N_4 based Ceramics	15
2.3 Oxidation - induced Subsurface Transformations	19
2.4 Determination of Oxidation Kinetics	21
<u>CHAPTER 3 - FRACTURE OF CERAMIC MATERIALS: A REVIEW</u>	23
3.1 Brittle Fracture	23
3.1.1 Fracture mechanics approach to strength	23
3.1.2 Statistical nature of strength	26
3.2 Fracture Toughness and K_{IC}	27
3.3 Sub-critical Crack Growth	29
3.3.1 Low temperature results and the general K_{IC} relationship	30
3.3.2 High temperature s.c.g. mechanisms	31
3.4 Failure Prediction	33
3.5 Measurement of Fracture Toughness and Slow Crack Growth	33

	<u>PAGE</u>
<u>CHAPTER 4 - GENERAL EXPERIMENTAL TECHNIQUES</u>	36
4.1 Oxidation	36
4.2 Fracture Toughness Testing	37
4.2.1 The jig	38
4.2.2 The test specimen	38
4.2.3 The procedure	39
4.3 Sub-critical Crack Growth Testing	40
4.3.1 The specimen	40
4.3.2 The D.T. jig	41
4.3.3 Test procedure	41
4.3.3(a) Load relaxation method	42
4.3.3(b) Constant displacement	43
4.3.3(c) Constant load	43
4.3.4 Poisson's ratio determination	44
4.3.5 Compliance change method	45
<u>CHAPTER 5 - CERAMIC FABRICATION AND MICROSTRUCTURE</u>	48
5.1 Fabrication	48
5.1.1 Introduction	48
5.1.2 Fabrication route	49
5.2 Techniques for Microstructural Analysis	50
5.2.1 Microstructural features	50
5.2.2 The detection of g.b. films	51
5.2.3 Chemical micro-analysis	52
5.3 The Microstructural Characteristics of Sintered Alloys	54
5.3.1 Microstructure of alloys with low "polytypoid" addition	54
5.3.2 Microstructural development with increasing "polytypoid" addition	56
5.3.3 Determination of N content in g.b. glass	58
5.3.3(a) The techniques	58
5.3.3(b) Electron energy loss spectroscopy	58
5.3.3(c) Summary of results	60

	<u>Page</u>
5.3.4 Sintered Densities and Porosity Levels	61
5.3.5 X-Ray Diffraction	62
5.4 The Microstructural Characteristics of Annealed Alloys with Crystalline Matrices	62
5.4.1 Alloys with low "polytypoid" additions	62
5.4.1(a) Matrix devitrification products and mechanisms	62
5.4.1(b) Pore development and optimal matrix crystallisation	65
5.4.2 Alloys with high "polytypoid" additions	67
5.4.2(a) The effect of "polytypoid" addition on matrix crystallisation	67
5.4.2(b) Factors influencing matrix crystallisation	69
5.5 Summary of Significant Microstructural Data	70
<u>CHAPTER 6 - STABILITY OF MICROSTRUCTURE IN OXIDISING ENVIRONMENTS</u>	72
6.1 Oxidation of As-sintered β' + glass alloys	72
6.1.1 Alloys with low "Polytypoid" Content	72
6.1.1(a) Oxide Surface Observations	72
6.1.1(b) Mechanisms for development of oxide features	74
6.1.1(c) Oxide and sub-oxide kinetics	74
6.1.2 Sintered Alloys with High "Polytypoid" Addition	76
6.1.2(a) Oxide and sub-oxide features	76
6.1.2(b) Oxide Development mechanisms	78
6.1.3 Oxidation mechanisms for (β' + glass) Alloys	79
6.2 Oxidation of Annealed Materials	79
6.2.1 Low 21R Additive Alloy with α -Y ₂ Si ₂ O ₇ matrix	79
6.2.2 High 21R Additive Alloys with YAG Matrices	80
6.3 A Unified Oxidation Mechanism	81
6.4 Sub-oxide Microstructural Stability in YAG Matrix materials	85

	<u>Page</u>
6.4.1 Reversion of YAG to the liquid state	85
6.4.2. Dissolution of β' Grains	86
6.4.3 Kinetics of YAG Reversion	87
6.4.4 Microstructural Stability in the Absence of Oxidation Reactions	88
6.5 Sub-oxide Microstructural Stability in β' + Glass Materials	89
6.5.1 As-sintered Materials	89
6.5.2. Materials with Reverted-Glass Matrices	89
6.6 The Development of Silicon Oxynitride	90
6.6.1 Microstructural Observations	91
6.6.2 Development of an O' + β' layer	92
6.6.3 Mechanisms for O' Formation	94
6.7 Discussion	96
6.8 Conclusions	98
<u>CHAPTER 7 - HIGH TEMPERATURE FRACTURE</u>	100
7.1 Analysis of K_{IC} Results	100
7.1.1 Variation of K_{IC} Level with microstructure	100
7.1.2 Dependency of K_{IC} on microstructural parameters - a model	101
7.1.3 Variation in K_{IC} level between alloys	103
7.1.4 Slow crack growth during K_{IC} determinations and its threshold temperature	105
7.2 Analysis of K_I -V Results	106
7.3 Microstructural analysis of Slow Crack Growth Mechanisms	108
7.4 Discussion and Conclusions	109
<u>CHAPTER 8 - LASER INDUCED STRUCTURAL DAMAGE</u>	113
8.1 Introduction	113
8.2 Materials and Experimentation	114
8.3 Microstructure of the Reconstituted Surface Layer	115

	<u>Page</u>
8.3.1 Two-phase ceramics	115
8.3.2 Single-phase ceramics	118
8.4 Material Loss and Reconstitution Mechanisms	120
8.5 Potential for Precision Laser Machining of Si-Al-O-N ceramics	124
<u>CHAPTER 9 - OVERVIEW AND FUTURE WORK</u>	126
9.1 Overview	126
9.2 Microstructurally Modified β' + YAG alloy	129
9.2.1 The significance of the YAG instability phenomena	129
9.2.2 Solutions to YAG-reversion via microstructural modification	130
9.2.2(a) Isolated YAG	131
9.2.2(b) Isolated YAG + O'	132
9.2.2(c) O' + β' Zone	133
9.2.3 Conclusions on microstructural modifications	133
9.3 Future Work	134
<u>Appendix 1.1</u>	136
<u>Appendix 4.1</u>	137
<u>Appendix 4.2</u>	138
<u>Appendix 4.3</u>	139
<u>Appendix 4.4</u>	140
<u>References</u>	143

LIST OF FIGURES

<u>Fig No</u>	<u>Follows</u>
	<u>Page</u>
1.1 The crystal structure of β - Si_3N_4	4
1.2 The relationship between β and α - Si_3N_4 crystal structures	4
1.3 Schematic representation of liquid phase sintering mechanism for (i) Si_3N_4 and (ii) Si-Al-O-N	7
1.4 General approaches to improvement of high temperature properties of Si_3N_4 materials	8
1.5 Si-Al-O-N system representation, expressed in equivalents. Phase equilibrium at 1570°C	11
2.1 Atmospheric induced catastrophic strength reduction of β' + YAG material	19
3.1 The three modes of fracture	25
3.2 Generalised form of the stress intensity (K) - crack velocity (V) relationship for brittle materials	30
4.1 Construction of K_{IC} jig and dimensions of K_{IC} specimen	38
4.2 Sectional view of furnace and Instron arrangement	38
4.3 Specimen and jig for double torsion testing	41
4.4 Schematic representation of load/time trace	42
4.5 Load/displacement curve for constant displacement	43
4.6 Schematic of Instron chart record during constant load method	43
4.7 Compliance change method of K_I -V relationship determination from a K_{IC} specimen	45
5.1 Microstructure of as-sintered alloy SO	54
5.2 S.E.M. images of alloys SO (a and c) and S13 (b and d)	55

LIST OF FIGURES

<u>Fig No</u>		<u>Follows</u> <u>Page</u>
5.3	The range of observed β' substitution (from EDAX) for each alloy and the overall variation with 21R content	55
5.4	Equilibrium diagrams illustrating the compositional modifications to the matrix glass (a) and overall microstructure (b,c) due to polytypoid addition	56
5.5	E.E.L.S. spectra obtained from bulk reference glasses and intergranular glasses of Y-Si-Al-O-N ceramics	60
5.6	Micrographs of alloy SOC having been annealed for 15 hours at 1300°C	63
5.7	Alloy SOC, annealed for 20 hours at 1300°C	64
5.8	SEM micrographs (b.s.e.) of alloy SOC identifying microscopic zones of porosity between surface nucleated fingers of α -Y2S	65
5.9	Microstructure of NSC (TEM) showing constant YAG orientation and range of YAG compositions	68
6.1	Oxide surface of alloy SO after oxidation at 1200°C for 16 hours	72
6.2	The development of the oxide surface features at 1300°C for alloy SO	73
6.3	Oxidation kinetics for alloy SO, showing discontinuity derived from oxide thickness measurements and weight gain	75
6.4	Plots of average oxide thickness against time for R' + glass alloys at 1300°C and 1350°C	76
6.5	Arrhenius plot of parabolic rate constants for the range of alloys	76
6.6	SEM sections of oxide film on the glass matrix alloy S13, at 1300°C	77
6.7	Features (from SEM) of oxide product of glass matrix alloys at 1350°C	77
6.8	SEM section of alloy SOC with crystalline (Y2S) matrix at 1350°C	79
6.9	Arrhenius plot of parabolic rate constants for oxidation of various types of Si_3N_4	80
6.10	Oxide thickness kinetics for a range of alloys with a crystalline (YAG) matrix at 1300°C and 1350°C	81

LIST OF FIGURES

<u>Fig No</u>		<u>Follows</u> <u>Page</u>
6.11	a) Schematic diagram of Si_3N_4 oxidation and driving forces for Y, Al, Ca out-diffusion b) Oxidation mechanism, via solution of Si_3N_4	82
6.12	SEM (b.s.e.) section of glass matrix alloy showing a sub-oxide zone, rich in Y	83
6.13	Formation of concentric shells of oxide on high 21R additive alloys at 1350°C (SEM)	83
6.14	SEM and TEM of sub-oxide zone of β' + YAG alloy oxidised above 1300°C	85
6.15	Kinetics of sub-oxide (reverted YAG) zone at 1300°C and 1350°C	87
6.16	TEM section of 'bulk' β' + YAG alloy annealed at 1475°C (with no oxidation interaction) showing isolated "YAG" morphology	88
6.17	Kinetics of sub-oxide zone of as-sintered alloy S13 and Arrhenius plot of parabolic rate constants	89
6.18	Sub-oxide of β' + YAG material, N6, after 100 hours in air at 1320°C, SEM and TEM identification of O'	90
6.19	E.D.A.X. profile across SEM section of alloy N8C, oxidised for 1000 hours at 1320°C	91
6.20	X.R.D. profile of sub-oxide of alloy S10C oxidised for 151 hours at 1350°C	91
6.21	Development of sub-oxide O' (TEM)	93
6.22	Schematic diagram of compositional change of β' + Y2S bi-phase alloy when oxidised at 1350°C	96
7.1	K_{IC} variation with temperature in air and vacuum for glass matrix alloys S0 and S13	100
7.2	SEM micrographs of fracture surface of glass matrix alloys at a) room temperature, b) above 1100°C	102
7.3	a) SEM micrograph of high temperature fracture surface b) Model of K_{IC} -enhancing grain pull-out mechanism	102
7.4	K_{IC} variation with temperature for alloys with crystallised matrices	104

LIST OF FIGURES

<u>Fig No</u>		<u>Follows</u> <u>Page</u>
7.5	a) Plot of threshold temperature for s.c.g. (in vacuum) against nitrogen level in the glass matrix of a range of alloys b) Plot of softening temperatures of bulk glasses with various nitrogen levels	105
7.6	V-K _I relationship for alloys SO and S13 at various temperatures	106
7.7	Plot of K _I /K _{IC} against crack velocity (V) for materials SO and S13 at 1200°, 1250° and 1300° C	107
7.8	Comparison of SO and S13 K _I -V data with other published data for Si ₃ N ₄ based materials at 1200° C in air	108
7.9	S.E.M. sections across crack path at 1200° C for high K _I value a) Near crack tip showing cavity formation b) View inside well-opened crack with grains standing proud	108
7.10	a) S.E.M. section across crack tip of material SO at 1200° C at high K _I levels. Extensive cavity nucleation and linkage is observed b) High mag. S.E.M. of crack tip showing cavity nucleation in glassy phase due to partial grain pull-out c) Crack arrest and regrowth	108
7.11	Material SO at 1300° C a) S.E.M. micrograph of notch tip showing crack branching b) S.E.M. micrograph showing extensive multiple crack growth c) Light zone (representing creep) extending from notch on the tensile side which corresponds to the reduced section groove of the specimen's other side (d)	108
7.12	a) S.E.M. of section across crack path of alloy SOC at 1300° C showing "square wave"-like shape. b) High mag. S.E.M. micrograph of crack tip region in S13C at 1300° C showing cavity formation in glassy region residual to matrix crystallisation to YAG (Y)	109
8.1	Microscopic view of laser pulsed holes in SEM	115
8.2	Schematic representation of technique used to produce electron transparent sections of the reconstituted layer lining the hole	115
8.3	SEM micrographs of the reconstituted layer in two-phase materials	116
8.4	TEM micrograph of the two-phase reconstituted layer microstructure with EDAX spectra of the various features	116
8.5	TEM micrograph of interface between original and reconstituted material in bi-phase alloy	117

LIST OF FIGURES

<u>Fig No</u>		<u>Follows</u> <u>Page</u>
8.6	TEM micrographs of dendritic globule in two-phase material showing crystalline interdendritic phase	117
8.7	SEM micrographs of the layer surface in single phase material along the bore	118
8.8	TEM section of reconstituted layer in single phase alloys	119
8.9	SEM micrographs (b.s.e.) of globule overlying the layer in the single phase material with a detectable second phase	120
8.10	Equivalence prism for Y-Si-Al-O-N system showing compositional modifications to β' and matrix during laser irradiation	120
8.11	Diagrammatic representation of the material loss/redeposition mechanism in single phase hot-pressed materials due to laser irradiation	121
8.12	Y_2O_3 - Al_2O_3 - SiO_2 Ternary phase diagram representing the shift in composition of the matrix phase in sintered materials during laser irradiation	122
8.13	Diagrammatic representation of material loss and reconstitution mechanisms in two-phase sintered materials due to laser machining	124
9.1	a) Schematic of s.g.c. mechanism possible by YAG reversion at the crack tip b) Predicted K_I -V relationship for s.c.g.	130
9.2	Sub-oxide layer depth after 1000 hrs at 1320°C for β' + YAG alloys with increasing 21R content	131
9.3	a) TEM section of sub-oxide zone showing isolated and reduced volume YAG phase b) Schematic of mechanism of YAG volume reduction and "isolation". c) SEM section identifying transition stage	132
9.4	Oxide thickness with time for material with "isolated" YAG and O' matrix at 1350°C	132
9.5	a) SEM section of β' + YAG material oxidised for 1000 hrs at 1350°C to produce a β' + O' layer b) Comparison of oxidation rates for the range of Si-Al-O-Ns at 1350°C	133
A1.1	Y-Si-Al-O-N system representation, expressed in equivalents	136
A4.1	Schematic route for determining the machine relaxation	138
A4.2	Actual machine relaxation relationships at 1200°C	139
A4.3	Young's modulus variation with temperature for the various alloys	140

LIST OF TABLES

		<u>Follows</u> <u>Page</u>
1.1	Comparison of properties of high performance metals and ceramics	2
1.2	Government financial support for ceramics	2
1.3	Properties of current high temperature structural ceramics	3
2.1	Molar volume changes of unstable secondary phases compatible with Si_3N_4	19
3.1	K_{IC} values for Si_3N_4 ceramics and other brittle materials	28
5.1	Fabrication details of the range of Y-Si-Al-O-N studied	49
5.2	The β' grain size distribution for the as-sintered alloys S0 and S13	55
5.3	Densities and porosity levels for as-sintered alloys	61

CHAPTER ONE

INTRODUCTORY REVIEW AND OBJECTIVES

In this chapter, a brief history of ceramic development for high temperature engineering applications is presented emphasising (i) the significance (financial and political) of potential ceramic deployment, (ii) the degree of future commitment, (iii) the current level of commercialisation of these ceramics. The microstructure and properties of Silicon Nitride and development of Si-Al-O-N ceramics are described in detail. The important high temperature limitations (oxidation, fracture, phase equilibria) of a specific range of commercial Si-Al-O-N materials are discussed and the objectives of this research presented.

1.1. ENGINEERING WITH CERAMICS

Gas Turbine Engine (G.T.E.) developments since the 1930's have been aimed at achieving their greater potential efficiency mainly by increase of the operating temperature. The need for higher temperature structural materials led to major modifications of the existing metals to arrive at the current metallic superalloys (commonly Nickel based with up to 15% Chromium). However, further efficiency improvement to the levels now sought by manufacturers is limited by the small potential rise of operating temperature with continuous development of already complex and expensive metals. At high temperatures ($> 1000^{\circ}\text{C}$) metals plastically deform and are chemically attacked by the atmosphere and corrosive fuel elements. Overcoming these inherent problems has required the use of strategic metal alloying (Ni, Cr), cooling systems, protective coatings, fuel purification etc., all of which are complex and expensive processes.

An alternative approach to a major efficiency increase was to relook at ceramics with their inherent high temperature ($> 1200^{\circ}\text{C}$) stability and chemical resistance. The required properties were high elastic modulus, low density and high melting or decompositional temperature. All of these demand high interatomic bond strengths implying covalent bonding. The short-list of covalently bonded ceramics may be reduced to Silicon Carbide (SiC) and Silicon Nitride (Si_3N_4) when the engineering properties of thermal shock resistance (which eliminates Alumina) and oxidation resistance are considered. A comparison of properties of these ceramics with present Ni-based superalloys (Table 1.1) indicates the potential of ceramics as high temperature structural materials.

The projected benefits of a ceramic based G.T.E are numerous. Firstly, the raising of operating temperatures to a targeted 1370°C (presently 1050°C) could result in efficiency improvements up to 20% (1), fuel savings up to 50% (2) and minimized exhaust pollution. Secondly, ceramic employment would reduce component weight (increasing efficiency and also speed of response), and allow the use of cheaper low grade fuels. The high temperature mechanical stability advantage would eliminate the necessity for cooling systems, greatly reducing the cost and weight of a G.T.E.

At present, America, Japan and West Germany are heavily involved in ceramic development and its application to energy conservation. The driving force behind this commitment is to minimise their dependence on imported oil (motivated by two oil crises) and imported strategic metals. With full implementation of ceramic-based G.T.E.s and heat exchangers a \$17.5 billion saving on imported oil could be possible (3) in America alone. Ceramic component/product sales could also enhance the pay-off for this high risk development. A partial ceramic

PROPERTY	Ni-BASE ALLOY	SiC/SN
High Temp Use	~ 1250°C melts	1700°C/1450°C
Corrosion Res.	Need coating	No coating
Mat. Cost	\$5-30/lb (ingot)	\$0.4-2/lb (powder)
Density	~ 8g/cm ³	3.2g/cm ³
Strategic materials	Ni + ~ 15% Cr	Si, C and N ₂

Table 1.1. COMPARISON OF PROPERTIES OF HIGH PERFORMANCE METALS AND CERAMICS (AFTER 1)

COUNTRY	PREVIOUS FUNDING ON AD. GAS TURBINES	PORTION SPENT ON MAT. DEV.	FUTURE COMMITMENT
USA	'71-'83 \$258m	\$28m	Continued support - emphasis on reliability & automotive applications
Japan	-'83 \$150m	\$36m	10 year prog. (\$60m) to establish industrial standard ceramic base
W. Germany	'74-'83 \$48m	\$26m	Private companies supported in automotive & heat engine dev.

Table 1.2. GOVERNMENT FINANCIAL SUPPORT FOR CERAMICS (AFTER 5)

replacement (~ 10%) for metals in current engines (internal combustion and turbine) could alone be worth \$5 billion and the potential demand for all-ceramic engines could reach \$30 billion worldwide (4). The conversion of a cheap, readily available source to high value-added components (heat engines and also new applications) could enhance manufacturing efficiency and secure a new, expanding market in a similar way that micro-electronics has. Although there is much at stake and heavy market competition, a universal desire exists to utilise ceramics as a new technological base. Movement towards this ideal state has meant previous heavy Government investment and future financial commitment (Table 1.2). Silicon Nitride due to its high thermal shock resistance was initially considered the most promising engineering ceramic and was heavily researched and developed in its Hot-Pressed (HPSN) and Reaction Bonded forms (see Fabrication section).

The last five years, however, have witnessed rapid ceramic development. Now materials such as Partially Stabilized Zirconia (P.S.Z) and glass ceramics have appeared along with new Si_3N_4 processing techniques (see Fabrication). A range of engineering ceramics and processing routes can now be considered specifically for each application on the basis of shape complexity, strength, oxidation resistance, temperature etc. (Table 1.3). This has stimulated competition and made ceramics manufacturers more cost-effective, bringing the advent of cheap, easy to shape, reliable engineering ceramics closer.

The current (1983) momentum and commercial success of some of these materials should be noted. Nissan Motor Co. (5) have given a working demonstration of a prototype vehicle containing a ceramic G.T.E., whilst Kyoto Ceramics Co. (5) have developed and tested the worlds first ceramic diesel engine, utilizing Si_3N_4 pistons, sleeves, tappets etc.

MATERIALS	DENSITY (g./cm. ³)	FLEXURAL STRENGTH (MPa)			ROOM TEMP.	HIGH TEMP.	K _{IC} (MPa.m ^{1/2})	YOUNG'S MOD. E (GPa)	MELTING OR DECOMPOSITION TEMP (°C)	ADDITIONAL CONSIDERATIONS
		PROCESSING	TEMP.	TEMP.						
Si ₃ N ₄ RBSN	2.7-2.8	Slip, Injection Moulding, etc.	359-200	320-200 (1200°C)	3-4	118-200	1897*(D)			High oxidation rate due to high surface area
SRBSN (8% Y ₂ O ₃)	3.26-3.31	Slip, Injection Moulding, etc.	742-1000	632 (1200°C)	-	-	1897*(D)			Oxidation expected to be high
Sintered SN	3.2	Slip, Injection Moulding, etc.	800 (MOR)	700 (1300°C)	8-10	-	1897*(D)			Poor oxidation resistance and mech. properties above 1000°C due to g.b.s.
HPSN	3.1-3.2	Only simple shapes then machining	965	~500	4-8	310	1897*(D)			Poor oxidation resistance and mech. properties above 1300°C due to g.b.s.
SiC sintered	3.1-3.2	Slip, Injection etc.			3-4	350-450	2723 (D)			Good resistance to oxidation and S.C.G. at high temps. However, low thermal shock resistance.
P.S.Z. (MgO + Y ₂ O ₃)	5.75-6.03	Slip, Injection etc.	700-980	-	8-10	210	2680 (m)			High thermal expansion coeff. - close match to steel.
L.A.S.		Slip, Injection, etc. + glass forming tech.	60-75 (MOR)	-	-	-	1100 (m)			Very low thermal expansion, excellent thermal shock resistance.

Abbreviations

RBSN	Reaction Bonded Si ₃ N ₄	6
SRBSN	Sintered Reaction Bonded Si ₃ N ₄	6, 7
HPSN	Hot-pressed Si ₃ N ₄	8, 9
SiC	Silicon Carbide	10
P.S.Z.	Partially Stabilized Zirconia	11
L.A.S.	Lithium Aluminosilicate	6
K _{IC}	Critical Stress Intensity Factor	

Source of Data

6
6, 7
8, 9
10
11
6

Table 1.3

PROPERTIES OF CURRENT HIGH TEMPERATURE

STRUCTURAL CERAMICS

American studies on diesel engines fitted with HPSN piston caps have given the highest ever level of fuel efficiency measured for an experimental vehicle engine (12). Ford (13) have converted to using Si_3N_4 and SiC turbo charger components with the 60% weight reduction significantly enhancing performance. Lucas (14) and Ford are producing successful high speed Si_3N_4 -based cutting tools along with bearings, seals, dies, etc. The future for these engineering ceramics looks secure, with continued Government funding, increased public awareness (through the "Space-Shuttle" tiles etc.) and manufacturers' commitments. Ford (15), Nissan, Toshiba (4) and Daimler-Benz all anticipate the commercialization of ceramic G.T.E powered automobiles by 1990. Before this are planned the ceramic diesel engine (Toshiba-4), Wankel engine with P.S.Z housing plus Si_3N_4 rotor and ceramic turbo-charger (13).

The biggest factor in the success of these ceramics is their acceptability by the general engineer. The ceramics traditional reputation of strength variability, brittle nature and lack of warning of imminent failure (via rubbing, distortion) are disadvantageous. Ceramics must prove themselves as reliable and reproducible materials before they will have wider application (to include the lucrative aerospace and heat pump applications).

1.2. SILICON NITRIDE CERAMICS

1.2.1. Crystal Chemistry of Si_3N_4

Si_3N_4 has two crystalline structures, α and β ; both are hexagonal. The crystal building unit is the covalently bonded SiN_4 tetrahedra which join together by sharing corners (Fig. 1.1a,b). The

β - Si_3N_4 structure is best visualised as the stacking of 8-atom rings (4 x Si, 4 x N) along the c-axis of an hexagonal symmetric structure (Fig. 1.1c) to give a stacking sequence of layers of

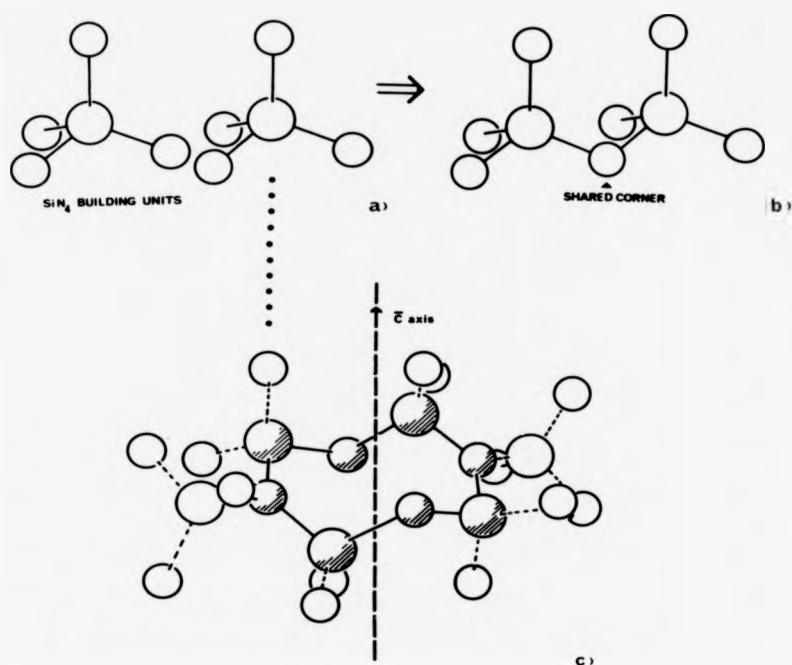


Fig.1.1 The crystal structure of $\beta\text{-Si}_3\text{N}_4$.

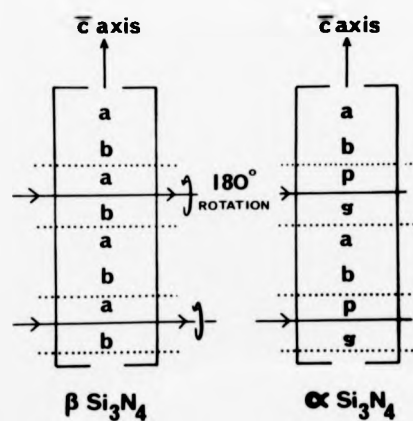


Fig.1.2 The relationship between β and $\alpha\text{-Si}_3\text{N}_4$ crystal structures.

ABABAB ... The β hexagonal unit cell size is then $a = 7.608 \text{ \AA}$ and $c = 2.911 \text{ \AA}$. The α - Si_3N_4 structure is similar to and can be derived from it by a 180° rotation of two basal stacking planes (Fig. 1.2) which doubles its unit cell size to $a = 7.608 \text{ \AA}$ and $c = 5.822 \text{ \AA}$. A transformation between structures occurs ($\alpha \rightarrow \beta$) but requires atomic reconstruction (either volatilization/ condensation or solution/ precipitation). Both α and β - Si_3N_4 structures exist over a range of temperatures but β is thought to be the thermodynamically stable form above 1500°C (e.g. transformations occur during densification of Si_3N_4 powders). These characteristic differences between structures become important during the fabrication of dense Si_3N_4 bodies where the ratio of starting powders has been shown to dominate microstructural and mechanical properties (16).

The Si-N covalent bonding, low atomic weights and co-ordination number, give Si_3N_4 the intrinsic mechanical properties of high elastic modulus, low density and high decomposition temperature. Densified Si_3N_4 is also endowed with excellent thermal shock, wear, corrosion and oxidation resistance, making it a useful engineering ceramic. Its utilisation depends on its ability to be fabricated to engineering component shapes.

1.2.2. Si_3N_4 Fabrication

Si_3N_4 does not occur naturally. The common synthesis route is the nitridation of silicon, a vapour phase reaction that produces mainly α - Si_3N_4 whiskers. The subsequent powders are claimed (17) to have low impurity levels and a fine uniform grain size ($0.1 - 1.0 \text{ \mu m}$) with large specific surface area (beneficial for densification). Alternative synthesis routes have recently appeared. (i) Volatile silicon compound reactions ($\text{Si}(\text{NH})_2$, SiH_4) produce an amorphous product which is controllably crystallised to fine, uniform, low

impurity powder. Low α -yield and specific surface area are limitations (18, 19). (ii) Carbothermic reduction of silica (20), which although has a high α -yield results in unacceptable impurity levels (21).

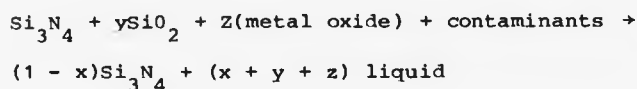
Impurities are present in all commercial Si_3N_4 powder and are derived from the raw materials and subsequent powder production (i.e. ball milling, acid washing, etc.). The major contaminant is oxygen (varying between 0.3 and 3 weight %), present as the unavoidable surface oxide SiO_2 on each Si_3N_4 particle. The SiO_2 content can vary between 1.2 and 12 molar % depending on particle surface areas. These contaminants can have a significant effect on the final microstructure and properties of a dense Si_3N_4 body (detailed later).

"Pure" Si_3N_4 powder shows a remarkable resistance to sintering. Very high pressures and temperatures have been required to obtain acceptable densities (22). The resistance is due to insufficient volume diffusion (a consequence of the low self-diffusivity characteristic of covalently bonded solids) and also the volatilization phenomena of Si_3N_4 (23).

Two basic fabrication routes for Si_3N_4 bodies exist; Reaction Bonding and Liquid-phase sintering. In reaction bonding a preform from compacted silicon powder (produced by any conventional ceramic processing; slip, extrusion etc.) is nitrided ($\sim 1400^\circ\text{C}$) to give a Si_3N_4 body with approximately 25% porosity. The original dimensions of the silicon compact remain virtually unchanged allowing complex and precise Si_3N_4 shapes to be produced. High porosity is a prerequisite of the silicon compact. It allows permeation of N_2 to all parts of the component ensuring complete nitridation and reduction of detrimental free silicon levels. The porosity unfortunately dominates mechanical properties

giving low strength (due to high flaw density) and reduced oxidation resistance (due to high surface area).

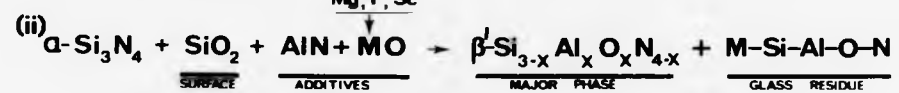
The first dense Si_3N_4 (24) was prepared by "Hot-Pressing" α -powder (at 1700°C) together with a densification aid. Today, many metal oxides (e.g. MgO , Mn_2O_3 , Y_2O_3 , Al_2O_3) and some nitrides are known densification aids (25, 26, 27). Densification is attributed to the presence of a liquid formed by the reaction of all constituents above a eutectic temperature.



The SiO_2 is derived from the Si_3N_4 surface oxide layer. A typical Hot-Pressed Silicon Nitride (HPSN) microstructure is then **polyphase** consisting of fine ($\sim 1 \mu\text{m}$) equiaxed β - Si_3N_4 grains with a glassy phase (the cooled residue of the sintering liquid) distributed along the grain boundaries.

The Hot-Pressing densification mechanism is usually visualised (Fig. 1.3) in 3 overlapping steps. (1) Stress assisted α particle re-arrangement upon initial liquid formation and flow. (2) Further densification concurrent with a solution-precipitation mechanism. The α -particles are taken into solution and reprecipitated as β - Si_3N_4 crystals at α -liquid boundaries. The subsequent diffusion and removal of material thus reduces pore volume. (3) A rapid fall in densification upon formation of a solid framework.

The grain-boundary glass phase softens above 1000°C and the excellent high temperature properties promised by Si_3N_4 (high strength, creep and fracture resistance) are all drastically degraded. This phase also acts as a rapid diffusion channel for segregated impurity/additive ions and oxygen which can degrade the oxidation



resistance of Si_3N_4 . A review of high temperature fracture and oxidation of Si_3N_4 is included in Chapters Two and Three.

The major limitations of HPSN are the residual glass phase and also the restrictions on component shape, size and cost imposed by the fabrication route. Hot-pressing offers advantages over conventional sintering by providing additional densification mechanisms via stress-assisted rearrangement, plastic deformation and creep of α particles and enhanced diffusional atomic transport. However, the high pressures restrict the die configurations to only small and simple shapes. Additional expensive diamond tool machinery is required to produce complex shaped HPSN.

Demand for complex engineering shapes of dense Si_3N_4 (formed by traditional ceramic processing) stimulated fabrication development with an emphasis on pressureless sintering. Other materials can generally be successfully sintered at temperatures higher ($\sim 200^\circ\text{C}$) than the hot-pressing temperature. With Si_3N_4 these higher temperatures cause rapid thermal decomposition with weight loss of Si, SiO and N_2 . Nitrogen overpressure (29) and powder beds (30), acting as buffers, have considerably reduced this problem. However the present sinterability of Si_3N_4 is mainly due to improved $\alpha\text{-Si}_3\text{N}_4$ starting powders which have finer, uniform sized particles (giving high pre-sinter densities) with high surface area (giving greater surface SiO_2 volumes). Without the stress assistance, a larger sintering liquid volume than used for HPSN is required. The enhanced SiO_2 volume is therefore reacted with larger sintering additions to give this required liquid volume.

Selection of an appropriate sintering aid can lead to a lower eutectic liquidus temperature and hence reduce liquid viscosity at the sintering temperature. Enhanced densification is thereby facilitated by greater particle rearrangement during step 1, and a greater rate of

material diffusion during step 2. Although dense complex shapes can be produced cheaply and have excellent low temperature properties, Pressureless-Sintered Si_3N_4 (PSSN) has even larger grain boundary glassy residuals and consequently its high temperature properties suffer to a greater extent (31, 32) than HPSN.

An alternative route to dense, shapeable Si_3N_4 is the recent development of Post-Sintering of RBSN (33). A RBSN component has sintering aid added to it (either as a powder before silicon nitridation or by liquid/vapour impregnation of nitrided body) and is then pressureless sintered. Post sintering drastically reduces pore density which increases component densities (from $\sim 75\%$ to 100% theoretical). The room temperature strength of RBSN is doubled and the improvement is maintained up to 1400°C . The technique also offers reduced sintering shrinkage over a PSSN body.

A new processing technique, Hot Isostatic Pressing (H.I.P), is currently being successfully applied to Si_3N_4 fabrication (34) and offers hot-pressing advantages (i.e. low liquid volumes + high, uniform densities) without the shape restriction. A complex shaped $\alpha\text{-Si}_3\text{N}_4$ powder compact (complete with sintering additive) is sprayed with glass beads which form an envelope around the body upon heating. Subsequent sintering is performed under a very high pressure (10^3 Atms) inert atmosphere.

1.2.3. Improvement of Grain Boundary Phase Properties

The previously discussed fabrication routes for dense complex shaped Si_3N_4 still produce a residual grain-boundary (gb) glassy phase. The identification of this phase as the major influence of high temperature properties (Chapters 2 and 3) has stimulated research and development of this phase to bring about significant improvements in the total performance of these ceramics. Generally, two routes have

been followed and are summarized in Fig.1.4. Firstly the reduction of the total amount of g.b. phase, mainly by reducing the sintering liquid volume requirement. This can be facilitated by H.I.P.ing, higher sinter temperatures, choice of more reactive sinter aid and continual α - Si_3N_4 powder development (increasing reactivity and green densities). However, even very small quantities of g.b. glass ($\sim 10 \text{ \AA}$ thick) can maintain significant high temperature property degradation.

The second route is the accepting of a large liquid volume during sintering but improving the high temperature properties of the residual g.b. glass or crystallising it to be a refractory medium, thereby also reducing or eliminating the glass. The use of Y_2O_3 instead of MgO as a sintering aid in HPSN gave high temperature property improvements which were associated with the higher viscosity of the subsequent residual glass. Variations in metal oxide types (studied as sintering aids) together with impurity concentrations have shown significant influence on residual glass properties and hence those of polyphase Si_3N_4 materials.

Crystallisation to a refractory structure offers the potential of complete g.b. glass removal and also possible property enhancement of the polyphase Si_3N_4 through the properties of the new phase. However complete g.b. crystallisation has been elusive (35, 36) and some crystalline phases have shown catastrophic composite degradation due to oxidation instabilities (38).

An alternative route of residual glass removal could be for evolving grains to take the g.b. elements into solid solution.

1.3. Si-Al-O-N CERAMICS

It was discovered concurrently in Japan and England (39, 26) that Al_2O_3 was soluble in β - Si_3N_4 . In this substituted β - Si_3N_4 , Al^{3+} replaces Si^{4+} if simultaneously O^{2-} replaces N^{3-} to

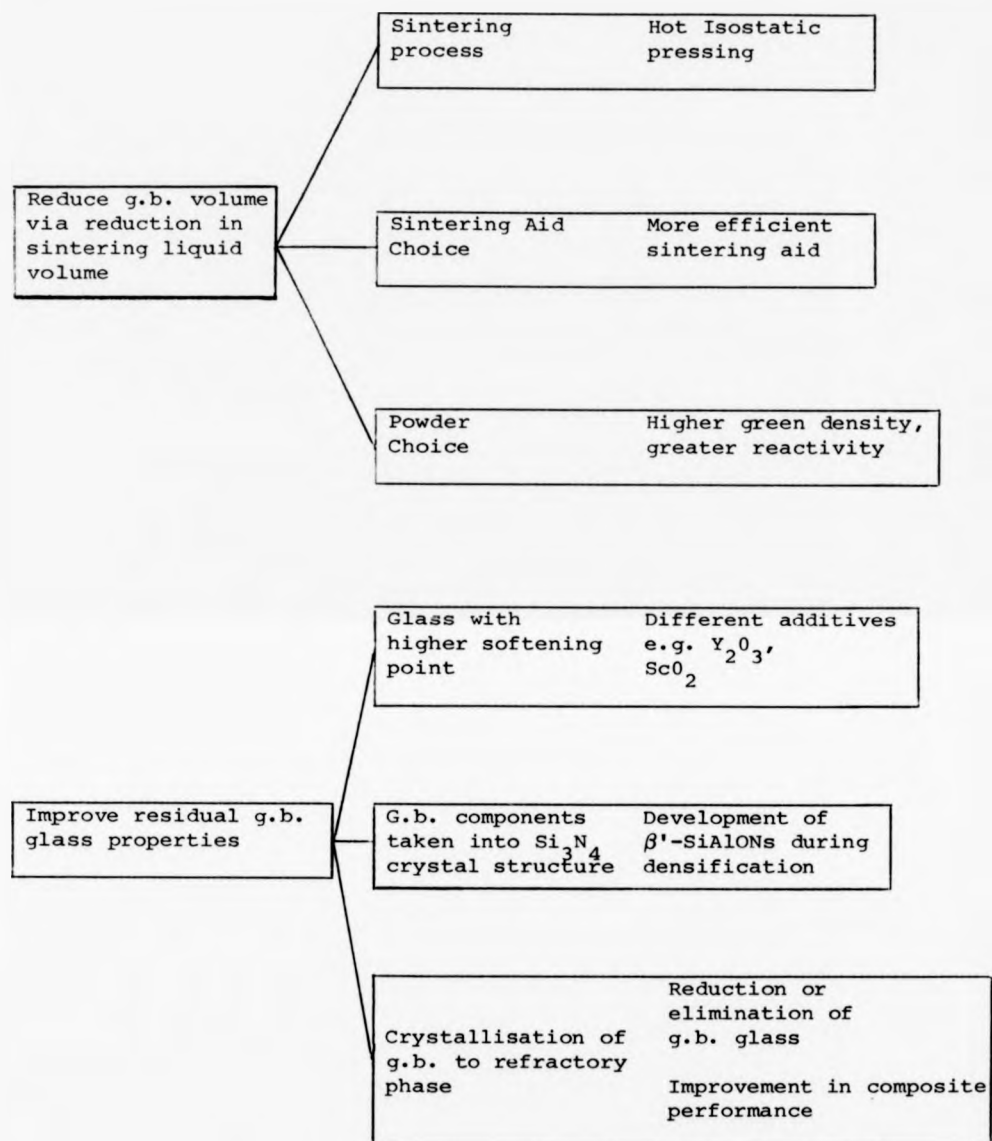
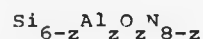


Fig. 1.4. General approaches to improvement of high temperature properties of Si_3N_4 materials.

maintain charge neutrality. The crystal structure is expanded but remains hexagonal and is termed β' (beta prime). Materials resulting from fabrication of suitable mixtures of only $\alpha\text{-Si}_3\text{N}_4$ and Al_2O_3 however, still contained a residual glass (40). Lumby et al. (25) showed that using a mixture of $\alpha\text{-Si}_3\text{N}_4$, AlN and SiO_2 , single phase materials were obtainable if the surface SiO_2 addition were accounted for and "balanced" by an increased AlN level. The composition of this nominally single-phase "balanced" material is approximately represented by



(where z is the Al substitution level and can rise continuously up to ~ 4 , the limit of Al^{3+} substitution). Mixtures of Si_3N_4 , Al_2O_3 , SiO_2 and AlN can be hot-pressed to give balanced $\beta'\text{-Si}_3\text{N}_4$ and also a range of materials known collectively as Si-Al-O-N ceramics.

The usual representation is Fig. 1.5 (see Appendix 1.1 for explanation). The densification mechanism is essentially similar to that of HPSN. (i.e. solution/reprecipitation) but with the modification (42) of reprecipitation of β' crystals from a silicate liquid, initially formed mainly by AlN reaction with surface SiO_2 at 1600°C . The use of metal oxides (MgO , Mn_2O_3) speeds up densification by lowering the liquidus-temperature and viscosity of the silicate liquid (42). In "balanced" compositions some of the ions (Al_2O_3) present in the silicate liquid were incorporated within the β' structure resulting in residual glass being detectable only at triple-grain boundaries. This reduction in g.b. glass gave dramatic improvements in creep resistance (25).

Following a similar development route as Si_3N_4 , pressureless sintered $\beta'\text{-Si-Al-O-N}$ ceramics with an accepted substantial residual

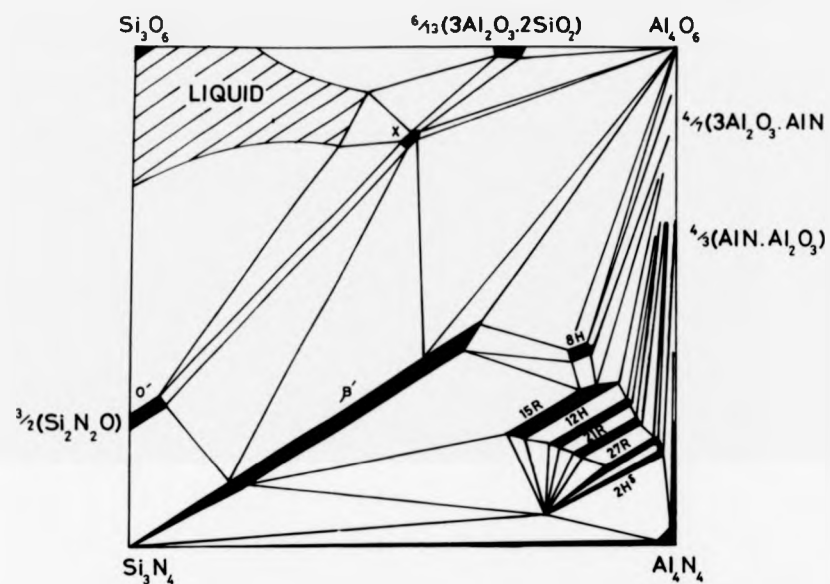


Fig.1.5 Si-Al-O-N system representation, expressed in equivalents. Phase equilibrium at 1570°C. After ref.37.

"matrix" phase are now being explored and are the subject of this thesis. These materials offer important advantages over PSSN. The large sintering liquid volume (whose viscosity is further reduced by the Al_2O_3 addition) allows ease of sinterability and full densification and therefore cheaper, reliable, complex-shaped components. Further, the increased flexibility of the "matrix" composition (by M:Al:Si:O:N balance) permits the idea of a range of ceramic alloys which can be tailored to specific applications. Glass matrix composition and volume optimisation has produced commercially successful low temperature material for uses as cutting tool, dies, bearings, etc. (14). For high temperature applications, requiring reduced g.b. glass volumes, this flexibility allows matrix compositions optimal for post-sintering crystallisation. Crystallisation to products based on the major additives MgO and Y_2O_3 have been obtained (43). In addition complete matrix crystallisation is feasible by the incorporation into the β' structure of residual (post crystallisation) glass components.

Bhatti (44) appears to have successfully crystallised a Y-Si-Al-O-N matrix completely to a substituted Yttrium Aluminium Garnet ("YAG") and produced a sintered material with excellent high temperature mechanical properties. This promising material is marred by an instability in air above $\sim 1320^\circ\text{C}$ which results in catastrophic oxidation kinetics and structural degradation (45). A matrix/ environment reaction was suggested to explain these phenomena although not confirmed. In HPSN, similar interactions with oxidising environments can alter the composition and structure of the fine but continuous g.b. phase to a considerable depth within a material (46). This can lead to drastic high temperature creep and fracture improvements (47) in amorphous g.b. materials but also catastrophic structural failure (38) with certain crystalline matrix phases.

In the present materials the g.b. phase is substantial and any instability (resulting from matrix crystallisation to environmental interactions) would be expected to be amplified. To be deemed reliable high-temperature materials, these instabilities and their consequence for the principle mechanical properties (oxidation resistance, fracture) must be determined.

1.4. OBJECTIVES

- (i) To determine the high temperature ($> 1200^{\circ}\text{C}$) microstructural stability of range of sintered Y-Si-Al-O-N ceramics, with respect to initial composition and test environment. The identification of the β' + YAG material instability mechanism is paramount.
- (ii) To determine the oxidation behaviour of these materials, the nature, rate limiting mechanisms and routes to subsequent improvement within the field of compositional variability.
- (iii) To compare the microstructural stability of these materials with a range of Hot-Pressed Si-Al-O-N ceramics when subjected to the ultra high-temperature ($> 1450^{\circ}\text{C}$) heating, facilitated by laser irradiation. The feasibility of laser machining of Si-Al-O-N ceramics is also to be assessed.
- (iv) To study the influence on fracture parameters and fracture mechanisms of initial microstructure, temperature and environment.

CHAPTER TWO

STABILITY OF CERAMIC MICROSTRUCTURE IN OXIDISING ENVIRONMENTS:

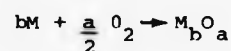
A REVIEW

In this chapter, the general oxidation phenomenon is presented followed by a review of the oxidation mechanisms of Si_3N_4 -based ceramics and their measurement.

2.1. OXIDATION MECHANISMS

Microstructural resistance to hostile environments is an important requirement for a successful engineering material. Oxidation can give rise to dimensional instabilities, a spalling oxide scale, premature fracture, deleterious gaseous by-products, all intolerable in a high performance design.

In metals, an initial reaction with atmospheric Oxygen produces an M-O bond (due to electron transfer from the metal's conduction band) and allows O^{2-} ion incorporation into the metal surface which then constitutes an oxide layer, i.e.



where a and b are the cation and anion valence states respectively. Initially the oxide thickness is controlled by reaction rate and ease of O ion incorporation. Usually, M and O ions will then have to move through a developed coherent oxide scale to the reaction interface and their diffusion contributes to the oxidation process. As the scale grows in thickness, the ion flux decreases and the rate of scale growth becomes inversely proportional to scale thickness. For many metals which develop dense non-porous scales, their oxide thickness (x) with time (t) can be represented by the Parabolic Rate Law:-

$$x^2 = K \cdot t + C_0 \simeq K \cdot t \quad (2.1.)$$

where K = Parabolic Rate Constant and C_0 the initial oxide formation (usually neglected for high oxidation rates). Parabolic dependence was theoretically predicted by Wagner (48) who considered oxidation rates controlled by diffusion. The rate constant varies with diffusion coefficients, oxygen pressure and temperature and can be represented by

$$K = K_0 \exp \left(\frac{-\Delta H}{RT} \right) \quad (2.2.)$$

where ΔH = Activation Enthalpy for oxidation

R = Gas Constant

T = Absolute temperature of oxidation process

K_0 = Constant.

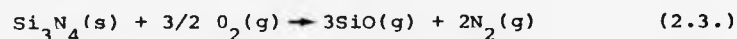
The exponential temperature dependence simply reflects a diffusion phenomenon. Oxidation is controlled by the slowest reaction and therefore ΔH in a diffusion rate-controlled oxidation is equivalent to the activation energy for diffusion and identifies the rate controlling diffusive species. Some metals have oxide scales which are porous, semi-porous or have time dependent porosity. This will alter the oxygen access to the underlying metal and hence the oxidation rate. With perfectly free oxygen access, the rate becomes linear with only reaction rate dependency. With a variety of scale types, oxidation rates can become pseudo-linear, para-linear etc. Oxidation rate measurement can identify the rate limiting process (reaction, diffusion) and lead to oxidation resistance improvements

2.2. OXIDATION OF Si_3N_4 -BASED CERAMICS

There are two types of oxidation reaction for Si_3N_4 , "Active" and "Passive";

(i) **Active Oxidation**

This occurs under very low oxygen potentials. In oxygen atmospheres the reaction is



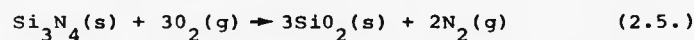
For reactions with low oxygen potential non-gaseous sources, such as the passive SiO_2 oxide (eqn. 2.5), this can lead to



Active oxidation is characterised by overall specimen weight loss due to gaseous SiO formation. However, any $\text{SiO}(\text{g})$ formed at the $\text{Si}_3\text{N}_4/\text{SiO}_2$ interface should be oxidised to $\text{SiO}_2(\text{s})$ in the pores and fissures formed by N_2 evolution (49). Up to 1400°C , the $\text{SiO}(\text{g})$ gas pressures are not appreciable (49).

(ii) **Passive (Parabolic) Oxidation**

This reaction is observed under normal atmospheres (high oxygen potential). The oxidation rate usually follows the Parabolic Rate law and the reaction is represented by:-



although $\text{Si}_2\text{N}_2\text{O}$ may form as an intermediate phase. The SiO_2 is usually amorphous and viscous and leads to an overall specimen weight gain. The generated N atoms are dissipated either by ionic diffusion through the oxide or, more usually, by N_2 gas bubble formation. If bubbles exceed the ambient pressure, they are released to the atmosphere, causing oxide perforation and modification of the parabolic rate. The $\text{SiO}_2(\text{s})$ has good thermal stability, with the evolution of its predominant volatile species, $\text{SiO}(\text{g})$, being negligible at the temperatures of interest. The oxidation enthalpy

for pure (C.V.D.) Si_3N_4 (between 1100°C - 1300°C) is $\approx 145 \text{ kJmol}^{-1}$ (49) and is similar to those obtained for SiC , Si and $\text{Si}_2\text{N}_2\text{O}$ which also produce protective SiO_2 oxides (50). The activation energy for diffusion of Oxygen through SiO_2 glass and melts (51) is very close to this value, and O^{2-} in-diffusion was concluded to be the rate determining mechanism for pure Si_3N_4 (50). This extremely low ΔH , coupled with the viscous, self-healing oxide at high temperatures gives these materials their superior oxidation resistance over metals.

The transition from active to passive oxidation varies with oxygen potential and temperature (52).

Dense HPSN also exhibits parabolic oxidation kinetics, although rate constants are considerably higher than pure C.V.D. Si_3N_4 . The reason is believed to be enhanced O^{2-} diffusion through a reduced viscosity oxide. Viscosity reduction occurs with the considerable compositional shift brought about by large outdiffusion of impurities (additive and contaminants) derived from the continuous g.b. residual glass. Cubiccioti and Lau (53), however, showed that the parabolic rate law observed during formation of a considerable oxide thickness was unaltered if this oxide were removed. The oxidation rate was not then dependent on oxide thickness or diffusion through it but indirectly controlled by the rate of outdiffusion of metallic impurity cations into the SiO_2 film. This outdiffusion from a limited volume g.b. channel would form a gradient of depleted elements, which has consistently been confirmed by chemical analysis (53,54,55). A compositional gradient therefore exists beneath the oxide layer whose extent is governed by the parabolic rate law.

A revised oxidation mechanism (53) considers the oxide as an SiO_2 melt in which Si_3N_4 has increasing solubility with impurity content. Reaction of dissolved Si_3N_4 with dissolved O^{2-} leads to

increased oxide kinetics. Not all diffusing metallics reduce SiO_2 viscosity, for example Al^{3+} solubility (derived from β' Si-Al-O-N), is claimed to maintain high oxide viscosities (54).

Cation flux into the oxide (and hence oxidation resistance), is determined by g.b. elemental concentrations, their rate of diffusion and the g.b. cross-section. These parameters have been studied indirectly by altering the amount of sintering aid (mainly MgO and Y_2O_3). Increasing MgO additive to HPSN has been shown by many workers (55, 56, 57, 58, 59) to increase oxidation rates. Babini (58, 59) assumed a constant g.b. composition and from a simplified diffusion model showed a direct correlation between average g.b. cross-section and oxidation rate. Lange (56) also showed a rate increase due to MgO content increase in a fixed g.b. volume. This effect has been replicated with Y_2O_3 additives (60) although Wu et al. (57) found oxidation rates uninfluenced by Y_2O_3 or ZrO_2 additive variations.

Large g.b. volumes can be tolerated if they contain slow diffusing species. Metallic cation diffusivity is strongly affected by g.b. glass viscosity and cation type. The observation of increased oxidation resistance when using Y_2O_3 sintering aid instead of MgO is credited to the higher viscosity of the Y containing g.b. residual glass. Bulk glass viscosity (61, 62) and Si_3N_4 sinterability studies confirm the viscosity differences. Variations in diffusive cation radii can alter diffusion profiles. The excellent oxidation resistance of HPSNs with ScO_2 (63) and ZrO_2 (64) additives is believed to be due to enhanced network bonding in the g.b. glass and therefore slower cation diffusion. The influence of Al_2O_3 additives to Si_3N_4 alloys is confusing. In H.P. Si-Al-O-N ceramics, increasing Al-substitution results in greater oxidation resistance (65, 54), credited to the out-diffusing dissolved Al^{3+} which increases the oxide

viscosity (54). However, increasing Al_2O_3 additives to HPSN (66) reduced oxidation resistance, although no explanation was developed.

2.3 OXIDATION-INDUCED SUBSURFACE TRANSFORMATIONS

Where g.b. volume is small, the depletion of metallics from the SiO_2 rich g.b. glass increases its viscosity and decreases its volume. Subsequent cation outdiffusion (and oxygen indiffusion) through this g.b. are then both reduced which leads to the enhanced oxidation resistance. The g.b. volume is thought to effectively vanish in certain β' -Si-Al-O-N compositions after extensive oxidation, resulting in stronger intergranular cohesion (67) which gives enhanced creep and fracture resistance.

Parabolic kinetics of some Si_3N_4 compositions are, however, drastically disrupted by long term mechanisms or particular temperature intervals due to deleterious phase-changes in the oxide scale or sub-oxide g.b. Since the SiO_2 oxide is more voluminous than the β substrate, compressive stresses normally develop with scale growth. Stress also arises from gaseous oxidation products ($\text{N}_2 + \text{SiO}$) which accumulate at the oxide/ Si_3N_4 interface. Stress accommodation in the scale is usually by viscous flow. The lowering of viscosity by impurities can catalyse oxide crystallisation which can lead to larger compressive stresses and, more critically, reduced oxide plasticity. These mechanisms can thus result in a cracked, non-protective, oxide allowing direct access of atmosphere to the Si_3N_4 . Accelerated oxidation attributed to these mechanisms has been reported in many HPSN and PSSN studies (39 , 54). Induced substrate cracking can also occur leading to premature mechanical failure. Substrate pit formation by oxide attack (usually attributed to W, WC impurity concentrations) is also thought to be a source for premature failure (57).

If the g.b. phase can be crystallised, passive oxidation resistance should be increased due to the lower cation mobility. However, catastrophic degradation may occur as this phase will be subject to oxidation or reaction with the SiO_2 at the surface layer. If g.b. phase oxidation or reaction leads to large molar volume changes and the subsequent compressive stress cannot be accommodated by surface layer plasticity (due to low temperatures), surface spalling and eventual specimen disintegration can occur (68). Table 2.1. gives the molar volume changes of unstable secondary phases compatible with Si_3N_4 .

If the crystalline g.b. phase were to react with SiO_2 , a eutectic liquid could be produced at a high enough temperature. The now amorphous g.b. would reduce both oxidation resistance and mechanical stability. This reaction was proposed (45) in explanation of the catastrophic strength reduction of β' + "YAG" materials when tested in air above a critical temperature (1320°C). Fig. 2.1. illustrates a four-point bend creep bar tested in air below (Fig. 2.1a) and above (Fig. 2.1b) 1320°C. A major research objective is therefore to precisely identify (through a microstructural study) the mechanisms responsible and develop fabrication routes to overcome this degradation.

Although extensive oxidation data on HPSN exists, little work has been performed on the more practical PSSN (with larger g.b. volumes). However, oxidation resistance is usually found to be worse (32,58) due to the reservoir of impurities. In sintered Si-Al-O-N ceramics, the g.b. glass composition is complicated by N and Al elements (which may be advantageous as viscosity enhancers). The assessment of oxidation resistance, and determination as to whether this increased g.b. volume will undergo the similar beneficial volume reduction and compositional changes upon long term oxidation as HPSN, are other objectives of the present work.

SECONDARY PHASE	OXIDATION PRODUCT	VOLUME CHANGE (%)
$Y_2Si_3O_3N_4$	$Y_2Si_2O_7 + SiO_2$	+30
$YSiO_2N$	$0.5Y_2Si_2O_7$	+12
$Y_5(SiO_4)_3N$	$0.75Y_4Si_6O_{13} + 0.75Y_2SiO_5$	+ 4
$Ce_5(SiO_4)_3N$	$5CeO_2 + 3SiO_2$	+ 8
$CeSiO_2N$	$CeO_2 + SiO_2$	+14
$Ce_2Si_2O_7$	$2CeO_2 + 2SiO_2$	+ 7
$ZrO_{2-X}N_{4X} (X=0.2)$	ZrO_2 (monoclinic)	+ 5

Table 2.1. Molar Volume Changes of Unstable Secondary Phases Compatible with Si_3N_4 after (68).

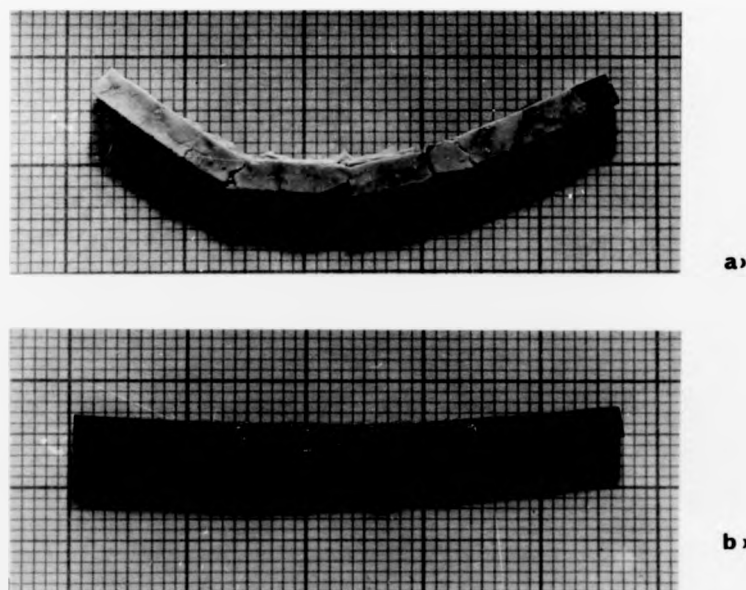


Fig. 2.1. Atmosphere Induced Catastrophic Strength Reduction of $\beta' + YAG$ material, illustrated with a 4-point bend creep bar above (a) and below (b) 1320°C.

SECONDARY PHASE	OXIDATION PRODUCT	VOLUME CHANGE (%)
$Y_2Si_3O_3N_4$	$Y_2Si_2O_7 + SiO_2$	+30
$YSiO_2N$	$0.5Y_2Si_2O_7$	+12
$Y_5(SiO_4)_3N$	$0.75Y_4Si_6O_{10} + 0.75Y_2SiO_5$	+ 4
$Ce_5(SiO_4)_3N$	$5CeO_2 + 3SiO_2$	+ 8
$CeSiO_2N$	$CeO_2 + SiO_2$	+14
$Ce_2Si_2O_7$	$2CeO_2 + 2SiO_2$	+ 7
$ZrO_{2-x}N_{4x} (x=0.2)$	ZrO_2 (monoclinic)	+ 5

Table 2.1. Molar Volume Changes of Unstable Secondary Phases Compatible with Si_3N_4 after (68).

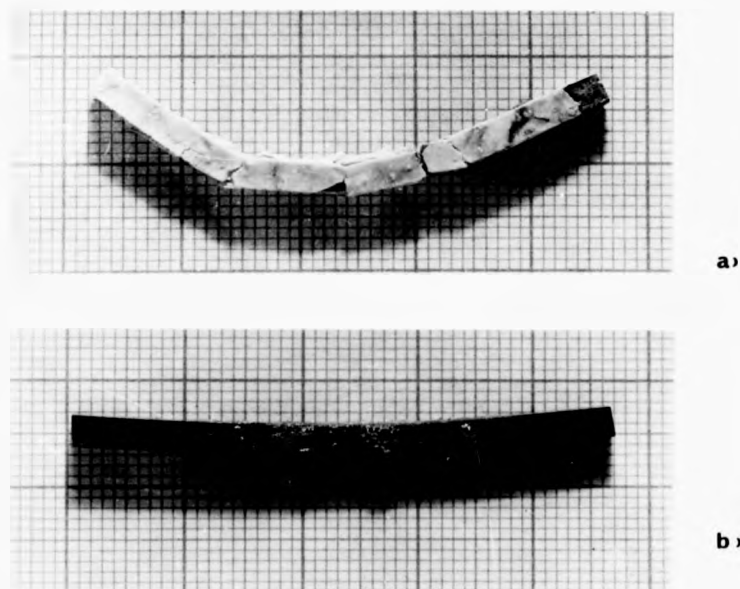


Fig. 2.1. Atmosphere Induced Catastrophic Strength Reduction of β' + YAG material, illustrated with a 4-point bend creep bar above (a) and below (b) 1320°C.

2.4 DETERMINATION OF OXIDATION KINETICS

The most common method of determining oxidation kinetics is Gravimetric (specimen weight gain). Assuming a constant density oxide, weight gain/unit area is directly proportional to oxide thickness and leads to oxidation kinetics according to Equation 2.1. Continual weight measurement at temperature gives accurate results and identification of time dependent rate changes. Room temperature weight measurement at predetermined intervals yields similar information. However, the constant oxidation interruption and thermal cycling can lead to oxide and sub-oxide cracking. If α -cristobalite forms in the oxide, its 5% volume change if transformed to β -cristobalite at 250°C can cause oxide cracking (69, 70). Subsequent reoxidation rates will be increased.

Weight gain and the stoichiometry of the oxidation reaction can be obtained by the Volumetric method which measures oxygen uptake and nitrogen release via a gas handling system and gas chromatograph. This method successfully replicated (53,71) gravimetric-derived oxidation kinetics for HPSN.

Actual oxide thickness measurement from sections of many specimens oxidised for different times yields the least accurate kinetic data due to the oxide thickness variability. Other drawbacks include non-continuous monitoring, possible deleterious phase-changes during cooling and increased number of specimens (albeit smaller than required for gravimetric). However, due to the large volume fraction and complex chemistry of the g.b. phase in the materials studied here, data from weight gain is not expected to define unequivocally the rate-determining steps. As the sub-oxide phase changes have been shown to be critical, this method uniquely offers classification and monitoring of the evolution of these changes on a microstructural level. Optical examination can reveal macroscopic chemical/

microstructural changes and the SEM allows accurate mapping of these variations. This direct measurement method offers supplementary study by TEM of thin sections of the sub-oxide zone and also by X-ray diffraction (this will be discussed in Chapters 5 and 6).

CHAPTER THREE

FRACTURE OF CERAMIC MATERIALS: A REVIEW

This chapter introduces general ceramic fracture theory and defines the terms and concepts to be subsequently used. Normally, ceramics fail by brittle fracture or delayed fracture. In the former, pre-existing micro-flaws are rapidly extended (at catastrophic speeds) at a critical applied stress. In delayed fracture, or static fatigue, cracks can slowly extend at lower-than-catastrophic stresses until they reach some critical length. In ceramics, this slow crack growth, although observed at low temperatures in particular chemical environments, is more usual at high temperatures. This review concentrates on these high temperature mechanisms which are particularly relevant to this research.

3.1. BRITTLE FRACTURE

3.1.1 Fracture Mechanics Approach to Strength

Most ceramics have fracture strengths orders of magnitude below their very high theoretical strength σ_{th} based on their covalent interatomic bond strength. They also exhibit strength variability dependent on specimen dimensions and measuring techniques. Griffith (72) in 1920 suggested that fracture arose from minute surface notches (flaws and cracks). Based on a theoretical treatment by Inglis (73), which showed an applied stress (σ_h) could be magnified near a notch tip, Griffith related this concentrated stress (σ_c) to notch length (a) and tip radius (r) by:

$$\sigma_c = \sigma_h \sqrt{2 \sqrt{\frac{a}{r}}} \quad (3.1.)$$

For atomically sized flaws, σ_c could reach σ_{th} and fracture a material although the applied stress was low. For atomically sharp cracks, the notch model was unsuitable and Griffith developed an energy argument involving (a) energy without a void; (b) surface energy due to the creation of 2 new surfaces (assumed to be surface energy T); (c) energy released on crack advance, U_R .

$$\text{Total Energy } U_T = U + 2T - U_R$$

As the crack moves strain energy is released, but surface energy is consumed. The crack is unstable when

$$\frac{\partial U_T}{\partial c} = 0$$

which gives the critical stress σ_g for crack extension as:-

$$\sigma_g = \left(\frac{2YT}{a\pi} \right)^{1/2} \quad (3.2)$$

where Y = Young's Modulus.

Griffiths' assumption that the surface energy term is just the reversible thermodynamic surface tension is invalid in real materials where energy dissipative mechanisms such as plasticity and slow crack growth occur with crack advance. Orowan (74) derived a similar equation by force considerations and modified the surface energy term (E_s) to include plastic deformation

$$\sigma_g = \left(\frac{2E_s Y}{\pi a} \right)^{1/2} \quad (3.3.)$$

Both of the above relations require difficult surface tension and plastic deformation energy measurements. The first practical application of fracture mechanics began with Irwin who again considered

the energy balance and defined a new term G - the strain energy release rate, where

$$G = \frac{1}{2} \left[\frac{\partial U}{\partial A} \right] \quad (3.4.)$$

which equals the rate of change of energy with crack growth.

His generalisation (75) of the Griffith Equilibrium Condition ie, energy unbalance and thus brittle fracture, occurs when G = critical strain energy release rate = G_c gives

$$\sigma_g = \left(\frac{G_c Y}{a \pi} \right)^{1/2} \quad (3.5.)$$

G_c although readily measurable, is a defined quantity, not a basic material property. Its constancy and use in determining material fracture resistance depends critically on testing conditions, although under limited plastic flow G_c is related to σ_g . Another difficulty is its complex energy concept. The difficulty is removed if fracture is based on crack tip stress calculations.

At this point it should be noted that crack extension is not limited to directions perpendicular to the applied stress plane (all the above analysis), and 3 basic "modes" of crack surface displacement exist (Fig. 3.1). However, brittle cracks tend to seek an orientation which minimises shear loading rendering mode I (normal separation of crack walls under tensile loading) most pertinent to ceramic crack propagation. Fracture mechanics parameters for the various loading systems are differentiated thus: G_I , G_{II} , G_{III} .

Westergaard's mathematical analysis (for review see 76) of a 2-dimensional elastic continuum containing a perfectly sharp slit, allowed the crack-tip field to be expressed in terms of the applied load σ_a at any point (whose polar co-ordinates are centred on the crack tip). The stress σ_I for any point in that field (subjected to

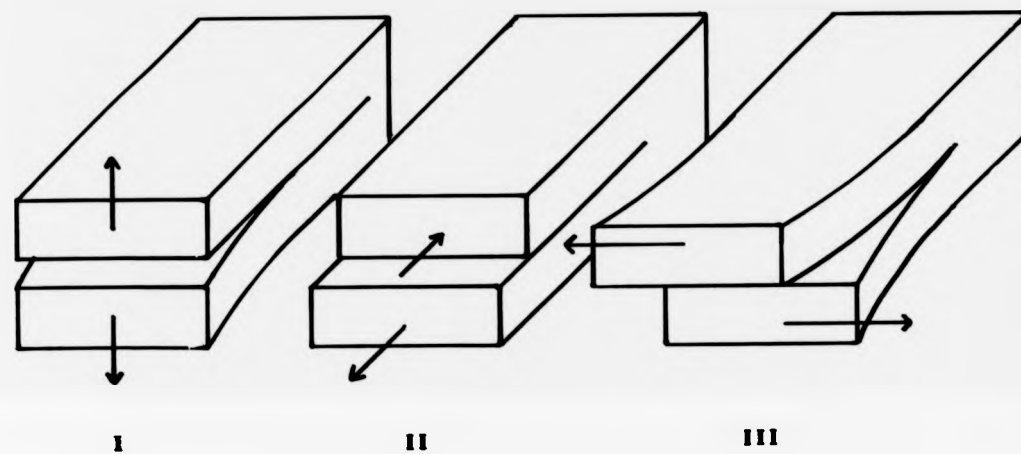


**Fig.3.1 The three modes of fracture:I(opening mode),
II(sliding mode),III(tearing mode).**

mode I loading) could be expressed as series expansions of the form:

$$\sigma_I = \frac{\sigma_a(\pi a)^{1/2}}{(2\pi r)^{1/2}} \left\{ \cos\left[\frac{\theta}{2}\right] \left[1 + \sin\left[\frac{\theta}{2}\right] \sin\left[\frac{3\theta}{2}\right] \right] \right\} \quad (3.6)$$

$\sigma_a(\pi a)^{1/2}$ is thus an independent term which multiplies stress around the stress-raised crack-tip and has been termed the "Stress Intensity Factor", K_I . Its general relationship is:

$$K_I = \sigma_a Y \sqrt{a} \quad (3.7)$$

and it uniquely characterises the loading level in the crack tip near-region. The Y term is a geometric factor, to some extent dependent on loading system but mainly on crack shape, and determined by stress analysis.

When the stress intensity reaches a critical level (K_{IC}) to rupture crack tip bonds, brittle fracture ensues under a critical applied stress σ_c . A simple relationship exists between K_I and G_I as, during elastic loading, the strain energy is uniquely defined by the stress intensity distribution. Therefore, for a thick plate under plain strain,

$$G_{IC} = K_{IC}^2 \cdot \frac{(1-\nu^2)}{E} \quad (3.8.)$$

where ν = Poisson's ratio. K_{IC} and G_{IC} provide empirical assessments of a material's brittleness or resistance to fracture, commonly known as "fracture toughness".

3.1.2 Statistical Nature of Strength

A consequence of the above theory, that brittle fracture develops from Griffith flaws, is that the fracture strength of ceramic materials is statistical, dependant on the probability of the existence of a flaw capable of catastrophic fracture at a specific applied stress. The statistical nature of the flaws explains the fracture stress

distribution. The assumption that flaws could be distributed (size and location) according to some standard distribution function provided a simplification that allowed W. Weibull (See 77) in 1937 to produce the best known of the many statistical theories of strength. The probability of failure (P) of a specimen subjected to a stress (σ), therefore becomes a more reasonable representation of strength and is expressed (78) as:

$$P = \exp \left[- \int_V \left(\frac{\sigma}{\sigma_0} \right)^m dv \right] \quad (3.9)$$

where σ_0 = normalizing factor, V = volume of material and m is the Weibull modulus, a constant related to the materials' homogeneity. A high m value indicates a reduced scatter in fracture stresses and a more predictable material.

A large body of empirical statistical data now exists for ceramics from which many attempts towards a statistical theory of brittle fracture have developed. However they all assume a relationship between dangerous flaw population and specimen volume or surface area. This relationship varies between materials (as the flaw distribution is usually determined by fabrication routes). Any generalised form of the statistical analysis cannot therefore be reasonably extended to other materials. In studying fracture mechanisms (hopefully leading to material improvement) the lack of explicit consideration of the nature and origin of flaws, limits the usefulness of the statistical approach.

3.2 FRACTURE TOUGHNESS AND K_{IC}

Unlike the strength variability of engineering ceramics, K_{IC} offers a true material characteristic un-influenced by flaw size or distribution and independent of specimen configuration and test method.

It also has the potential to relate strength, impact resistance and thermal shock and fatigue resistance. The virtual impossibility of flaw-free production of complex brittle components implies embodiment of σ_c and K_{IC} concepts in component design. The K_{IC} values determined from standard specimens can be readily applied to these components. Although brittle materials have high tensile strengths, the usable strength is determined by K_{IC} and flaw populations and recent ceramic developments have been towards improving these quantities.

Although a material characteristic, the K_{IC} value can be optimised within a material system as its value is variable with microstructure, environment and temperature. Table 3.1 shows the variability in the Si_3N_4 system and gives current K_{IC} values for competing structural materials. Although the K_{IC} dependence on grain size is unclear (having opposite effects on different materials), the importance of grain shape, usually aspect-ratio (length/width), has been demonstrated in Si_3N_4 (16). The production of increasingly elongated Si_3N_4 grained microstructures (indirectly by higher β/α ratios) raises the K_{IC} level and the more tortuous (and hence energy dissipative) fracture path is thought to be responsible. Porosity has a limited effect. However high porosity Si_3N_4 (best represented by RBSN) gives lower room temperature K_{IC} values than dense HPSN. Also rounding of inherent flaws can increase K_{IC} . This effect has been linked to an environmental influence, where the increased K_{IC} of RBSN in air was attributed to oxidation of flaws and their subsequent blunting by the SiO_2 oxide film (81). The occurrence of any energy dissipative mechanisms at the crack tip increases K_{IC} and is exemplified in Partially Stabilised Zirconia where the high crack tip stress induces phase transformations and microcracking which

MATERIAL	REFERENCE	ROOM TEMP. K_{IC} (MPa.m ^{1/2})	K_{IC} AT 1300°C (MPa.m ^{1/2})	
HPSN (8% Y_2O_3)	79	8	17 (s.c.g.)	} Si_3N_4 Alloys
HPSN (Y_2O_3)	80	7	9	
HPSN (2.5% MgO)	81	8.5	8.5	
PSSN 1 wt% SrO, 4 wt% MgO, 5 wt % CeO_2	32	5	5	
HP Si-Al-O-N	82	5	20 (s.c.g.)	
HP Si-Al-O-N Z = 1	83	3	4	
H.P.S.N. No Additive No g.b. glass	22	3.85	3.85	}
RBSN (AIR)	81	3	7	
RBSN (VAC)	81	3	4	
PSZ	11	10	-	}
Al_2O_3 dispersed with PSZ particles	84	8.5	-	
Al_2O_3	85	4.5	3	
Refel Self bonded SiC	86	4.4	3.5	} Other High Temp. Ceramics
HPSiC	85	3.5	3	
HPSiC	87	2.6	2.6	

TABLE 3.1. K_{IC} VALUES FOR Si_3N_4 CERAMICS AND OTHER BRITTLE MATERIALS

dramatically improves its toughness (11). The dispersion of PSZ particles in Al_2O_3 led to a doubling of its K_{IC} by crack tip shielding where the strain energy is dissipated by transformation in a zone surrounding the crack (84).

With all Si_3N_4 that contains a g.b. glassy phase, HPSN (80), RBSN (81), SSN (32), K_{IC} increases substantially above $\sim 1000^\circ\text{C}$. This is due to g.b. glass softening which increases crack tip plasticity and leads to other additional energy dissipative mechanisms, most notably slow crack growth (see section 3.3). SCG is commonly proposed to occur by a g.b. sliding, cavity formation, cavity linkage sequence (88). An alternative crack tip energy dissipative mechanism resulting in s.c.g., which has previously been proposed for Al_2O_3 (89), may be operative for Si_3N_4 . Here strain energy is consumed by the flow of a viscous film bridging two grains being mutually separated (as opposed to mutually displaced, e.g. g.b. sliding). The branching and deviation of this slow growing crack can further increase K_{IC} . In HPSN without g.b. glass (22) there is no K_{IC} temperature dependence. Unfortunately the s.c.g. mechanism that enhances K_{IC} values at high temperatures also renders these materials unsuitable as structural components.

The properties and volume of a g.b. glass is expected to influence the extent of energy dissipation and therefore K_{IC} . The g.b. structure is also altered by its crystallisation, the extent and crystal type may also have important effects. These variables have only been briefly studied in Si_3N_4 systems. In the present Si-Al-O-N ceramics with larger g.b. volumes the effect of these variables may be amplified. This important engineering parameter, K_{IC} and its dependency on temperature and microstructure is therefore a subject of this thesis.

3.3 SUBCRITICAL CRACK GROWTH

Mechanisms exist in brittle materials, to propagate pre-existing cracks

and flaws at stresses below the critical σ_c level and the phenomenon is known as subcritical crack growth or slow crack growth (s.c.g.). This manifests itself as a gradual strength decay under long term thermal, mechanical and/or chemical loading. Strength degradation is also determined by high temperature and chemical processes that can alter flaw populations and modes of failure. These instabilities control the reliability of ceramics and give them a detrimental "limited lifetime" before failure. This delayed fracture in structural ceramics has meant components are designed to support only 10-20% of the average material strength. Greater understanding of s.c.g. could reduce this massive safety factor and also increase reliability.

3.3.1 Low Temperature Results and the General K_{I0} -V Relationship.

From the large volume of data collected from glasses and other brittle materials at low temperatures, the extent of s.c.g. is found to be dependent on applied stress and test environment. A general relationship exists between stress intensity factor (K_I) and crack velocity (V), schematically represented in Fig 3.2, in which 3 distinct regions of s.c.g. have been identified. The K_{I0} value is the minimum stress intensity required to initiate crack advance (90) and its existence in many brittle materials is an important parameter for life-time predictions. In Regions I and III, crack velocity is dependent on K_I defined by fracture mechanics or the rate of the environmental reaction at the crack tip. In region II, V is stress independent and determined only by the rate of diffusion of corrosive species to the crack tip. Examples of Region II s.c.g. occur during fracture at room temperature of silicate glasses (91,92), sapphire (93), Al_2O_3 (85), porcelain (94) in water or moist environments. In Region III the crack quickly "runs away" to catastrophic speeds. The mechanism is not fully understood and only of academic interest.

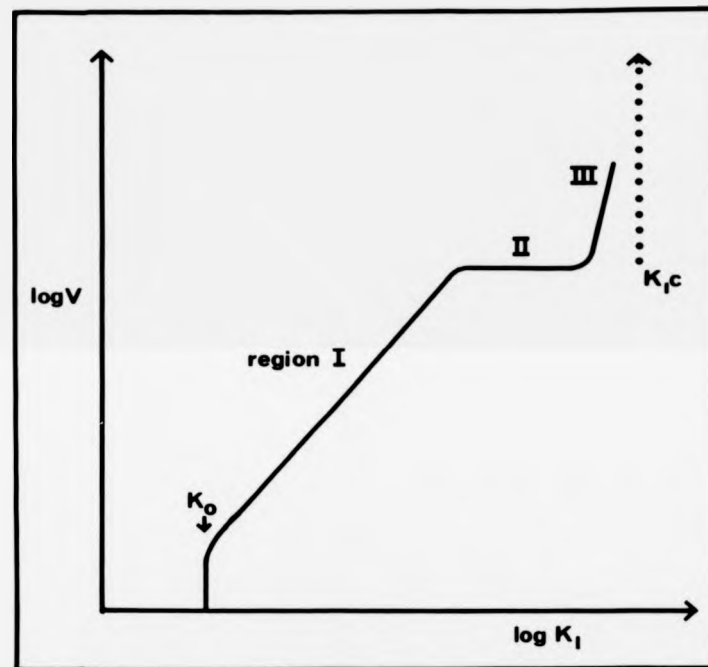


Fig.3.2 Generalized form of the Stress Intensity(K) - Crack Velocity(V) relationship for brittle materials.

Thus in inert atmospheres, Region I is assumed to characterise crack growth for engineering design purposes. Collected data for many ceramics and especially Si_3N_4 at high temperatures are most commonly fitted empirically to the power function proposed by Charles (95) and expressed by Evans (96) in the form:

$$v = A(K_I)^N \text{ or more generally } v = v_0 \exp \left[\frac{-Q}{RT} \right] \left(\frac{K_I}{K_{IC}} \right)^N \quad (3.10)$$

where N and v_0 depend on the environment and material composition, Q is activation energy for fracture and R is the gas constant. Although other relationships have been determined (97), Equation (3.10) fits data very conveniently and its analytical consequences for many load/time histories can be worked out rigorously.

3.3.2 High Temperature s.c.g. Mechanisms

In single crystals or glass, s.c.g. occurs by rupture of highly strained atomic bonds at the crack tip by thermal fluctuations or chemical reaction. In many polycrystalline structural ceramics the grain-boundary (g.b.) provides a mechanical, chemical and diffusive weak-link. At high temperatures the g.b.s can assist the s.c.g. of existing flaws and also nucleate new flaws. The propagation and nucleation of flaws is basically due to thermal, diffusive or plastic mechanisms occurring in the crack tip zone centred on the g.b. The s.c.g. mechanism is largely dependent on the nature of the g.b. In materials with g.b.s free from viscous components, diffusive crack propagation (98, 99, 100) is limited by the rapidly diffusing g.b. channels (47). Flaw nucleation ahead of a crack-tip also due to atomic and vacancy diffusions has been proposed (101) and suggested for triple g.b. cavity formation in some Si-Al-O-N ceramics (47).

Flaw generation and s.c.g. due to plastic flow are usually due to

dislocation motion or g.b. sliding. Models of cavity nucleation by dislocation generation, mobility and agglomeration (102, 103) are not supported by direct experimental evidence although data has been qualitatively fitted for Al_2O_3 (103). Evans (103) proposed a g.b. sliding mechanism for cavity nucleation where mutual sliding of solid grains separated by a g.b. viscous film develops a cavity under sufficient hydrostatic tension. If this model is extended to the high stress field at a crack tip, multiple cavitation formation would be expected with subsequent cavity linkage and extension of the primary crack. This mechanism has been used to explain the s.c.g. observations of many structural ceramics (SiC , Si_3N_4 , Si-Al-O-N) at high temperatures with the viscous film being the softened g.b. residual glassy phase. However detailed microstructural evidence has been limited. The extent of cavity formation and subsequent s.c.g. should be influenced by the g.b. film characteristics (ie. viscosity, distribution, volume, etc.), and this led to g.b. developments aimed at understanding and improving the s.c.g. behaviour in these materials. The chemical composition of g.b. viscous phases affects the s.c.g. and mechanical properties of Si_3N_4 (c.f. materials sintered with MgO and Y_2O_3 additives). Similarly, increasing CaO impurity in Al_2O_3 (which is segregated at the g.b.) also leads to greater s.c.g. (104). These variations are believed to be due to viscosity alterations of the g.b. glass. However chemical variations have been restricted to metallic ions and the influence of volume and distribution have not been dealt with systematically.

The s.c.g. mechanisms for the present range of sintered Si-Al-O-N ceramics are therefore studied in Chapter 7, with reference to a K_I -V relationship. An emphasis is placed on the influence on s.c.g. of the chemistry, distribution and degree of crystallisation of a matrix phase

in Si-Al-O-Ns, as these parameters of this large second phase are relatively flexible in the present Y-Si-Al-O-N system.

3.4 FAILURE PREDICTION

Subcritical crack growth in a material dictates a limited component lifetime before catastrophic failure and must be accurately known for any particular in-service stress. The time to failure (t_f) under constant stress can be expressed (105) as:

$$t_f = BS_1^{N-2} \sigma_a^{-N} \quad \text{where} \quad B = \frac{2}{AY^2(N-2)K_{IC}}^{N-2} \quad (3.11)$$

N and B are constants characterising the s.c.g., S_1 is fracture strength and σ_a is the applied tensile stress.

The values of N, A and K_{IC} for Eq. 3.11. can be determined statistically by static fatigue (106) and dynamic fatigue (107,108) or by actual crack velocity measurement. In the latter, controlled fracture (Section 3.5.) allows velocity measurement (V) of preformed macroscopic cracks under various K_I . These data are fitted to empirical relationships, commonly Eq. 3.10, which give values of A and N. Possible limitations of the crack velocity route for failure predictions are (1) conclusions for macroscopic crack propagation may not be relevant to the microscopic cracks in ceramic components (109); (2) the K_I -V relationship is for the extension of pre-existing cracks and does not account for flaw generation or flaw shape alteration during component lifetimes; (3) lifetime predictions generally require greater extrapolation from K_I -V data than from statistically derived data. However the crack velocity approach offers material conservation and most importantly a unique revelation of s.c.g. nature and mechanism that can readily point to material reliability improvements.

3.5 MEASUREMENT OF FRACTURE TOUGHNESS AND SLOW CRACK GROWTH

A range of K_{IC} determination techniques for structural ceramics

exists, whose advantages and disadvantages have been recently reviewed (110). The Single Edged Notched Beam (SENB) configuration is most common, being easy to machine and notch. The sawn notch is usually planar, although chevron notches (requiring more complicated machining) can give K_{IC} directly without crack length measurement (111).

An indentation initiated notch (using median crack) offers high reproducibility of crack size and shape. Recent Indentation K_{IC} determination (directly from impression measurements without subsequent fracture) have given reproducible results from small specimens (22, 112). High temperature values, however, are complicated by crack healing (due to high residual stresses) and crack veiling by any oxide products. Specimens most commonly used for K_I -V analysis, Double Torsion (DT) and Double Cantilever Beam (DCB), yield accurate K_{IC} values but with larger specimens and complex jigs.

A basic assumption of fracture mechanics is the unique value of K_{IC} for a specific material, independent of specimen dimensions or technique. However there is evidence for a dependence on test method. K_{IC} differences for large grained alumina and Refel SiC (113) were noted when determined by DCB and SENB and similar discrepancies exist for SiC using DT and SENB. In the Physics Department of Warwick University, Coventry, different K_{IC} levels for the same material(50) have resulted from SENB, DT and Indent determinations. Due to the large body of literature built up from the SENB technique, its ease of machining, its high temperature stability and potential for K_I -V data production (114) the SENB with sawn planar notch was used in this work.

Determination of the K_I -V relationship was via the DT specimen configuration which, in comparison with the DCB, is simpler, easier to machine and lacks pin/hole loading arrangements. Also most K_I -V data published are obtained by DT and therefore direct comparison is possible.

Using the DT specimens, crack growth can be detected and measured indirectly by its production of secondary phenomena which include change in electrical resistivity (115), photo and acoustic emissions. Photo- emission of Al_2O_3 (116) however shows no general correlation with any fracture mechanic parameters. The recently developed acoustic emission technique yields excellent K_I -V data for Al_2O_3 (117) comparable to traditionally obtained data (DT) and also offered accurate lifetime predictions. These techniques however are all unsuitable for high temperature application. The K_I -V relationship was therefore derived from crack length and specimen compliance changes with a DT specimen for various temperatures and environments.

The recent alternative technique of compliance change measurement of a SENB specimen exhibiting s.c.g. has only been applied to H.P. Si-Al-O-N. It offered; K_I -V data comparable to DT derived data, a range of crack velocities from one experimental run and small specimen size and consumption. Its potential for sintered Si- Al-O-Ns(which are expected to exhibit substantial s.c.g.) is to be studied. The experimental details of the DT and the SENB techniques used in this work are given in Chapter 4.

CHAPTER FOUR

GENERAL EXPERIMENTAL TECHNIQUES

In this chapter a discussion is given of the techniques used for determination of Oxidation characteristics and Fracture Mechanisms. A brief critical review of alternative methodology precedes to underline the relative merits. The techniques for Microstructural Characterisation are set out in Chapter 5.

4.1. OXIDATION

Prior to oxidation, all material was polished (as in S.E.M. specimen preparation) to a standard 6 μm finish on the major oxidation face and ultrasonically cleaned in acetone. After oxide surface examination the specimen was sectioned and polished to 1/4 μm finish. Oxide/sub-oxide thickness was determined optically and via S.E.M., only with respect to the major face. Where sufficient quantities of material were available (SO) weight gain was performed by room temperature measurement on a conventional microbalance (accuracy ± 0.005 mg). Weight measurement was therefore not continuous and oxidation was interrupted. The specimen was removed and reintroduced to the furnace at a constant rate ($\sim 20^\circ\text{C}/\text{second}$) aimed at retaining microstructural and oxide characteristics. Cyclic oxidation can result in oxide cracking (via stresses arising from the β/α cristobalite inversion or thermal expansion coefficient mismatch) which could render the oxide non-protective on subsequent reoxidation. However, cracks in the glass will be healed as it softens ($\sim 1200^\circ\text{C}$) and phase changes were not observed by X-Ray Diffraction (X.R.D.) of oxides cooled at various rates. All specimens were oxidised on a platinum

support (acting as knife edges touching only the specimen edges) resting in an alumina boat. The rate of oxidation of various Si_3N_4 has been shown to be independent of oxygen partial pressure and small humidity changes (118, 49, 119), therefore all oxidation was performed under normal laboratory atmosphere, in a purpose built furnace capable of temperatures up to 1450°C . The specimen chamber is a horizontal recrystallised alumina tube with SiC spiral-type heating elements controlled ($\pm 2^\circ\text{C}$) by a stepless Eurotherm controller with Pt/Pt 13% Rh thermocouple. The alumina tube is double open-ended and is annealed for 100 hours at 1350°C before any oxidation run to reduce its contaminant levels as furnace impurities can seriously affect the oxidation behaviour of Si_3N_4 (120). The ends are loosely plugged with a porous silica block to maintain thermal equilibrium.

The oxide scale was chemically analysed by EDAX in the S.E.M. and crystalline phases identified by X.R.D. after oxide removal and crushing (agate mortar and pestle) to a fine powder. Sub-oxide development was analysed from the polished section via optical and S.E.M. observations. Crystalline phases were identified, along with their growth and distribution by T.E.M. sectioning or on larger oxidised material by grinding successive layers back from the oxide and using XRD on the polished cross-section.

4.2 FRACTURE TOUGHNESS TESTING

The K_{IC} -temperature relation was derived from SENB specimens. The K_{IC} level required in the K_{I} -V relation was derived from DT experiments due to the K_{IC} discrepancies previously noted. For the SENB specimen 4-point bend loading was chosen as opposed to the more practical 3-pt bend due to (1) its greater region of pure bending; (2) its less critical loading point positioning; (3) its lack of contact stress interaction with the notch root stress, sometimes observed with the 3-pt bend configuration (121).

4.2.1 The Jig

The K_{IC} jig consists of two parts: the upper loading points in the form of 2 Hot-pressed SiC rods housed in a recrystallised alumina hemispherical head and the lower loading points, the rim of a recrystallised alumina tube (Fig. 4.1a). The hemispherical head ensures equal load transmission to the 2 upper contact points and the slot allows the broken specimen pieces to fall to the cooler furnace regions immediately after fracture (Fig. 4.1b) so reducing fracture surface oxidation which would complicate subsequent S.E.M. examination. The head must be sufficiently long to ensure its centre of gravity lies below the specimen. The notch and rounded shoulders of the tube provide specimen stability and an approach to a knife-edge loading configuration respectively. The H.P.SiC rods provide greater stability to fracture and specimen interaction at high temperatures than the more general alumina ones. Two jigs were produced. One for specimens of dimensions usually reported in the literature to allow direct comparison, the other for smaller specimens which could be salvaged from used DT specimens, thereby conserving material.

4.2.2 The Test Specimen

Due to their limited plasticity, K_{IC} determinations for ceramics can be performed on small specimens. Test bars (25 x 6 x 3 mm) were cut from the billet with a diamond annular saw and the smaller 20 x 4.8 x 2.4 mm bars diamond machined from the halves of broken K_I -V specimens. The major faces were polished to a standard 14 μ m diamond finish. On specimens where crack growth in vacuum was to be arrested and studied in S.E.M., polishing was continued to 1/4 μ m finish. Using a clock gauge to accurately monitor cutting depth, the specimens were notched to 30% of the bar width. Accurate K_{IC} values for ceramics are only obtained (122) for $0.1 < \frac{a}{w} < 0.6$ (see fig 4.1c). A relative notch length of $\left(\frac{a}{w}\right) = 0.30$ was chosen which allows

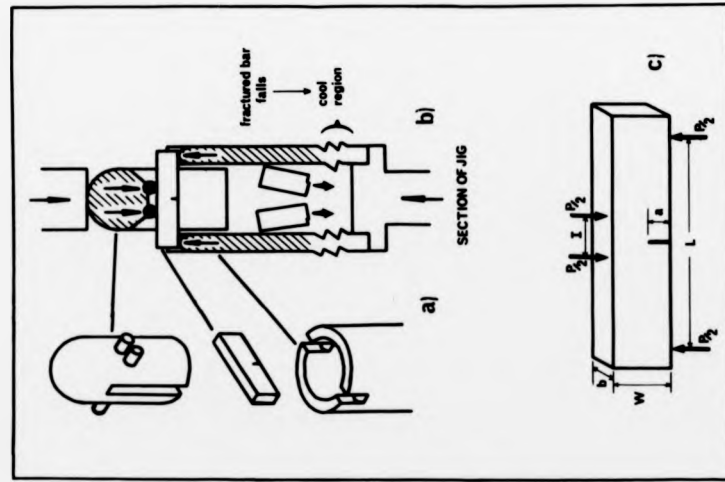


Figure 4.1. (a) Construction of K_{IC} Jig. (b) Sectional view of assembled Jig. (c) Dimensions of K_{IC} specimen.

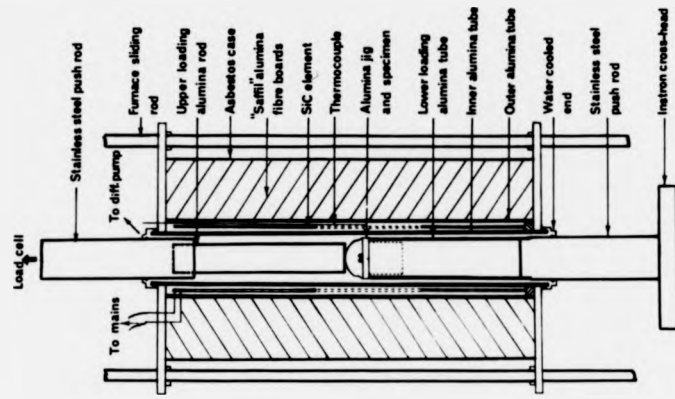


Figure 4.2. Sectional view of furnace and Instron arrangement used for high temperature K_{IC} and K_{I-V} determinations.

considerable s.c.g. to occur whilst still giving accurate K_{IC} values. The sharp crack requirement is sometimes satisfied by quenching prestressed material, but it has been shown (123,124,86) that machining can produce atomically sharp cracks at the notch tip. However, specimen configuration effects have been shown to increase K_{IC} with increasing radius (122) and so the finest "Capco" diamond annular blade was used to give a notch radius of $\sim 150 \mu\text{m}$. The notch was centralised and squared to the specimen with the jig used for DT specimen notching.

4.2.3 The Procedure

For consistent and accurate K_{IC} results it is important that all loading is symmetric to the notch. The jig and specimen were assembled and fixed with Durafix adhesive on a test bench after symmetry was checked with a travelling microscope. The assembly was introduced to the furnace hot zone leaving a gap ($\sim 2 \text{ mm}$) between the jig and upper loading rod to allow for thermal expansion. The furnace is incorporated into a floor-mounted Instron Testing Machine which facilitates the high temperature loading (Fig. 4.2). With the specimen chamber open the furnace was initially run-up to 200°C to drive off the adhesive and either left open (for air tests) or linked to a vacuum system before a controlled ($400^\circ\text{C}/\text{hour}$) run-up and subsequent run-down to the test temperature to avoid thermal shock. The cross-head speed was standardised at $0.002 \text{ cm min}^{-1}$ although slower speeds of 0.001 and $0.0005 \text{ cm min}^{-1}$ were used to observe and arrest extensive s.c.g. The K_{IC} determinations were all derived from the $0.002 \text{ cm min}^{-1}$ as load rate dependency has been shown for HPSNs (83) which exhibit large plastic components and has led to discrepancies between published K_{IC} results. All specimen dimensions including notch depth, a , were measured using a travelling optical microscope. Together with the load for catastrophic failure P_F , K_{IC} was evaluated using Srawley's

expression (125):-

$$K_{IC} = \frac{3P_f d}{bw^2} a^{1/2} \left[3.86 - 6.15 \left[\frac{a}{w} \right] + 21.7 \left[\frac{a}{w} \right]^2 \right]^{1/2} \quad (4.1)$$

where d is the bending arm length = $(L - I)/2$ and I = inner span (5 mm and 4.1 mm) and L is the outer span (22 mm and 19.3 mm), b is specimen width and w specimen height, shown in Fig. 4.1c. Various derivations and equations for K_{IC} exist (83,86), however the above equation has been shown to be the most reliable and least dependent on $\frac{a}{w}$ or specimen dimensions (86) for 4-pt bend SENB ceramic testing. Although Eqn.4.1 accounts for various specimen $w:b:d$ ratios, tests (Appendix 4.1) only gave similar K_{IC} values for the specimen sizes used here.

4.3 SUB-CRITICAL CRACK GROWTH TESTING

4.3.1 The Specimen

Tablets (20 x 15 x 3 mm) were diamond cut from sintered billets. Although 2 mm thick specimens have given identical K_I -V data to 3 mm (127) and conserved material, here 3 mm specimens allowed 20 x 4.8 x 2.4 mm K_{IC} bars to be salvaged after K_I -V experiments and optimised material use as standard K_{IC} specimens could also be obtained from the same 3 mm cut slab. Specimens were mounted (using "Lakeside" resin) onto a purpose-built jig fitted to a surface grinder. The jig simultaneously holds several specimens square to a 1 mm thick slitting wheel and parallel to the machining plane. A 1 mm wide groove was accurately machined down the centre of the major face to a depth of exactly half the specimen thickness (1.5 mm) because of the d^3 dependence in Eqn.4.2. The ungrooved face was polished to 1/2 μ m diamond finish to allow accurate S.E.M. measurement of crack growth. The groove guides the growing crack in a direction parallel to the specimen length as deviations can complicate K_I and crack velocity measurements. An atomically sharp crack is introduced via a 5 mm notch at one end of the groove, similar to the K_{IC} specimen. To ensure exact central

location in the groove and accurate monitoring of notch depth a purpose built clamp (Fig.4.3a) was used.

When treated as two elastic torsion bars loaded at one end, mathematical stress analysis of a DT specimen (128,129) yields a Stress Intensity Factor, K_I , expressed by

$$K_I = P W_m \frac{3(1 + \nu)^{1/2}}{W d_n^3} \quad (4.2)$$

P is the applied load, W , d , d_n , W_m are specimen dimensions as in Fig. 4.3b and ν is the Poisson's ratio. K_I is derived assuming initial crack length (a) independence. However, subsequent finite element stress analysis (130) shows the relationship holds only for $a/w > 0.55$ as bending of specimen tails and shear strains were previously neglected. Room temperature fracture of glass specimens having dimensions identical (20 x 15 x 3 mm) to those in the present study show K_I constancy only for 5 mm $< a < 15$ mm (127); hence the introduction of a 5 mm notch.

4.3.2 The DT Jig

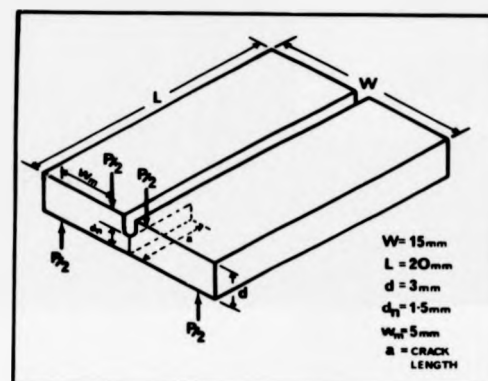
The DT jig consists of three recrystallised alumina parts (Fig.4.3). A freely-moving upper piece has a curved head which facilitates equal load distribution to the knife-edge protrusions. These protrusions constitute the inner loading points applied to one end of the specimen. The lower piece has raised shoulders (acting as outer loading points) and is fixed into the tube which also acts as a sliding guide for the upper piece. The specimen fits between the pieces with its ungrooved face down (maximum tensile stress) Fig.4.3c.

4.3.3 Test Procedure

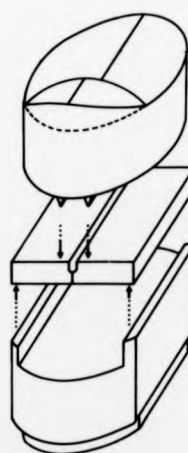
The same Instron machine (incorporated with vacuum furnace) as described in 4.2.3. produced K_I - V data for various temperatures and environments and similar jig installation and furnace run-up precautions were observed. Apart from its advantages stated in Section 3.5., the DT specimen also offers several modes of s.c.g. rate



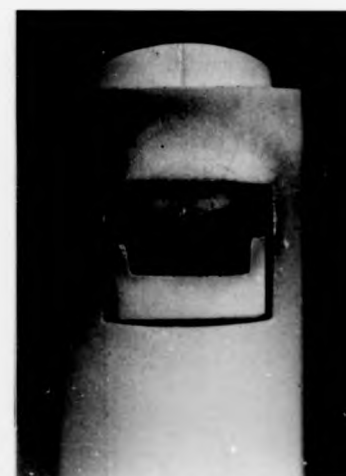
a)



b)



c)

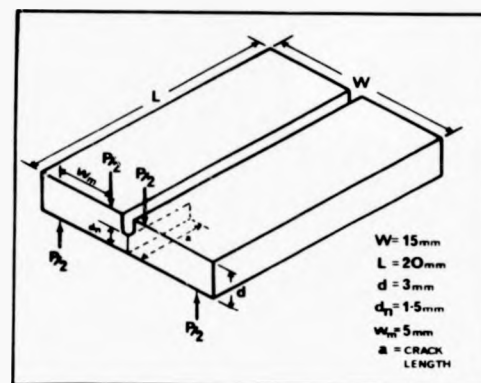


d)

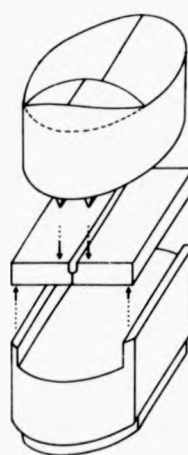
Figure 4.3. Specimen and Jig for Double Torsion Testing showing (a) The jig for accurate notch machining (b) D.T. Specimen dimensions (c) Schematic diagram of jig/specimen configuration (d) Actual assembly.



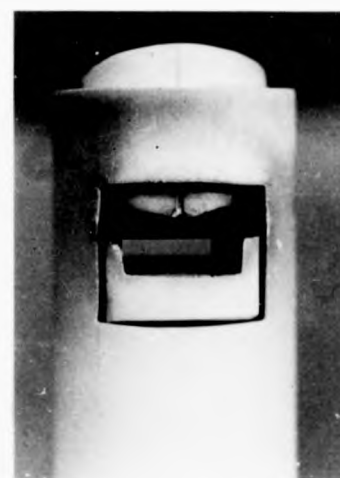
a)



b)



c)



d)

Figure 4.3. Specimen and Jig for Double Torsion Testing showing (a) The jig for accurate notch machining (b) D.T. Specimen dimensions (c) Schematic diagram of jig/specimen configuration (d) Actual assembly.

measurement, which can be performed sequentially. This gives greater specimen efficiency and ensures K_I -V data that is technique independent and has greater precision (as the separate methods have greater accuracies in certain regions of the K_I -V relationship).

4.3.3(a) Load Relaxation Method

Measurements of s.c.g. rates for ceramics have been most easily and successfully determined directly from the rate of load relaxation. Using a high cross-head speed (0.5 cm/minute), the specimen is rapidly loaded to P_i (a level just below the critical fracture load P_f , predetermined for a similar DT specimen). Loading was then stopped. The specimen and loading components (jig, machine, etc.) relax and their rate of relaxation $\frac{dP_f}{dt}$ is determined from the continuous load/time record (Fig.4.4), which simply gives the compound of the relaxation rates of the specimen $\frac{dP_s}{dt}$ and loading components $\frac{dP_m}{dt}$. The crack velocity (V) has been derived from the DT relaxation rate at various levels of sophistication (96, 129, 130) although the most practical expression is:-

$$V = - \frac{a_i P_i}{P^2} \left[\frac{dP_s}{dt} \right] \quad (4.3)$$

where a_i is the initial length, and P is the load on the load/time curve at which the rate $\frac{dP_s}{dt}$ is determined. The corresponding K_I for the determined V is obtained by substituting the instantaneous load (P_n for $\frac{dP}{dt_n}$) into Eqn 4.2.

For the above analysis to hold, machine relaxation must be accounted for. The procedure is given in Appendix 4.2 along with that for crack velocity determination.

Where crack growth is accompanied by gross specimen plasticity then applied stress is relaxed by crack growth and plasticity. The correction for plasticity at low velocities is large and so only the high V/K_I values were determined with this method. Linear viscoelasticity is accounted for however using another DT technique, constant displacement.

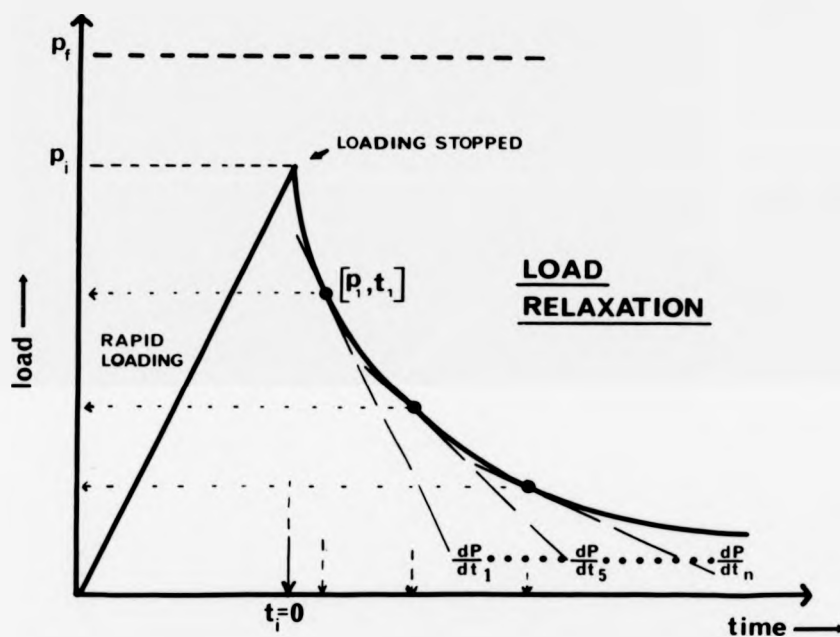


Figure 4.4. Schematic representation of load/time trace recorded during load-relaxation method for K_I -V Relationship Determinations.

4.3.3(b) Constant Displacement

Specimen loading with a set cross-head displacement speed (\dot{y}) can show departure from elastic linearity on the load/displacement curve and a load plateau (Fig.4.5). In this region the displacement strain is relieved by crack propagation. The crack travels at a constant velocity V which is related to \dot{y} (if the plastic displacement is small) and the plateau load P_p by:-

$$V = \frac{\dot{y}}{BP_p} \quad \text{where} \quad B = \frac{3W_m^2}{Wd^3G} \quad (4.4)$$

B is an analytically determined constant (129), G = shear modulus of the material at the test temperature. W_m , W , and d are given in Fig.4.3b. The corresponding K_I for this calculated V is determined by P_p substitution into Eqn.4.2.

The range of crack velocities that can be determined is limited by the \dot{y} range of the testing machine and also a lower velocity limit, imposed by non-plateau behaviour (Fig.4.5) at low strain rates where substantial plastic deformation can occur. For these materials at 1200°C the velocity limit was 10^{-6} m/sec. To maximise data collection from each specimen, a series of increasing crosshead speeds is used, each starting after the observed plateau of the previous (Fig.4.5). In practice, only a few values of \dot{y} were used on each specimen and were initiated from short crack lengths. During this test, the exact crack position is unknown and crack extension into the final 5 mm of the specimen (where K_I is not constant) will invalidate results. Accurate interpolation of K_I - V data for long-term failure prediction requires knowledge of the velocity regime below 10^{-6} m/sec.

4.3.3(c) Constant Load

Measurement of s.c.g. under a constant load allows the DT specimen to produce the required very low crack velocities. K_I is

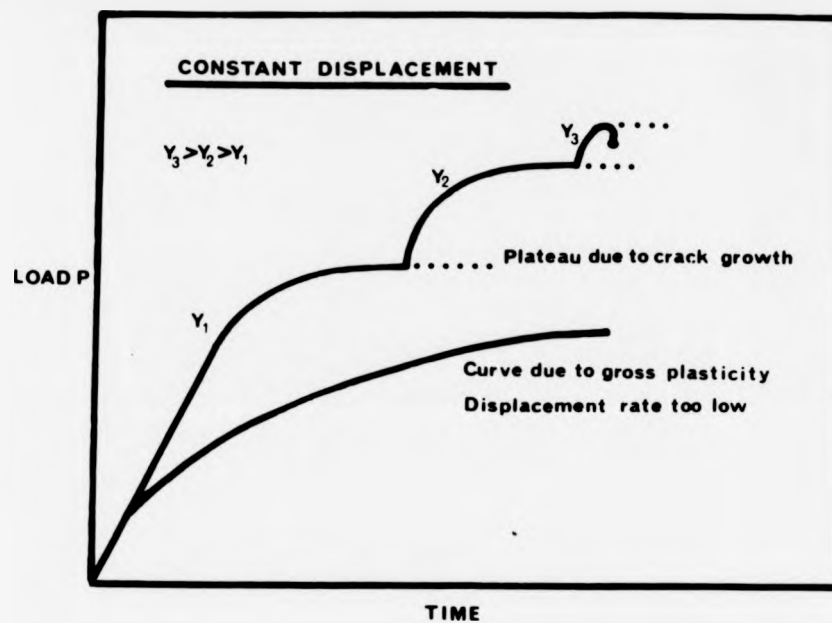


Figure 4.5. Load/Displacement Curve for Constant Displacement.

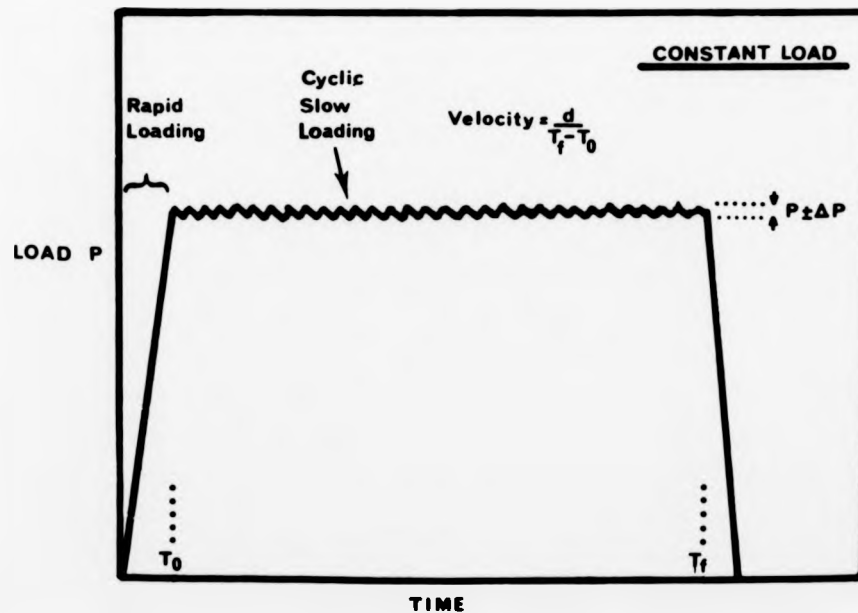


Figure 4.6. Schematic representation of Instron Chart Record during Constant Load Method of K_I -V Determination.

determined from the constant load (P_c) by Eqn.4.2 and the implied constant velocity can be obtained directly from the crack tip extension measurement (Δa) in a predetermined time interval (Δt) ie. $V = \Delta a / \Delta t$. Very low Δa (and hence velocities) can be measured with a S.E.M. An optical microscope measured $\Delta a > 3 \text{ mm}$. In materials exhibiting substantial plasticity, the validity of Eqn.4.2 is questionable. K_I is found to be reduced (131) after plastic deformation. However, the extent is small (maximum of 20% K_I correction for plastic displacement \sim three times DT specimen thickness) and not considered critical to the K_I /load relationship. The constant loading is facilitated by the Instron cyclic loading mechanism (Fig. 4.6). The variation about the set load P_c is reduced to $\sim 1\%$ P_c using low cycling crosshead speeds, which lessen load overshoot. The load was not applied for longer than 6 hours due to these materials' susceptibility to matrix crystallisation. This gives a lower velocity limit determined by the S.E.M. resolution of Δa . Crack resolution is also complicated by the overlying oxide which readily forms with these materials (Chapter 6). Most tests were therefore performed in vacuum,

To maximise the K_I -V data and reduce the holding times at temperature, the following sequence of techniques was usually used on each run: (1) constant load (for short times); (2) a load relaxation (as the initial crack length must be known); (3) series of constant displacement runs.

4.3.4. Poisson's Ratio Determination

The corresponding value of K_I for all crack velocities determined by the previous DT techniques is given solely by Eqn.4.2. This equation now only requires the corresponding material's Poisson's ratio (ν) for the given test temperature and this was indirectly determined from the Young's Modulus (E) and Shear Modulus (G) values, related by the common expression:

$$\nu = (E/2G - 1)$$

(4.5)

Room-temperature values of E and G were accurately obtained using a mechanical resonance technique described by Spinner et al. (132).

Induced torsional and longitudinal vibrations in a square section bar gives resonant frequencies leading to G and E respectively. The testing of only one bar (80 x 3 x 3 mm), of shorter than normal length (imposed by material availability) inevitably leads to inaccuracies (132, 127). However both rectangular specimen sides were used to obtain average values of $E = 295 \pm 5$ GPa, $G = 113 \pm 2$ GPa and hence Poisson's Ratio (ν) = 0.28 ± 0.005 for material (SO) at room temperature.

The temperature variability of these properties could not be determined on this equipment but was extrapolated (as explained in Appendix 4.3) and is given in Fig A4.3. All alloys show a peak at 800°C and fall-off above 1200°C. The hump is observed with CVDSiC and HPSN and is still not understood. The higher temperature fall-off occurs in HPSN and PSSN (32) and is believed due to g.b. glass softening which allows viscous flow under the operating strain rate. This is supported by the reversal of the downward trend with increased crystallisation of glass matrix specimens.

The high temperature measurement of Shear Modulus G requires complex and expensive experimentation and so was derived from E variations, using equation 4.5 and assuming a temperature independent Poisson's ratio. This assumption is possible if E and G have similar temperature dependencies, which has frequently been found the case in HPSN, HPSi-Al-0-N and PSSN.

4.3.5 Compliance Change Method

If substantial subcritical crack growth occurs during a K_{IC} determination this can yield K_I -V data, albeit qualitative. The occurrence of s.c.g. is characterised by a zone of rough topography on the fracture surface and a deviation from elastic linearity on the load/displacement curve (Fig 4.7 a). Under identical specimen dimensions and loading conditions, the extent of s.c.g. as a function

Figure 4.7. Compliance Change Method of K_I -V Relationship Determination, from a K_{IC} specimen.

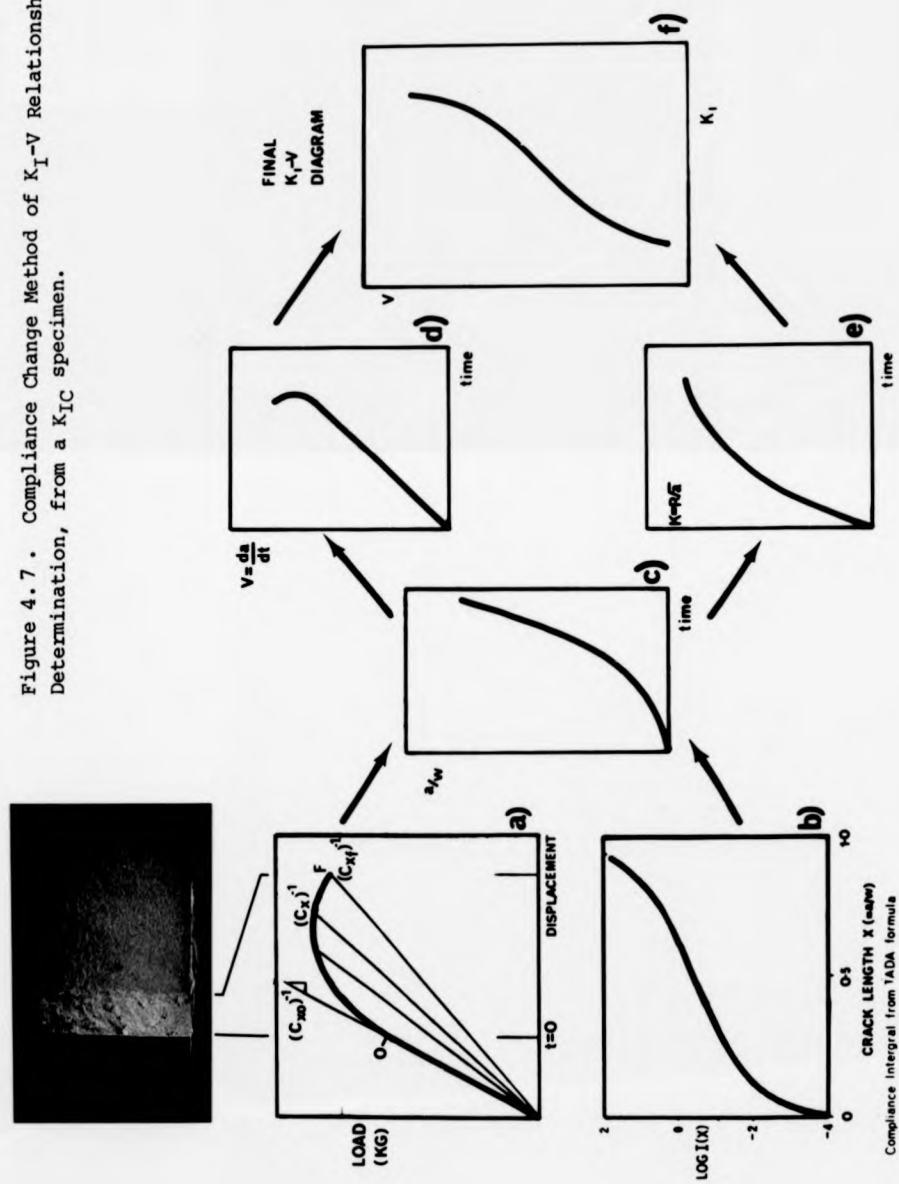
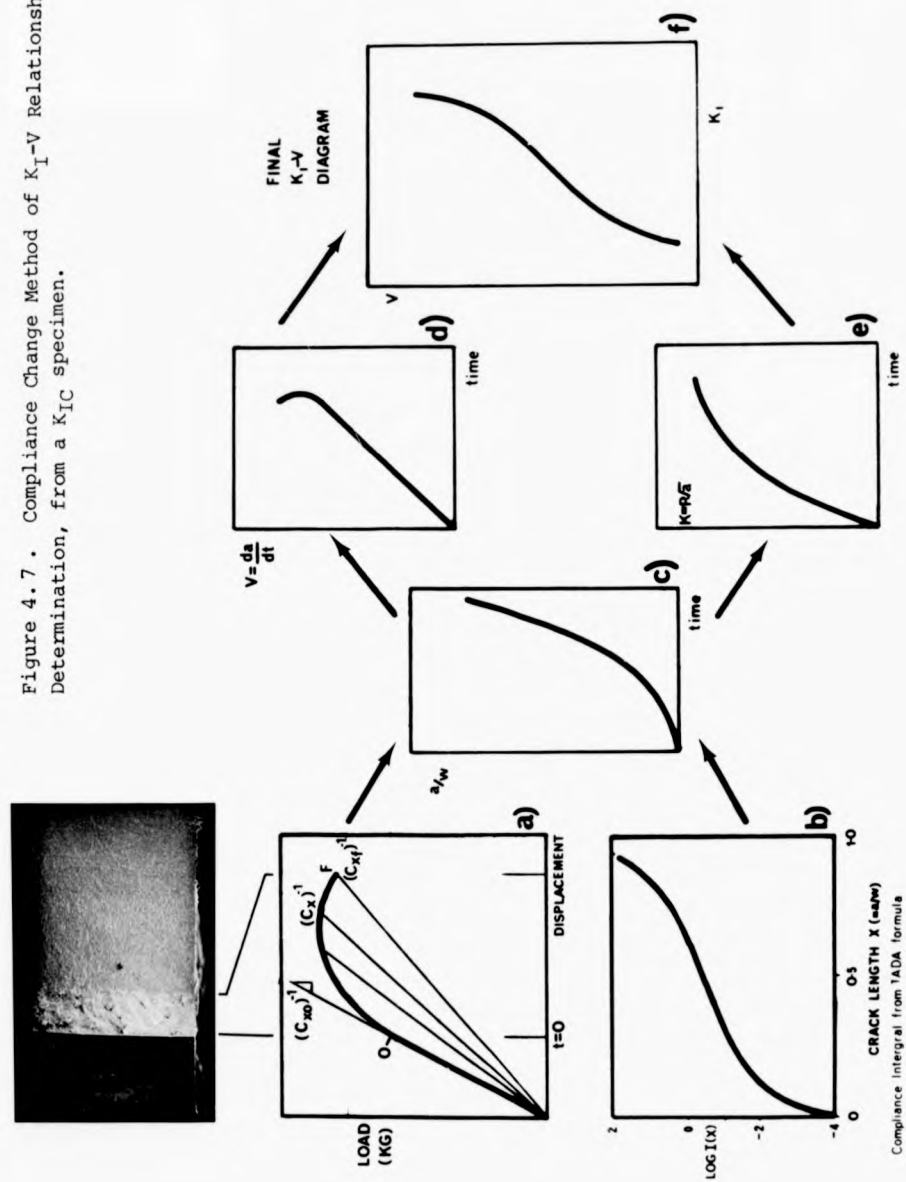


Figure 4.7. Compliance Change Method of K_I -V Relationship Determination, from a K_{IC} specimen.



of temperature or material composition can be quickly ascertained. More quantitative analysis of this data by Fields et al. (114) gave rise to a continuous range of K_I data for Hot-Pressed Si-Al-O-N material but did show a discrepancy from the established DT derived data for similar materials. In comparison with the DT technique, this method does not require a knowledge of material properties E, G or ν and offers reduced material size and usage with a simplified experimental process that can yield both K_{IC} and K_I - ν data in one break. The suitability of this method for sintered Si-Al-O-Ns was therefore investigated over a temperature range. In the analysis, the load/displacement curve, initiated at 0 (Fig.4.7), is assumed to be due to stable crack growth which makes the bar increasingly compliant. Rapid unloading at any point along the curve would give a straight line through the origin whose slope (C^{-1}) is proportional to the crack depth. Specimen unloading is not required and a series of lines can just be drawn. Using this procedure, the crack length 'a' and load may be obtained as a function of time during the test. This information is converted, graphically and from a series of fracture mechanics derived relationships (Appendix 4.4.), into crack velocity as a function of stress intensity (schematically shown in Fig 4.7). The key to this analysis is the measurement of the s.c.g. zone which gives the only definite crack length after a known time and allows all prior crack velocities to be interpolated.

The success of the technique for the present materials was limited. At the temperatures where the required extensive s.c.g. occurred, fracture was accompanied by extensive plastic deformation which invalidated the assumption of compliance change only due to crack growth. Test temperature reductions to suppress plasticity also considerably reduced the extent of s.c.g. which greatly influenced subsequent K_I - ν derivation and highlighted the following limitations of this technique. (1) In practice a problem exists in exactly

locating the point 0 (critical for this analysis) due to plastic deformation. (2) Exact s.c.g. zone measurement is complicated by a non-linear and diffuse crack front (which assumes greater importance with small s.c.g. zones. (3) Only small curve sections (0-F) were obtained which did not give large compliance variations. (4) The graphic manipulation cannot be reasonably performed on the narrow and suspect data spread. (5) Only a narrow upper portion of the K_I -V regime could be determined.

In conclusion, this technique could not give the complete K_I -V relationship, but is useful, where material is limited, in supplementing data derived from DT. An important advantage it offered over DT for the unstable matrix materials was its rapid warm-up, rapid fracture and rapid cooling cycle potential which ensured the matrix remained in a stable state during fracture.

CHAPTER FIVE

CERAMIC FABRICATION AND MICROSTRUCTURE

This chapter describes not only the technique of fabrication and subsequent microstructural analysis of the current range of ceramics, but also presents and interprets the results of a detailed microstructural characterisation with emphasis on grain boundary matrix compositions and their stability.

5.1 FABRICATION

5.1.1 Introduction

All materials were fabricated by LUCAS-COOKSON-SYALON LTD., Solihull, England, who have been involved in a collaborative research effort with the Physics Department, University of Warwick, (for the last 15 years), in the development of Si-Al-O-N ceramics towards a commercial goal. The supply of material (quantity and type) is largely controlled by Lucas. Their heavy manufacturing commitment to current production compositions, and the constant development towards commercially reproducible materials has meant the supply of a large material range of limited quantity. The industry's highly competitive nature also means that some composition and fabrication details may not be published.

The majority of the present work was performed on materials prepared from an α - Si_3N_4 source (L.C.10) produced by H.C. Starck, Berlin. Material sinterability, homogeneity and therefore properties and reliability can be considerably controlled by the initial SiO_2 constituent level. The most effective route to controlling the SiO_2 content and its distribution is via the SiO_2 surface oxide on the

α - Si_3N_4 particles. For a reliable, uniform final microstructure, the SiO_2 level must be predictable and consistent. The level is controlled by the specific surface area (s.s.a) and powder fineness. L.C-10 offers a reliable powder with a narrow particle-size-distribution and one of the highest s.s.a. values currently available (17). Production is by nitridation of Si powder. Powders are chemically purified with acids and consequently have low impurity concentrations, i.e. Ca = 0.02, Al = 0.08, Fe = 0.03, C = 0.1%. The major impurity is oxygen (~1.5%) regulated by control of the SiO_2 layer thickness ($5\text{\AA} \rightarrow 30\text{\AA}$). β - Si_3N_4 (~3%) is also detected.

Previously (44), AlN was used as an unreacted starting component for sintering Y_2O_3 -Si-Al-O-N ceramics, but was found to have high and variable O and free Al impurity levels. However, replacement by one of the "polytypoid" phases based on AlN (37), usually 21R, improved this situation.

5.1.2 Fabrication Route

The typical fabrication route is as follows. The α - Si_3N_4 , 21R and Y_2O_3 (supplied by Rare Earth Products) are wet milled with propanol in alumina media (in rounded cylindrical form) for several days in polythene pots in order to reduce particle size and increase s.s.a. The alumina medium is weighed before and after to determine the Al_2O_3 pick-up and the composition is then determined. The slurry is sieved (90 μm mesh), dried and resieved (1000 μm mesh) to break up any large aggregates. The powder is poured into billet preforms and isopressed to 1.38 Kbars. After removing the preform bag, the green billet is coated with a colloidal mixture which protects the surface finish and acts in a similar way to a powder bed. Two stage sintering, 1600°C and ~1750°C under a small N_2 overpressure is performed in a programmable sintering furnace (details of time and temperature are given in Table 5.1).

CODE	α -Si ₃ N ₄ SOURCE	Wt. % 21R	Wt. % Si ₃ N ₄	Wt. % Y ₂ O ₃	Wt. % Al ₂ O ₃	SINTERING TEMP. (°C)	ANNEAL
SO	STARCK LC10	0	92.3	7.7	-	1800/5HRS	-
S10	STARCK LC10	10	83	7	-	1600/2 HRS 1800/5 HRS	-
S13	STARCK LC10	13	74	7	6	1500/2 HRS 1800/5	-
N2	NORTON	2	91	7	-	1830/1 HR	1400/5 HRS
N4	NORTON	4	89	7	-	1830/1 HR	1400/5 HRS
N6	NORTON	6	87	7	-	1830/1 HR	1400/5 HRS
N8	NORTON	8	85	7	-	1830/1 HR	1400/5 HRS
L10	LATEST SOURCE	8 7	86 85	6 5	 3	1650/2 HRS 1800/5 HRS	1250/7 HRS 1400/5 HRS

TABLE 5.1

FABRICATION DETAILS OF THE RANGE OF Y-Si-Al-O-N STUDIED

800) of SiC grit paper and then successively diamond lapping (14, 6, 1 and finally 0.25 μ m grade) until score-free under an optical microscope. Specimens were ultrasonically cleaned in acetone before carbon-coating or optical examination.

The S.E.M. was fitted with a J.K. Back Scattered Electron (b.s.e.) detector which, on a perfectly flat specimen, gave image contrast due to atomic number differences. Under optimal conditions the detector gave macroscopic elemental distributions and had sufficient spatial resolution to distinguish matrix phase features. Also the excellent spectral resolution gave contrast between phases with very small atomic number differences (vis. Si_3N_4 and $\text{Si}_2\text{N}_2\text{O}$ in Chapter 6). The macroscopic variations of matrix phase (extent and type of crystallinity) could therefore be measured in S.E.M. and with a statistical precision greater than in T.E.M. A low (~ 7 kV) accelerating voltage was used as it gave a more accurate "surface" profile, reduced subsurface fluorescence and bright region "spill-over", which can reduce resolution.

5.2.2 The Detection of g.b. Films

In T.E.M. the "lattice-imaging" technique (133) has successfully given direct evidence of very fine amorphous g.b. films in HPSN (134) and H.P. Si-Al-O-N ceramics (47), which were previously indicated from high temperature s.c.g. phenomena. However, for characterisation of a varying g.b. phase, the technique is severely restricted by the critical grain and g.b. inclination requirements (127). Also subsequent g.b. interpretation can be complicated by lattice fringe modulations (135) and the fact that the most readily observed g.b. constitutes the boundary most susceptible to leaving a glassy phase.

The alternative "dark-field" imaging of the g.b. glass (using diffracted electrons having an intensity distribution corresponding to an amorphous phase) has been used for HPSN (136). However, the g.b. phase must still be parallel to the incident beam and the g.b. contrast

can also be achieved by multiple electron scattering.

Any analyses derived from the above techniques are therefore very selective and ambiguous. More importantly, following theoretical calculations by Raj (137), the size of a triple g.b. glassy pocket needed for the formation of a cavity under mechanical loading was found to be within the resolution limit of the conventional diffraction contrast image. Conventional imaging (up to 250,000 x) was therefore employed. To support T.E.M. evidence for the distribution of critically-sized glassy volumes, materials were fractured (as K_{IC} bars) in vacuum (above 1400°C) to produce s.c.g. (via a cavity nucleation and inter-linkage mechanism). The large crack front samples many thousands of g.bs. and gives a statistically more accurate characterisation. A slow displacement rate (0.001 cm/min) allowed for extensive s.c.g.

5.2.3 Chemical Micro-Analysis

Chemical micro-analysis was performed in both S.E.M. and T.E.M. instruments via Energy Dispersive X-ray Analysers (E.D.A.X. systems 9100 and 707B respectively), capable of detection of elements with atomic numbers down to $z = 11$ (sodium). Various advantages exist with each system. In the T.E.M. the electron transparent sections are transparent to the generated X-rays and it is frequently assumed X-ray absorption and fluorescence can be neglected. The relationship between the ratio of detected characteristic X-ray intensities of 2 elements (I_1/I_2) and the actual elemental weight fractions (C_1/C_2) of the ionized volume is simplified to:

$$\frac{C_1}{C_2} = K_{12} \frac{I_1}{I_2} \quad (5.1)$$

where K_{12} is a factor representing the ratio of probabilities for emission and detection for the 2 elements. K is related to ionization cross-section, fluorescence yield, detector efficiency. Values of K have been calculated (138) for $K\alpha$, $L\alpha$ and M X-rays of many elements. However the negligible absorption assumption is invalid for ratios with

large mass absorption differences (i.e. Al/Y) and correction factors (up to ~1.3) have been calculated (43).

When analysing "bulk" material in the S.E.M., a large pear-shaped volume (which varies with probe penetration) is ionized beneath the surface cross-section of the incident electron beam. The collected X-ray spectra from this volume do, therefore, need fluorescence and absorption corrections. The 9100 system has a full data processing unit, with background removal (Bremsstrahlung), peak deconvolution (particularly important for the $Y_{L\alpha}/Si_{K\beta}$ peak overlap), peak integration and calculated Z.A.F. (Atomic Number, Absorption, Fluorescence yield) correction for the particular analysed volume and elemental ratio. All calculated correction factors were checked by analysing stoichiometric standards of "YAG" and Eutectic Y, Al, Si, O glass, both made up in this laboratory. The integrated peak ratios Al/Y, Si/Y, Al/Si were measured and compared with expected weight fraction ratios. Additional empirical correction factors were then determined to account for light element absorption by the detector's beryllium window (Al/Si) and mass absorption differences (Al/Y, Si/Y). All S.E.M. analysis was subsequently performed at a standard accelerating voltage (10 kV) and probe size. If relevant microstructural features can be solely enveloped within the calculated excitation volume (by parameter optimisation - Section 5.2.1) then rapid statistical and quantitative microstructural (β' + matrix) analysis and characterisation is possible.

The area analysed in T.E.M. is more selective and reduced to a cylinder ($\ll 0.1 \mu\text{m}$ diameter) extending below the electron beam entry surface. The specimen tilt requirements for quantitative analysis however, when compounded with a spot size larger than most intergranular features, can reduce spatial resolution and increase the probability of X-ray fluorescence and absorption from underlying and

surrounding material. Analysis was therefore obtained only from very thin, large and preferably peninsular areas. The probe diameter (and hence analysed volume) is reduced using the S.T.E.M. facility (probe size $< 0.01\mu\text{m}$) but at the expense of low X-ray yield and imprecise probe location.

The fluorescence problem is also reduced by dispersing a finely crushed T.E.M. thinned section onto a copper T.E.M. grid (previously deposited with a carbon film). Isolated fragments of the various crystals (unattached to any other phases) can result and allow unambiguous analysis. This technique was also used for identification of crystalline phases present in the oxide layer and laser specimen surfaces, where there was insufficient material for X.R.D.

5.3 THE MICROSTRUCTURAL CHARACTERISTICS OF SINTERED ALLOYS

The type and quantity of sintering aid used during fabrication of Y-Si-Al-O-N ceramics will be shown to significantly effect their final microstructure and also mechanical properties. In the present materials, the effect of Al and N variability within the sintering aid is facilitated essentially by the variable 21R "polytypoid" and a constant Y_2O_3 addition. The influence of a different source of $\alpha\text{-Si}_3\text{N}_4$ is also explored. Material SO (without 21R addition) is described in detail to highlight subsequent microstructural development through compositional alterations.

5.3.1 Microstructure of Alloys with Low "Polytypoid" Content

Figure 5.1a is a T.E.M. micrograph of material SO which readily illustrates its bi-phase microstructure and is also typical of all the as-sintered compositions. The major phase is identified by Selected Area Diffraction (S.A.D) and X.R.D. as β' -Si-Al-O-N. It has a range of low Al and O substitution levels ($z \approx 0.14 \rightarrow 0.25$), primarily

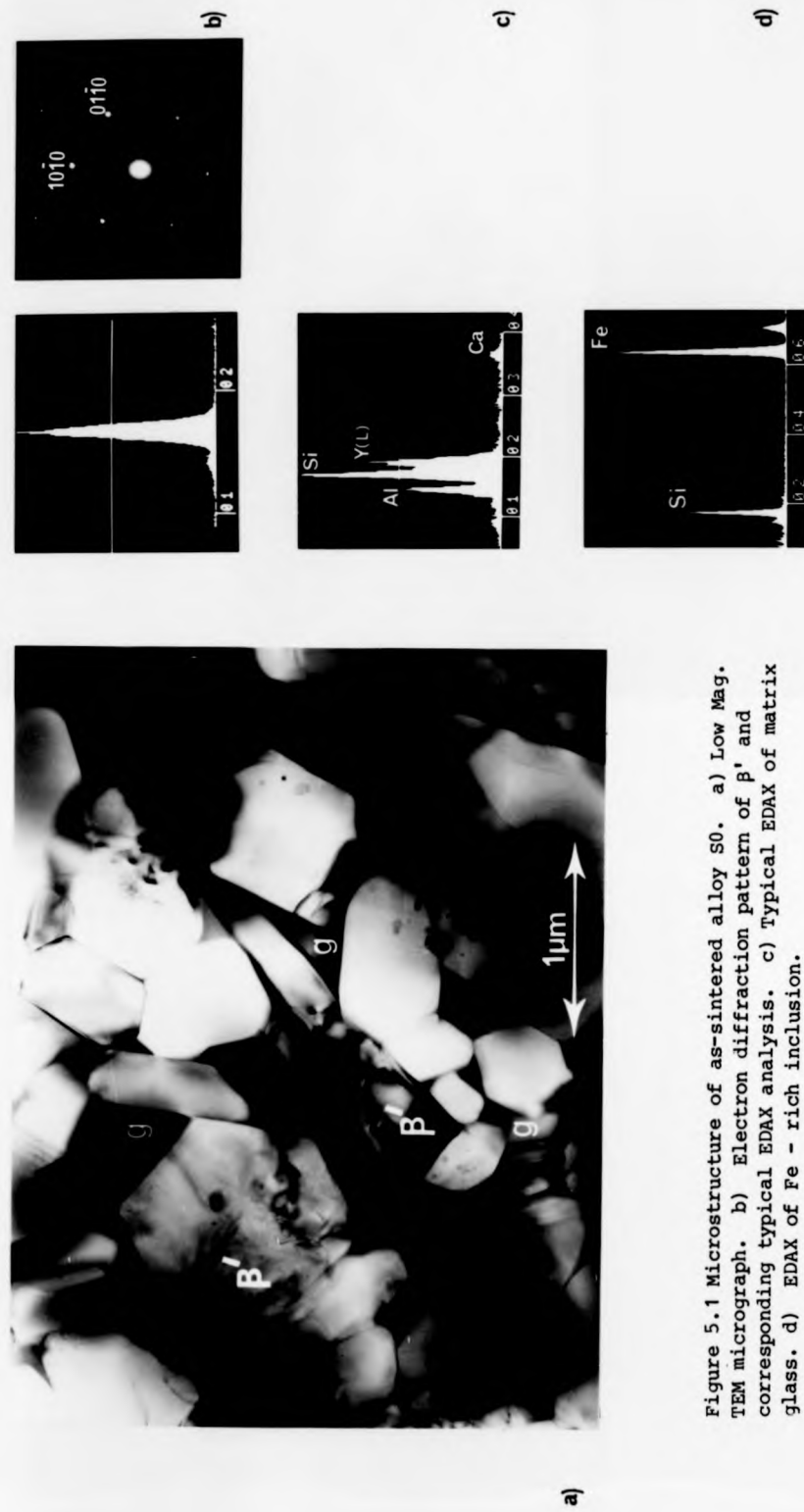


Figure 5.1 Microstructure of as-sintered alloy S0. a) Low Mag. TEM micrograph. b) Electron diffraction pattern of β' and corresponding typical EDAX analysis. c) Typical EDAX of matrix glass. d) EDAX of Fe - rich inclusion.

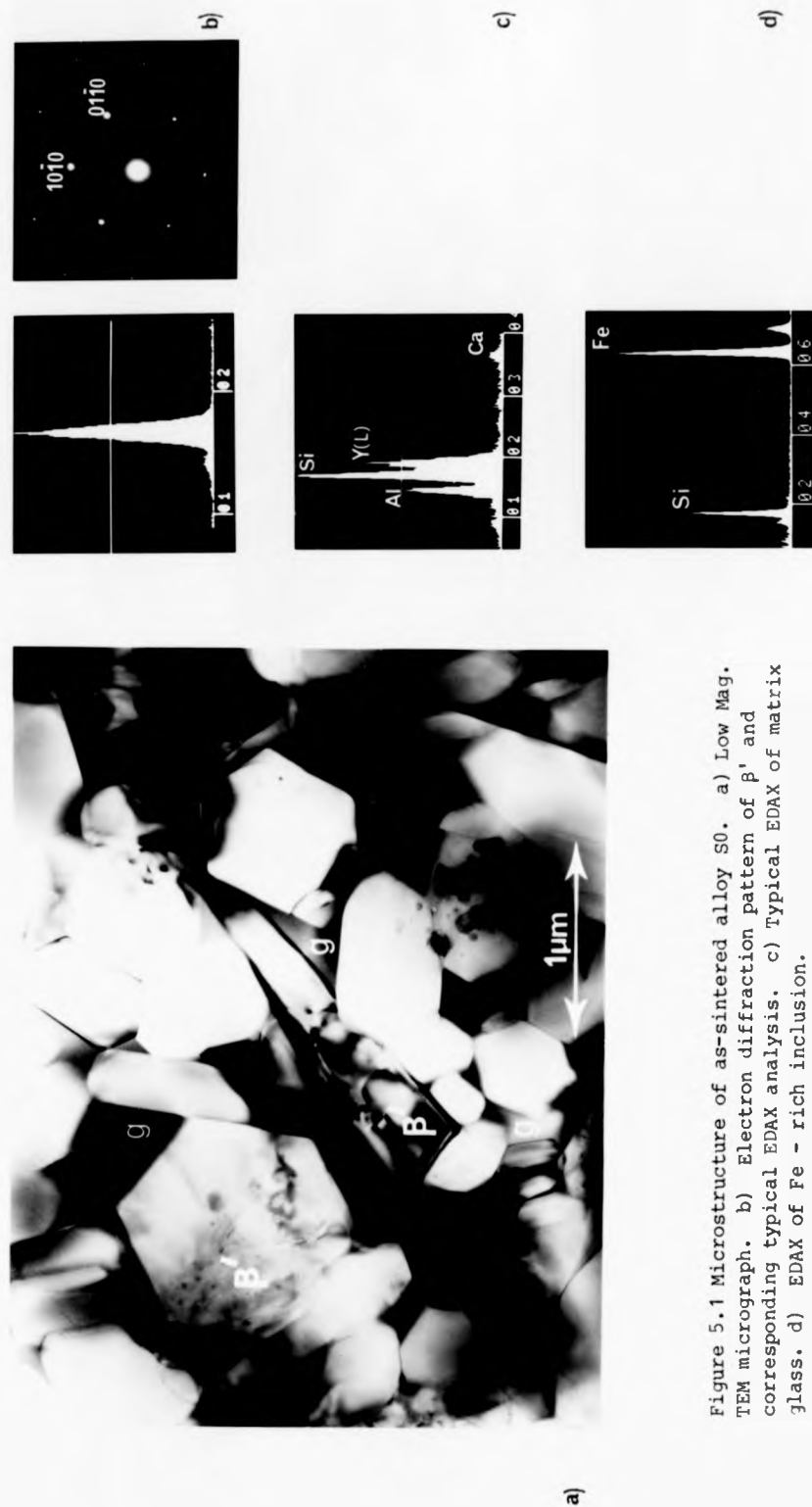


Figure 5.1 Microstructure of as-sintered alloy S0. a) Low Mag. TEM micrograph. b) Electron diffraction pattern of β' and corresponding typical EDAX analysis. c) Typical EDAX of matrix glass. d) EDAX of Fe - rich inclusion.

determined from E.D.A.X. (Fig.5.1b) but supported by X.R.D. The differing diffraction conditions in T.E.M. together with X.R.D. peak ratios show the β' grains to be randomly orientated.

The second phase "matrix" appears semi-continuous and for material SO totally non-crystalline, this being ascertained from (1) its lack of diffraction contrast during specimen tilting, (2) characteristic diffuse "halo" S.A.D. pattern, (3) "speckled" appearance due to electron beam irradiation damage, (4) β' identified as the only crystalline phase by X.R.D. This glass contains the heavy element sintering additives and impurities Y, Fe and Ca (Fig.5.1ac/d), which gives the matrix high electron absorption contrast in T.E.M. and also excellent b.s.e. contrast in S.E.M. The Fe is sometimes in the form of randomly distributed iron silicides (Fig.5.1d), derived from the powder production process.

The β' grains have crystallographically faceted hexagonal sections indicating prior unhindered growth. Together with the matrix glass, this confirms the usual solution/precipitation mechanism for densification. The 3-dimensional S.E.M. image of a high temperature fracture surface more accurately shows their elongated prismatic morphology and interlocking nature (Fig.5.2a). Unlike H.P. Si-Al-O-N (127) with equivalent β' grains, the present β' grains are not satisfactorily characterised by an average grain size. Based on measurements of some 200 identifiable grains (from S.E.M. b.s.e. and fracture surfaces like Figs.5.2a/b), dimensional histograms (0.4 μ m interval) indicated mainly elongated grains with a tri-modal size distribution given in Table 5.2.

If the nitrogen content is neglected (reasonable for SO with no 21R additive) then the residual glass composition can be represented as metallic oxides and the E.D.A.X. spectra plotted on the Y_2O_3 - SiO_2 - Al_2O_3 ternary phase diagram (the end face of the Y-Si-Al-O-N

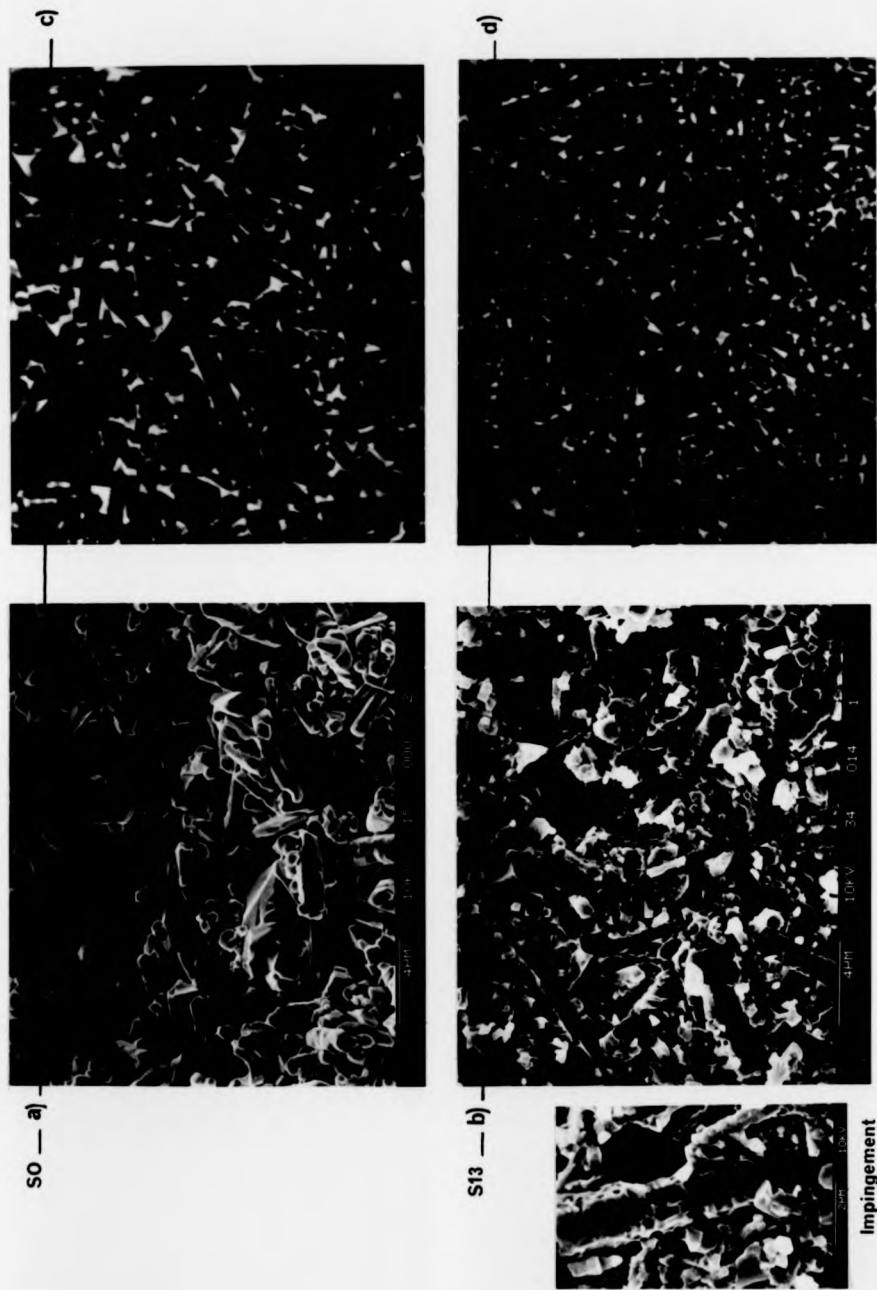


Figure 5.2 Scanning Electron Microscope images of alloys S0 (a and c) and S13 (b and d) using bse imaging of polished sections (c and d) and high temperature fracture surfaces (a and b). All micrographs to the same scale.

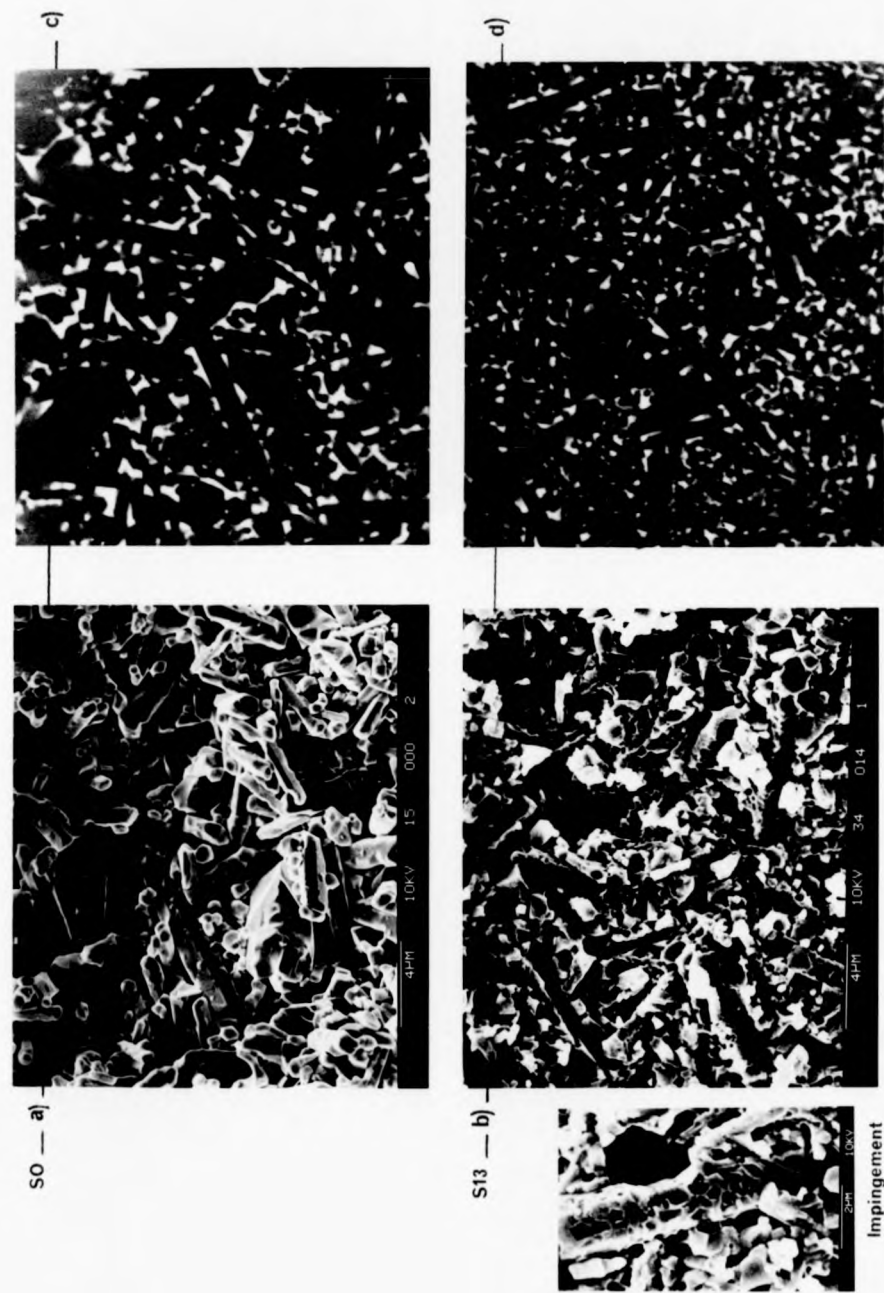


Figure 5.2 Scanning Electron Microscope images of alloys S0 (a and c) and S13 (b and d) using bse imaging of polished sections (c and d) and high temperature fracture surfaces (a and b). All micrographs to the same scale.

Table 5.2. The β' grain size distribution for the as-sintered alloys S0 and S13. All values are $\pm 0.2 \mu\text{m}$.

Alloy S0			Alloy S13		
	$\bar{a}(\mu\text{m})$	$\bar{c}(\mu\text{m})$		\bar{a}	\bar{c}
1.	0.5	2.2-3.0	1.	0.3	1.0-2.2
2.	1.0	4.0-5.8			
3.	2.0	4.2	2.	0.8	4.0

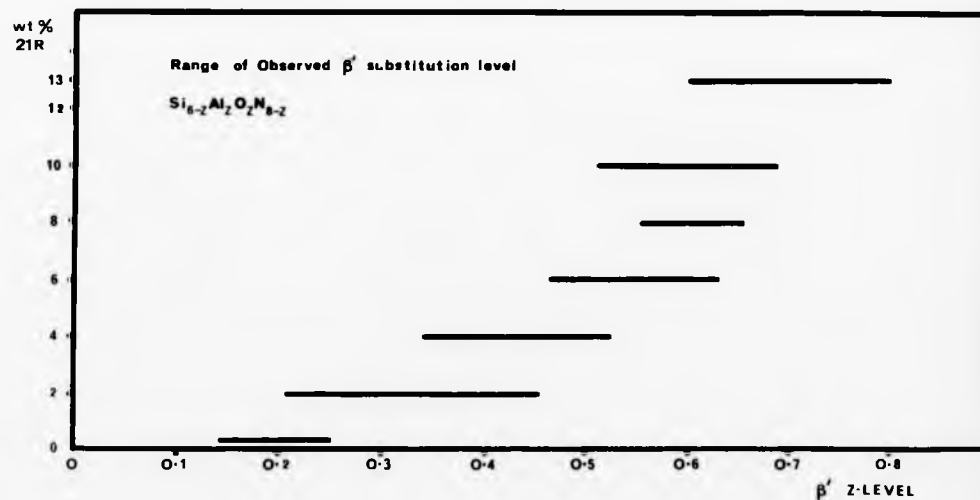


Figure 5.3. The range of observed β' substitution (from EDAX) for each alloy and the overall variation with 21R content.

pseudo-quaternary prism in Fig.1.6).

5.3.2 Microstructural Development With Increasing "Polytypoid" Addition

Materials N2, N4, N6 and N8 show small but significant microstructural developments due to their incremental steps of 2 wt. % 21R additive. The variation is most dramatically revealed by comparison of SO with extreme 21R addition materials (S10 and S13). Trends identified are:

1. Increase in the Al substitution level (and implied z level) of β' grains (Figs.5.3). The variation in Al substitution between grains leads to the observed range of z-levels. Initial mixing inhomogeneities which vary the local sintering liquid composition is probably responsible.
2. A reduction in overall grain size (Fig 5.2) and loss of very large grains, although the interlocking prism morphology is retained.
3. A volume reduction and finer distribution of matrix glass.
4. Increase in grain impingement, particularly noticeable on the surface of large grains (Fig 5.2b).
5. Increase in residual porosity level (see Section 5.3.4).
6. Increase of $(Y + Al)/Si$ ratio in residual glass composition and its general movement away from the SiO_2 corner and towards Al_2O_3 in the ternary phase diagram (Fig 5.4).

Observations 2, 3, 4 and 5 suggest a more efficient densification mechanism operating for SO, where the $\alpha \rightarrow \beta'$ Si_3N_4 conversion occurs early at the sintering temperature leaving an effectively extended hold time for β' grain growth. Mean grain size intercept values have been shown to increase with hold time with HPSN (139). With increasing 21R additive this reduced efficiency is partially due to a reduced sintering liquid volume (implied by the

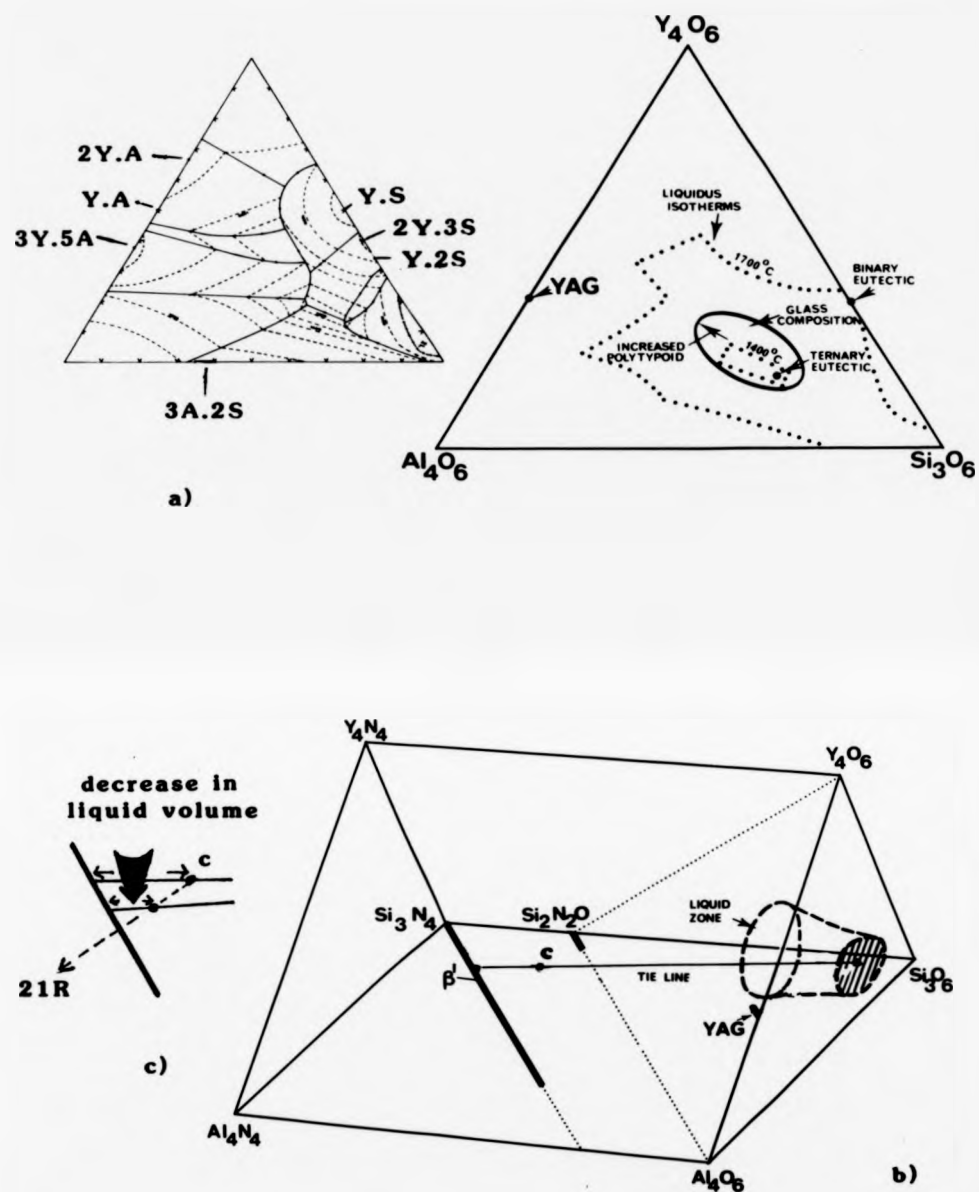


Figure 5.4 Equilibrium diagrams illustrating the compositional modifications to the matrix glass(a) and overall microstructure(b,c) due to polytypoid addition.

reduced g.b. residual glass). The smaller grain size and increased porosity also suggest a slower diffusion of species through the liquid and lower β' - liquid wetting, both indicative of an enhanced liquid viscosity.

The above variations with additive level are explained via the relevant phase diagrams (Fig 5.4). The movement of the matrix glass composition away from the ternary eutectic implies that the glass will have a higher glass transition temperature (T_g) and that, during densification, the sintering liquid would have a higher viscosity. The "bulk" (β' + matrix) composition can also be plotted within the pseudo-quaternary prism, on a line joining β' and glass compositions. The position on this line is determined by the lever rule using calculated relative phase volume fractions. Conversely, plotting "bulk" compositions should predict glass matrix volumes. In Fig 5.4b increasing 21R (up to S13) moves the "bulk" composition (point c) of SO closer to the AlN corner and β' line and predicts the observed reduction in glass volume.

The observed β' z-level increase with 21R addition implies the rejection of N and Si into the liquid matrix during sintering (assuming overall compositional conservation). The N concentration would be expected to be further enhanced by the reduced liquid volume and general level of 21R component. Indirect glass matrix N-level determination from initial composition is complicated by N loss during sintering and the variable β' z-level. Direct determination is considered important as "bulk" Y-Si-Al-O-N glass properties (61,140) vary substantially with small N alterations and the high temperature properties of the present bi-phase materials are dominated by the properties of the matrix.

5.3.3 Determination of N Content in g.b. Glass

5.3.3(a) The Techniques

The detection of light elements ($z < 9$) using E.D.A.X. is limited by several fundamental factors. Firstly, X-ray fluorescence yield decreases rapidly with z and this low yield is coupled with relatively poor collection and detection efficiencies in most X-ray detectors. Also low energy X-rays are easily absorbed by the detector's window and semi-conductor dead layers or specimen coating. Currently, light element detection is by Auger Electron Spectroscopy or Electron Energy Loss Spectroscopy (E.E.L.S). Whilst A.E.S. has detected O and N at Si-Al-O-N g.b.s (127) it is limited by poor spatial resolution and its analysis of only near-surface material. E.E.L.S. is considered a more powerful tool. Firstly, each inner-shell ionization produces an electron with a characteristic energy loss, therefore fluorescence yield is unity (c.f. 0.025 for E.D.A.X). Secondly, electrons suffering energy losses (due to interactions with low z elements) are scattered through relatively small angles and thus collection efficiency is $\sim 0.1 \rightarrow 1.0$.

5.3.3(b) Electron Energy Loss Spectroscopy

E.E.L.S. was successfully used to detect N at the g.b. of HPSN (141) fabricated in the Si_3N_4 - $\text{Si}_2\text{N}_2\text{O}$ - Mg_2SiO_4 phase compatibility triangle, where $\text{Si}_2\text{N}_2\text{O}$ was readily identified by its N_K loss peak. In the present study a Phillips T.E.M. with GATAN E.E.L.S. unit (at Birmingham University) was used in its convergent beam diffraction mode. The g.b. glass of low and high Nitrogen materials (S0 and S13 respectively) were studied. The characteristic diffuse diffraction halos were obtained to ensure only the amorphous phase was being subsequently analysed. Only thin areas were probed, to reduce multiple scattering which complicates the spectra and decreases the minimum

detectable element concentration. Specimens were not coated (to reduce surface charging) as carbon, gold, aluminium, etc., all have plasmon loss tails which were found to interfere with the N and O peaks. The spectra obtained just showed the presence of N above the background for material S13. Similarly inconclusive spectra have been obtained by other workers including Thomas and Ahn (142) studying bulk Y-Si-Al-O-N glass with a calculated 13 atomic % N and Clark et al. (141) studying a model HPSN with a greatly enhanced volume fraction of g.b. glass (which contained MgO). The latter estimated that a detection limit of ~ 5 at. % N existed for existing equipment.

To determine the N detection limit for the present equipment and provide N standards, thin sections of previously made-up "bulk" Y, Si, Al, O, N glasses with varying N/O ratio were analysed. The N/O could be accurately determined from the "As-mixed" composition, assuming no losses during fabrication. A detection limit ~ 7 at. % N was determined and the technique was concluded to be too qualitative for the levels of N here (max ~ 12 at. %). However, the E.E.L.S. technique is a developing one and the sensitivity has very recently been improved. Identical materials have also been recently studied by a colleague. His spectra are the most accurate to date and are repeated here with his analysis (143).

The N/O atomic ratio for each probed area was determined using the expression given by Clarke et al. (141):

$$\frac{C_N}{C_O} = \frac{A_N(\alpha, \Delta E)}{A_O(\alpha, \Delta E)} \times \frac{q_O(\alpha, \Delta E)}{q_N(\alpha, \Delta E)} \quad (5.2)$$

where for a given collection angle (α) and energy window after the edge (ΔE), $A_N(\alpha, \Delta E)$ and $A_O(\alpha, \Delta E)$ are the areas under the nitrogen K edge and oxygen K edge after background subtraction, respectively. $q_N(\alpha, \Delta E)$ and $q_O(\alpha, \Delta E)$ are the partial ionization cross-sections for N and O applicable under the experimental conditions. For the experimental

conditions of 8.33 m.rad. acceptance angle and 40 eV energy window, the ratio $q_0/q_n = 585/1279 = 0.457$ was obtained.

5.3.3(c) Summary of Results

Based on the spectra (reproduced in Fig 5.5a), Winder concluded that the N/O ratio in the residual g.b. glass increased with 21R additive and calculated N/O ratios of 0.00 and 0.256 (equivalent to 13 at. % N) for materials S0 and S13 respectively. The accuracy of the N/O ratios however must be questioned on three counts. (1) Clarke (141) calculated that systematic errors associated with partial ionization cross-section determinations always give an $\sim 10\%$ uncertainty to determined elemental compositions. (2) With such small N_K loss peaks, their exact area integration depends critically on the extrapolated background. An on-line computer usually extrapolates from the background curve prior to the edge (between 50 and 100 eV). This curve can be represented by $A.E^{-r}$ (where A and r are constants and E is the energy loss). Here, the background curves were extrapolated purely by eye. (3) The N_K loss peaks are not smooth and the random variation between energy channels is readily observed in spectra S13. Integration of these low signal-to-noise peaks must lead to the largest error. The inaccuracy of Winder's quoted N/O ratios is apparent when spectra S13 ($N/O = 0.256$) is directly compared with the superior spectra obtained by Clarke (141) for a calculated similar N/O ratio (0.250) in an Mg-Si-Al-O-N g.b. glass. Clarke's result is not subject to errors (2) and (3) but still has a 10% systematic uncertainty associated with it. A calculated uncertainty for Winder's N/O ratio values is 30% (from simple compound error theory) and g.b. glass N levels of 13.0 ± 4 a/o for material S13 and up to 2 a/o (detectability limit) for S0 are considered realistic and still fall within the N range 0-15 a/o N for similar bulk glasses previously produced and studied (140, 144, 145).

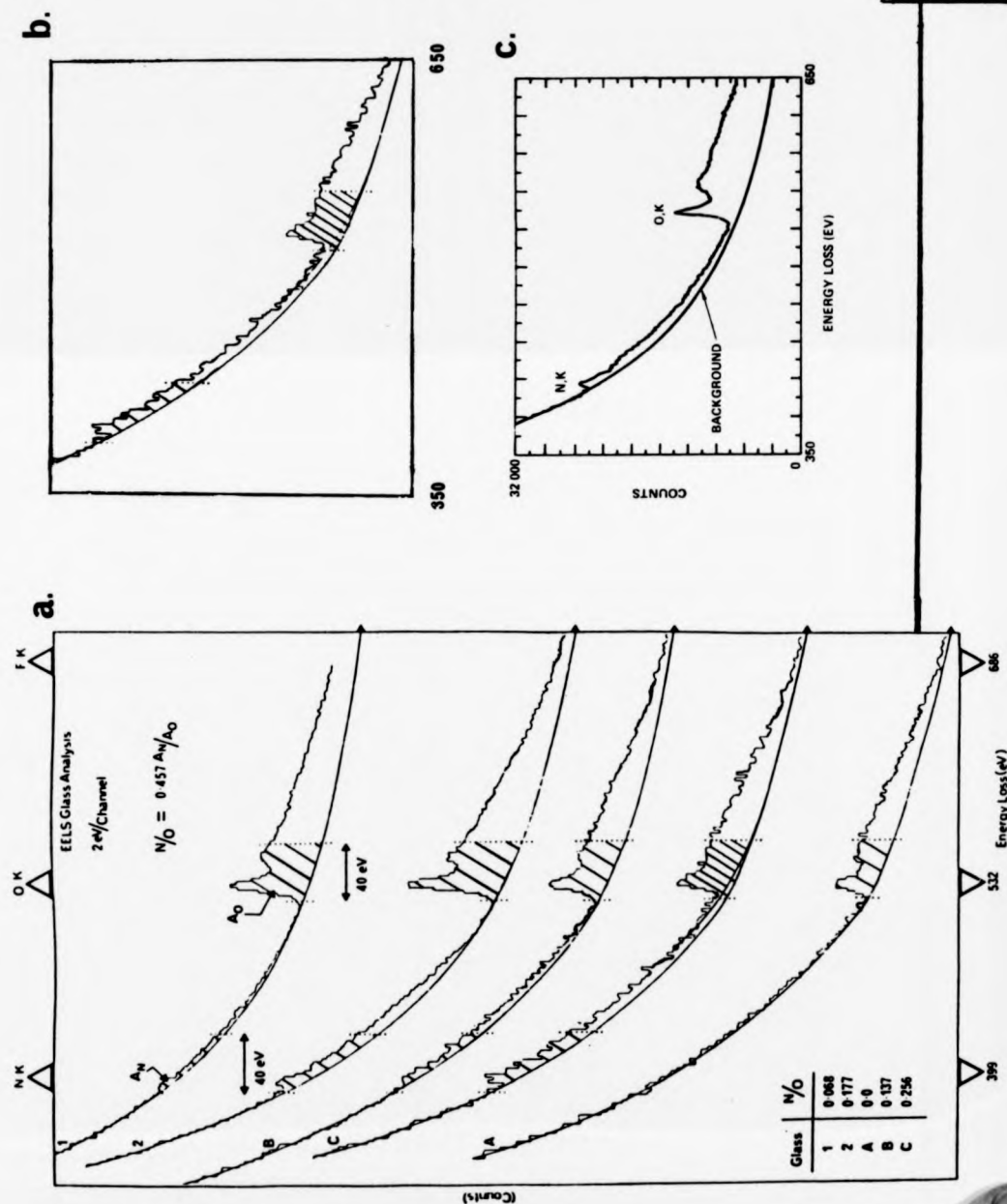


Figure 5.5.a) EELS spectra obtained from bulk reference glasses 1 and 2, and intergranular glasses of Y-Si-Al-O-N ceramics A, B and C after (149) b) Spectrum for 13 at. % Nitrogen after (149). c) Equivalent spectrum for 13 at. % N from Clarke et al (148). Note Y-Si-Al-O-N ceramic A \equiv S0, B \equiv N4 and C \equiv S13.

In each case, N/O values listed in the table were obtained from the equation $N/O = 0.457 A_N/A_O$ where A_N and A_O are the areas, after background subtraction, under the Nitrogen K edge and oxygen K edge within the energy windows, respectively. The 40 eV energy windows are indicated and A_N and A_O are made obvious by shading. The acceptance angle was taken as 8.13 mrad.

These E.E.L.S. results (even with the large error) are important as direct evidence for g.b. glass N/O variation with 21R polytypoid additive and suggest the properties of bulk Nitrogen glasses may be confidently used to calculate g.b. glass properties.

5.3.4 Sintered Densities and Porosity Levels

A knowledge of residual porosity is important because pores can act as critical flaws and drastically influence mechanical strengths and material reliability (as exemplified by the poor mechanical properties of low density R.B.S.N.). Residual porosity can be obtained by (1) comparison of a material's actual (measured) density with its theoretical full density, or (2) by the more strenuous examination of polished sections in the S.E.M. All densities were measured by Lucas using the Archimedian technique (with water).

Theoretical full densities of these bi-phase ceramics were calculated from the densities of the phases and their respective volume fraction (see Table 5.3). The latter was obtained from S.E.M. b.s.e. images used in conjunction with an image analyser. The density of β' - Si_3N_4 is readily calculable but the matrix glass values were derived from the literature. An error is introduced here as density values were unavailable for compositions corresponding exactly to the present glasses.

Within the experimental error, density measurements indicate that material 50 is sinterable to full theoretical density and an S.E.M. study supports this predicted low porosity level. This density level not only represents an improvement over previous sintered Y-Si-Al-O-N (43) but approaches that usually associated only with hot-pressed materials. The improvement is probably due to the LC-10 α - Si_3N_4 starting powder whose fine uniform grain size achieves greater green densities and whose uniform distribution and control of surface silica

MATERIAL	VOLUME % OF MATRIX PHASE (+ 1)	CALCULATED DENSITY* $\text{KgM}^{-3} \times 10^3$ (+ 0.015)	MEASURED DENSITY (LUCAS) $\text{kgM}^{-3} \times 10^3$ (± 0.001)	EST. VOL.% POROSITY FROM DENSITY	EST. VOL % POROSITY FROM SEM
S0	9	3.225	3.239	0	0
S13	7	3.26	3.253	0.7	2.5 + 0.5

*Using:	MATERIAL	β'	GLASS (LOW N) (1)	GLASS (HIGH N) (2)
	DENSITY	3.15	3.88 + 0.05	4.55

Where: (1) From 140,144

(2) Density of this glass composition unknown - so density of "YAG" used, the crystalline form of this glass (Section 5.4.1)

TABLE 5.3

DENSITIES AND POROSITY LEVELS FOR AS-SINTERED ALLOYS

aids sintering. This density increase using LC-10 has also been noted by Pompe et al. (30).

For higher 21R additive material (e.g. S13), density measurements indicate a porosity level of ~ 0.7 volume %. However S.E.M. examinations suggest a more realistic 2-3 vol. % level, highlighting the limitations of the Archimedian technique. This porosity increase with 21R is a repeatable effect, as intermediate levels of 21R additive using a different $\alpha\text{-Si}_3\text{N}_4$ source (N2, N4, N6, N8) also show the same trend when studied via S.E.M.

5.3.5 X-Ray Diffraction

A Phillips X-ray diffractometer with Cu ($K\alpha$) source was used to analyse "bulk" materials (after being cut from the billet and polished to a standard 14 μm diamond finish). Phase content, variation with position within the bulk and degree of preferred crystallographic orientation could be determined. The X.R.D. unit was calibrated with a silicon (001) reflection before each run. Scanning was from 10° to 80° (2θ) at a rate of $2^\circ/\text{minute}$

5.4 THE MICROSTRUCTURAL CHARACTERISTICS OF ANNEALED ALLOYS WITH CRYSTALLINE MATRICES

Above 1200°C the entire range of sintered alloys is unstable with regard to matrix devitrification, although the crystallisation product, rate and extent vary considerably as detailed in this chapter. Although the increased addition of "polytypoid" gives a range of crystalline features, the materials fall into categories based on their differing major crystalline products.

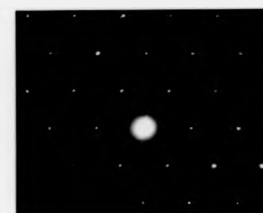
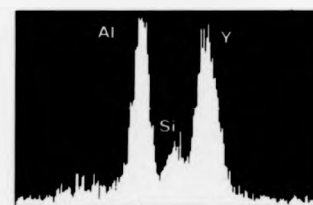
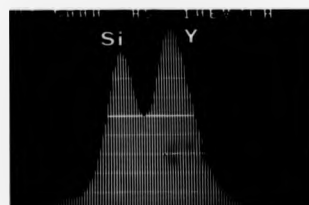
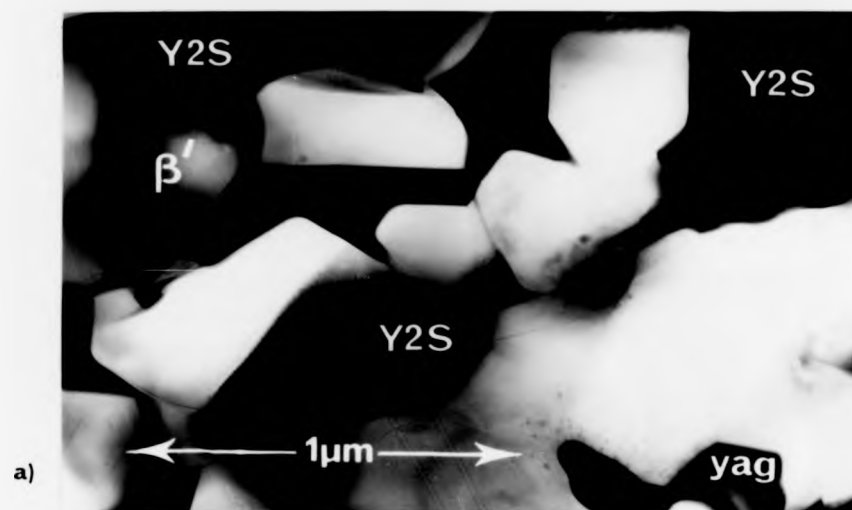
5.4.1 Alloys with Low "Polytypoid" Additions

5.4.1(a) Matrix Devitrification Products and Mechanisms

After a 150 hour anneal at 1300°C in vacuum, an optical examination of the cut section of material 80 showed inhomogeneities

uncharacteristic of its previous uniform light colouring. Subsequent X.R.D. revealed the crystallisation of two additional minor phases identified from the American Standards for Testing of Materials (A.S.T.M.) Powder Diffraction Files. They are $\alpha\text{-Y}_2\text{O}_3\cdot 2\text{SiO}_2$ (A.S.T.M. No. 22-994) subsequently referred to as $\alpha\text{-Y2S}$ and $3\text{Y}_2\text{O}_3\cdot 5\text{Al}_2\text{O}_3$ (146) known as Yttrium Aluminium Garnet or "YAG". The relative maximum X.R.D. peak intensity heights for β' , $\alpha\text{-Y2S}$ and YAG were 100:13:1.5. Unfortunately direct translation to relative volume fractions is inaccurate due to preferred crystallographic orientation of the minor phases, although the order of magnitude is realistic.

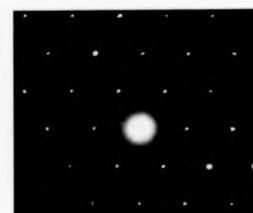
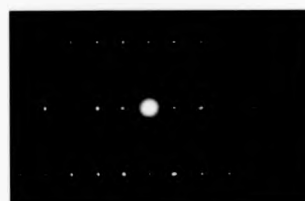
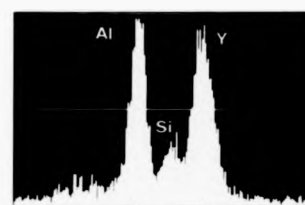
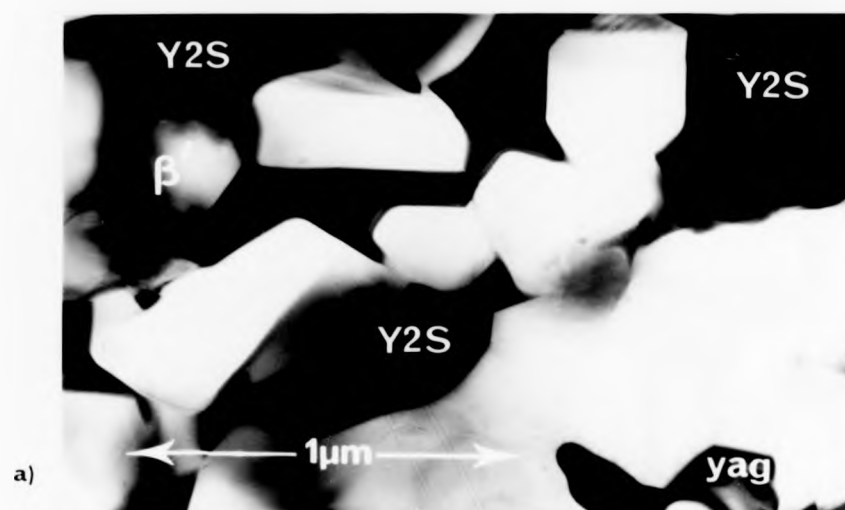
T.E.M. sections show these additional crystalline phases distributed within the g.b.matrix. By specimen tilting to various rational orientations with respect to the electron beam, the contrast of the matrix is enhanced and made uniform over an area containing many β' grains (Fig 5.6a). This feature, similarly observed for MgO and $\text{Y}_2\text{O}_3 + \text{Al}_2\text{O}_3$ additive Si_3N_4 alloys (42, 43), identifies a constancy of crystal orientation (further confirmed by Selected Area Diffraction (S.A.D.)) and suggests matrix crystallisation from a single nucleus. A series of such S.A.D. patterns coupled with E.D.A.X. (Fig 5.6b) confirm the identity of the majority of crystalline matrix as $\alpha\text{-Y2S}$. Similarly YAG was identified (Fig 5.6c) as the minor matrix phase and also had constant phase orientation. No unequivocal change in β' substitution level (within the range of z levels) was observed to accompany crystallisation. Matrix devitrification was incomplete and the large area of thin section in T.E.M. revealed the various matrix phases not to be homogeneously distributed on a microstructural level, but to exist in overlapping macroscopic bi-phase zones ($\beta' + \alpha\text{-Y2S}$, $\beta' + \text{YAG}$ and also $\beta' + \text{glass}$).



b) Y2S

Measured d (Å)	α -Y2S
5.35	5.31
4.09	4.07
3.71	3.63
3.20	3.16
3.02	3.09
2.60	2.62

Figure 5.6. a) TEM micrograph of alloy S0C having been annealed for 150 hrs at 1300°C. The matrix is crystalline and identified by EDAX and SAD b) as α -Y₂O₃·2SiO₂ (Y2S). YAG is also identified c) as a minor phase.



b) Y2S

Measured d (Å)	α -Y2S
5.35	5.31
4.09	4.07
3.71	3.63
3.20	3.16
3.02	3.09
2.60	2.62

Figure 5.6. a) TEM micrograph of alloy S0C having been annealed for 150 hrs at 1300°C. The matrix is crystalline and identified by EDAX and SAD b) as α -Y₂O₃·2SiO₂ (Y2S). YAG is also identified c) as a minor phase.

Reducing the anneal time to 20 hours (1300°C) more clearly shows the development of these macroscopic features. Fig 5.7a gives the optical and corresponding S.E.M. b.s.e. images of a section perpendicular to the specimen surface. The optically dark ingrowing fingers of zone 1 must be due to macroscopic chemical changes (implied from their strong b.s.e. contrast). A section parallel to the surface ($\sim 50\mu\text{m}$ below it) shows dark circles (Fig 5.7b) corresponding to the fingers, suggesting their columnar nature. A light grey peripheral region (zone 2) is distinguished optically from the darker background (zone 3). By careful sectioning, T.E.M. specimens of each zone were produced. After manually thinning a T.E.M. section, using an optical microscope the macroscopic feature of interest is positioned at the exact centre of the mounting ring. Accurate ion-beam erosion only of the centre position ensures consistent feature discrimination. Zone 1 was found to consist of a constant orientation α - Y2S matrix but with small glass pockets detectable at triple g.b.s. Zone 3 was solely β' + glass with similar phase compositions as the pre-crystallised material. Therefore the fingers of zone 1 are confirmed as surface nucleated α -Y2S intergranular columnar crystals. Their size and regular nature suggest a relatively unhindered growth through the g.b. glass matrix. This implies that the matrix may be regarded as continuous and its crystallisation treated similarly to that of a bulk glass ceramic.

Traversing from zone (1) \rightarrow (2) sees a rapid increase in matrix glass volume up to an area of entirely β' + glass (fig 5.7c). The glass composition is Al-rich in comparison to the as-sintered composition. Next is a finite zone β' + YAG (covering up to $10 \times 10 \beta'$ grains) with YAG in constant orientation and little g.b. glass. This zone abruptly fades into zone 3. An explanation for these observations is based on the compositional difference between α - Y2S and the parent

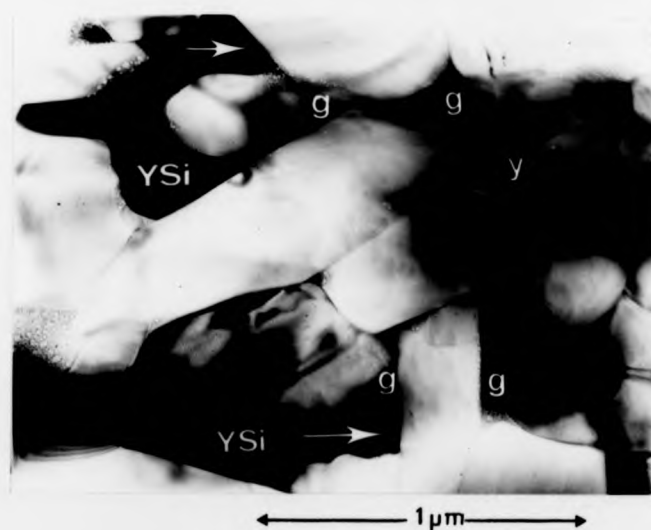
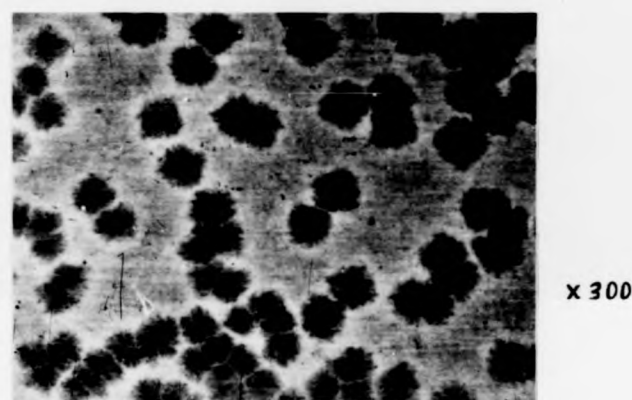
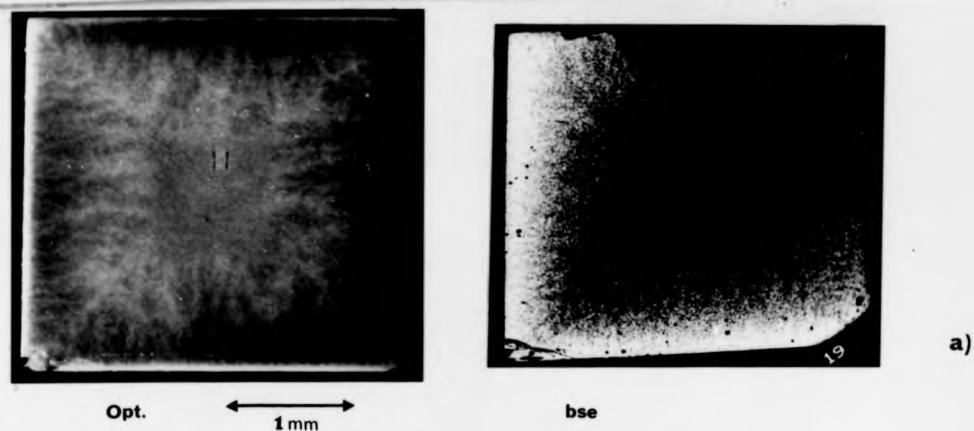


Figure 5.7. Alloy S0C, annealed for 20 hrs at 1300°C.. Optical (a) and corresponding bse images of cross-section showing crystallisation features. Optical of sub-surface section (b) showing columnar growth and the three zones. c) TEM Section identifying the zones.

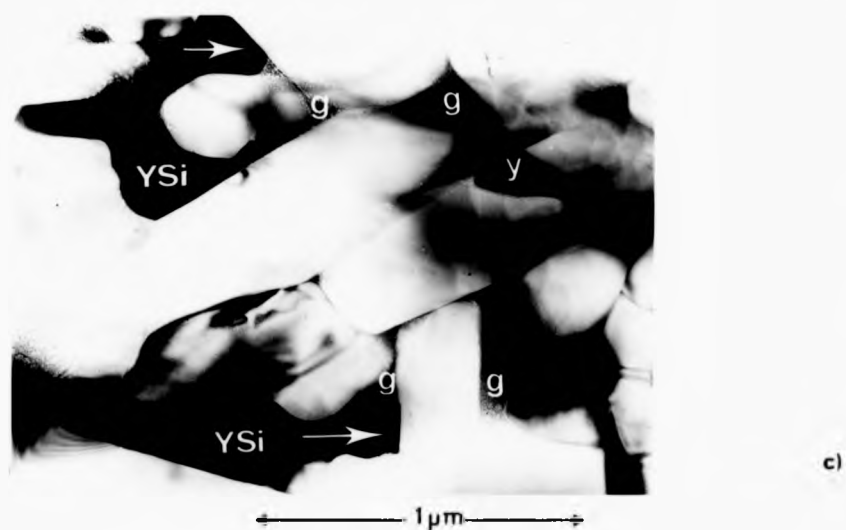
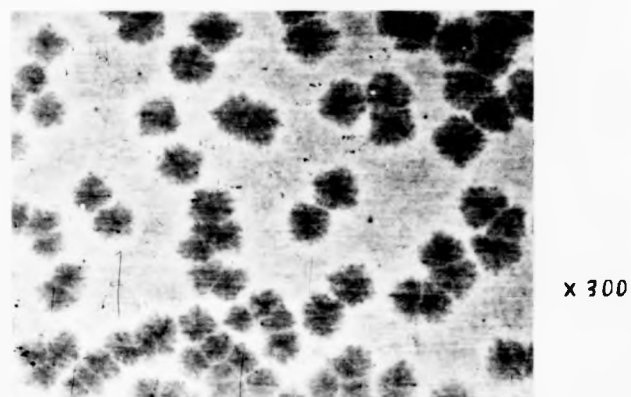
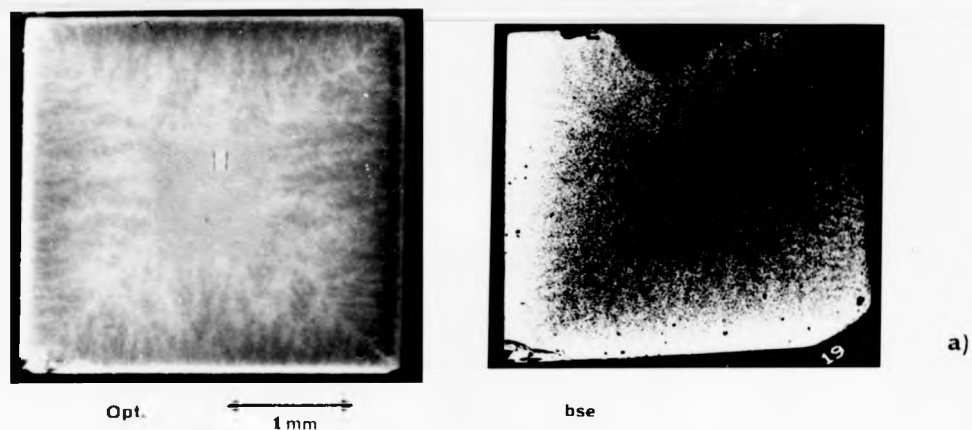
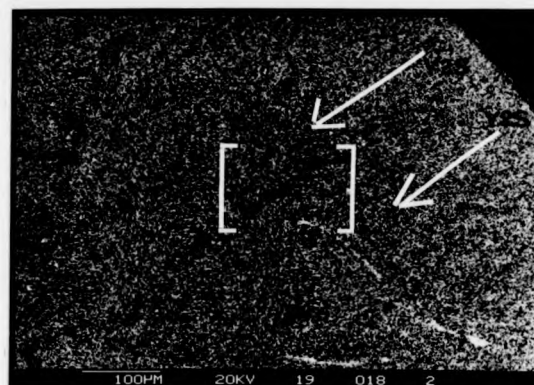


Figure 5.7. Alloy SOC, annealed for 20 hrs at 1300°C.. Optical (a) and corresponding bse images of cross-section showing crystallisation features. Optical of sub-surface section (b) showing columnar growth and the three zones. c) TEM Section identifying the zones.

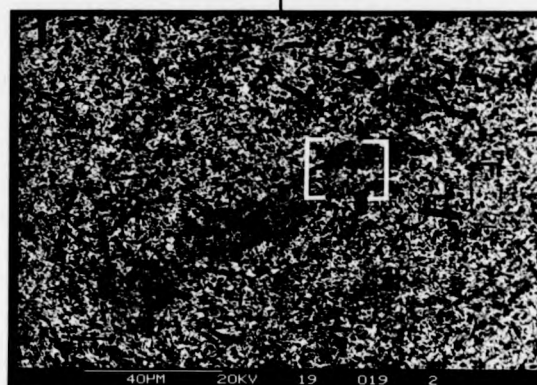
glass. The solubility of Al and N in $Y_2Si_2O_7$ is not reported in the literature and not expected as the usual Al substitution for Si (as in Si-Al-O-Ns) could not be charge-balanced by any similar non-metal elements (i.e. 0 for N). Elements Al, Si and possibly N in the parent glass would therefore be in excess of the stoichiometric $Y_2Si_2O_3$ and would be expected to be rejected at the crystallisation front and enrich the interfacial glass. The overall composition of this glass would move towards the YAG phase field (Fig 5.4a) where YAG would nucleate and grow until the Al concentration in the glass was sufficiently reduced. A similar effect has been noted in Y-Si-Al-O-N g.b. glass where prior phase separation of SiO_2 indirectly heterogeneously nucleates YAG (43).

5.4.1(b) Pore Development and Optimal Matrix Crystallisation

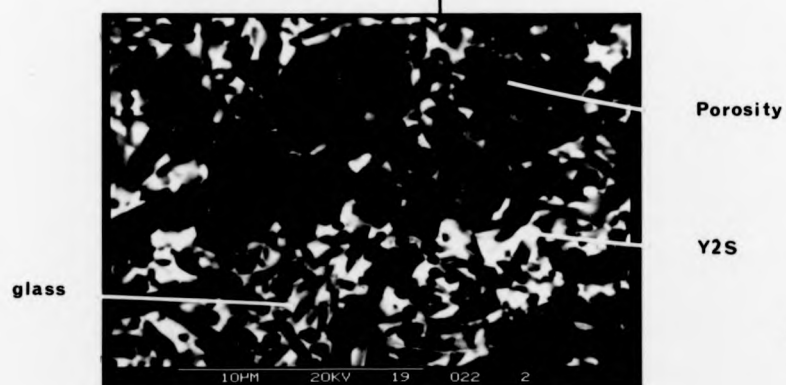
Another feature optically observed in polished sections of well annealed SO material are thin ($\sim 15\mu m$) dark zones occurring at the interface between α - Y2S fingers (Fig 5.8a). From S.E.M. the zone is identified as consisting of a matrix of pores and what is thought to be the glass. The uncertainty arises from the lack of confirmation from T.E.M. since, due to the porosity, a satisfactory T.E.M. section could not be produced. However, it has the correct b.s.e intensity and as demonstrated above, glass exists in large zones at the α - Y2S periphery. The porosity is therefore thought to develop in the stable glass matrix zones upon α - Y2S crystallisation and glass products are seen to link individual pores (Fig 5.8c). Possible mechanisms for the pore formation are (1) volatilisation of glass species, (2) g.b. sliding induced cavity formation, (3) cavitation due to hydrostatic tension in the viscous phase. As the pores occur deep within the specimen, at relatively low temperatures, and no external pressure is applied, mechanism (3) is most probable. The proposed



a)

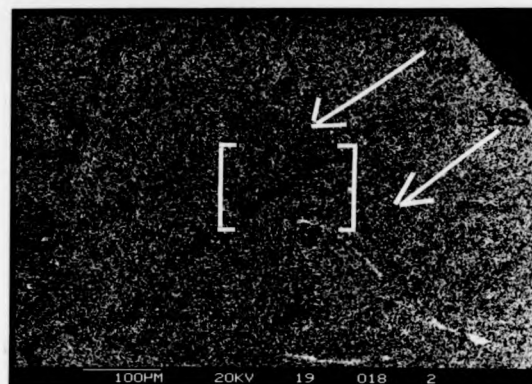


b)

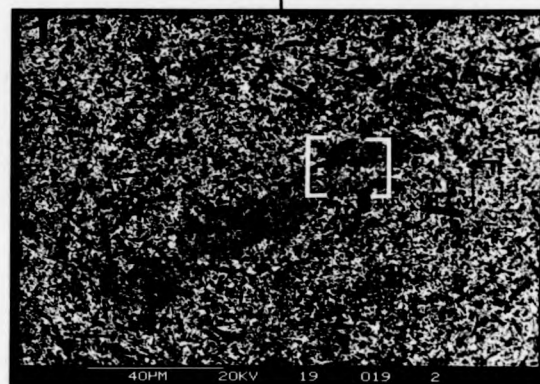


c)

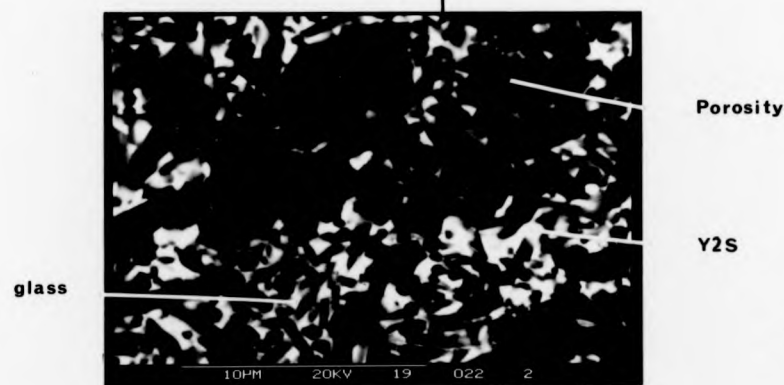
Figure 5.8. SEM micrographs (bse) of alloy SOC identifying macroscopic zones of porosity between surface nucleating fingers of α -Y₂S.



a)

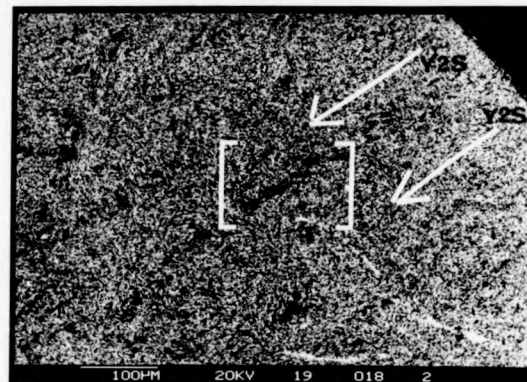


b)

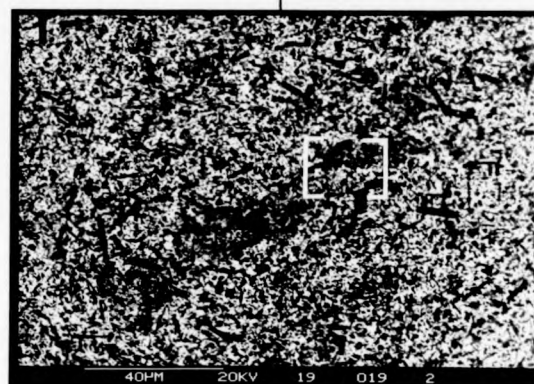


c)

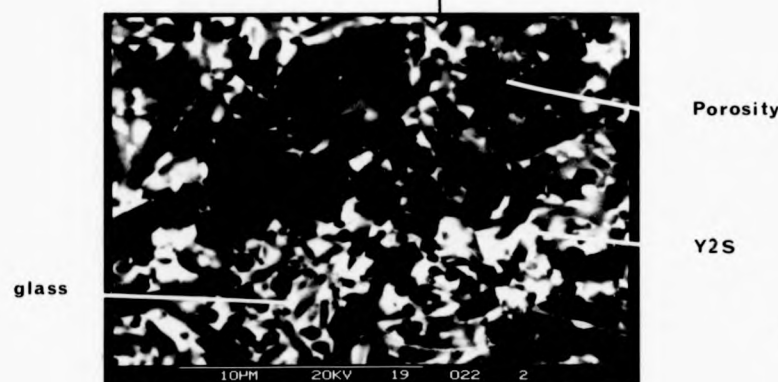
Figure 5.8. SEM micrographs (bse) of alloy SOC identifying macroscopic zones of porosity between surface nucleating fingers of α -Y2S.



a)



b)



c)

Figure 5.8. SEM micrographs (bse) of alloy SOC identifying macroscopic zones of porosity between surface nucleating fingers of α -Y2S.

mechanism is based upon the initial surface matrix crystallisation which effectively produces a rigid shell. The molar volume change accompanying the glass matrix crystallisation to a denser phase sets up hydrostatic stresses. The relief of the associated strain energy by plastic deformation is constrained by the rigid shell and local cavity formation in glass remnant to the matrix crystallisation occurs. This mechanism is supported by observations of porous zones starting, not at the surface, but consistently at $\sim 200\text{ }\mu\text{m}$ below it (fig 5.8a). Also the preference for porous zones in small g.b. glass zones and between approaching crystallisation fronts is explained, as the hydrostatic tension would be greatest here.

Complete matrix crystallisation in the set of alloys did not occur and stable β' + glass zones were left, being due to the glass either having an unfavourable composition or size for crystallisation at the anneal temperatures.

In order to enhance the degree of g.b. crystallisation and reduce the coarseness of crystallisation features (and hopefully therefore the porosity zones), the nucleation/growth approach was adopted (147). Anneals of 24 hours at various temperatures below 1300°C identified matrix crystallisation (via T.E.M.) at 1200°C and this was standardised as the nucleation stage. The growth stage was conducted for 80 hours at temperatures of 1250°C , 1300°C and 1320°C . The higher temperature lowers the viscosity of the glass, increasing atomic diffusion rates and therefore the speed of growth. The features of these 3 two-stage crystallised materials (now collectively referred to as SOC) are very similar. From optical examination, compared to the single stage 1300°C crystallised material, the extent of the predominant surface nucleation was reduced, crystallisation zones were smaller, with β' /glass and β' + porosity zones considerably reduced. In T.E.M. very few β' /glass zones were evident although triple g.b. glass was

frequently found. High temperature fracture (1200°C in Vacuum) of the three SOC materials showed that whatever the nucleation/growth regime considerable slow crack growth occurs. In S.E.M. the fracture face of the s.c.g. zone reveals a dominant intergranular fracture mode (Chapter 7). Extensive s.c.g. at such relatively low temperatures usually indicates the presence of a low viscosity film distributed at all g.b.s.

Complete matrix crystallisation is therefore not considered possible for this low 21R material. However material SOC should be regarded as a material with a continuous g.b. glassy phase similar to SO but of considerably reduced volume fraction.

5.4.2 Alloys with High "Polytypoid" Additions

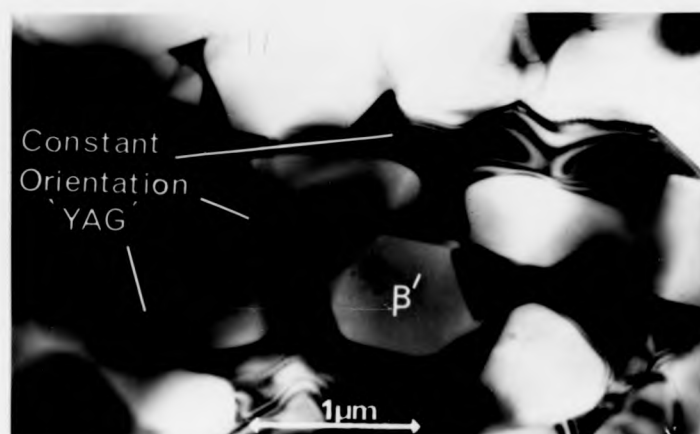
5.4.2(a) The Effect of "Polytypoid" Addition on Matrix Crystallisation

The ease of matrix crystallisation to α - Y2S is considerably reduced with a small increment of 21R, represented by material N2. Even upon extended anneals (1000 hours at 1300°C) stable macroscopic β' + glass zones exist. Anneals at 1400°C for 5 hours to material N4 show the onset of considerable matrix crystallisation to YAG with a corresponding reduction in glass and α - Y2S volume fractions. Further increasing levels of 21R additive (represented by materials N6 and N8) give a crystalline matrix solely of YAG. An increased temperature is required to successfully crystallise YAG, and enhanced nucleation kinetics at 1400°C are suggested by the fine spotty optical sections. The above crystallisation phenomena can be successfully explained in terms of an increasing glass matrix nitrogen level (due to the 21R addition) which is known to increase glass viscosity (61). The bulk Y-Si-Al-O-N glasses mentioned in Section 5.3.3(b) replicate these findings by not only showing a reduced α - Y2S crystallisation when solely increasing the N/O ratio, but also a transition to YAG crystallisation at higher N/O ratios and temperatures (148). Thomas

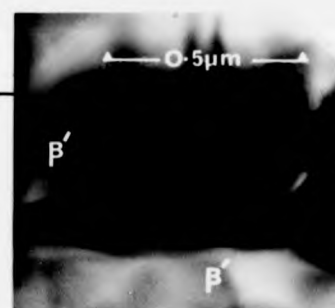
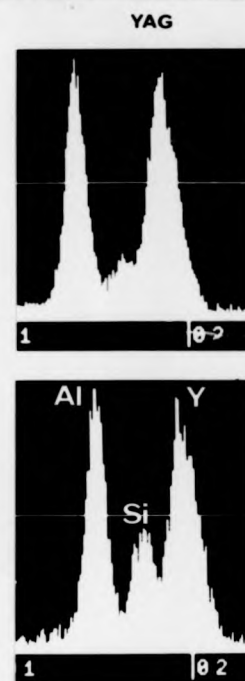
et al. (142) have credited a similarly hindered α - Y2S crystallisation in glasses to N levels.

The T.E.M. section in Figure 5.9a shows a typical annealed microstructure. Surface nucleation of large intergranular YAG single crystals (having hemispherical macromorphology) is prevalent. The YAG peak intensity ratios from X.R.D. of a subsurface section, when compared to the corresponding powder ratios, show a preferred crystallographic growth. The YAG peak intensities for planes (444) and (400) are consistently 5 x greater and 10x smaller respectively than the other peaks (which correspond to the ratios for a powder). This is explained by the preferred nucleation of YAG crystals from (111) planes (lying parallel to the surface) and growth in a $\langle 111 \rangle$ direction into the specimen bulk.

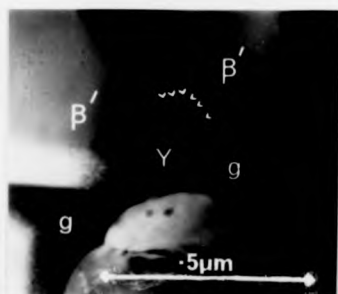
There is some T.E.M. evidence for heterogeneous YAG nucleation (within the specimen bulk) from the rare observation of a spherically capped YAG crystal attached to a β' grain and growing into a pocket of glass (Fig 5.9b). McMillan (147) has shown that this crystal morphology and the phase contact angles are usually associated with an easy heterogeneous nucleation in glasses. However the case for β' acting as a heterogeneity is small as this would predict a far greater YAG nucleation density than that observed. However, an indirect heterogeneous nucleation mechanism could be due to micro phase-separation, prior to crystallisation. Fig 5.9c shows the YAG crystal having grown around these heavy element depleted zones. This new phenomenon is only observed in Starck-based alloys. Phase separation could be due to local inhomogeneities in glass mixing, shifting its composition towards the SiO_2 corner and liquid immiscibility region (Fig 5.4a). The enrichment of Al, Y and N at the phase interface would favour heterogeneous YAG nucleation.



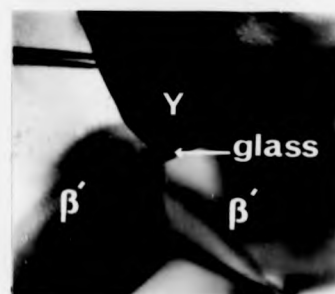
a)



c)



b)



d)

Figure 5.9. a) Microstructure of N8C (TEM) showing constant YAG orientation and range of YAG compositions. b) Heterogeneous nucleation of YAG on β' grains. Arrows indicate the YAG/ β' interface. c) Glass phase-separation prior to YAG crystallisation, contrast change produced by specimen tilting. d) Incomplete YAG crystallisation of the matrix, leaving glass pocket.

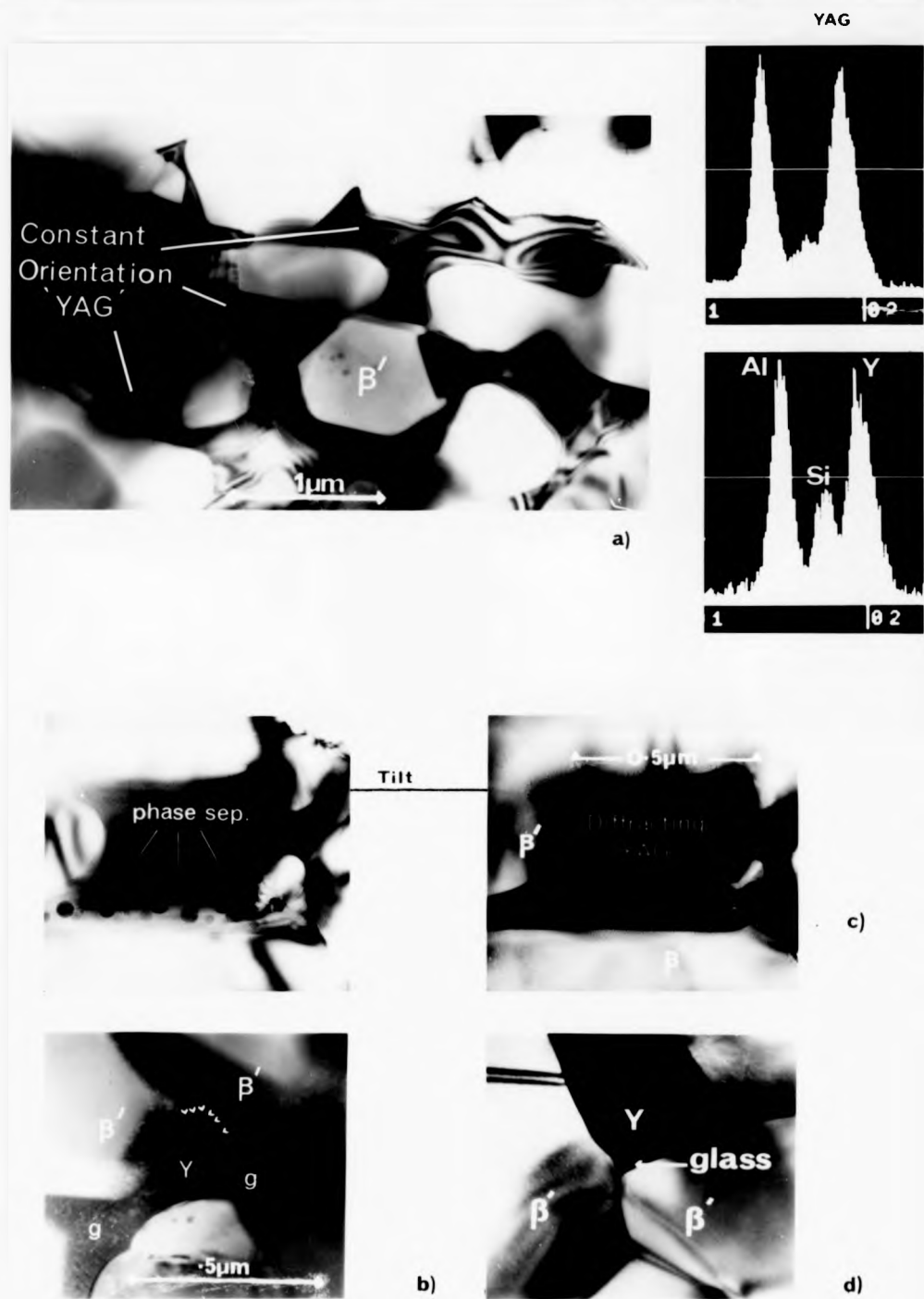


Figure 5.9. a) Microstructure of N8C (TEM) showing constant YAG orientation and range of YAG compositions. b) Heterogeneous nucleation of YAG on β' grains. Arrows indicate the YAG/ β' interface. c) Glass phase-separation prior to YAG crystallisation, contrast change produced by specimen tilting. d) Incomplete YAG crystallisation of the matrix, leaving glass pocket.

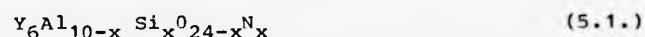
5.4.2(b) Factors Influencing Matrix Crystallisation

Higher 21R content materials (**S10**, **S13**, **N8**) were used to produce optimal β' + **YAG** materials. Material **S13** readily crystallises at 1300°C but at considerably reduced kinetics to material **S0**. This suppresses the formation of β' + porosity and β' + glass zones. A systematic range of single and two-stage anneals at temperatures 1250°C, 1350°C, 1400°C and 1450°C for times between 24 hours and 150 hours shows "**YAG**" (from XRD) as the only crystalline second phase. Complete g.b. devitrification was again elusive. Although only occasionally detected in T.E.M. (fig 5.9d), the high temperature K_{IC} criteria (s.c.g. at 1200°C) showed that these crystallised materials (termed **S10C** and, **S13C**) must be considered to have a continuous g.b. glass film. This result was surprising as a material with similar overall composition (but with difference α - Si_3N_4 source) was reported (43) to give complete devitrification. Unfortunately materials **S10C** and **S13C** were the best bi-phase examples available for the majority of this study and mechanical and oxidation tests were conducted with consideration to the third phase.

Very recently, Lucas have been exploring an alternative α - Si_3N_4 source. This latest material **L10** (of similar composition to **S10**) readily produced a fully crystalline **YAG** matrix after a 1400°C/5 hour anneal with no residual glass present as determined by the total lack of s.c.g. at 1400°C in vacuum (Chapter 7). This highlights an additional factor influencing matrix crystallisation and is most probably related to the inherent impurities derived from source materials and subsequent milling and acid washing. The influence of impurities on glass stability have been reported. Chlorine prevents Y2S formation in g.b. Y-Si-O-N glasses (149) and Fe and Ca can hinder crystallisation of MgO-SiO₂ bulk glasses (150). The lack of complete matrix devitrification in the present work is then most likely

attributable to the high impurity levels associated with Starck α - Si_3N_4 powders.

The successful complete matrix crystallisation previously reported (43) was partially attributed to the variable compositions of β' and also the **YAG** phase which together take into solution any residual glass components. Based on E.D.A.X., a general composition was proposed for the Garnet structure of



(where Si substitution for Al is balanced by N substitution for O) with $x \leq 3$. This high level of Si substitution is questionable and could be credited to fluorescence from surrounding β' grains. The present work does not confirm this. Although all E.D.A.X. analysis (from crushed and dispersed specimens) consistently indicated Si (Fig 5.9a), a maximum substitution level of $x \sim 1.5$ was established. Work on N solubility in **YAG** (151) revealed a 3 atomic % limit and from equation (5.1) suggests the present Si levels are inflated. If the Si levels are assumed correct, this then questions the validity of equation (5.1). This equation can be suitably modified if the charge compensation for the Si for Al substitution occurs via divalent impurity cations (rather than N). This is possible, as Ca^{2+} for Y^{3+} is reported for Si-substituted $\text{Y}_4\text{Al}_2\text{O}_9$ (152) and Ca^{2+} is an impurity detectable in the present **YAG** analysis. In conclusion, although Si-substituted **YAG** exists, it does not offer the compositional flexibility initially suggested.

5.5 SUMMARY OF SIGNIFICANT MICROSTRUCTURAL DATA

1. Increasing 21R addition to Y-Si-Al-O-N as-sintered materials significantly alters their microstructure, and when annealed dictates the extent and type of g.b. crystalline product.
2. The above changes are consistent with a predicted variable Nitrogen/Oxygen ratio in the g.b. residual glass, which is supported by E.E.L.S. analysis.

3. The initial α - Si_3N_4 powder controls the SiO_2 and impurity levels which considerably influence the final microstructure.
4. Matrix crystallisation must be considered on a macroscopic scale.

CHAPTER SIX

STABILITY OF MICROSTRUCTURE IN OXIDISING ENVIRONMENTS

In this chapter an analysis is made of the kinetics and mechanisms for oxidation of a range of Y-Si-Al-O-N ceramics with varying "polytypoid" content. A detailed study has been made of sub-oxide microstructural transformations which may have a dominant influence on high-temperature mechanical behaviour.

6.1 OXIDATION OF AS-SINTERED β' + GLASS ALLOYS

6.1.1 Alloys with Low Polytypoid Content

The oxide development during short term, relatively low temperature, oxidation is of insufficient thickness to be characterised by a study of its cross-section. An S.E.M. survey of this oxide surface proved more appropriate.

6.1.1(a) Oxide Surface Observations

The work described in Section 5.4 showed the susceptibility to crystallisation of material SO above 1300°C and a temperature-related crystallisation rate. To compare oxidation mechanisms and kinetics of materials with glass and α - Y2S matrices, limited oxidation exposures at 1150°C, 1200°C and 1300°C, for a range of times only up to 16 hours, were used. The retention of a non-crystalline matrix could not be assumed for longer times or higher temperatures.

The oxide produced after 16 hours at 1150°C (Fig 6.1a) is predominantly glass (presumed from its wetting characteristics and fracture surface) but is covered in two distinct crystal types which both exhibit strong contrast which imaged with back scattered electrons. Just visible in the dark matrix are darker isolated grains

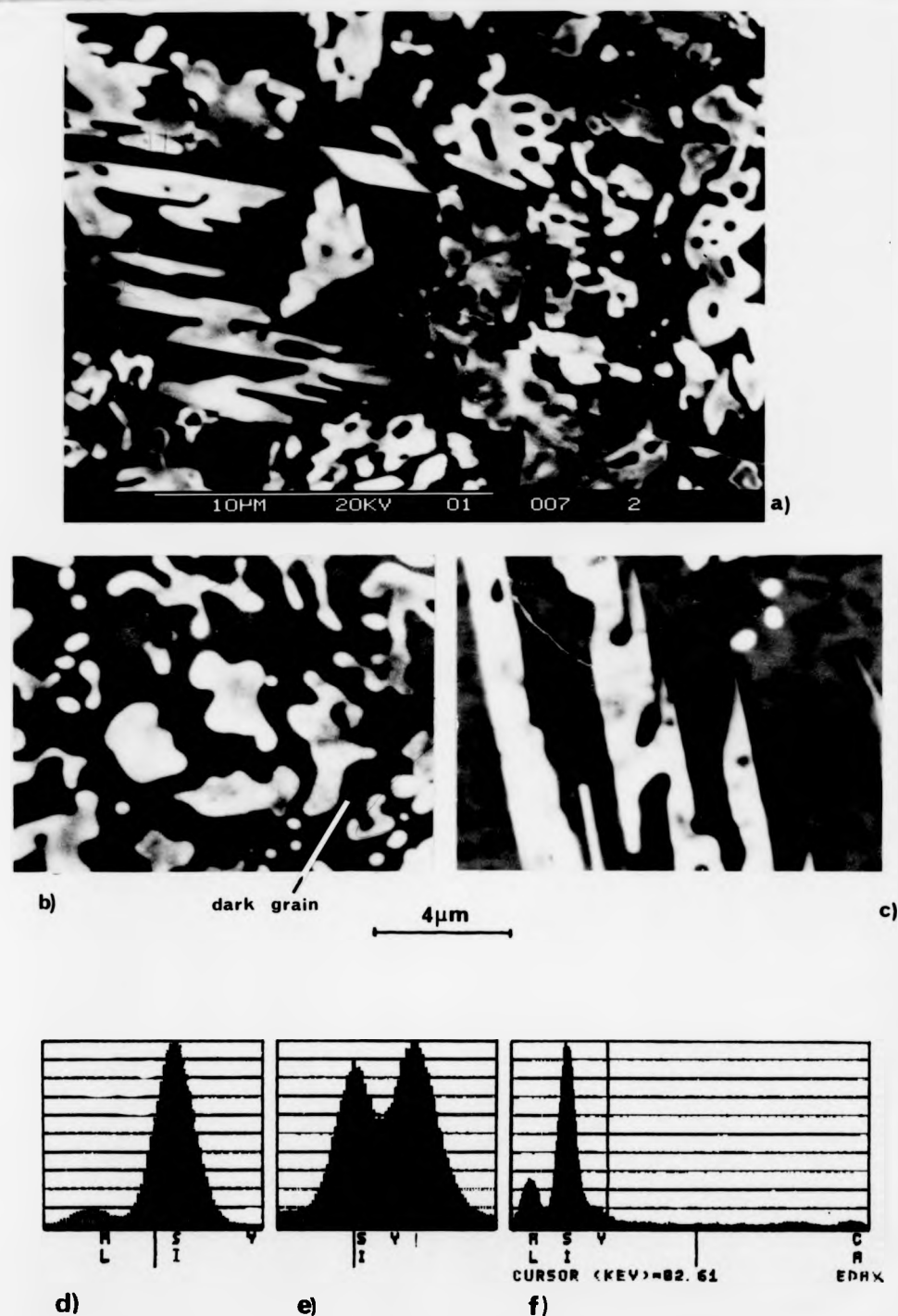


Figure 6.1. Oxide surface of alloy S0 after oxidation at 1200°C for 16 hrs. a) Low Mag. (bse) image illustrating crystal morphology types. b) Needle type. c) Chinese scripture type. d) EDAX of dark underlying β' grains, e) bright β - Y2S crystals, f) oxide glass. Scale for b) and c) equals 4μm.

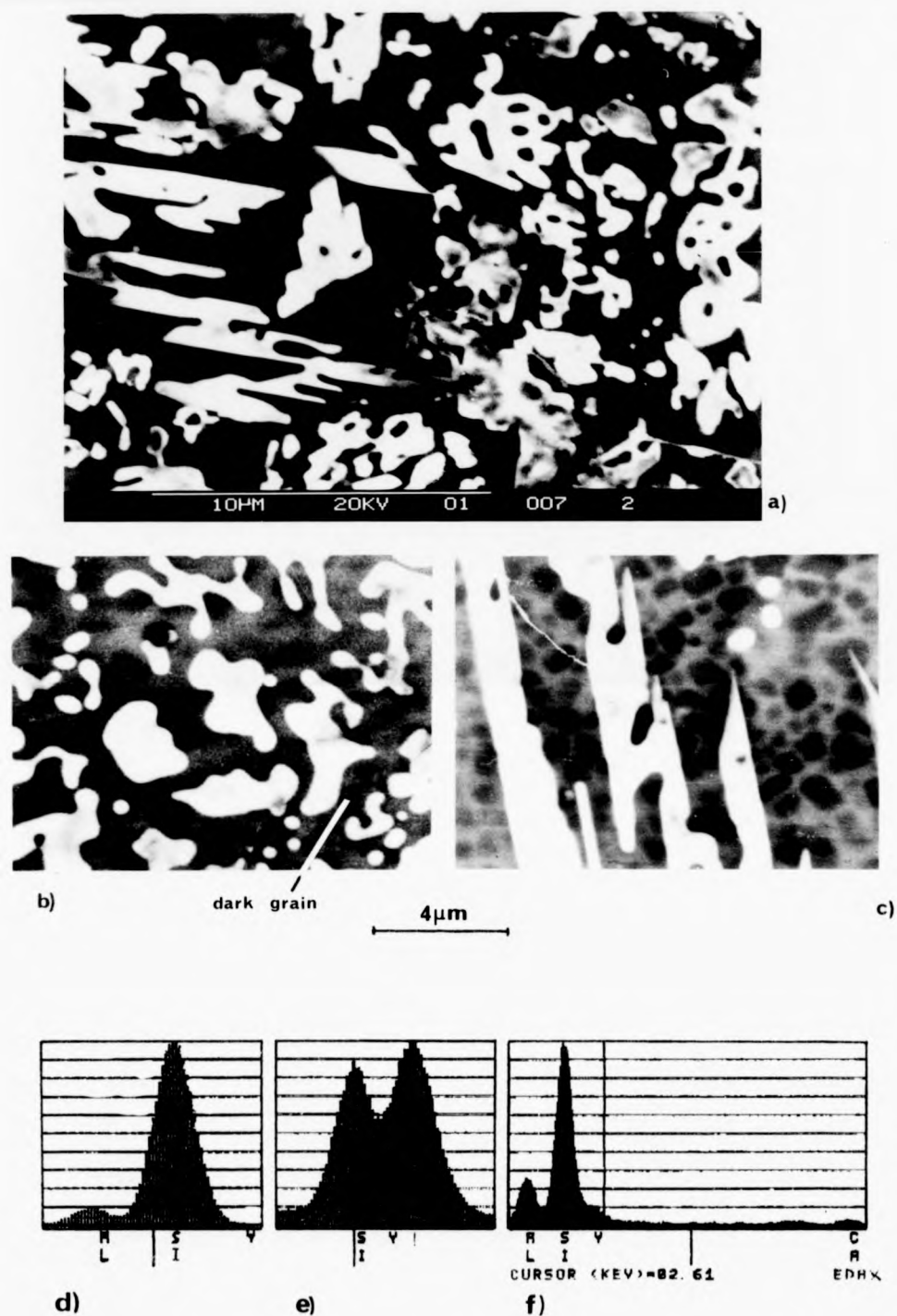


Figure 6.1. Oxide surface of alloy S0 after oxidation at 1200°C for 16 hrs. a) Low Mag. (bse) image illustrating crystal morphology types. b) Needle type. c) Chinese scripture type. d) EDAX of dark underlying β' grains, e) bright β - Y2S crystals, f) oxide glass. Scale for b) and c) equals 4μm.

($\sim 1 \mu\text{m}$ diameter), which are also usually associated with the indentations in the Chinese Script and Needle morphologies (Figs 6.1b and 6.1c).

E.D.A.X. shows (Fig 6.1e) that these two morphological types are identical, with a composition very close to $\text{Y}_2\text{O}_3 \cdot 2\text{SiO}_2$ (when expressed as stoichiometric metallic oxides). X.R.D. of the powdered oxide film also only identifies one $\text{Y}_2\text{Si}_2\text{O}_7$ phase, the β' structure (A.S.T.M. No. 22-1103). Therefore during oxidation the same β -Y2S crystal develops with 2 distinct morphologies and an explanation is given in Section 6.1.1(b). The very dark grains, due to their shape, distribution and chemical analysis (Fig 6.1d) are believed to be underlying β' , made visible by the relative "transparency" of the glassy oxide film.

Increasing the oxidation temperature to 1200°C sees a retention of the basic oxide features but growth of the bright crystals without any apparent crystal density change. At 1300°C , unlike the 1150°C and 1200°C observations, the oxide characteristics considerably alter with oxidation time. Fig 6.2a shows the transition. The original chinese script now develops a more uniform faceted "tablet" morphology (fig 6.2b) which is indicative of growth within a low viscosity liquid matrix at this temperature. Surface porosity is now significant, typically observed as porosity zones separate from the β - Y2S crystals. (fig 6.2c). The large β - Y2S plates develop not by single crystal growth but merger of the smaller "tablets" and needles (fig 6.2b). After 12 hours, new dark crystals appear and rapidly grow (Fig 6.2d). E.D.A.X. gives only a silicon peak and together with X.R.D. of the powdered oxide film identifies them as the SiO_2 polymorph, α - cristobalite (A.S.T.M. No. 11-695). When the oxide is sectioned (Section 6.1.1(c)) these SiO_2 crystals are seen to nucleate on the underlying β' grains and grow as spheres into the glass oxide (as in Fig 6.6b).

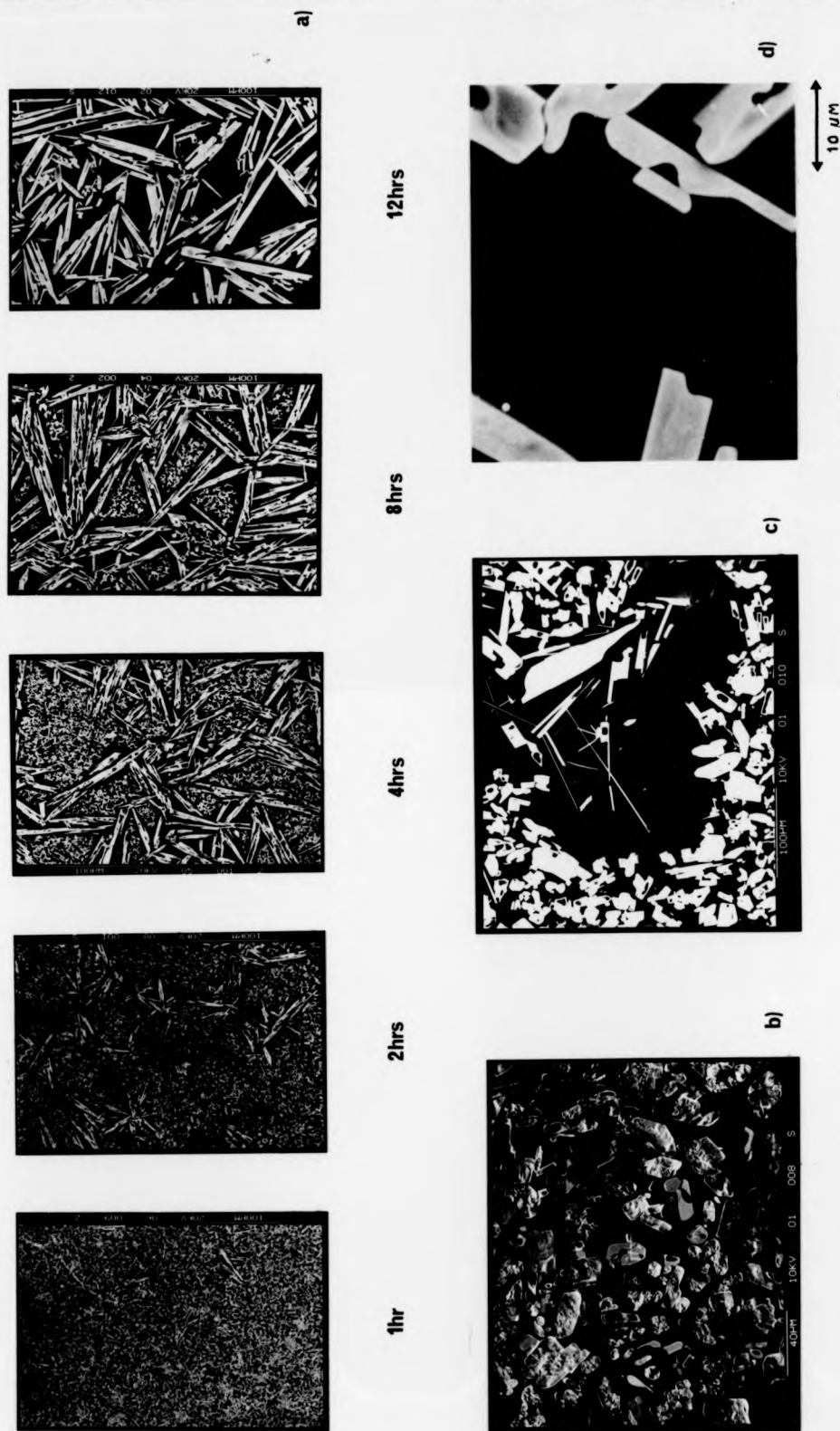


Figure 6.2. a) The development of the oxide surface features at 1300°C for alloy S0. b) Platelet development and merger. c) Porosity zones. d) Appearance of dark, α - cristobalite grains after 12 hours.

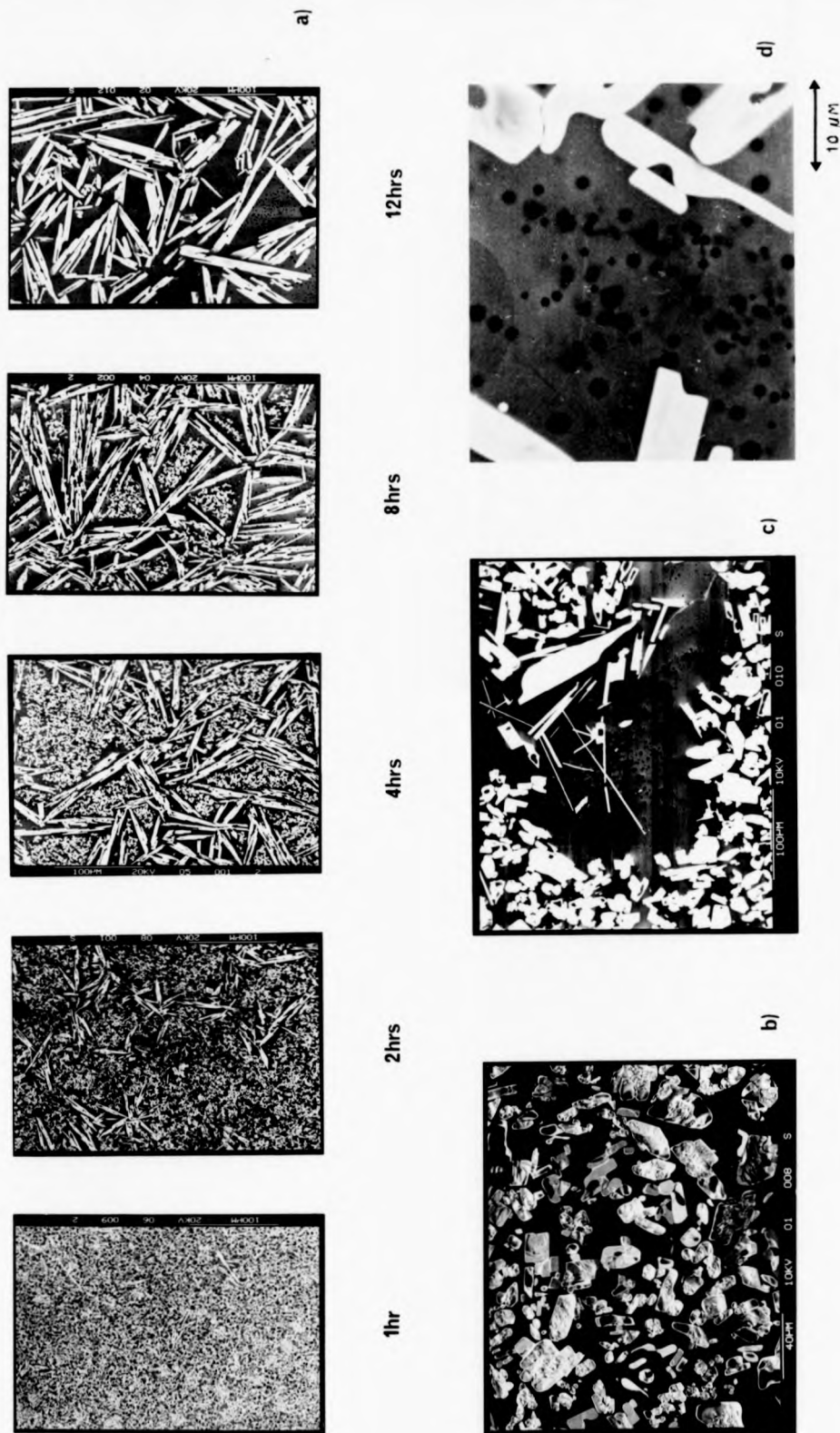


Figure 6.2. a) The development of the oxide surface features at 1300°C for alloy S0. b) Platelet development and merger. c) Porosity zones. d) Appearance of dark, α - cristobalite grains after 12 hours.

The observations of β - Y2S growth on top of each other and impingement on pores is evidence that oxide crystallisation occurs at temperature rather than on cooling.

6.1.1(b) Mechanisms for Development of Oxide Features

Short oxidation "flashes" of $1/2$ hour at 1100°C and 1200°C showed a rapid development of a high density of β - Y2S with chinese script morphology. This ease of formation at such low temperatures in the oxide is in contrast to the α - Y2S crystallisation kinetics in the bulk glass matrix (Section 5.4.1). This behaviour indicates: (1) a rapid Yttrium diffusion to the oxide; (2) an increased nucleation rate, probably due to the free surface and higher oxygen potential, with nucleation easily occurring in each glass pocket of the matrix that forms the specimen surface.

The chinese script type morphology is due to cellular instability coupled with faceted growth morphology, i.e. crystal growth is constrained to the surface section of the β' g.b. matrix, which gives the unusual outline. As temperature increases, the reduction in the degree of undercooling reduces the nucleation density. The oxide and matrix glass viscosities are also reduced, which allows more faceted β -Y2S grain growth. Out-diffusion of Y is enhanced and this accelerates the oxidation process by reducing the oxide viscosity further.

The pores in the glassy oxide film are burst bubbles of most probably N_2 (derived from the Si_3N_4 oxidation reaction of Eq. 2.5). Their proliferation at 1300°C indicates an enhanced oxidation reaction and a drastically reduced oxide viscosity that allows N_2 bubble formation and their subsequent ease of migration to the oxide surface.

6.1.1(c) Oxide and Sub-Oxide Kinetics

Oxide surface observations give useful information about macroscopic compositional changes and best illustrate short term, low

temperature, oxidation mechanisms and the transient nature of element diffusion to the oxide. Oxidation kinetics were determined from oxide film thickness measurement (in S.E.M.) of sectioned specimens. Oxide/substrate reactions and long range bulk changes were simultaneously monitored.

The sectioned specimens reveal a uniform zone below the oxide where the β' g.b. matrix has a Y and Al depletion (from E.D.A.X. and b.s.e. contrast). This matrix also appears reduced in volume, becoming porous with increased time or temperature. Its presence at 1150°C supports the rapid Y outdiffusion rates indicated by the previous oxide surface studies. However, zone growth at 1300°C is effectively halted after 5 hours and matrix porosity increases. Subsequently the α -cristobalite phase, developed in the oxide film (Section 6.1.1(a)), grows inward filling this matrix porosity. This $\beta' + \text{SiO}_2$ layer ($\sim 2 \mu\text{m}$ thick) is protective as extended oxidation to 115 hours shows little change in oxide or sub-oxide features.

A plot of oxide thickness with time at 1300°C shows a discontinuity after ~ 4 hours (Fig 6.3a). The linearity of the (oxide thickness)² vs. time graph shows two distinct parabolic oxidation rate constants. The discontinuity is thought to be due to β' g.b. matrix crystallisation, possibly enhanced by the oxidation induced compositional changes. Sufficient quantities of material SO were available to allow accurate oxidation weight gain measurement at 1300°C so as to further examine this phenomenon. The (weight gain)² vs. time (up to 20 hours) plot replicates the kinetics determined by oxide thickness measurement and shows a discontinuity at 6 hours (fig 6.3b). Optical, S.E.M. and T.E.M. sections of the sub-oxide show a macroscopic crystallisation zone similar to those in section 5.4.1. X.R.D. confirms the $\alpha - \text{Y}_2\text{Si}_2\text{O}_7$ and YAG matrix crystallisation products which, after ~ 6 hours, give rise to the reduced oxidation rate. Oxidation

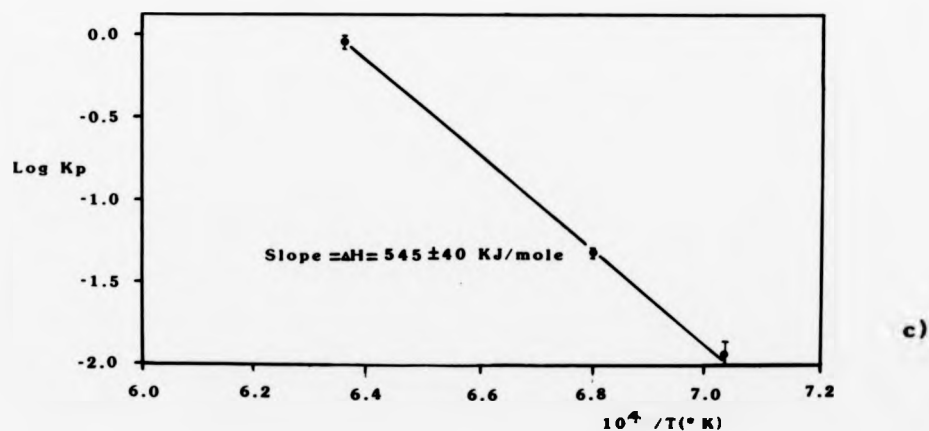
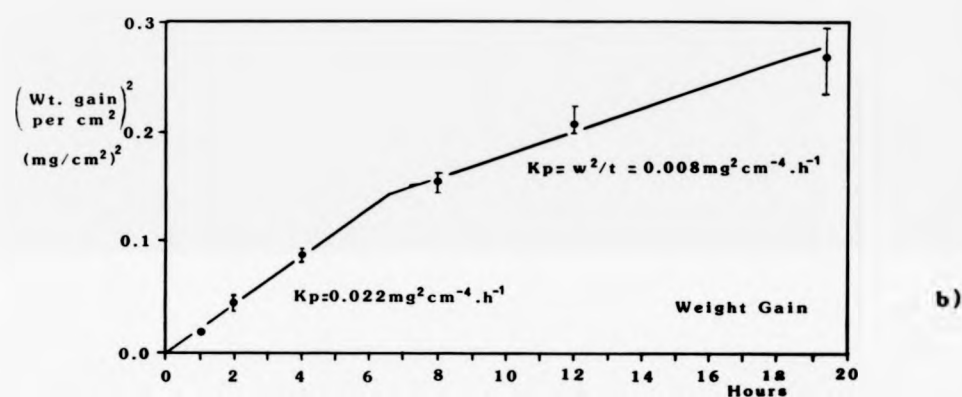
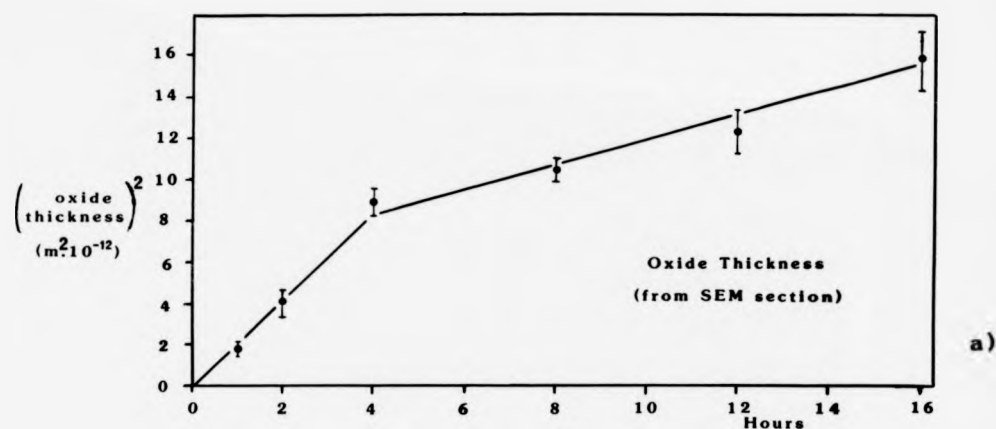


Figure 6.3. (a),(b) Oxidation Kinetics for alloy S0, showing discontinuity, derived from oxide thickness measurements and weight gain respectively. (c) Derivation of oxidation activation energy for S0.

kinetics (from oxide thickness) for material SO (β' + glass), could only be unambiguously collected at low temperatures and for short oxidation periods due to its susceptibility to matrix crystallisation. However, as mentioned in Section 5.4.1(b), by suitable annealing, partial matrix crystallisation can be controlled to produce large zones with a stable glass matrix. When subsequently oxidised, these annealed materials produce two distinct oxidation regimes which allowed oxide thickness determinations at 1300°C for β' + glass materials. All oxidation data gave good fit to the parabolic rate law and a series of rate constants (K_p) for different temperatures was obtained (Fig 6.3c). From equation 2.2, $\log K_p$ was plotted against $10^4/T$, which gave a straight line (Fig 6.3c) and an oxidation activation energy of 545 ± 40 kJ/mole for both material SO and N2 (with a glass matrix).

6.1.2 Sintered Alloys with High "Polytypoid" Addition

A range of β' + glass materials (with variable 21R and α - Si_3N_4 source) consisting of N6, S10, S13 and one of the L alloys were oxidised and for completeness their 1300°C and 1350°C oxidation kinetics are plotted in Fig 6.4. Within the error imposed by the oxide thickness determination (see below), all kinetics and oxide scale features are similar. Material S13 best represents this group and its Starck α - Si_3N_4 source also allows its direct comparison with SO.

6.1.2(a) Oxide and Sub-oxide Features

Below 1300°C, the oxidation kinetics are parabolic and give lower parabolic rate constants but a slightly higher activation energy than material SO (Fig 6.5). A similar sub-oxide zone develops, again with a planar front, but with increased kinetics. Selective T.E.M. sections of this region confirm that the matrix remains as a glass but with reduced Y and Al levels. The increased Y outdiffusion is readily observed by the approximate doubling in area of β - Y2S grains covering

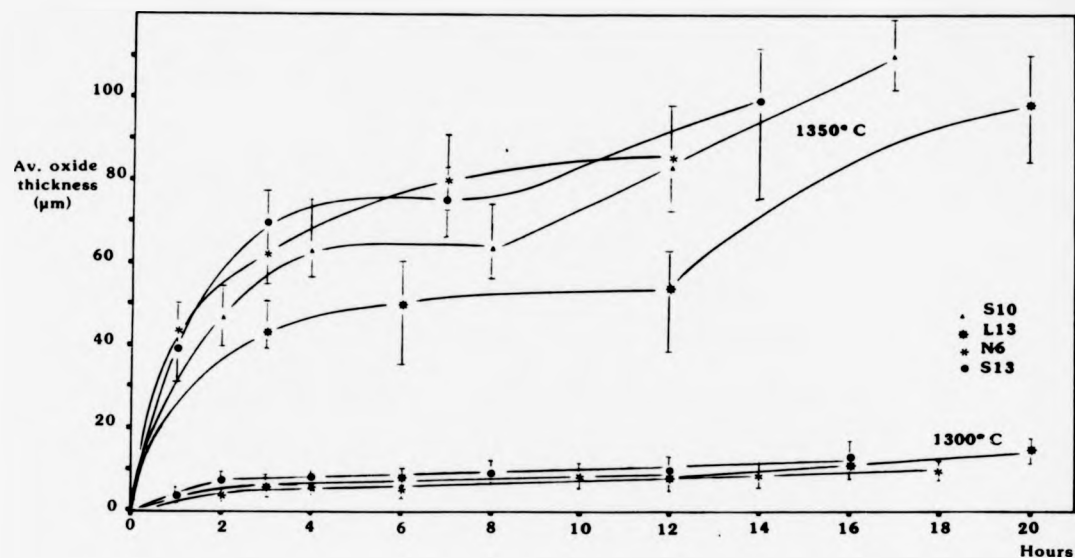


Figure 6.4 Plots of Average Oxide Thickness Against Time for β' + Glass Alloys at 1300°C and 1350°C. Error Bars Indicate the Range of Oxide Thickness.

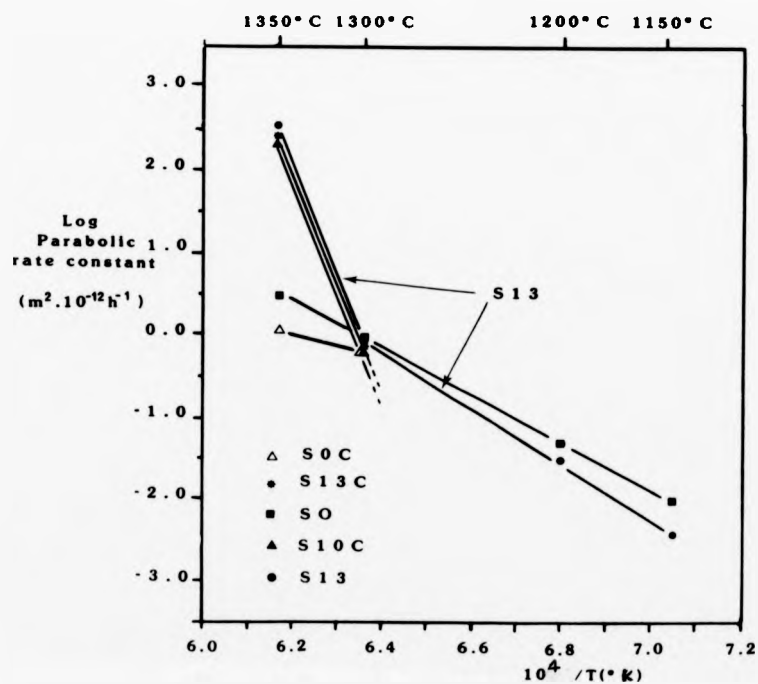
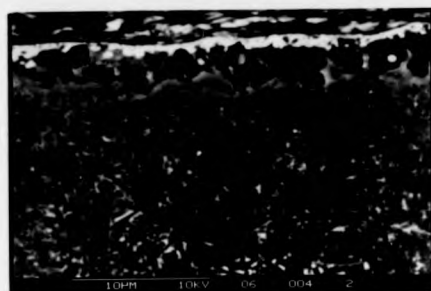


Figure 6.5 Arrhenius plot of Parabolic rate constants for the range of alloys.

the oxide surface. These β - Y₂S grains are finer and have a dendritic morphology but appear to have grown by the mechanisms outlined in section 6.1.1(b) for material SO.

At 1300°C however, although the oxide surface features appear relatively unchanged from those at 1200°C (apart from an increase in surface break-up), a sectional study of the oxide even after 1 hour reveals a radically different nature to material SO. The thick undulating oxide scale (Fig 6.6a) is due primarily to a massive development of α - cristobalite and large bubbles at the oxide/substrate interface. The oxide scale is essentially glassy but with an almost continuous surface zone of β - Y₂S crystals. Fig 6.6b,c,d show the typical oxide development with time. Initially, the gas bubble growth is sufficient to burst through the protective viscous oxide and considerably reduces the direct oxygen path to the substrate (as the atmosphere fills the bubbles). If the access to the oxide surface of these growing bubbles is restricted (by a coherent SiO₂ or β' - Y₂S layer), then bubble expansion and consolidation along the reaction interface can occur, resulting in a gaseous layer. Subsequent oxide scale rupture fills this cavity with oxygen resulting in the repetition of the parabolic oxidation reaction on this fresh face. After 12 hours the oxide then has the appearance of a sandwich of two of the 2 hour oxides.

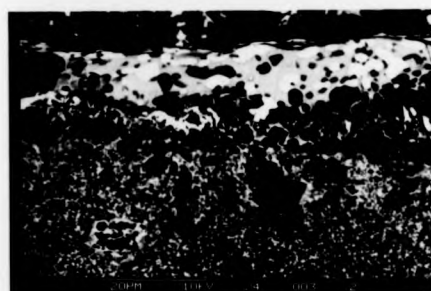
At 1350°C, the reduced viscosity of the oxide glass results in large scale oxide crystallisation to α - cristobalite and also increased gas evolution from the increased β' oxidation. The consequence, after 1 hour, is the development of a very bumpy oxide scale in the form of a shell entirely separated from the substrate (Fig 6.7a). The bumps are due to large gas bubble development within the glass volume between the large SiO₂ grains. This produces



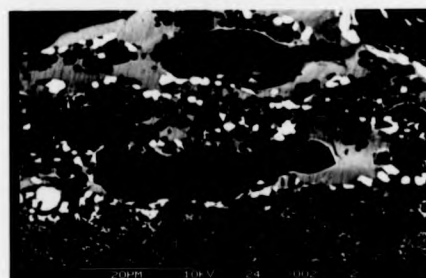
a)



b)

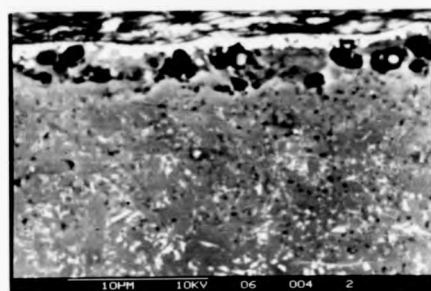


c)

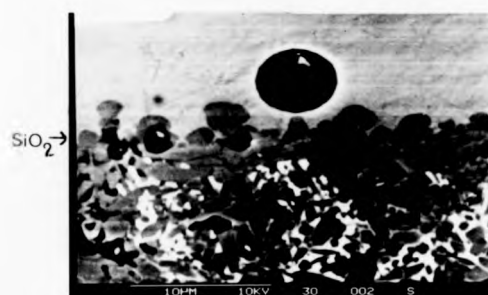


d)

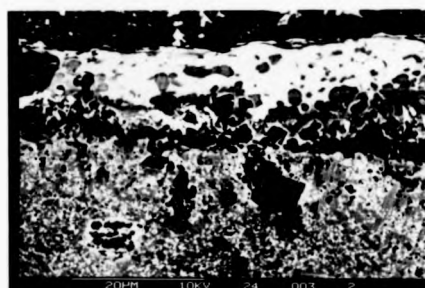
Figure 6.6. SEM Sections of oxide film on the glass matrix alloy S13, at 1300°C. (a) After 1 hour. (b),(c),(d) Typical development of oxide with time.



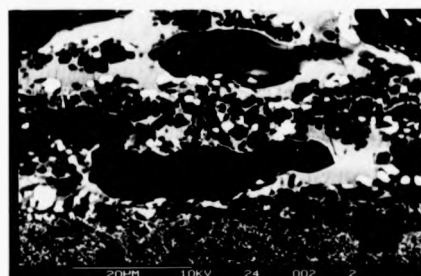
a)



b)

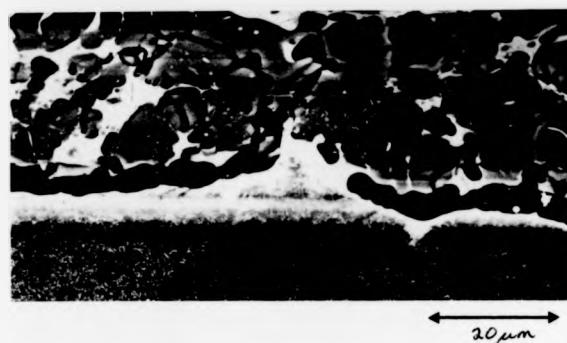


c)

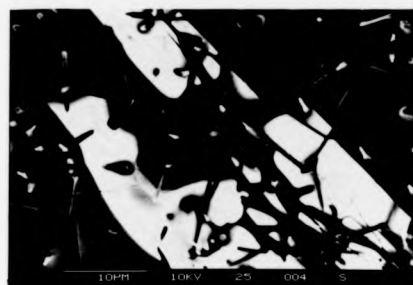


d)

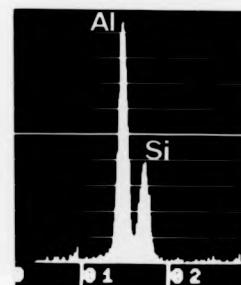
Figure 6.6. SEM Sections of oxide film on the glass matrix alloy S13, at 1300°C. (a) After 1 hour. (b),(c),(d) Typical development of oxide with time.



a)



b)

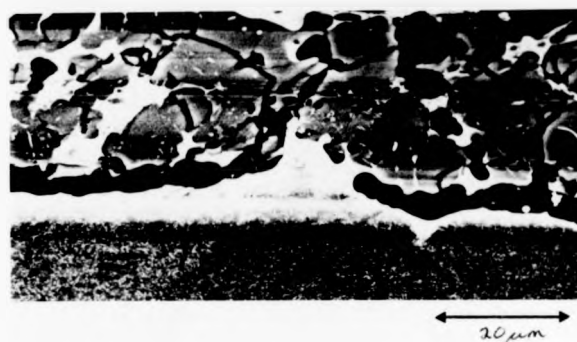


c)

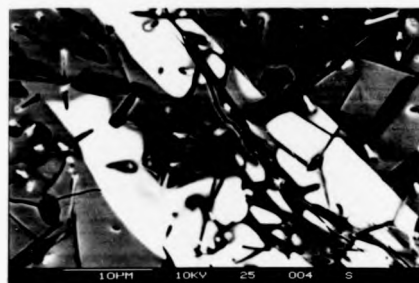


d)

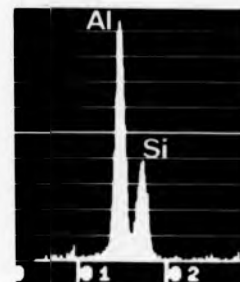
Figure 6.7. Features (from S.E.M.) of oxide product of glass matrix alloys at 1350°C. a) Section showing oxide shell formation and bump on oxide surface associated with a cavity. b) Mullite needles (dark) growing into dissolved Y₂S grains on oxide. c) E.D.A.X. analysis of dark, Mullite needles. d) Gas bubbles developing in glass regions (bright) within the oxide, producing intergranular cracking.



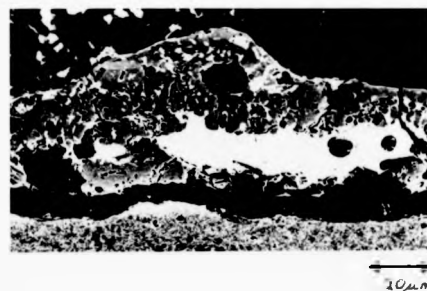
a)



b)



c)



d)

Figure 6.7. Features (from S.E.M.) of oxide product of glass matrix alloys at 1350°C. a) Section showing oxide shell formation and bump on oxide surface associated with a cavity. b) Mullite needles (dark) growing into dissolved Y₂S grains on oxide. c) E.D.A.X. analysis of dark, Mullite needles. d) Gas bubbles developing in glass regions (bright) within the oxide, producing intergranular cracking.

intergranular cracking and a friable oxide. Within this glass also nucleate many dark needles, mainly at the oxide surface (fig 6.7b). Their chemical analysis suggests a composition $2.96 \text{ Al}_2\text{O}_3:2\text{SiO}_2$ (fig 6.7b) and X.R.D. of the powdered oxide confirms this phase as Mullite ($3\text{Al}_2\text{O}_3:2\text{SiO}_2$). The observation of mullite growth into a partially dissolved β - Y2S grain on the oxide surface (Fig 6.7b) indicates a rapid initial β - Y2S nucleation followed by a steady increase in Al concentration in the surrounding oxide glass. This Al-rich glass takes the β - Y2S into solution and then allows nucleation of the mullite. The presence of mullite only at 1350°C could indicate the slower out-diffusion rate of Al compared to Y, but is more likely the consequence of SiO_2 crystallisation which would significantly increase the Al concentration in the contracting oxide glass volume.

6.1.2(b) Oxide Development Mechanisms

There are two possible reasons for the oxide shell formation. (1) The molar volume difference between SiO_2 and β' implies the development of compressive stresses in the crystallising oxide scale. The ability to accommodate these stresses by the viscous oxide glass is reduced with its contracting volume. The oxide expands, overcomes the hydrostatic tension conferred by the interfacial viscous film and parts from the substrate. (2) The developing interfacial gas pressure cannot be relieved by the previous bubble formation and outward drift mechanism as both the oxide glass volume and access to the surface are reduced by oxide crystallisation. This highly strained oxide scale develops a substantial cavity network within the viscous phase between SiO_2 grains (Fig 6.7d) which gives direct access (for the environment) to the substrate. Substrate oxidation proceeds at a slightly reduced rate (as the underlying g.b. matrix is Y and Al depleted from the

initial oxidation mechanism) but develops similar oxide features. The effective oxide is grossly inflated by the porous volumes and oxide thickness measurement is unsuitable for detailed kinetic parameter determinations.

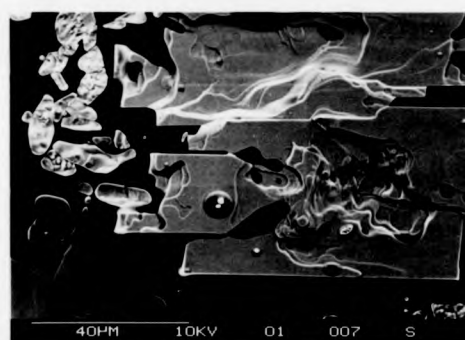
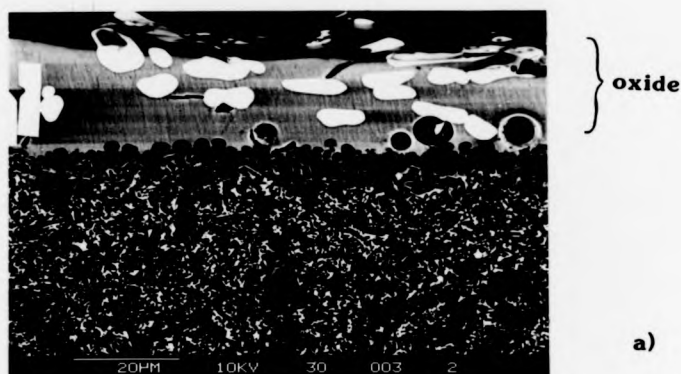
6.1.3 Oxidation Mechanisms for (β' + glass) Alloys

The similarity of oxidation kinetics and oxide characteristics for the range of high 21R materials indicates that the radically different oxidation mechanism from SO is not dependent on (1) impurities (type or level) derived from the α - source, (2) the g.b. matrix volume, (3) the Y level. Deleterious oxidation is therefore due to the non-protective oxide. The excessive bubble formation is believed to be derived not only from enhanced oxidation reactions but also the enhanced g.b. glass Nitrogen content. The previously mentioned high-N bulk glasses readily oxidise (148) to produce a highly expanded foam-type material, similarly noted (145) in preparation of Y-Si-Al-O-N glasses. The detrimental α - cristobalite crystallisation is due to a lowering of the T_g of oxide glass, and the increase in oxide Al^{3+} content is deduced to be responsible. Increasing Al_2O_3 content is known (31) to increase the fluidity of Yttrium silicate liquids.

6.2 OXIDATION OF ANNEALED MATERIALS

6.2.1 Low 21R Additive Alloy with α - $Y_2Si_2O_7$ matrix

The oxide film of material SOC at 1300°C and 1350°C is coherent and glassy, although the varying surface features reveal the underlying bulk material's distribution of β' + glass and β' + α - Y2S zones. The oxide above β' + α -Y2S zones is completely amorphous (Fig 6.8a) whilst the β' + glass zones give rise to large coarse, faceted β - Y2S grain growth. In comparison with the pre-annealed (β' + glass) materials (Section 6.1.1(a)) at similar oxidation temperatures, this morphology indicates a reduced Y outdiffusion rate with the consequential delayed β' - Y2S nucleation and growth. Also after 13 hours at 1350°C the β -



57 hrs.

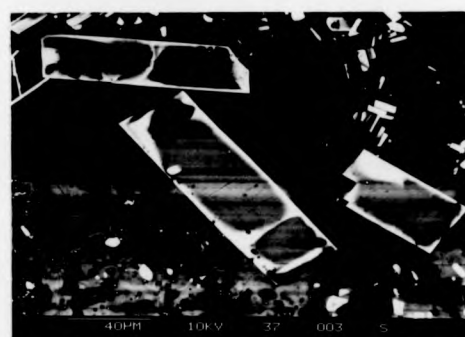
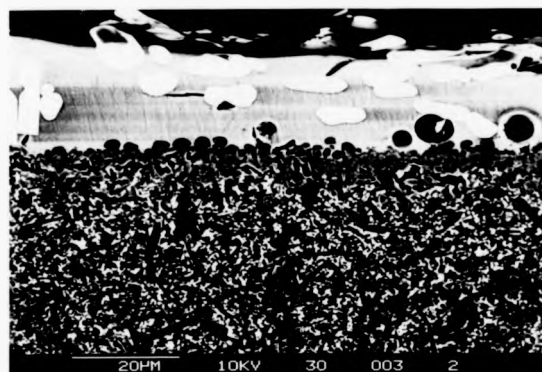
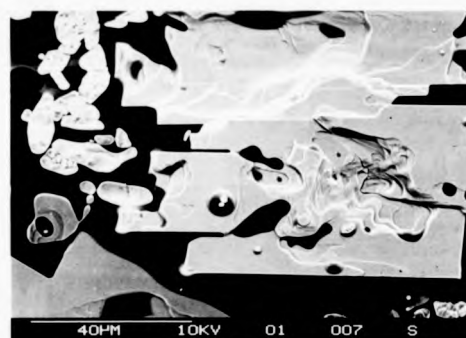


Figure 6.8. a) S.E.M. section of alloy SOC with crystalline (Y₂S) matrix showing protective glassy oxide produced at 1350°C. b) Oxide surface showing onset of dissolution of β - Y₂S platelets after 13 hrs. c) Skeletal β - Y₂S platelets after 70 hrs.



} oxide

a)



b)

57 hrs.



c)

Figure 6.8. a) S.E.M. section of alloy SOC with crystalline (Y₂S) matrix showing protective glassy oxide produced at 1350°C. b) Oxide surface showing onset of dissolution of β - Y₂S platelets after 13 hrs. c) Skeletal β - Y₂S platelets after 70 hrs.

- Y2S grain change morphology and appear to be taken back into solution, as observed in Section 6.1.2a. After 70 hours most grains are represented as only skeletal structures (Fig 6.8c). This change is associated with an increased oxide concentration of Al.

These features together with subsequent fine β - Y2S reprecipitation and SiO₂ growth replicate the finding of SO and a similar oxide formation mechanism is concluded to operate, but at higher temperatures.

This confirms the slower Al outdiffusion rate than Y, and the dominant effect of Al on the oxide characteristics and its degree of protection. The low Y level in the oxide indicates the stability of the α - Y2S matrix phase. Even with a residual g.b. glass present, this material exhibited parabolic oxidation kinetics yielding a very low activation energy of $\sim 180 \pm 25$ kJ/mole, which represents a dramatic improvement over the parent SO material (Fig 6.5). Not only is oxidation resistance comparable with hot-pressed Si₃N₄ or Si-Al-O N (Fig 6.9) but a pressureless sintering route and reduced sintering temperature are also offered.

Whilst incomplete matrix crystallisation only slightly increases the oxide growth rate, it has a significant adverse effect on the sub-oxide microstructure material stability (Sections 6.6.2, 6.6.3) and high temperature mechanical behaviour (Chapter 7).

6.2.2 High 21R Additive Alloys with YAG Matrices

Materials S10, S13, L10 were studied in detail, and represent matrices with a range of degree of YAG crystallisation, volume and distribution. Below 1300°C only minor oxidation occurred, with the oxide film being barely detectable in S.E.M. section and the sub-oxide microstructure unaltered. The oxide is mainly glassy, with β - Y2S crystallisation observed only for S10 and S13 (materials having g.b. glass residual to the matrix crystallisation). This illustrates the

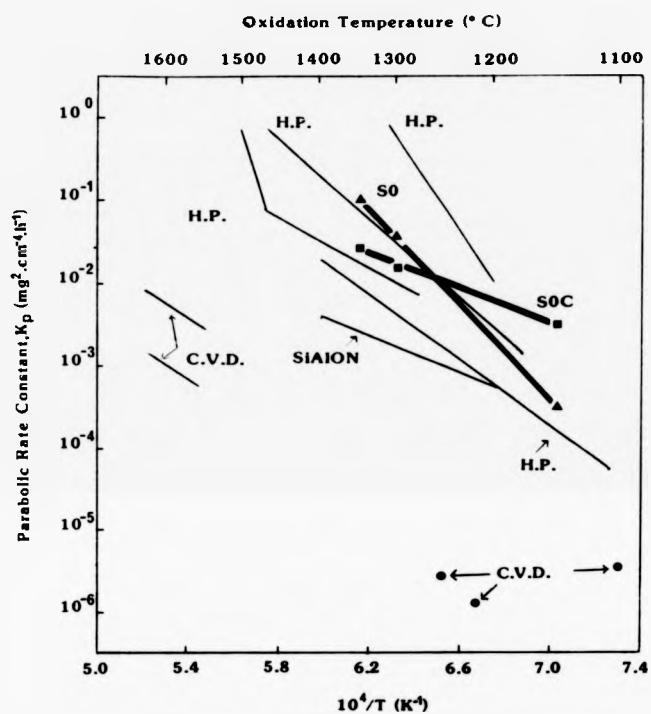


Figure 6.9. Arrhenius plot of parabolic rate constants for oxidation of various types of Si_3N_4 (after 153).

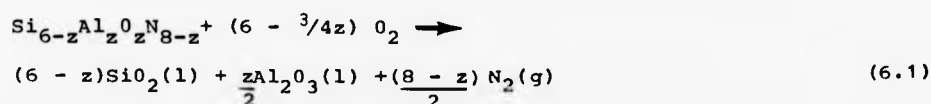
stability of YAG to oxidation below 1300°C.

However, this excellent oxidation resistance is not extrapolated to temperatures above 1300°C, where kinetics abruptly increase and approach those of the parent β' + glass materials (Fig 6.10). Similar oxide characteristics and kinetics are produced for the whole range of materials, and are typified by L10. At 1300°C, the oxide has partially crystallised to β - Y₂S and SiO₂ and developed porosity at the viscous reaction interface which can produce surface rupture after ~ 70 hours. At 1350°C any oxide variability between materials converges to produce almost identical oxidation behaviour (Fig 6.10). This indicates the independence of the oxidation mechanism from subtle phase volume changes or distributions and, more importantly, degree of matrix crystallisation. Initially YAG-matrix materials exhibit reduced oxide development over parent glass-matrix materials, but above 12 hours the kinetics and features are similar, with the previously observed oxide shell formation occurring after 24 hours.

Fig 6.5 shows that although the parabolic rate constants are different, a similar activation energy and therefore rate-limiting process exists for ceramics which initially have either glass or YAG matrices. The abrupt change in activation energy at 1300°C is also shown. The reason for this change and replication of the oxidation of β' + glass is that a subsurface β' + YAG zone reverts to β' + glass during oxidation by a mechanism activated above 1300°C and explained fully in Section 6.4.1.

6.3 A UNIFIED OXIDATION MECHANISM

Initial β' oxidation produces an Al-containing SiO₂ glass by a reaction of the type:



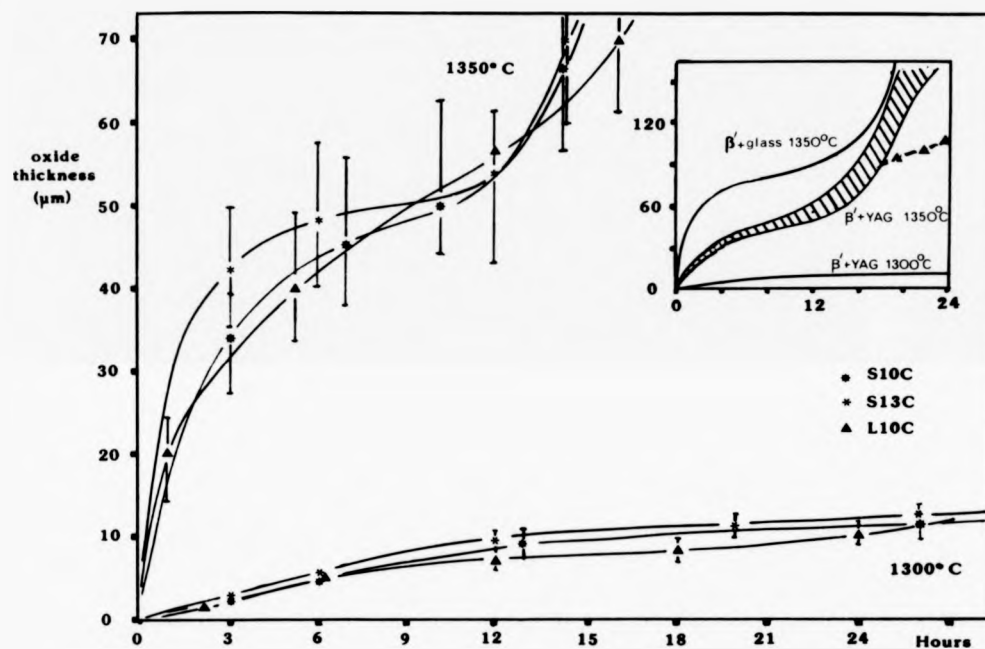
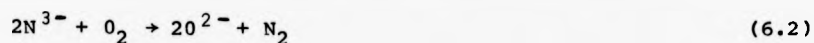


Figure 6.10. Oxide thickness kinetics for a range of alloys with a crystalline (YAG) matrix at 1300°C and 1350°C.

where z takes on values given in Fig 5.3. There is ample proof that Al and Y subsequently diffuse to this oxide from the bulk from (1) the suboxide elemental gradients (from SEM and TEM), (2) the higher volume fraction of β - Y₂S types in the oxide relative to the bulk. The chemical difference between g.b. and oxide glasses renders them chemically unstable at these oxidation temperatures. They form a diffusion couple in order to arrive at an average composition and this elemental equilibration provides the driving force for the g.b. outdiffusion of cation impurities (Y, Ca, Al, etc.) to the "purer" SiO₂ rich oxide (Fig 6.11a). Further, this chemical difference is maintained by (1) the increasing SiO₂ content in the oxide from the continuous β' oxidation (2) the rapid oxide surface crystallisation to β' - Y₂S which reduces the Y³⁺ ion concentration at the reaction interface. The net Y³⁺ concentration at the interface is therefore determined by a balance between the arrival and removal (to the surface) of Y³⁺ ions.

The observation of an increased oxide thickness for material SO over SOC, associated with increasing oxide cation (Al, Y, Ca) levels, is explained by two possible oxidation mechanisms:-

1. Impurities reduce the SiO₂ rich glassy oxide viscosity, allowing increased O²⁻ diffusion to the reaction interface.
2. Oxidation occurs via the dissolution of β' in a silica glassy oxide whose solubility is increased with impurity content (previously shown (71) for Si₃N₄ with MgO impurity). The dissolved N³⁻ ions react with oxygen molecules:-



and



This gives N₂ bubbles and an oxide glass which can crystallise to

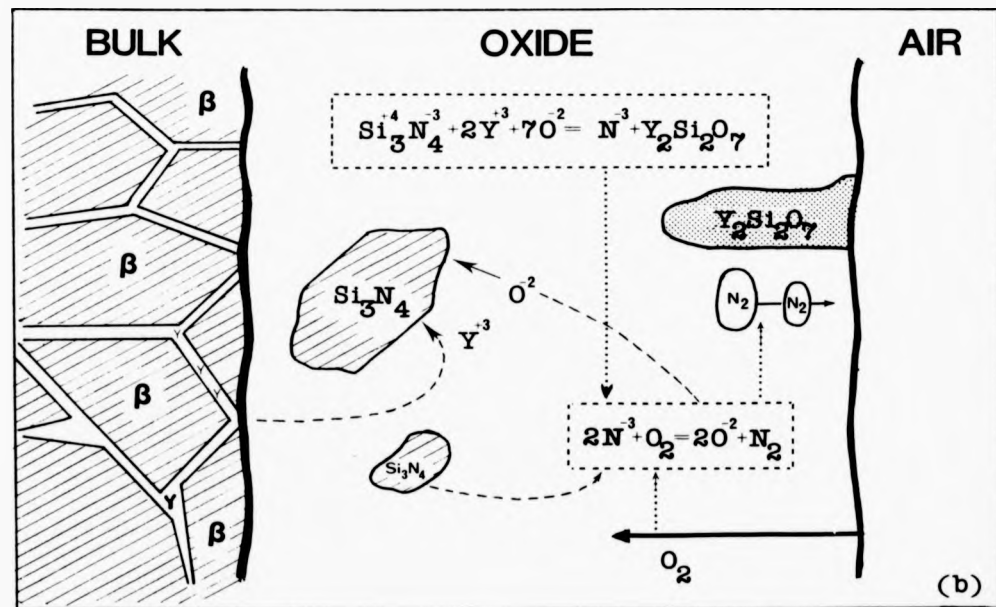
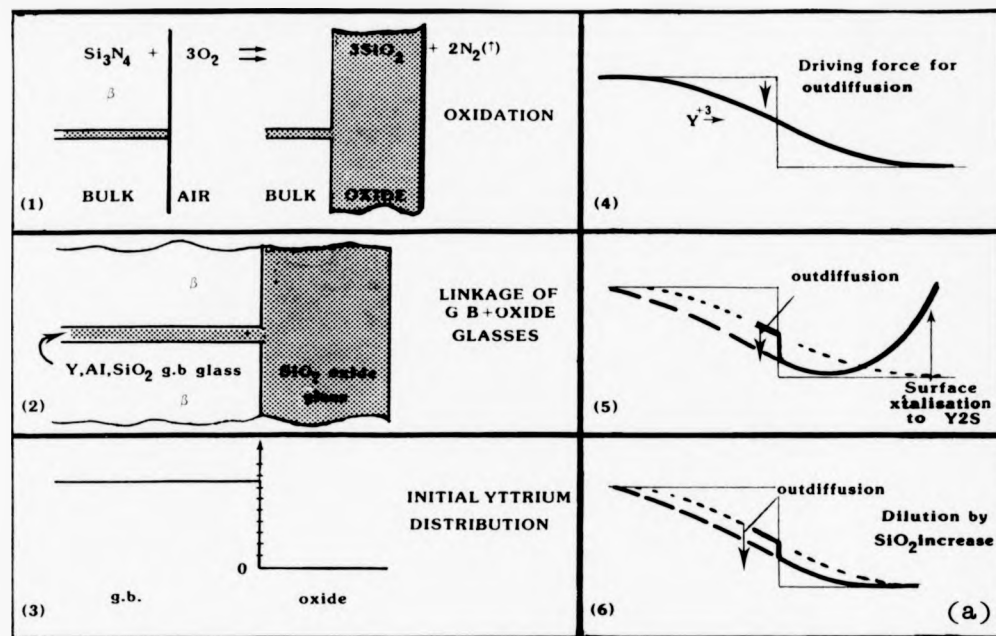


FIGURE 6.11 - (a) Si_3N_4 OXIDATION AND DRIVING FORCES
Y, Al, Ca OUT DIFFUSION FROM g.b.s. TO OXIDE
(b) OXIDATION MECHANISM VIA DISSOLUTION OF
 Si_3N_4 IN SILICA-RICH GLASSY OXIDE

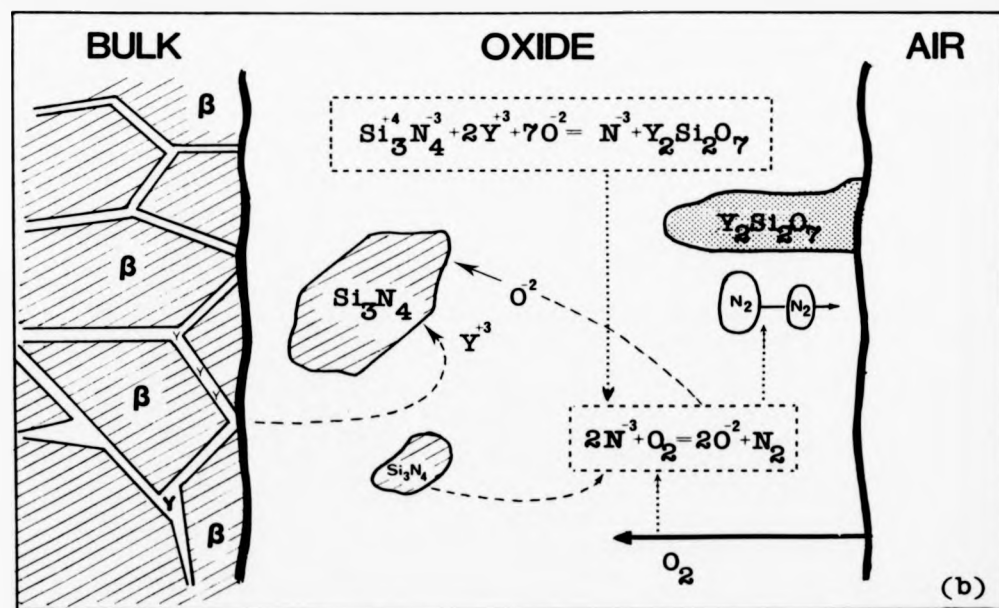
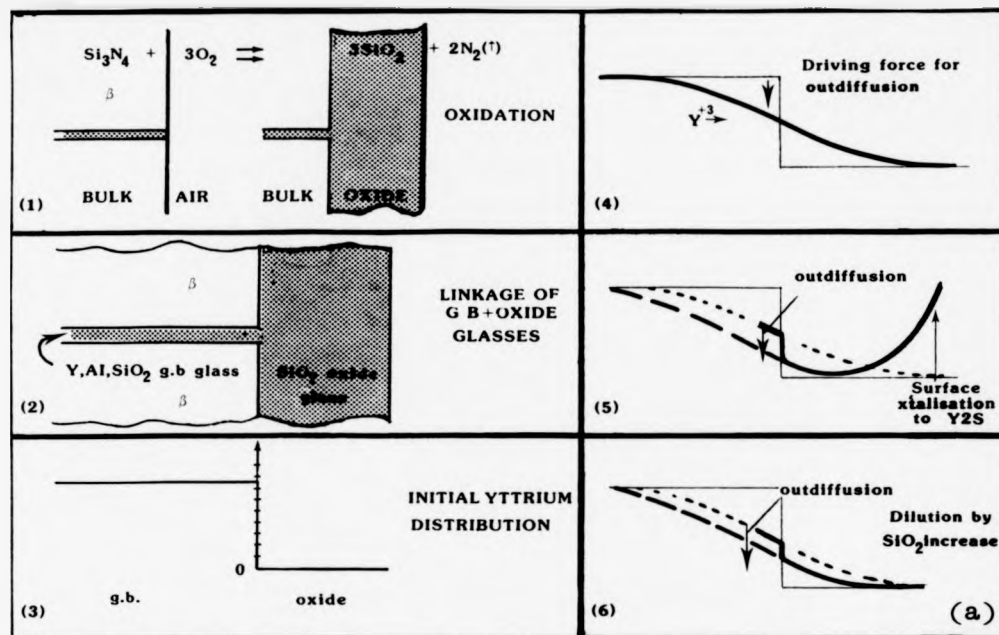


FIGURE 6.11 - (a) Si_3N_4 OXIDATION AND DRIVING FORCES
Y,Al,Ca OUT DIFFUSION FROM g.b.s. TO OXIDE
(b) OXIDATION MECHANISM VIA DISSOLUTION OF
 Si_3N_4 IN SILICA-RICH GLASSY OXIDE

Y₂S types under suitable conditions (fig 6.11b). Therefore high levels in an oxide would promote β' dissolution. The rate would increase with ease of Y outdiffusion from the bulk matrix.

There is direct evidence for the latter oxidation mechanism (increasing β' solubility with Y concentration) in the present materials, facilitated by the large pores formed at the oxide-bulk interface. Here the pore abruptly stifles inward diffusion of oxygen to the bulk material and creates several unusual conditions. Within the remnant of oxide glass in contact with the bulk, the dissolved nitrides will not therefore be all oxidised. Also the build up of Y³⁺ ions (out-diffusing from the bulk) is not relieved by β -Y₂S crystallisation. Fig 6.12 shows that the g.b. glass matrix acts as the silica-rich oxide and an increasing Y concentration is seen to enhance the matrix volume with consequently β' grain size reduction, via a rounding of morphology which is also observed in Chapter 8. This matrix volume enhancement is in accordance with the matrix volume reduction observed in Section 6.4.4. associated with Y concentration depletion. These changes can be regarded in terms of the overall $\beta' +$ glass composition within the pseudoquaternary prism (as in the sintering process) where, in the equilibrium case, the application of the lever rule determines the volume changes (Figs 5.4b).

The effect of Al³⁺ cations (within the glassy oxide) on subsequent oxidation kinetics is also complex but also unlike that of Y. The Al³⁺ ions are derived not only via outward diffusion from the matrix phase but also from direct oxidation of β' crystals. Initially being an intermediate ion in silicates, it will increase the oxide viscosity but not to any extent to compensate for the effect of Y outdiffusion. In single phase (Si₅AlON₇) materials, this viscosity increasing role for Al was concluded (54) to be responsible for their increased oxidation resistance over β -Si₃N₄. However, with the increasing Al concentration in the present oxides, the surface β -Y₂S grains are taken into solution. This immediately reduces the oxide

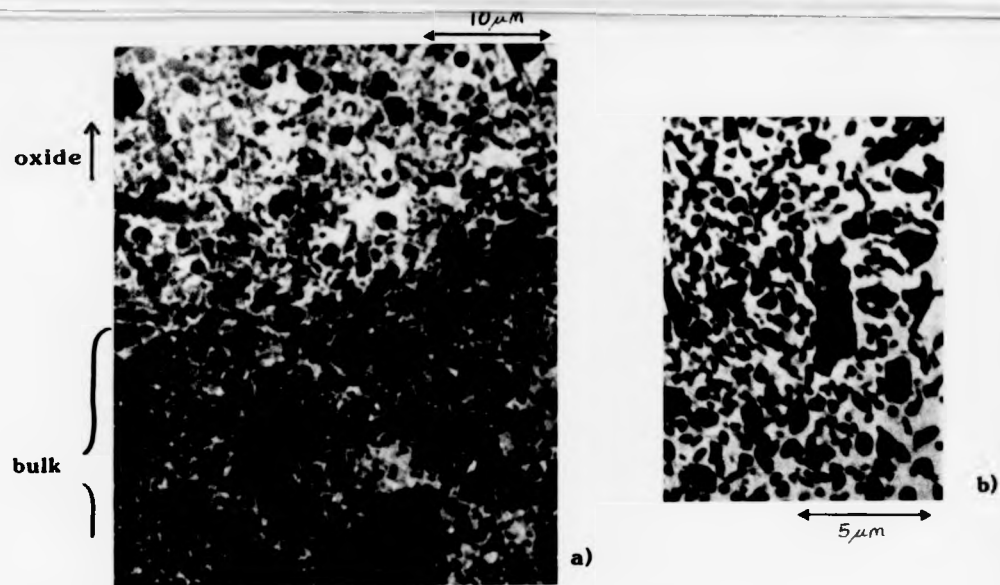


Figure 6.12. a) S.E.M. (hse) section of glass matrix alloy showing a sub-oxide zone, rich in Y, where the matrix volume has greatly increased. b) High mag. bse image showing the rounding of the β grain morphology (dark phase) that accompanies the matrix volume enhancement.

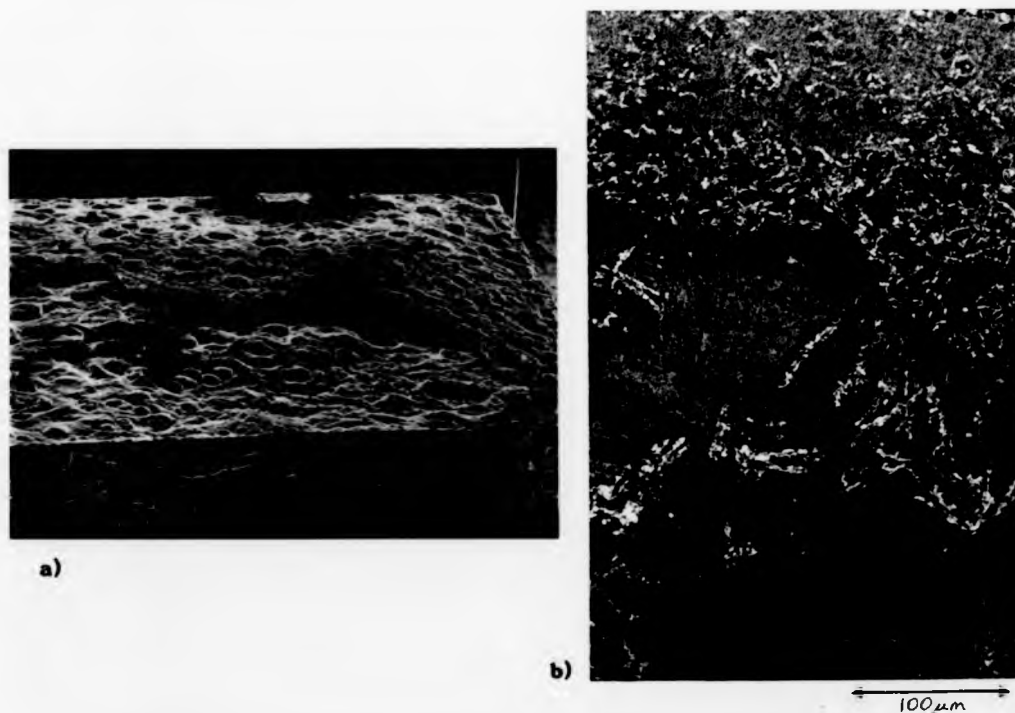


Figure 6.13. a) Formation of concentric shells of oxide on high 21R additive alloys at 1350°C . b) Normal view of oxide showing three successive layers of oxide. Contrast from bse imaging illustrates the depletion of Y-rich phases (bright regions) in successive oxide shells.

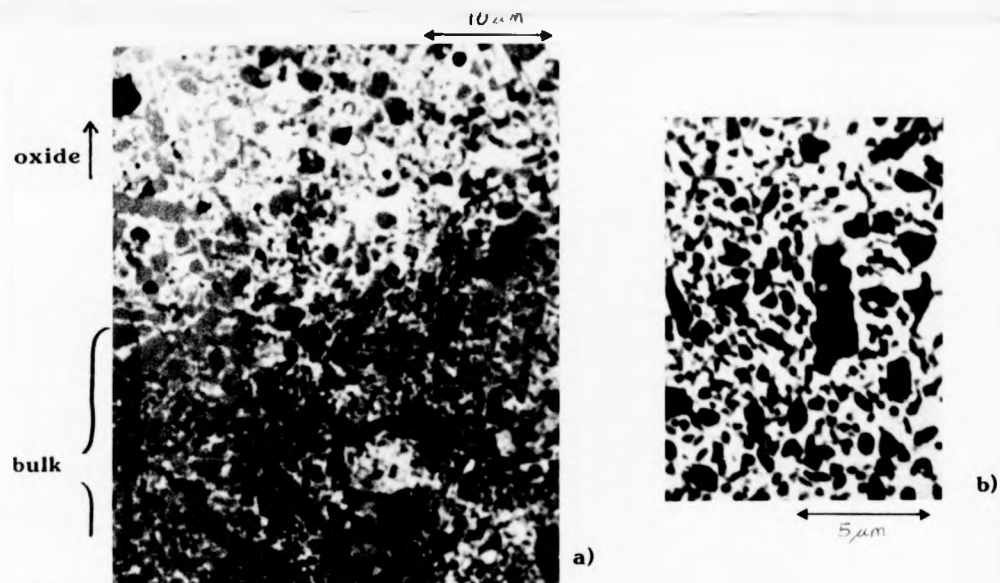


Figure 6.12. a) S.E.M. (bse) section of glass matrix alloy showing a sub-oxide zone, rich in Y, where the matrix volume has greatly increased. b) High mag. bse image showing the rounding of the β grain morphology (dark phase) that accompanies the matrix volume enhancement.

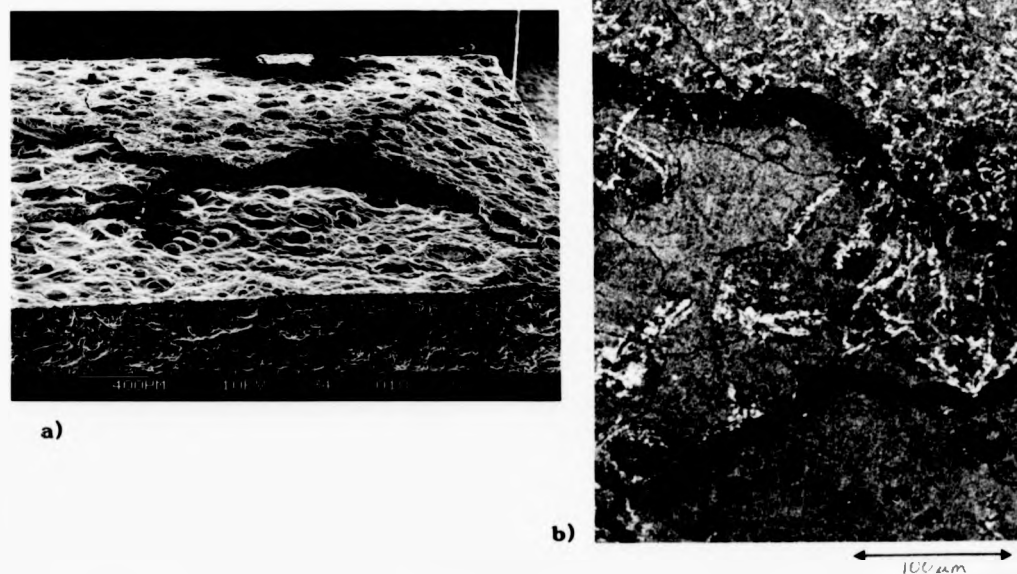


Figure 6.13. a) Formation of concentric shells of oxide on high 21R additive alloys at 1350°C. b) Normal view of oxide showing three successive layers of oxide. Contrast from bse imaging illustrates the depletion of Y-rich phases (bright regions) in successive oxide shells.

viscosity which allows devitrification to the detrimental, but equilibrium, α -cristobalite.

The abrupt reduction in oxidation kinetics for material SO at 1300°C, due to matrix crystallisation, directly shows that Y outdiffusion is the oxidation rate limiting process for this short term oxidation. Since α -Y₂S is stable with SiO₂ at the present oxidation temperatures (from the SiO₂-Y₂O₃ phase diagram), partial matrix crystallisation to α -Y₂S represents a substantial reduction in the g.b. glass volume and therefore Y, Al flux.

The parabolic kinetics for material SOC are therefore derived from the depletion of a finite Y concentration within the fine g.b. glass (residual to the matrix crystallisation). Various diffusion models for impurity out-diffusion based on effective g.b. width have been proposed and successfully explained experimental oxidation kinetics for Y₂O₃ doped Si₃N₄. Applying the Babini model (59) to the present materials readily accounts for the activation energy (ΔH) differences determined for materials SO and SOC. For SOC this ΔH is lower than that for HPSN with Y₂O₃ dopant and if an identical diffusion coefficient for Y³⁺ ions in glass is assumed, then this result indicates a finer and less continuous g.b. residual glass in the present crystalline matrix materials.

A larger g.b. diffusion channel is maintained in high 21R materials due to the YAG reversion to liquid above 1300°C. The large "reservoir" of metallics means that sufficient g.b. cation depletion cannot quickly occur in order to stabilise oxide development and produce parabolic kinetics. In order to establish whether kinetics for large Y flux materials are controlled by Y outdiffusion, material NB was initially oxidised for 150 hours at 1320°C, had its oxide removed and was similarly re-oxidised. The secondary oxidation kinetics were only slightly reduced in comparison with the initial kinetics and not

by the amount predicted by the Y outdiffusion rate-controlling model (53). However, even the very limited Y depletion occurring had an influence on kinetics. This is directly observed via the series of oxide shells (Fig 6.13) which have successively reduced Y concentrations and correspondingly reduced oxide thickness. Oxidation is, therefore, primarily controlled in these larger volume glass matrix materials by the oxygen diffusion through the oxide scale. The high oxidation kinetics are due to oxide rupture promoted by oxide crystallisation and gas pressure build up.

6.4 SUB-OXIDE MICROSTRUCTURAL STABILITY IN YAG-MATRIX MATERIALS

6.4.1 Reversion of YAG to the Liquid State

In all β' + YAG materials a sub-oxide zone of reduced matrix b.s.e. contrast, similar to that of β' + glass material (Section 6.1.1c), exists above 1300°C, (fig 6.14a). After 170 hours at 1335°C a well developed zone $\sim 100\mu\text{m}$ (optically darker) was carefully sectioned to produce thin foils from opposite ends of this zone. The T.E.M. reveals that the YAG matrix has totally reverted to a glass throughout the zone (fig 6.14b). The lack of similar observations in subsequent long term anneals at 1350°C in Argon, Nitrogen and Vacuum environments, proved that YAG "reversion" was due to reaction solely with oxidising environments and not an equilibrium reaction between a metastable YAG phase and β' . A minimum temperature for reaction of 1300°C $\pm 5^\circ\text{C}$ was defined for materials S10, S13, N10 by sub-oxide T.E.M. assessment for a series of 48 hour oxidising anneals between 1280°C and 1320°C (at 10°C intervals). This experiment also showed the phenomenon to be a general one for β' + YAG materials. From the $\text{Al}_2\text{O}_3\text{-Y}_2\text{O}_3$ binary phase diagram (152), the 'YAG' solidus is over 1900°C. However the $\text{Al}_2\text{O}_3\text{-Y}_2\text{O}_3\text{-SiO}_2$ phase diagram shows a ternary eutectic at $\sim 1350^\circ\text{C}$. A reaction couple between the SiO_2 rich oxide

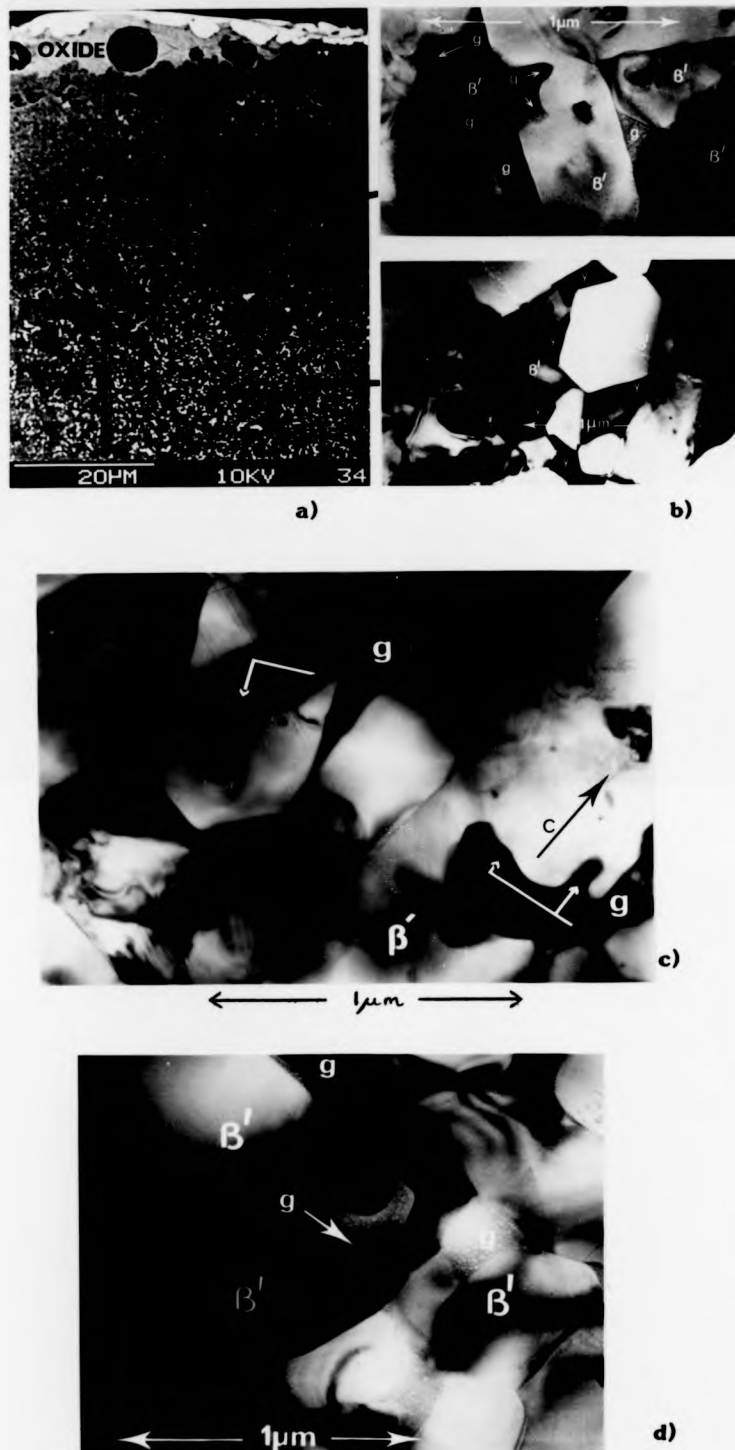


Figure 6.14. a) S.E.M. (bse) section of β' + YAG alloy oxidised above 1300°C showing a sub-oxide zone whose matrix is reduced in contrast. b) T.E.M. sections of sub-oxide zone and bulk, showing reversion of YAG matrix (y) to glass (g). c) Dissolution front proceeding along c axis of β' gains. d) Preferential β' dissolution along (10 $\bar{1}$ 0) type planes leading to hexagonal shaped glass core.

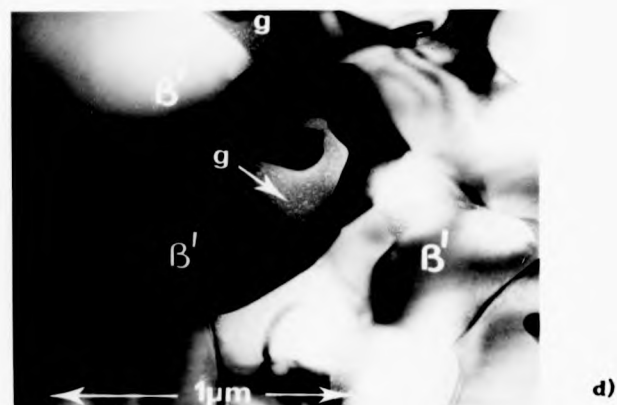
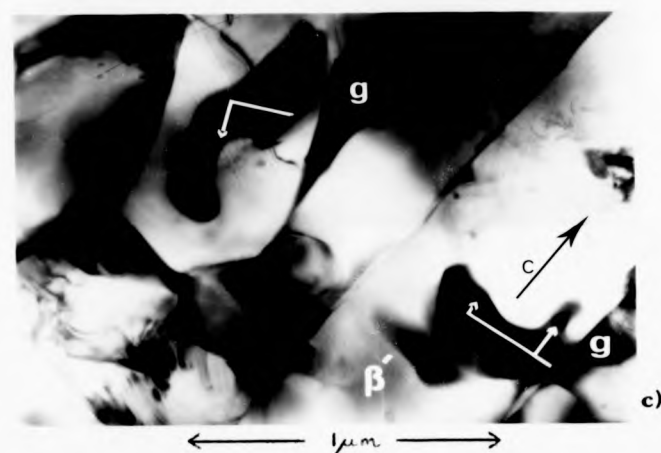
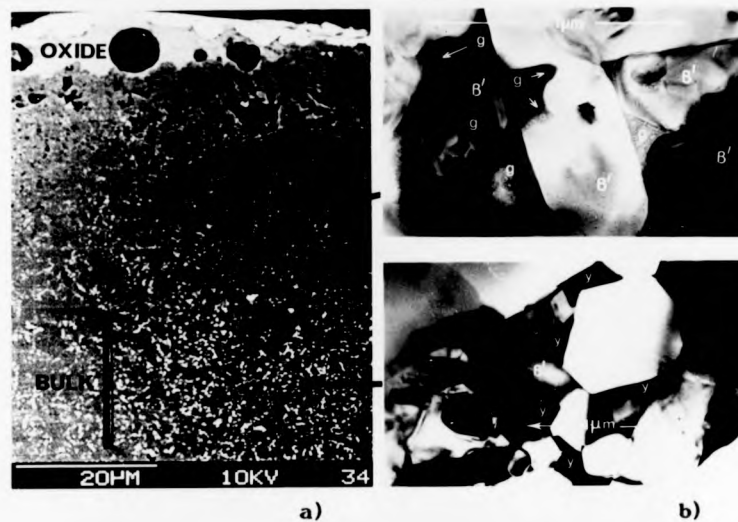


Figure 6.14. a) S.E.M. (hse) section of β' + YAG alloy oxidised above 1300°C showing a sub-oxide zone whose matrix is reduced in contrast. b) T.E.M. sections of sub-oxide zone and bulk, showing reversion of YAG matrix (y) to glass (g). c) Dissolution front proceeding along c axis of β' gains. d) Preferential β' dissolution along (10 $\bar{1}$ 0) type planes leading to hexagonal shaped glass core.

(oxidation product of β') and YAG is now proposed to account for the YAG reversion as a line joining them (Fig 5.4a) passes almost exactly through this eutectic. The further reduction in ternary eutectic temperature to 1300°C (implied from the determined reaction temperature) is most probably due to the presence of Ca and other impurities. Any oxide glass composition on the SiO_2 rich side of the eutectic will cause YAG reversion, the kinetics determined by the composition. This relatively low temperature instability with SiO_2 is unique to YAG. Other possible Al-Y-O matrix phases to react with SiO_2 are: (1) $2\text{Y}_2\text{O}_3\text{-Al}_2\text{O}_3$, which would only become unstable $\sim 1600^\circ\text{C}$ where β' decomposition occurs, (2) $\text{Y}_2\text{O}_3\text{-Al}_2\text{O}_3$, which is not considered as a matrix phase due to its highly metastable nature (152). In support of this YAG- SiO_2 reaction proposal, no zone is produced in α - Y2S matrix materials (SOC, N2C) during long term oxidation, the lowest eutectic in the binary $\text{Y}_2\text{O}_3\text{-SiO}_2$ system being above 1600°C (Fig 5.4a).

6.4.2 Dissolution of β' Grains

Within the zone is ample evidence of a subsequent β' crystal dissolution into the glass matrix. The β' volume fraction is notably reduced, producing a large continuous glass matrix. This occurs by the general β' morphology alteration, with the loss of sharp faceted edges, which must have dissolved due to their associated high chemical potential. More complex β' dissolution also occurs, which is characterised by liquid intrusion formation on crystal facets. This is probably initiated by local liquid composition variations (as β' solubility in liquid is enhanced by Y^{3+} concentrations). Once within the β' , the dissolution front appears to preferentially proceed along the prism's \bar{c} axis, dissolve the core, and leave a skeletal shell similar to the oxide β - $\text{Y}_2\text{Si}_2\text{O}_7$ grains (Fig 6.14c). This consistently observed 'coring' has several explanations. (1) A radial compositional gradient or distribution of fine inclusions exist in the β' grain,

developed during its initial growth. However, S.T.E.M. micro-analysis shows no conclusive variation in Si or Al nor the presence of impurity elements, although subtle variations may be sufficient. (2) More likely, preferred dissolution is due to chemical potential differences associated with various crystallographic planes. The critical observation of the dissolution front, within the β' grain, progressing parallel to the facet planes to produce a hexagonal shaped glass volume (Fig 6.14d), suggests preferred dissolution along $(10\bar{1}0)$ type planes. These planes have the highest linear density and largest interplanar spacing ($\sim 6.6 \text{ \AA}$) in the β' hexagonal structure and therefore the weakest interplanar bonding.

Closer to the oxide, the degree of β' dissolution is observed to increase. The driving force for the reaction and the variability are readily explained by the extent of oxygen indiffusion. In the 3-D prism representation (Fig 5.4b) increasing only eq. % O takes the overall $\beta' + \text{glass}$ composition (c) closer to the eutectic glass composition. Applying the phase rule to the $\beta' - \text{glass}$ tie-line dictates an increase in glass volume. However, β' dissolution at these oxidation temperatures is only possible because of the high Al^{3+} and Y^{3+} levels in the liquid conferred by the YAG reversion. Only limited dissolution is observed in oxidised as-sintered glass matrix materials due to their rapid Y, Al outdiffusion and matrix crystallisation.

6.4.3 Kinetics of YAG Reversion

The kinetics of the reverted-YAG zone growth show a dependence on material type at 1300°C , which diminishes at 1350°C (Fig 6.15). An accurate rate-limiting mechanism cannot be determined from zone dimensions due to the transient nature of the oxide. Non-protective oxide shell formation both rapidly increases the zone, indicating the dependence of surface oxygen potential, and decreases it via the rapid

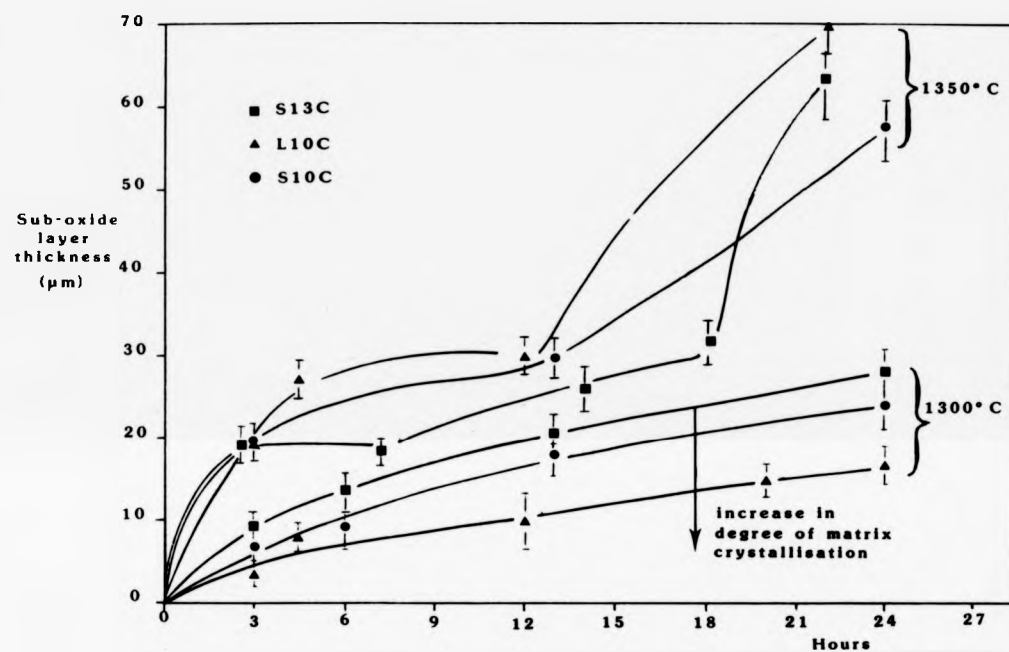


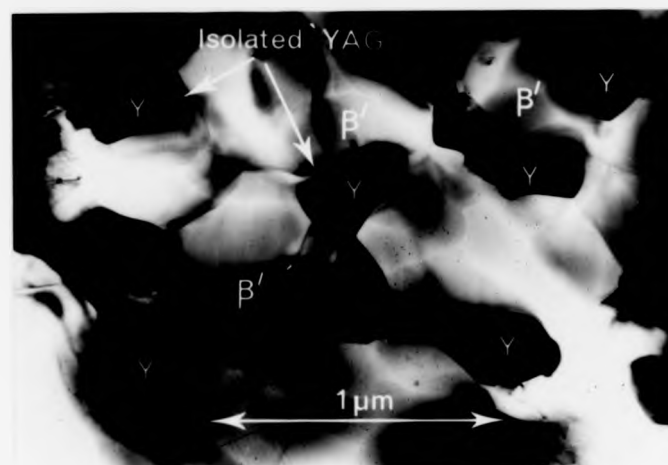
Figure 6.15 Kinetics of sub-oxide (reverted YAG) zone at 1300°C and 1350°C.

conversion of the reverted-YAG zone to an oxide scale. The complete YAG reversion and linear front requires the maintenance of an SiO_2 -rich phase at the reaction interface and is facilitated by 3 mechanisms.

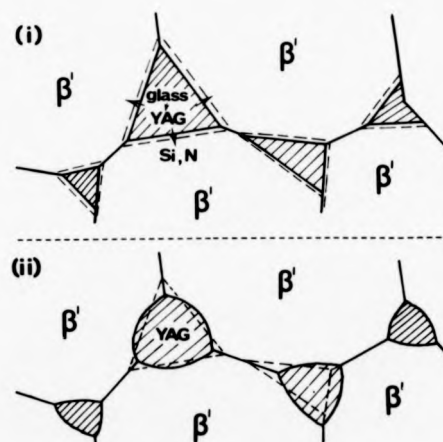
(1) The β' dissolution, with consequential glass enrichment of Si, Al, O, N. (2) The subsequent Y, Al outdiffusion leaving O^{2-} and Si^{4+} ions. (3) The O^{2-} indiffusion to react with the Si^{4+} -rich reaction zone glass. The driving force for indiffusion is simply chemical equilibration between the oxide and g.b. glass. Enhanced O^{2-} indiffusion (and therefore zone kinetics) would be expected if rapid diffusion channels of residual g.b. glass were present. There is direct correlation between degree of matrix crystallisation and zone kinetics, which explains the 1300°C variability and suggest O^{2-} indiffusion as the rate-limiting process. At 1350°C , the increased reaction rate lessens the importance of residual glass content, with the YAG volume and its continuity becoming critical (Chapter 9).

6.4.4 Microstructural Stability in the Absence of Oxidation Reactions

In the centre of a large specimen, where any oxidation effect is limited, the microstructure is still observed to be unstable. From supplementary experiments in Argon atmosphere, for varying temperature and alloys, the YAG is found to revert to liquid above 1525°C and this temperature defines the solidus for the β' ($z = 0.75$) and YAG binary. However, at sub-solidus temperatures above 1475°C , an important YAG morphology change is observed where the semi-continuous matrix progresses to a more isolated granular form (Fig 6.16a) with a corresponding reduction in surface area. This YAG "morphological stabilisation" is characterised by 3 interrelated features. (1) Primarily, the development of symmetric $\sim 120^\circ$ $\beta' - \beta' - \text{YAG}$ grain junctions, which dictates (2) curved β' YAG interfaces which results ultimately in (3) the loss of the β' faceted morphology and narrow



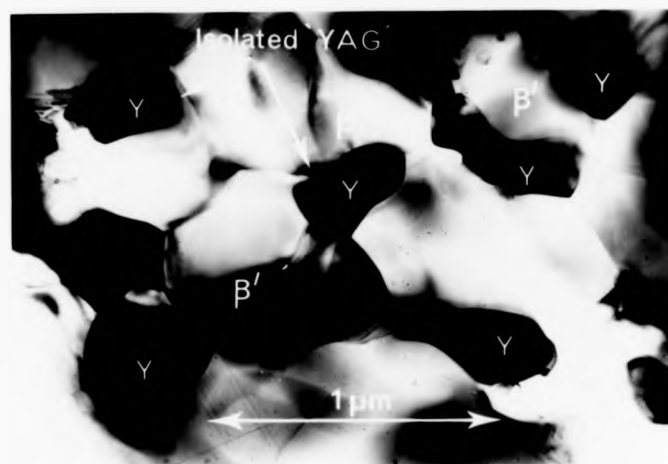
a)



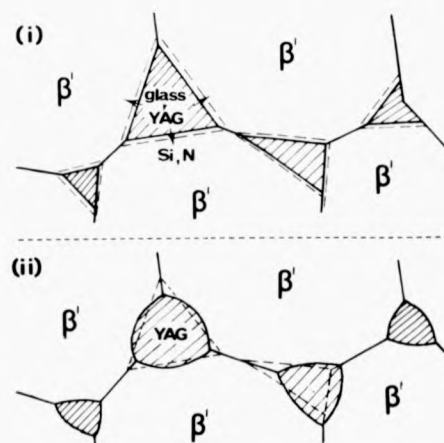
Anneal

b)

Figure 6.16. a) T.E.M. section of 'bulk' β' + YAG alloy annealed at 1475°C (with no oxidation interaction) showing 'isolated' YAG morphology. b) Schematic of route to isolated YAG via crystallisation of glass matrix and a reduction in surface energy anisotropy.



a)



Anneal

b)

Figure 6.16. a) T.E.M. section of 'bulk' β' + YAG alloy annealed at 1475°C (with no oxidation interaction) showing 'isolated' YAG morphology. b) Schematic of route to isolated YAG via crystallisation of glass matrix and a reduction in surface energy anisotropy.

interconnected "YAG" channels. The driving force for the transformation is the loss of surface energy anisotropy associated with the initial solid/liquid interface (of the as-sintered microstructure), and the replacement with approximately isotropic solid/solid interfaces between β'/β' and β'/YAG (Fig 6.16b). The β'/YAG g.b. movement will not be by atomic jumping across the interface (due to the lack of β'/YAG solid solution), but by transport along the g.b. with atomic removal and redeposition, producing the characteristic 'S' shaped boundaries. Morphological stabilisation is an important microstructural modification. In combatting the oxidation degradation mechanisms above 1300°C this loss of an interconnected YAG path through the microstructure will be shown (Chapter 9) to significantly reduce oxidation and reverted-YAG zone kinetics.

6.5 SUB-OXIDE MICROSTRUCTURAL STABILITY IN β' + GLASS MATERIALS

6.5.1 As-sintered Materials

In materials SO and S13, the sub-oxide zone contrast in b.s.e. mode is explained by out-diffusion of heavy elements through the matrix to the oxide driven by the SiO_2 g.b. glass diffusion couple. The kinetics of the zone's development appear controlled by the parabolic rate law (Fig 6.17a,b) and have an associated activation energy. Zone growth rate is therefore diffusion controlled, with the same mechanism operative over the temperature range studied. The rate limiting diffusive species is therefore concluded to be Y^{3+} . The initial high, non-parabolic, zone growth is probably due to the rapid oxide crystallisation to $\beta - \text{Y}_2\text{S}$ which tends to "draw" Y^{3+} ions to the oxide.

6.5.2 Materials with Reverted-Glass Matrices

Above 1300°C, after YAG reversion, the β' + glass sub-oxide zone undergoes Y, Al outdiffusion similar to the as-sintered materials. A unique difference exists however. As the reverted-glass composition

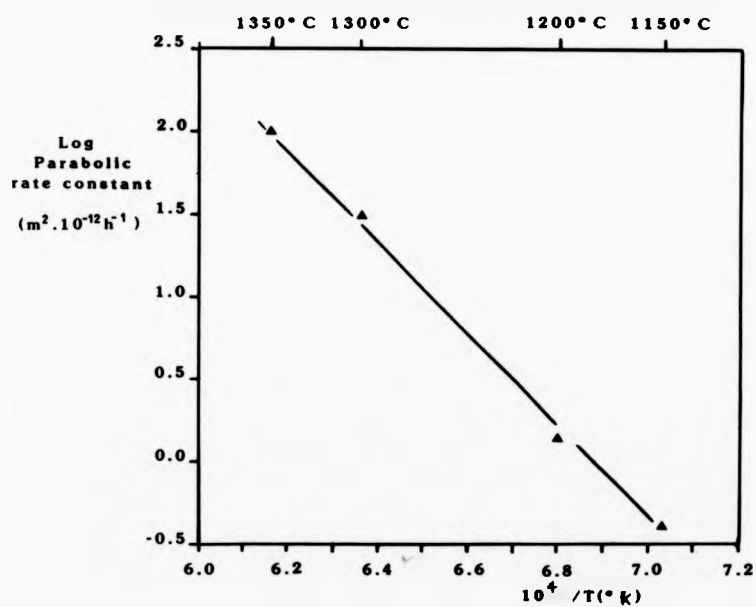
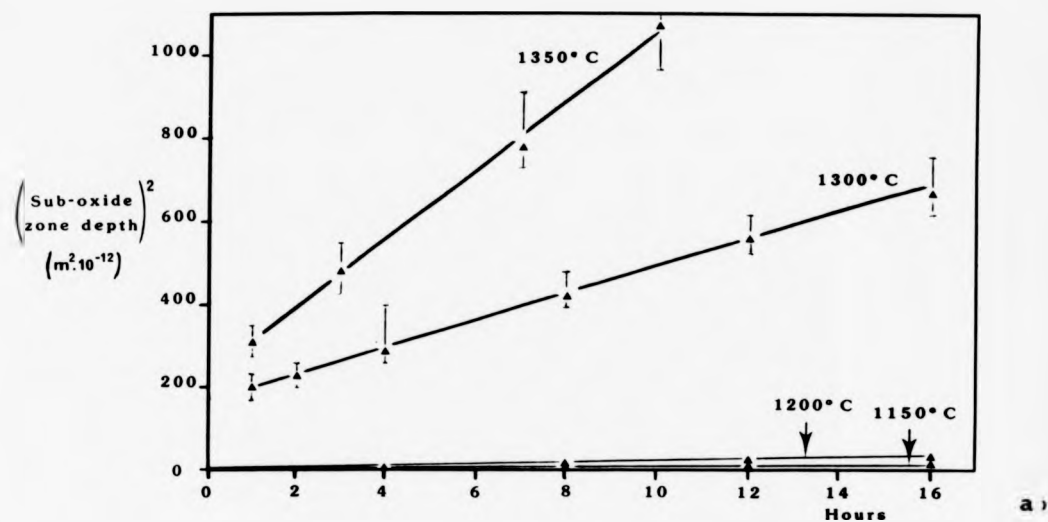


Figure 6.17. a) Kinetics of sub-oxide zone of as-sintered alloy S13. b) Arrhenius plot of parabolic rate constants.

does not recrystallise to YAG or α - Y₂S, the zone represents a material with a stable glass matrix (of greater volume and uniformity than stable zones in material N2C). Using T.E.M. sections throughout the zone, the profile of oxygen indiffusion is indicated by the eventual matrix crystallisation products. Close to the oxide, α - Y₂S crystals and phase separated SiO₂-rich globules appear, observations associated with reduced N levels in these glasses.

With extended oxidation, the near-surface glass matrix was also found to crystallise to a phase not previously observed in these materials and coincidentally the oxidation kinetics were observed to be reduced. This beneficial phenomenon was investigated.

6.6 THE DEVELOPMENT OF SILICON OXYNITRIDE

6.6.1 Microstructural Observations

The Norton series N2, N4, N6, N8 were annealed for 1000 hours in air at 1320°C. In former β + YAG materials (N6 and N8), a coherent porefree sub-oxide layer was produced (Fig 6.18a) with a substantial Yttrium depletion. The Yttrium present was confined to clumps of isolated YAG grains which reduced in volume fraction closer to the oxide. Zones therefore existed (up to 20 μ m in diameter) which were completely Yttrium denuded. Using maximum b.s.e. gain in S.E.M. made visible the two-phase nature of this zone (Fig 6.18b).

Semi-quantitative E.D.A.X. showed a slight Al level difference between the phases. A T.E.M. section solely from this denuded zone showed uniform electron absorption, making phase differentiation difficult. Initially, phases were distinguished by either microanalysis of all regions or where diffraction contrast revealed the characteristic morphologies indicated by S.E.M. (Fig 6.18c). The isolated, rounded grains (best observed in S.E.M.) were identified by electron

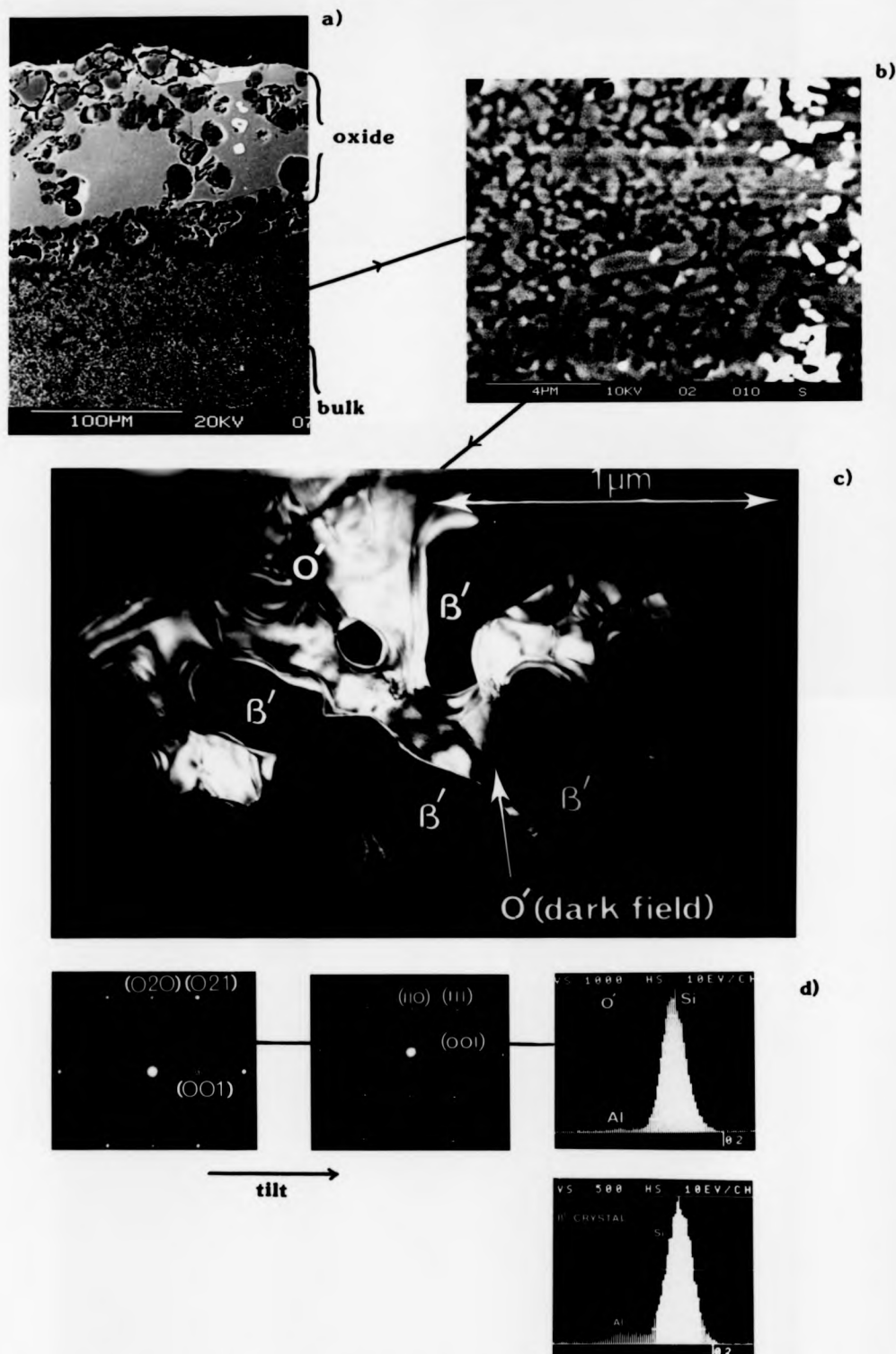


Figure 6.18. Sub-oxide of β' + YAG material, N6, after 1000 hrs in air at 1320°C. a) S.E.M. (bse) section showing Y depletion. b) S.E.M. (bse) section showing two-phase (O' + β') nature of Y depleted zone. Darker phase is O' . c) Dark field T.E.M. section of sub-oxide zone. d) E.D.A.X. and S.A.D. analysis of O' .

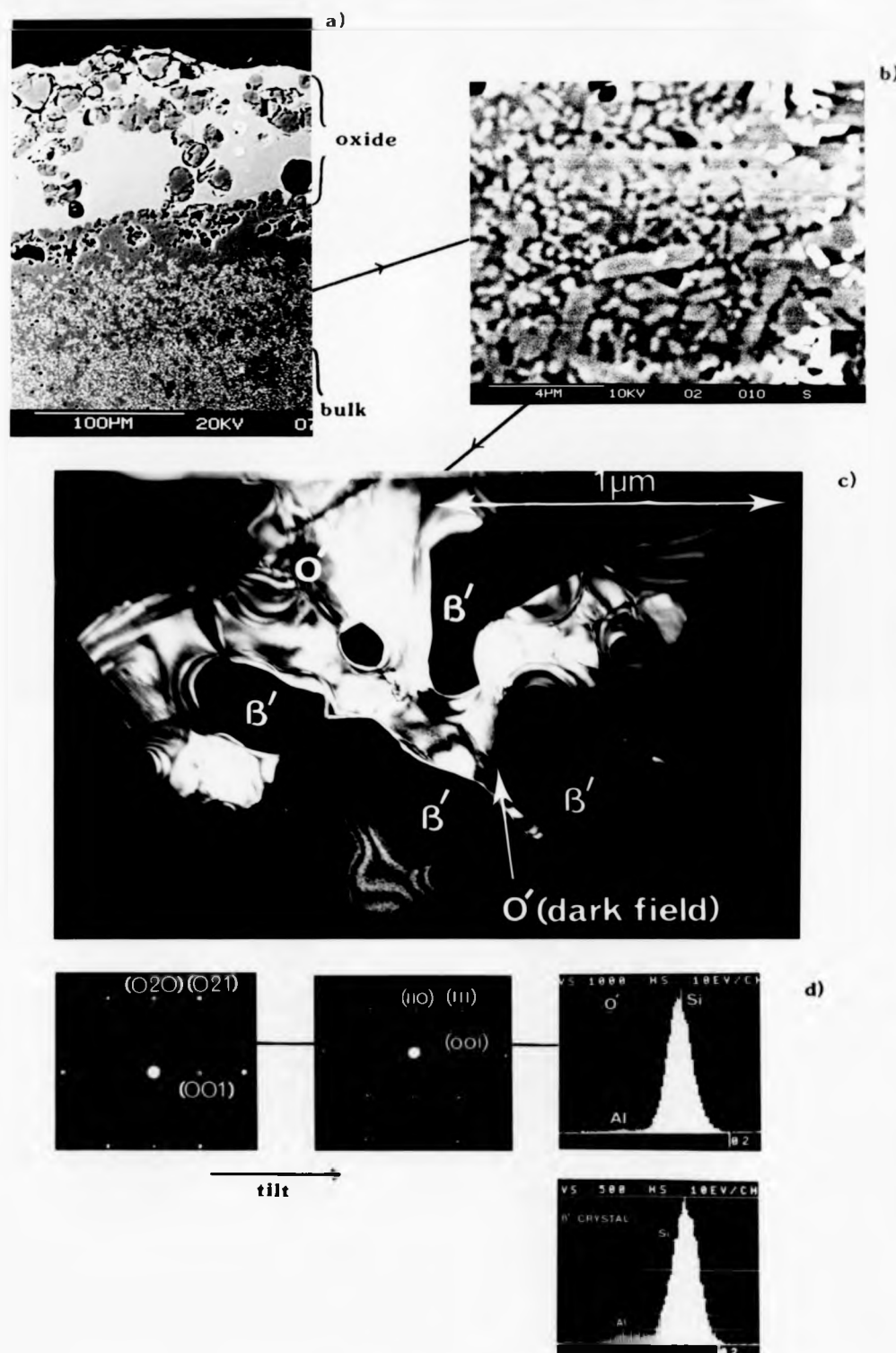
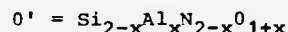


Figure 6.18. Sub-oxide of β + YAG material, N6, after 1000 hrs in air at 1320°C. a) S.E.M. (bse) section showing Y depletion. b) S.E.M. (bse) section showing two-phase (O' + β') nature of Y depleted zone. Darker phase is O' . c) Dark field T.E.M. section of sub-oxide zone. d) E.D.A.X. and S.A.D. analysis of O' .

diffraction and E.D.A.X. as β' (with z levels similar to initial material). The matrix was identified from a series of Selected Area Diffraction patterns taken at various goniometer settings. The crystal lattice has Orthorhombic symmetry with approximate lattice parameters $a = 9.000$, $b = 5.554$, $c = 4.861$ Å. Together with the microanalysis and the unusual pseudo-square diffraction pattern (Fig 6.18d) this phase was identified as the Al-substituted Silicon Oxynitride (lattice parameters $a = 8.843$, $b = 5.473$, $c = 4.835$ Å), commonly known as $0'$. Solubility of Al is by substitution for Si with corresponding substitution of O for N, giving the general formula of:



where $x < 0.4$ (see Fig 1.5d). The Al solubility was confirmed by microanalysis of isolated $0'$ fragments from crushed and dispersed T.E.M. specimens. The degree of solubility consistently increases ($x = 0.05 \rightarrow 0.1$) with initial β' z -level ($z = 0.3 \rightarrow 0.6$). Jack (26) in the fabrication of silicon oxynitride from Si_3N_4 and SiO_2 found that $0'$ resulted if β' starting material was used. The $0'$, however, does not take all the Al derived from the β' into solution although the Al levels concerned are well within the published solubility limit. Low Al substituted $0'$ is therefore either thermodynamically more stable or the solubility limit is incorrect. Excess Al to the $0'$ transformation outdiffuses along $\beta'/0'$ g.b.s. and explains the observation of Mullite ($3\text{Al}_2\text{O}_3-2\text{SiO}_2$) formation in the oxide with extended oxidation.

Importantly, at this latter development stage, the $0'$ has extended the original matrix volume and from a secondary phase become the major phase. Its volume fraction is seen in S.E.M. to increase towards the oxide, and is quantified by a large probe E.D.A.X. scan (whose excitation volume encompasses many grains) shown in Fig 6.19. The reduced Al-level is due entirely to the increased volume of low Al-containing $0'$ as contributions to the E.D.A.X. spectra from matrix

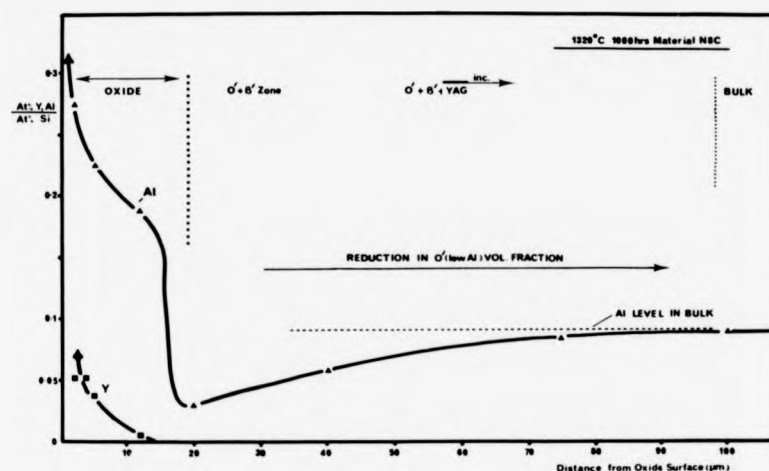


Figure 6.19. E.D.A.X. profile (using large probe/large area) across S.E.M. section of alloy N8C, oxidised for 1000 hrs at 1320°C.

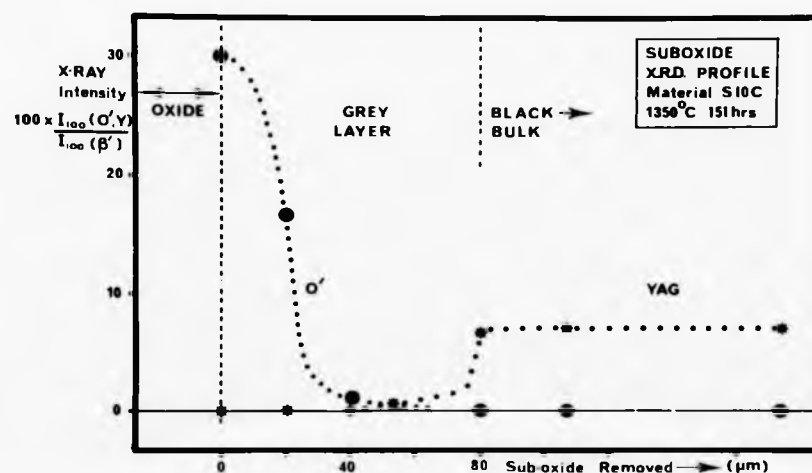


Figure 6.20. X.R.D. profile of sub-oxide of alloy S10C oxidised for 151 hrs at 1350°C. Produced by successive grinding back from the oxide.

volumes (Y, Al) are negligible. The β' grains have lost their faceted morphology and assumed curved boundaries similar to those in H.P.Si-Al-O-Ns (41). These phenomena indicate the formation of a solid state phase boundary whose shape is dictated by the minimisation of interfacial energies criterion. In support of a solid state g.b., no residual glass nor the presence of Yttrium were detected at 250,000X magnification. The occurrence of many O'/O' g.b.s. and only short range O' crystallographic constancy (Fig 6.18c) indicates a high O' nucleation density. Single O' crystals are not observed to totally envelope β' grains and therefore a short circuit for indiffusing oxygen along the O'/β' boundaries exists allowing for complete $\beta' \rightarrow O'$ transformation. The O'/O' boundaries also migrate to an equilibrium configuration during the transformation, illustrated by the symmetry of the $O' + \beta'$ region in Fig 6.18c.

6.6.2 Development of an $O' + \beta'$ Layer

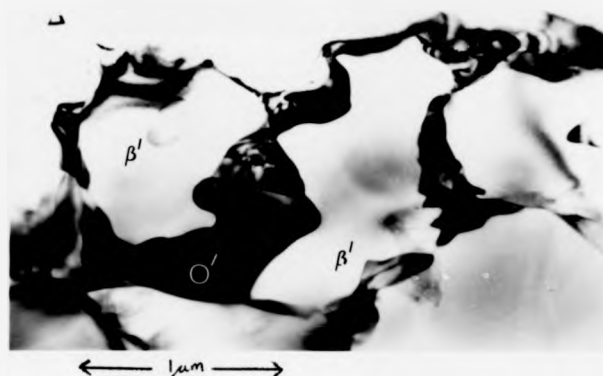
Sub-oxide Si_2N_2O has also been reported for various H.P.S.N., with MgO (46) and MgO + ZrO_2 (154) additives, its detection was however solely by X.R.D. No microstructural study into its nucleation, growth or distribution was reported.

A more complete understanding of the O' transformation and the development towards this coherent $\beta' + O'$ composite zone was obtained by shorter oxidation anneals, at various temperatures.

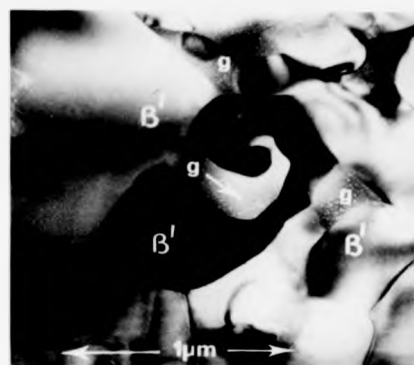
At 1300°C, the kinetics of O' development were very slow. Using S.E.M., initial O' formation is only observed after 70 hours and only at previously very narrow g.b. channels directly below the oxide. A $\beta' + O'$ zone of only 2 μm develops after 120 hours, growth probably hindered by the very porous sub-oxide microstructure.

At 1350°C, the range of materials (with glass, YAG and Y2S matrices) were oxidised and all exhibited unambiguous O' formation after 144 hours, although the extent and distribution varied

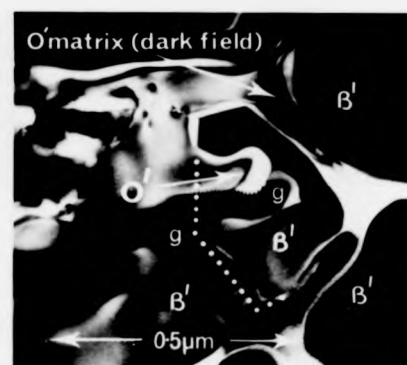
considerably. Material S10C (with a YAG matrix) showed extensive O' formation and an X.R.D. profile (Fig 6.20) of the sub-oxide (produced by successive grinding back from the oxide) showed the increasing amount of O' towards the oxide. This O' containing zone is differentiated optically by its grey colour ($\beta' + YAG$ is black) which facilitated its subsequent sectioning and thinning for T.E.M. examination. After short oxidation periods, the first O' was found at apparently clean $\beta' - \beta'$ boundaries rather than at $\beta' + \text{glass}$ (reverted YAG) interfaces. O' also developed preferentially within local regions with barely detectable volumes of g.b. glass to produce an extensive but very narrow intergranular phase (Fig 6.21a). This preference for low g.b. glass volumes is not thought to indicate a solid-state growth mechanism since the O'/β' interfaces are irregular and well developed. O' shows no crystallographic relationship to the surrounding β' grains. Therefore initial O' growth via a very small liquid phase (β' solution $\rightarrow O'$ precipitation) is considered most likely, the irregular O'/β' interface then explained by liquid composition fluctuations and solution front instabilities. There is also considerable supporting evidence for an intermediate O' growth mechanism via a liquid phase and Fig 6.21c represents a critical observation. Fig 6.21b illustrates a typical β' morphology after resolution by the reverted-YAG glass. Subsequent O' growth into this type of β' grain (Fig 6.21c) shows O' growth solely due to glass devitrification, with no reaction involving the β' grain having occurred to produce O' . In these large glass volumes, O' growth is unrestricted. It develops a faceted needle-like morphology (which is heavily faulted) before impingement on other β' grains and leaves residual Y, Al containing glass pockets at $O' - \beta'$ junctions (Fig 6.21d). The sharp O'/β' phase boundary at the intermediate O' development stage suggests a preferred O' growth orientation. The orientation may be identified from the faulting which



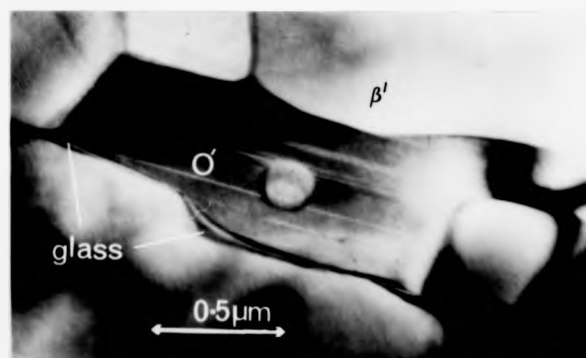
a)



b)



c)



d)

Figure 6.21. Development of sub-oxide O' . a) Initial development in narrow intergranular zones. b) Typical β' morphology after dissolution. c) Intermediate O' growth into β' (typical of dissolution type) via a liquid phase. d) Heavily faulted O' grain with glass pocket (residual to crystallisation).



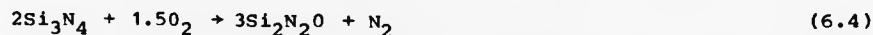
Figure 6.21. Development of sub-oxide O' . a) Initial development in narrow intergranular zones. b) Typical β' morphology after dissolution. c) Intermediate O' growth into β' (typical of dissolution type) via a liquid phase. d) Heavily faulted O' grain with glass pocket (residual to crystallisation).

extends along the needle's growth direction. The crystal structure of $\text{Si}_2\text{N}_2\text{O}$ is similar to Si_3N_4 but with an oxygen atom replacing one nitrogen in the SiN_4 tetrahedra building block. The open framework structure can then be realised as parallel sheets of silicon-nitrogen atoms joined by Si-O-Si bonds. Recent T.E.M. studies of Hot-Pressed $\text{Si}_2\text{N}_2\text{O}$ (155) show the faulting to be typical and along these sheets (due to the weaker Si-O bonding). The preferred growth direction of $\langle 001 \rangle$ can therefore be inferred.

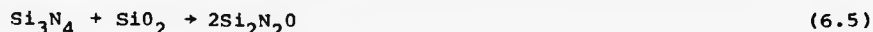
After the complete conversion of glass matrix to $0'$ within the transformed sub-oxide zone, the volume fraction of $0'$ is then observed to increase beyond the previous matrix proportions after 1000 hours. A solid-state transformation to $0'$ is thought to occur at this stage, suggested by the transition to the smooth convex $\beta'/0'$ equilibrium interface, described in Section 6.6.1., which also demonstrates the complete removal of interfacial glass.

6.6.3 Mechanisms for $0'$ Formation

In the present alloys then, $0'$ formation occurs by several mechanisms, the initial and major being via a liquid phase, with a solid state transformation occurring after the removal of interfacial glass. The initial $0'$ formation is proposed to be by oxidation of the β' , the g.b. glass acting as an oxygen source. $\text{Si}_2\text{N}_2\text{O}$ develops as an intermediate phase during the passive oxidation of "pure" Si_3N_4 to the usual SiO_2 oxide (Eq. 2.5) and it represents the oxide product in a reduced oxygen environment



alternatively it can be fabricated (26) by the reaction



$\text{Si}_2\text{N}_2\text{O}$ formation by Equation (6.4) requires an oxygen imbalance at the β' g.b. or β' /matrix interface. The most obvious mechanism is O^{2-} indiffusion through the g.b. diffusion channel from the oxide, driven by the equilibration of matrix and oxide glass oxygen levels. An additional oxygen source is that associated with both Y and Al in the g.b. or matrix glass. Upon the rapid Y^{3+} and Al^{3+} cation outdiffusion to the oxide, these associated oxygens will be left behind as anions to react with the β' by equation 6.4. The N^{3-} anions produced can then diffuse to the surface with the Y^{3+} cations to maintain charge neutrality. In fine g.b. volumes it was suggested (46) that the driving force for this O' formation mechanism was the attempt to maintain the original equilibrium g.b. glass composition. The glass has become SiO_2 rich and this excess portion is removed by reaction with β' to produce O' . The distribution profile of O' in the substrate correlates with the observed Y and Al depletion profiles and so supports this additional mechanism being operative. However, more importantly, the present work is able to conclude, with the observed continual O' growth in Y denuded zones with extended anneals, that O' formation occurs in the absence of this mechanism.

An additional O' formation mechanism is by direct β' oxidation by atmospheric O_2 gas, suggested by the observed transformation of an initially porous matrix to O' (SOC at 1300°C) with extended oxidation. This is similar to the g.b. SiO_2 oxide development in porous R.B.S.N., which increases its sub-surface density (122). The more restrictive gas diffusion path in the present materials would give the required low oxygen partial pressure. The extent of this mechanism is minor as (1) the densifying sub-surface restricts subsequent gas diffusion, (2) substrate porosity occurs at low temperatures where O' formation kinetics are low.

6.7 DISCUSSION

In the same way that other phenomena have been related to composition utilising the phase diagram in this thesis (e.g. matrix crystallisation, laser), this approach can be adopted with oxidation. Attempts (55) with HPSN in the Si-Mg-O-N system, using X.R.D. data, allowed important conclusions to be drawn. A similar approach was therefore adopted to confirm its validity for the present Si-Al-Y-O-N system. Greater quantification was possible due to the detailed micro structural examination of oxide and sub-oxide which supplemented X.R.D. studies.

To simplify representation in the 3-D prismatic phase diagram to a 2-D plane (4 components, Si-Y-O-N), the material SOC with α -Y₂S matrix was chosen and the presence of Al ignored, (fig 6.22). Its composition lies on the Si₃N₄-Y₂S tie-line, the position (1) represents the relative molar ratios (by the lever rule). The equilibrium oxidation product of this β -Y₂S composition can be determined by drawing a vertical line from the initial composition to the SiO₂-Y₂O₃ binary line. This represents the replacement of all nitrogen with oxygen and gives the reaction products of SiO₂ and Y₂S for the total oxidation of β + Y₂S, which was found experimentally as the oxide layer.

Total oxidation occurs only at the surface, but partial oxidation into the interior has been demonstrated to occur directly by indiffusion of oxygen or indirectly by Y, Al out diffusion. A gradient of oxygen concentration and therefore oxidised products will be produced from the oxide surface to the bulk interior. Temporarily ignoring Y outdiffusion, the compositional variation is represented by the compositions on the dotted line from the bulk (1) to the SiO₂-Y₂S binary line. However, substantial Y, Al outdiffusion to the oxide

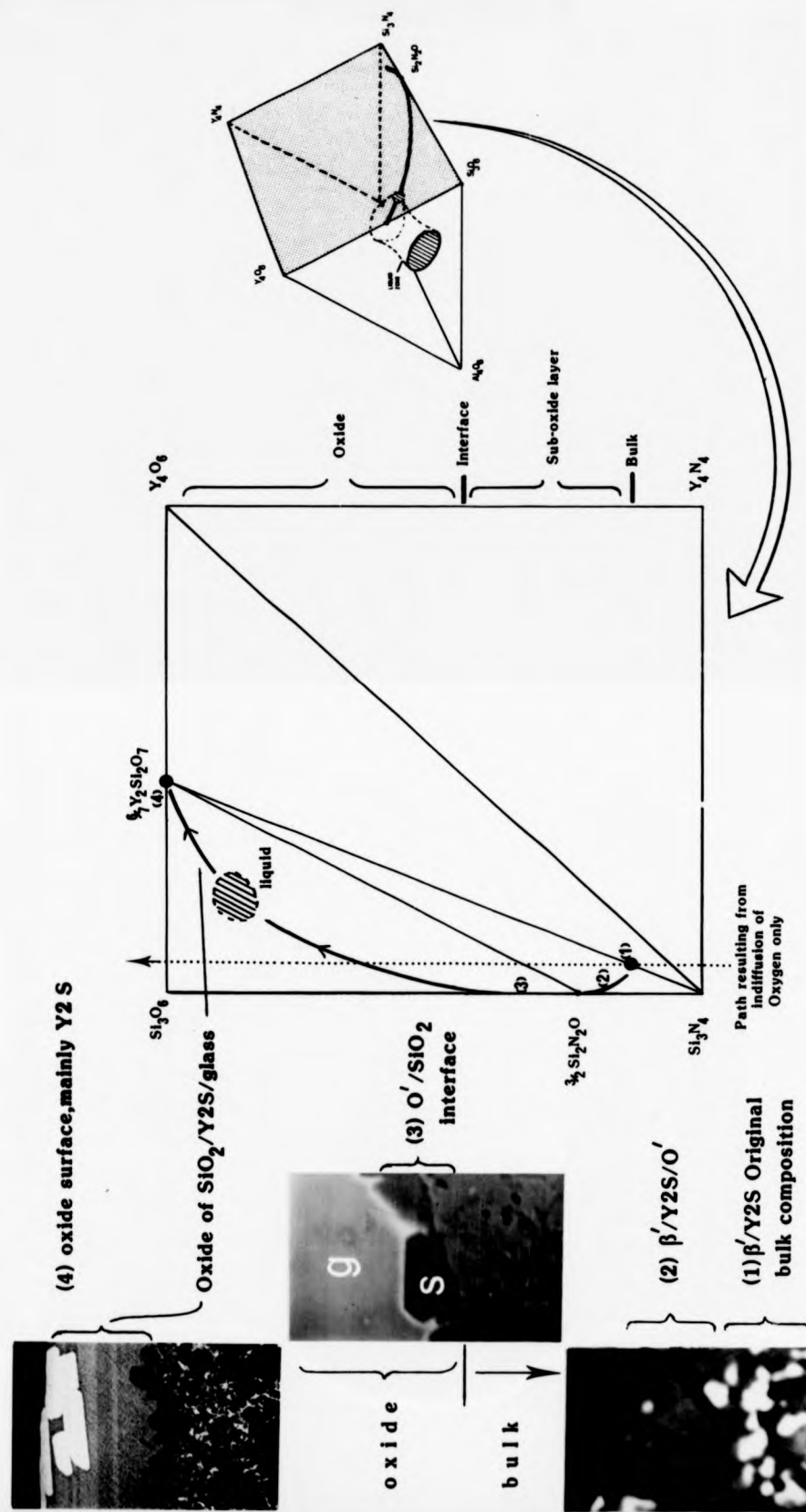


Figure 6.22 Schematic diagram of compositional change of β' Y2S bi-phase alloy when oxidised at 1350°C. Arrowed line represents the locus of compositions from the bulk (1) to the oxide surface (4), determined by sub-oxide microstructural analysis (micrographs).

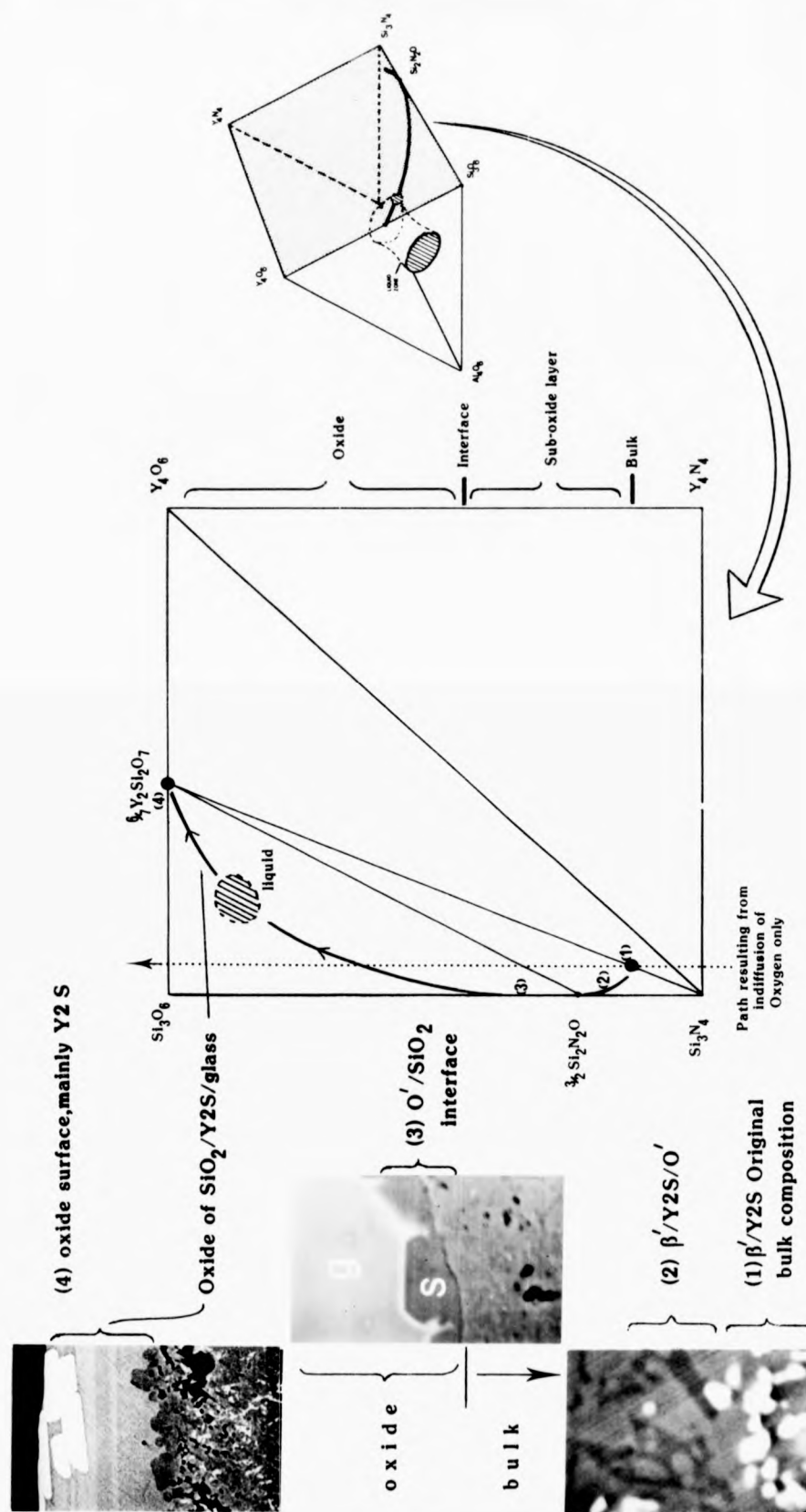


Figure 6.22 Schematic diagram of compositional change of β' Y₂S hi-phase alloy when oxidised at 1350°C. Arrowed line represents the locus of compositions from the bulk (1) to the oxide surface (4), determined by sub-oxide microstructural analysis (micrographs).

has been shown to occur here with the oxide Y-enriched and sub-oxide Y depleted. The locus of actual compositions from the bulk (1) to the oxide surface (4) can be plotted from the SEM microstructural observations across a polished section of material oxidised at 1350°C for 150 hours, (fig 6.22). Starting at the bulk interior (1), β' begins to form and increase its volume through the sub-oxide layer to the oxide. This is represented by the composition entering and moving across the $\text{Si}_2\text{N}_2\text{O}-\text{Si}_3\text{N}_4-\text{Y}_2\text{S}$ phase compatability triangle (2). A finite layer of SiO_2 is reached and the SiO_2/β' interface observed is then the region 3 on the binary tie-line. The oxide components are glass, SiO_2 and Y_2S which is represented by a pseudo-ternary phase field with the eutectic liquid region forming an end member. Close to the oxide surface, no SiO_2 is present and the composition is then on the binary liquid- Y_2S tie line and ends as just Y_2S on the oxide surface.

These observations give an accurate compositional locus (heavy arrowed line) and show this approach can be representative of the oxide and sub-oxide microstructural variations. This more detailed study supports the previous attempt in the $\text{MgO}-\text{Si}_3\text{N}_4-\text{SiO}_2$ system and suggests that this approach could be used to explain and predict the effect of oxidation on the sub-oxide and oxide for any composition, in any system. Indeed, if a similar approach is now taken with the $\beta' + \text{YAG}$ material, that a microstructural instability occurs becomes obvious.

The overall composition has to be plotted in the equivalence diagram prism (fig 5.4b) on a tie-line between β' and YAG. Assuming no Y, Al outdiffusion, then oxidation will take this composition in a direction perpendicular to and towards the oxide triangular face and through the liquid zone. The outdiffusion of Y and Al serve to steer the composition closer to the zone's centre and the lower

eutectic temperature glass compositions which accelerate reaction rates.

The choice of a desirable secondary phase for any system could be made at the phase diagram stage using this approach and the translation, during oxidation, across the field of a third phase (which may be liquid or have deleterious physical properties) can be avoided. In general, for oxidation, the most desirable would be a binary compound closest to SiO_2 in the SiO_2 - metal oxide system. Only at the higher binary eutectic temperature would the phase then react with SiO_2 .

6.8 CONCLUSIONS

- 1) The mechanism responsible for catastrophic oxidation and strength degradation in YAG matrix materials above 1300°C is a YAG - SiO_2 reaction which produces a ternary eutectic liquid. In choosing a matrix phase, its compatibility with SiO_2 must be considered. Compounds closest to SiO_2 in any metal oxide - SiO_2 system are desirable as reactions will not occur until their eutectic temperature is reached rather than occurring at the considerably lower temperature of the ternary eutectic.
- 2) Matrix crystallisation to $\alpha\text{-Y}_2\text{S}$ produces oxidation resistance with rates comparable to H.P.S.N., due primarily to the compatibility between $\alpha\text{-Y}_2\text{S}$ and SiO_2 . However, the material was mechanically weakened by an accompanying matrix porosity development.
- 3) At low temperatures (below 1300°C), the oxidation rate of β' -glass alloys is controlled by the rate of out-diffusion of Y ions from the g.b. to the oxide. There is microscopic evidence that oxidation occurs by solution of β' grains in an oxide glass made more reactive by an increasing Y concentration.
- 4) Oxidation of high N glass and YAG matrix alloys above 1300°C is severe. The rate controlling mechanism is oxygen access to the reaction front. Rapid oxidation is facilitated by a non-protective

oxide which is ruptured by oxide crystallisation and excessive straining from N_2 gas bubble generation at the oxide/bulk interface. Unlike that in α -Y₂S matrix materials, oxygen diffusion is then not via the solid-state.

5) In specimens annealed for long times, Al-substituted Si_2N_2O occurs as a matrix phase. Its crystallisation is primarily from the liquid state initiated by compositional changes in the matrix due to outdiffusion of Y, Al cations and enrichment with N and Si, components of dissolving β' grains in previously YAG matrix material. Partial oxidation of β' grains is also identified as a mechanism.

6) The as-crystallised YAG matrix morphology is unstable. The transformation (upon suitable annealing) to a more rounded and less semi-continuous morphology is driven by the reduction in surface energy anisotropy.

7) Microstructural examination allows the variation in composition throughout the oxide and sub-oxide to be presented in terms of a phase diagram. The out-diffusion of Y and indiffusion of O readily account for the observations. This representation allows the effects of oxidation on other systems to be predicted.

CHAPTER SEVEN

HIGH TEMPERATURE FRACTURE

The first part of this chapter presents the material parameter K_{IC} , for sintered and annealed alloys, over a wide temperature range. In the second half, slow crack growth (s.c.g), observed during K_{IC} testing at high temperatures ($> 1100^{\circ}\text{C}$) is quantified using K_I -V data. Crack propagation mechanisms are presented to explain the microstructural observations. The features limiting the high temperature stability to fracture for the present sintered alloys are presented.

7.1 ANALYSIS OF K_{IC} RESULTS7.1.1 Variation of K_{IC} Level with Microstructure

The critical stress intensity factor (K_{IC}) variations with temperature, for the end members of the β' + glass matrix alloy series (namely S0 and S13), are presented in Fig 7.1. Each point is the average of 2 or 3 fractures. The error bar indicates the degree of scatter. Above 1000°C , the measurement of an irregular s.c.g. zone length (explained later) gives an additional error in K_{IC} . Large scatter appears characteristic of the S.E.N.B. technique (see also 80) as the room temperature indentation method usually gives consistent results.

The susceptibility to oxidation-induced microstructural instabilities of these sintered alloys (detailed in Chapter 6) suggests a possible environmental effect on high temperature K_{IC} levels. A series of tests in air and vacuum were conducted (Fig 7.1). No marked

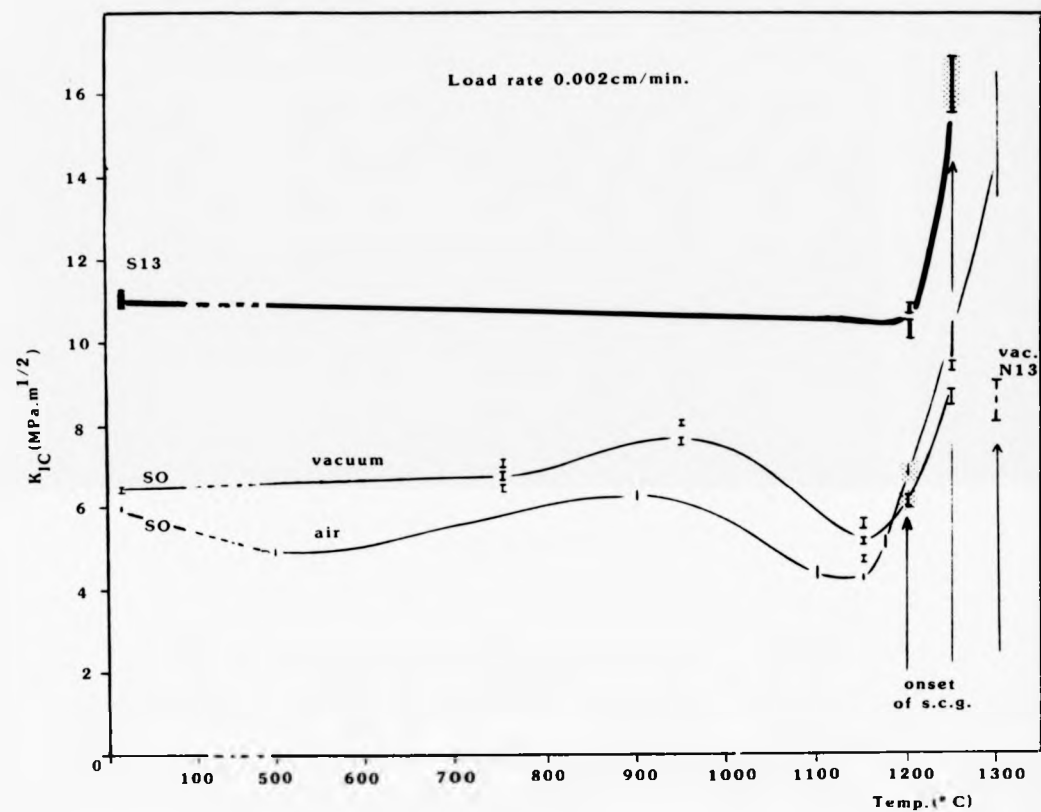


Figure 7.1. Critical Stress Intensity Factor (K_{IC}) Variation with Temperature in Air and Vacuum for Glass Matrix Alloys S0 and S13.

discrepancy was observed above 1150°C. This does not rule out an environmental influence on fracture but could indicate that any reaction is considerably slower than K_{IC} fracture event. Below 1100°C, the K_{IC} values for vacuum are consistently higher than for air although an explanation is not apparent.

The K_{IC} variation-with-temperature profile is similar in all the tests. Up to ~800°C, K_{IC} is fairly constant. There then follows a slight reduction before the sharp increase above ~1100°C. The gradual drop before 1100°C has also been reported for HPSN (80), PSSN (32) and also L.A.S glass ceramic (111) although no explanations were given. In the present materials it is believed due to the measured decrease in Young's Modulus which correlates over the same temperature range (Fig A4-3). The rapid K_{IC} increase approximately coincides with the appearance of a zone on the fracture surface having a rough morphology and low reflectivity (Fig 4.7a). A departure from linearity (before catastrophic failure) also occurs on the load/displacement trace (Fig 4.7b). These features identify this zone as a region of slow crack growth. Therefore, in calculating K_{IC} (equation 4.1), the true crack length is taken as the notch depth plus the s.c.g. zone length. The increase in K_{IC} above 1200°C is readily explained by s.c.g., which represents a mechanism for relieving the high stress concentration at the primary crack tip. The detailed s.c.g. observations and mechanisms are given in Section 7.4.1.

7.1.2 Dependency of K_{IC} on Microstructural Parameters - A Model

Comparison of K_{IC} values of alloys S0 and S13 for room temperature (5 and 10 MPa.m^{1/2}) and 1250°C (11 and 15 MPa.m^{1/2}) respectively) with other structural ceramics (Table 3.1) shows alloy S13 to represent a significant improvement. An S.E.M. microstructural study of fracture surfaces suggests an explanation for this

improvement. The essential features at room temperature and high temperature are similar for all glass matrix materials studied and therefore those of SO are presented. For room temperature and up to 1100°C, the fracture mode (from Fig 7.2a) is a mixture of transgranular (flat regions with characteristic brittle fracture features on large β' grains) and, more predominantly, intergranular (with a rougher morphology having many prismatic β' grains standing proud). However, above 1100°C, the fracture mode is virtually all transgranular (in both fast and slow crack growth zones) with an additional macroscopically rough morphology in the s.c.g. zone indicative of crack branching (Fig 7.2b).

The many hexagonal prismatic cavities and corresponding long β' prisms on the fracture surfaces (Fig 7.3a) indicates the predominance of a grain pull-out mechanism during crack growth. This mechanism explains the enhanced K_{IC} level for these sintered alloys, particularly at high temperatures as a similar mechanism is recognised as being responsible for the high K_{IC} of fibre composites (156). The factors most strongly influencing the K_{IC} level for this type of composite system may be highlighted by a model for an analogous material system (Glass Reinforced Plastic). A single fibre (radius r) is considered to fracture within the matrix and is pulled out by a force F , which is required to overcome the shear strength τ_i of the fibre-matrix interface (Fig 7.3b). It can be shown (156) that the work required to pull fibres as a function of crack size (c) is:-

$$W_T = \pi \tau_i \frac{L^2}{r} c^2 V \quad (7.1)$$

where V = area or volume fraction of fibres within the matrix orientated parallel to the applied load; L = length of fibres protruding from the fracture surface.

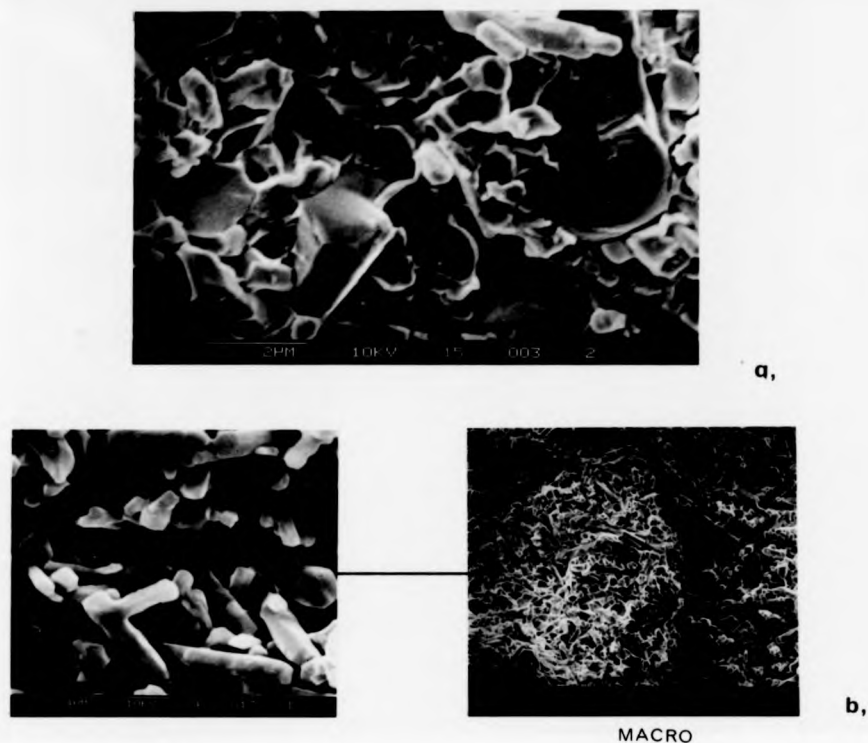


Figure 7.2 S.E.M. Micrographs of Fracture Surface of Glass Matrix Alloys at a) Room Temperature, b) Above 1100°C.

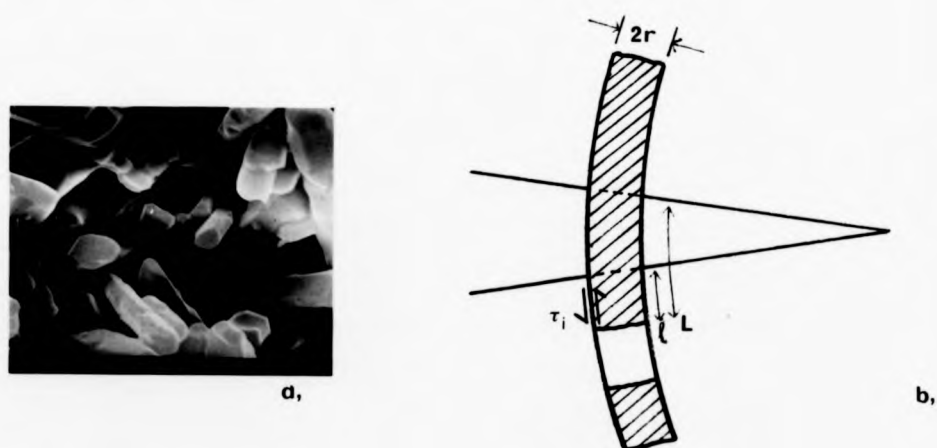
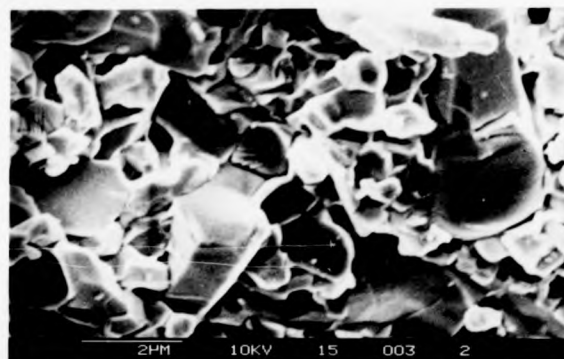
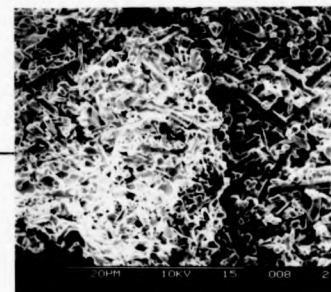
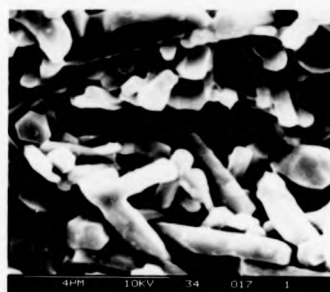


Figure 7.3 a) S.E.M. Micrograph of High Temperature Fracture Surface Showing Hexagonal Void after Prismatic Grain Pull-out.

b) Model of K_{IC} -Enhancing Grain Pull-out Mechanism.



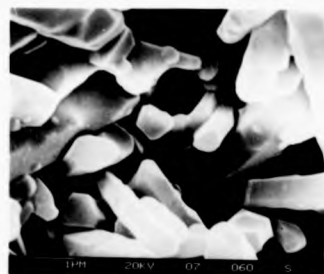
a,



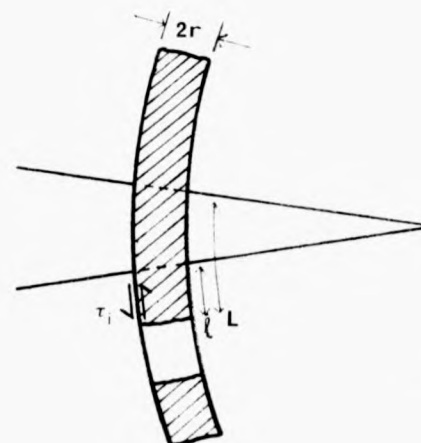
b,

MACRO

Figure 7.2 S.E.M. Micrographs of Fracture Surface of Glass Matrix Alloys at a) Room Temperature, b) Above 1100°C.



a,



b,

Figure 7.3 a) S.E.M. Micrograph of High Temperature Fracture Surface Showing Hexagonal Void after Prismatic Grain Pull-out.

b) Model of K_{IC} -Enhancing Grain Pull-out Mechanism.

By energy balance considerations, the critical strain energy release rate G_{IC} (which is related to K_{IC} by equation 3.8) is

$$G_{IC} = G_{IO} + V \tau_i \frac{L^2}{r} \quad (7.2)$$

If transposed to the present ceramics, the important parameters are indicated as the fibre (or β' grain) aspect ratio L/r , the volume fraction of fibres aligned parallel to the applied load and the fibre/matrix (β' /glass) interfacial bonding. In the H.P.Si-Al-O-N (not chemically dissimilar from S13), the glass matrix is minimal (only at triple g.b.s) and the β' grains are equiaxed. A grain pull-out mechanism is not therefore expected to dominate and transgranular fracture is indeed observed up to 1300°C. The highly fibrous nature of the present sintered materials is therefore considered the cause of their higher K_{IC} values. Grain pull-out and intergranular fracture can be seen to provide a more tortuous route from crack propagation and therefore an energy dissipative mechanism at the crack tip, which raises K_{IC} .

7.1.3 Variation in K_{IC} level Between Alloys

In glass matrix materials the higher K_{IC} level for S13 over S0, even at low temperatures, is accounted for by equation 7.2. The microstructural characterisation in Sections 5.3.1 and 5.3.2 showed a smaller average β' grain size for S13. The average β' radius (r) was also smaller, which also implies a larger grain density and, as grain orientation is random, a greater number of grains orientated parallel to the applied load. The shear stress, τ_i , is also expected to be higher for S13 as the high grain impingement identified for S13 in Fig 5.2 will provide enhanced mechanical contact and interlocking. Therefore parameters r , V and τ_i are all enhanced in S13 and satisfactorily explain the K_{IC} improvement over S0. Aspect ratio differences were not

included in this analysis as the bi or tri-modal grain size distributions are difficult to quantify.

The effects of glass matrix crystallisation on high temperature K_{IC} are contradictory (Fig 7.4). Matrix crystallisation to α -Y2S (SOC) enhances K_{IC} , but reduces it for YAG crystallisation (S13C). In a previous study (44) on a range of compositions of sintered Si-Al-O-Ns, at all temperatures (up to 1400°C), those with crystalline "YAG" matrices had lower K_{IC} values than their parent glass matrix alloys. The present results for S13 agree with this study and are explained by a loss of crack-tip plasticity via the viscous glass removal. Limited plasticity may still be conferred by the crystalline matrix (via dislocation motion) and also a weak matrix/ β' interface. The only partial matrix crystallisation to "YAG" in S13C is most probably the reason for the higher K_{IC} levels over fully crystallised material (44). Although, for material SOC the incomplete Y2S matrix-crystallisation enables g.b. sliding and s.c.g. to occur, the increased K_{IC} level is unexpected. This difference in K_{IC} behaviour between SOC and S13C can be explained by their major discrepancy in crystallisation features, i.e the production of micro-cavities during Y2S crystallisation (section 5.4.1(b)). This cavity distribution could be beneficial for the K_{IC} levels as the stress intensity at the primary crack tip could be relieved by propagation of these crack-like cavities in the crack-tip near region. This primary crack arrest mechanism is detailed in Section 7.4.

In fully crystallised alloys differences in K_{IC} due to matrix crystal type alone are expected due to variations in β' /matrix cohesion and degree of plastic deformation in the matrix.

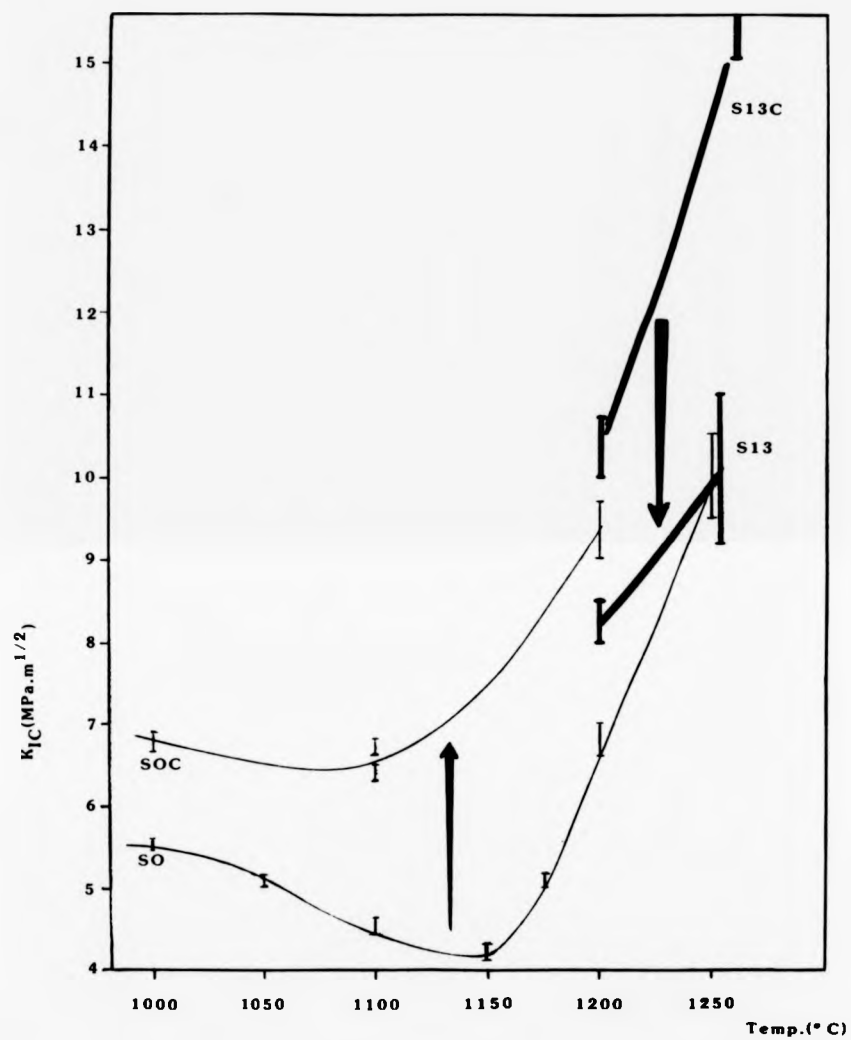


Figure 7.4 Critical Stress Intensity Factor Variation with Temperature for Alloys with Crystallized Matrices.

7.1.4 Slow Crack Growth During K_{IC} Determinations and its Threshold Temperature.

The s.c.g. zone length was found to increase with increasing temperature and also reduced cross-head speed. As the s.c.g. zone length is used in K_{IC} determination, K_{IC} tests were performed at a standardised 0.002 cm/min cross-head speed.

The susceptibility of these materials to s.c.g. can be quickly monitored (rather than via K-V experimentation) by observation of the temperature for the onset of s.c.g. This is defined here as the first appearance (optical) of a s.c.g. zone upon fracture at successive incremental temperatures (50°C). To amplify the s.c.g. zone a slower cross-head speed of 0.001 cm/min was used.

In the present glass and partially crystallised matrix alloys, s.c.g. readily occurs at 1300°C. The observed lack of s.c.g. up to 1500°C in vacuum in similar composition but fully crystalline YAG matrix alloys (157) is proof that s.c.g. is controlled by the viscous phase. It is now proposed that the viscosity/temperature relationship of the g.b. glass (rather than volume fraction) is the dominant influence on the s.c.g. threshold temperature and that in the present alloys, the variable N/O ratio can have a significant effect. Fig.7.5a is a plot of s.c.g. threshold temperature (in vacuum) for a number of alloys against the glass matrix Nitrogen level measured either directly (by E.E.L.S. in Section 5.3.3) or calculated indirectly from initial composition. It illustrates a correlation between threshold temperature and Nitrogen content. This can be explained by Nitrogen increasing the glass viscosity. Studies on bulk Y,Si,Al,O,N glasses (of compositions similar to the matrix glass here) indicate that changes solely in the N/O ratio (effectively 0 → 10 at. % N addition) can modify the viscosity considerably (61). The softening temperature of these bulk glasses (viscosity taken as $\sim 10^4$ poise), with various N levels, can be extrapolated from the viscosity/

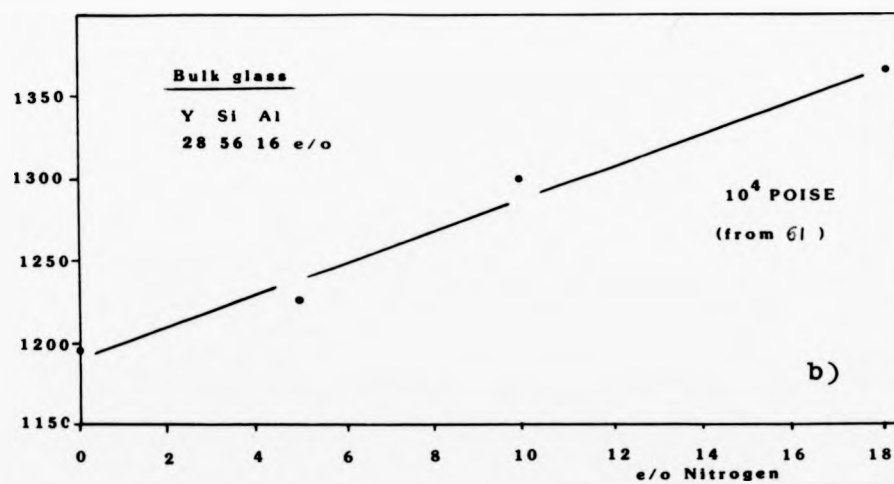
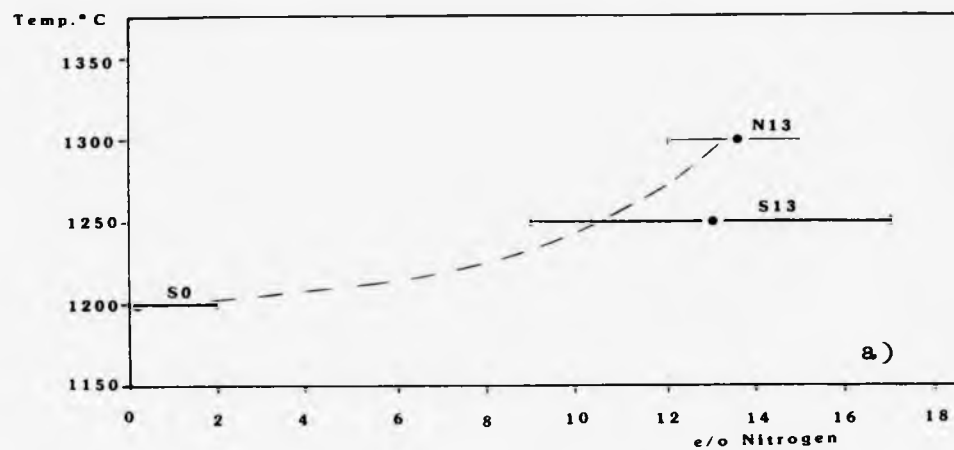


Figure 7.5 a) Plot of Threshold Temperature for s.c.g. (in vacuum) Against Nitrogen Level in the Glass Matrix of a Range of Alloys (61).

b) Plot of Softening Temperatures of Bulk Glasses with Various Nitrogen Levels.

temperature profiles. When plotted (Fig.7.5b) a close correlation with the threshold temperature/N level relationship is found. It is therefore concluded that glass matrix softening ($\sim 10^4$ poise) initiates g.b. sliding and s.c.g. and that the N/O variability in the present alloys allows the threshold temperature for s.c.g. to be increased by $\sim 200^\circ\text{C}$ to 1300°C . The increase in viscosity of Y-Si-Al-O-N glasses with nitrogen is believed due to N^{3-} substitution for O^{2-} in the glass network, which produces more crosslinking and a tightening up of the network (158).

Surprisingly threshold temperatures for S0C and S13C were identical to their parent glass matrix materials. This must be due to only partial matrix crystallisation and indicates 2 important points: (1) although the glass volume is substantially reduced upon crystallisation, even very fine residuals dominate the fracture phenomenon, (2) crystallisation does not significantly alter the residual glass composition in such a way to modify its viscosity.

Unless matrix crystallisation can be taken to completion, it offers few benefits over its glass matrix parent in terms of stability to s.c.g. at high temperatures.

7.2 ANALYSIS OF K_{I} -V RESULTS

The large material consumption for the Double Torsion technique restricted comprehensive testing to two alloys, S0 and S13. Data was collected at 1200°C , 1250°C and 1300°C as the K_{IC} work in section 7.1.4 indicated substantial s.c.g. here. Also most s.c.g. data on Si_3N_4 is reported for these temperatures, allowing comparison to be made.

The crack velocity (V)-stress intensity (K_{I}) data is presented in Fig.7.6. At 1200°C , the features for S0 and S13 were similar and the data showed reasonable continuity, considering the range of techniques used in its collection, giving straight line logarithmic

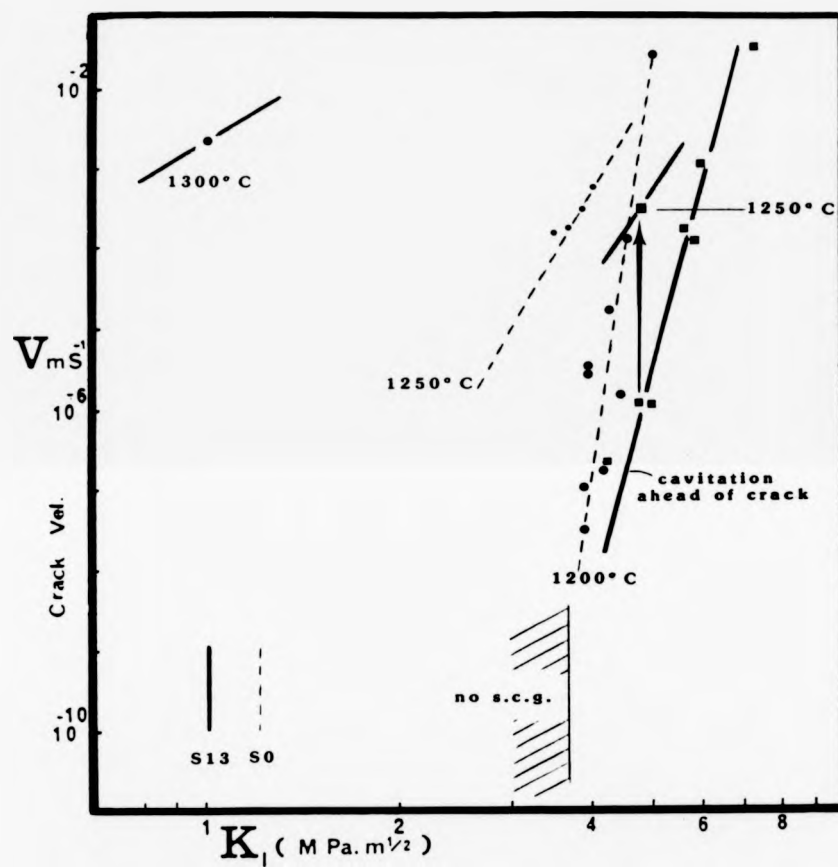


Figure 7.6 Crack Velocity (V) - Stress Intensity Factor (K_I) Relationship for Alloys S0 and S13 at Various Temperatures

plots. Data at 1300°C were erratic, varying considerably with technique for both materials. The problem arose from the gross plasticity dictated by the very fluid matrix at this temperature. The major assumption used in D.T. and compliance techniques is that compliance change is due solely to crack growth. Plasticity is so extensive that creep in an enhanced process zone occurs and growth of cracks other than the primary may occur (Section 7.4.). These large data scatter and data anomalies at 1300°C have been recorded for early HPSN (159) material having extensive triple-junction glass and the validity of all relaxation D.T. data at 1300°C published for all such HPSN (NC132) has been questioned. Trials at 1250°C were therefore briefly conducted on SO but although improved over 1300°C, data still showed considerable spread. These 1250°C and 1300°C data cannot therefore be satisfactorily used in determining s.c.g. parameters or the activation energies, Q , although they give important qualitative information.

Fig 7.6 demonstrates that at 1200°C materials SO and S13 exhibit different characteristics. The stress intensity exponent (n) from equation 3.10 for SO and S13 is 46 ± 3 and 28 ± 2 respectively and the constant $\log A$ is -34 and -25 respectively. Replotting K_I/K_{IC} (Fig 7.7) allows a more representative comparison, as in Fig 7.6 the maximum K_I for the various materials is set by its K_{IC} level. The temperature effect on ' n ' for SO and S13 is shown schematically. This effect is quantitatively demonstrated by measuring crack growth rate under the same constant load at 1200°C and 1250°C (Fig 7.6) where the rate increased from 1.0×10^{-6} to 3.5×10^{-4} m/sec. This behaviour illustrates the shortened time-to-failure with increasing temperature and the importance of raising the s.c.g. threshold temperature.

The larger n value for SO than S13 is contrary to the lower n predicted by its lower s.c.g. threshold temperature. An explanation is, as for K_{IC} , an effective s.c.g. reduction or arrest (crack

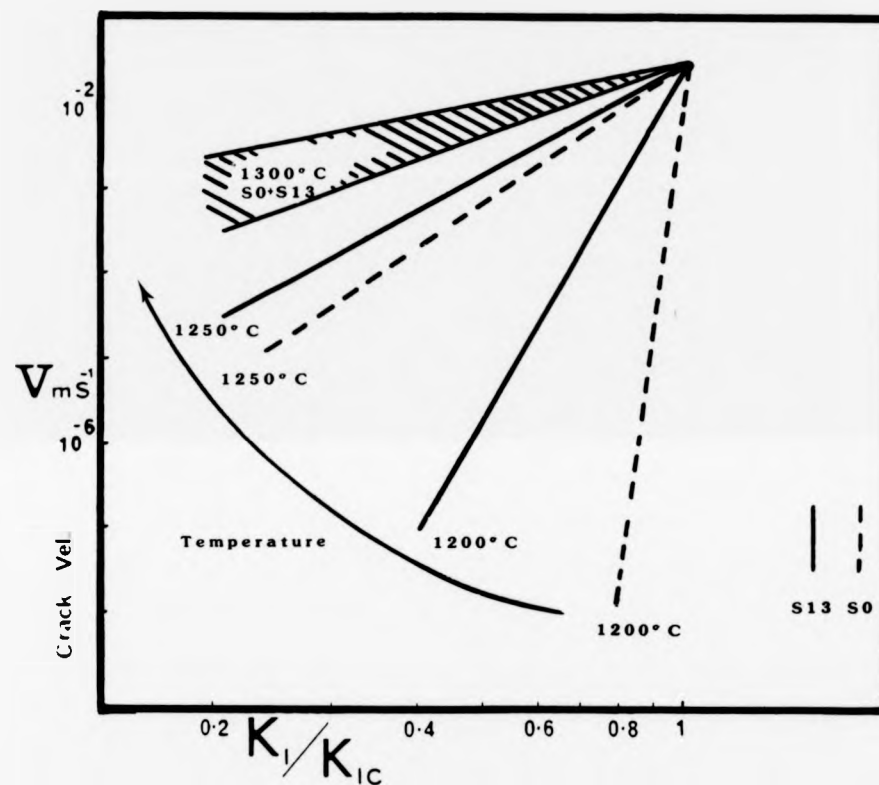


Figure 7.7

Plot of K_I/K_{IC} against crack velocity (V) for materials S0 and S13 at 1200°, 1250° and 1300° C.

blunting) via the more extensive creep and process zone cavitation.

A comparison of K_{I-V} data for material S0 and S13 with published data for other Si_3N_4 -based materials (all at $1200^\circ C$) shows them to be similar and in cases superior in terms of "n" values and crack growth threshold stress (fig 7.8). This is significant as the others are Hot-Pressed materials with their considerably reduced glass phase volume.

7.3 MICROSTRUCTURAL ANALYSIS OF SLOW CRACK GROWTH MECHANISMS

Although fracture surface examination is more common and provides useful information, the more difficult technique of fracture-interruption and S.E.M. examination parallel to the fracture face elucidated the crack growth mechanisms. Both K_{IC} and K_{I-V} testing at $1200^\circ C$ and $1300^\circ C$ were interrupted, for the range of alloys.

The microstructural s.c.g. features were identical for S0 and S13. At $1200^\circ C$, for high K_I values ($> 0.7 K_I/K_{IC}$), a single crack front tended to grow around β' grains (Fig 7.9a), where subsequent grain pull-out occurred leaving the parted surfaces with β' grains standing proud, (Fig 7.9b). Crack tip examination (Fig 7.10a) showed the s.c.g. mechanism to be one of nucleation of many individual cavities ahead of the crack tip (in a process zone), and cavity linkage. The most intensive cavity nucleation was not generally coplanar with the primary crack and consequently the crack path was irregular. Cavities can coalesce and then merge with the primary crack. Crack arrest (Fig 7.10c) and regrowth from nucleated cavities behind the original crack tip was also observed. At lower K_I ($< 0.5 K_{IC}$), the process zone size increased and the fracture path was even more irregular.

An increased process zone was produced by raising the temperature to $1300^\circ C$. This led to increased cavitation and also multiple crack branching (Fig 7.11a). Many cracks were nucleated and ran parallel to the primary crack and were either arrested, merged or became the

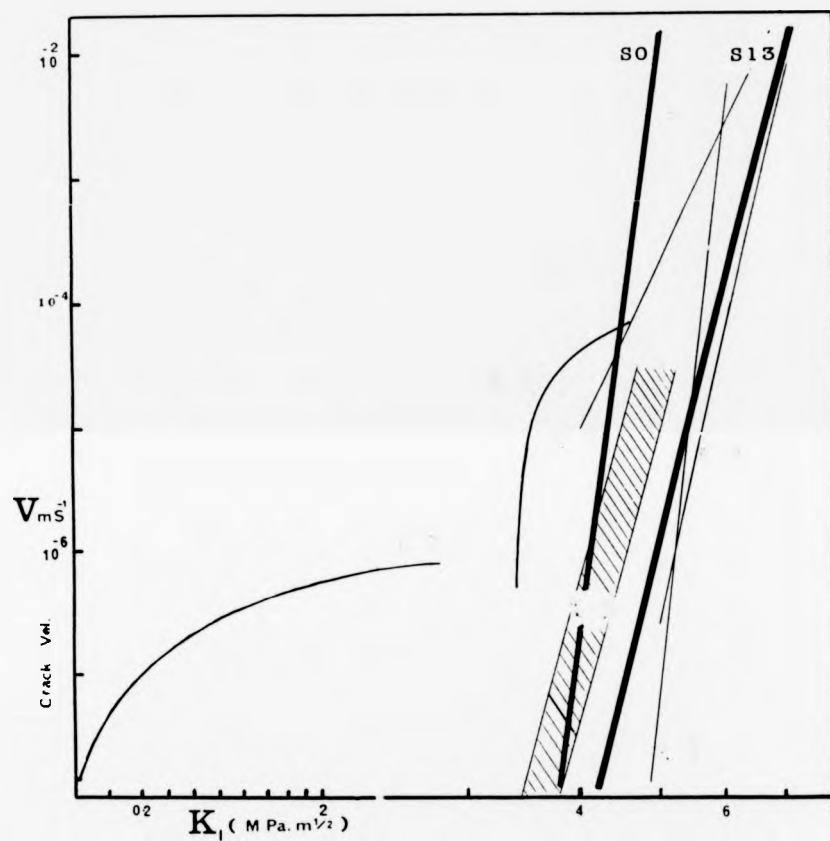


Figure 7.8

Comparison of SO and S13 K_I -V data with other published data for Si_3N_4 -based materials at 1200°C in air.

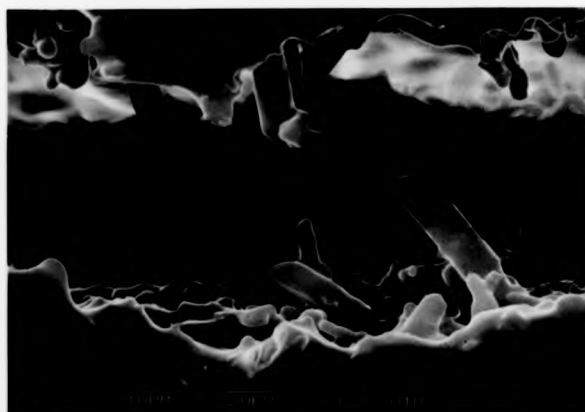
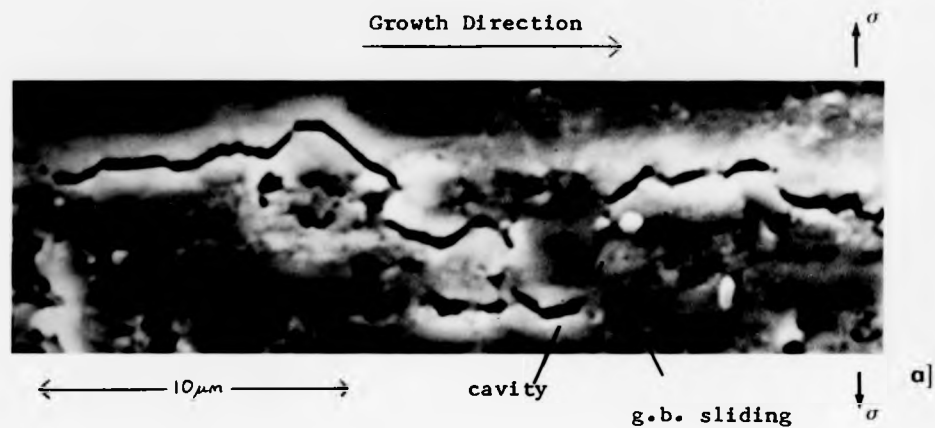


Figure 7.9

S.E.M. sections across crack path at 1200°C for high K_{I} value.

a) Near crack tip showing cavity formation.

b) View inside well-opened crack with β' grains standing proud.

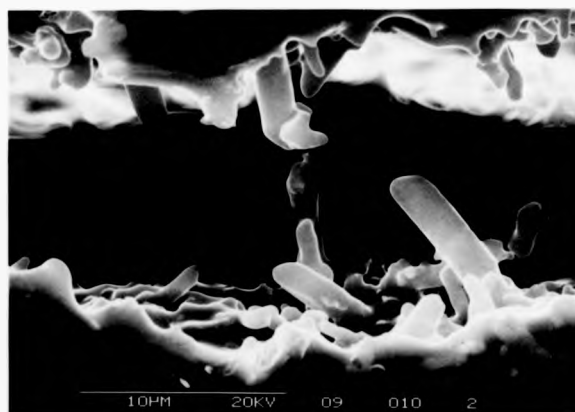
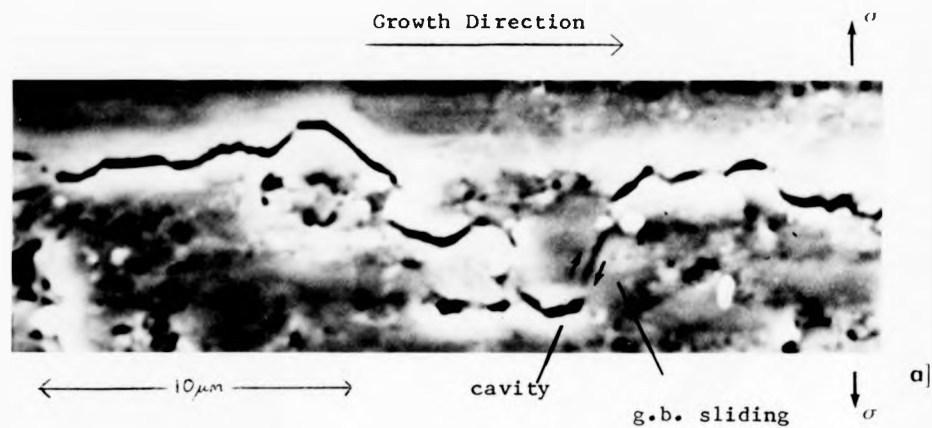


Figure 7.9

S.E.M. sections across crack path at $1200^{\circ}C$ for high K_I value.

a) Near crack tip showing cavity formation.

b) View inside well-opened crack with β' grains standing proud.

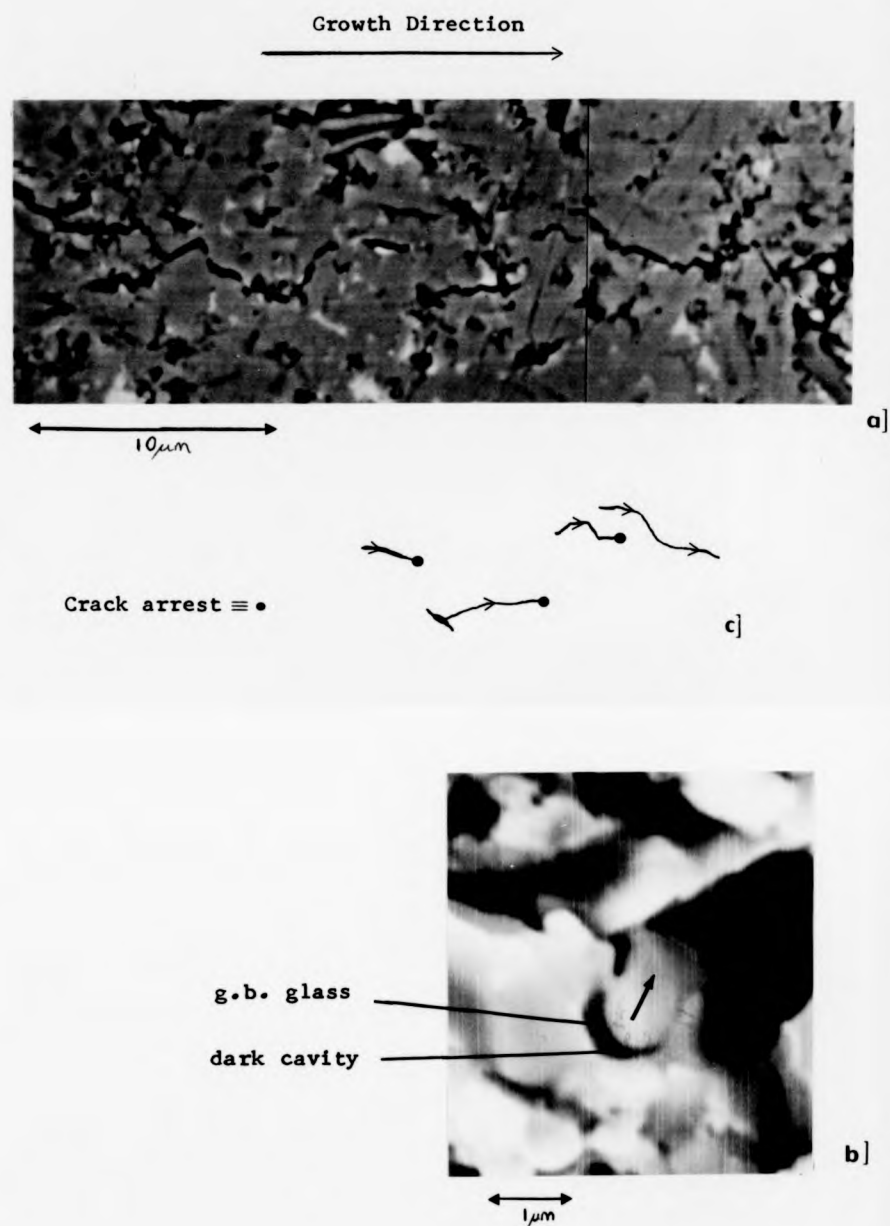


Figure 7.10

- a) S.E.M. section across crack tip of material SO at 1200° C at high K_I levels. Extensive cavity nucleation and linkage is observed.
- b) High mag. S.E.M. of crack tip showing cavity nucleation in glassy phase due to partial grain pull-out.
- c) Crack arrest and regrowth.

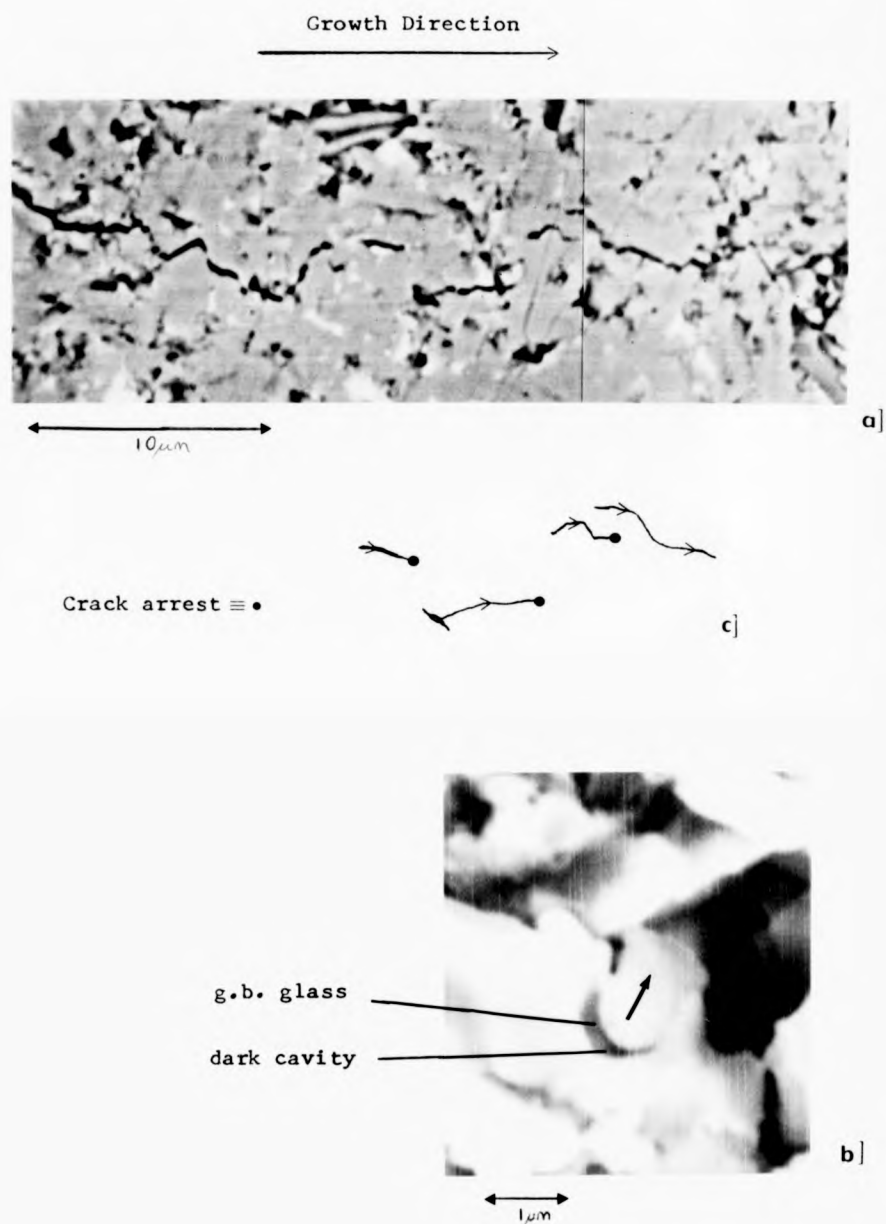
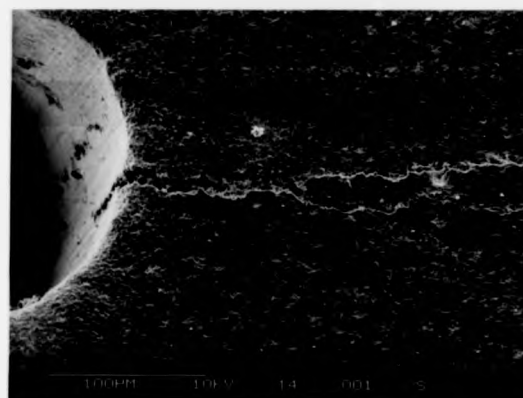


Figure 7.10

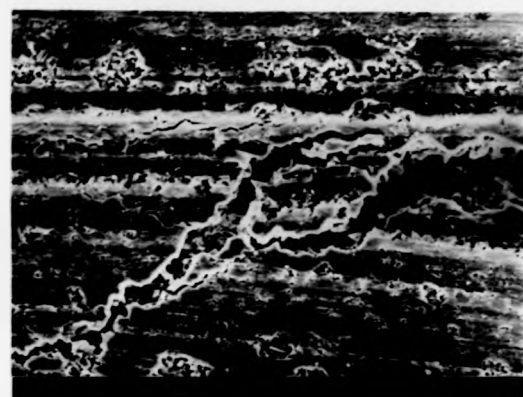
- a) S.E.M. section across crack tip of material SO at 1200° C at high K_I levels. Extensive cavity nucleation and linkage is observed.
- b) High mag. S.E.M. of crack tip showing cavity nucleation in glassy phase due to partial grain pull-out.
- c) Crack arrest and regrowth.

Growth Direction →

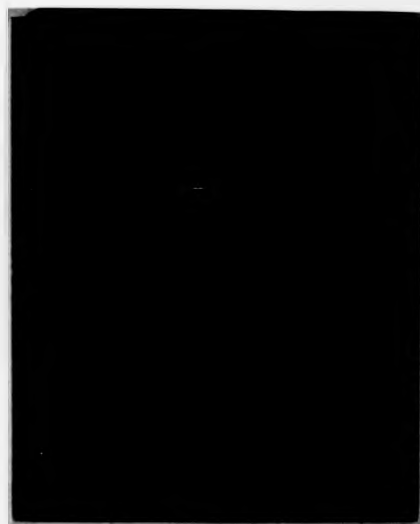
notch



a]



b]



c]



d]

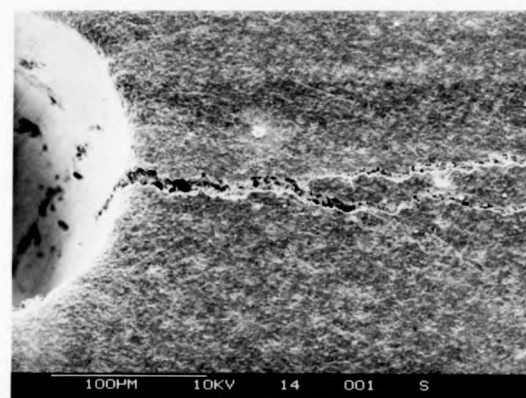
Figure 7.11

Material S0 at 1300° C.

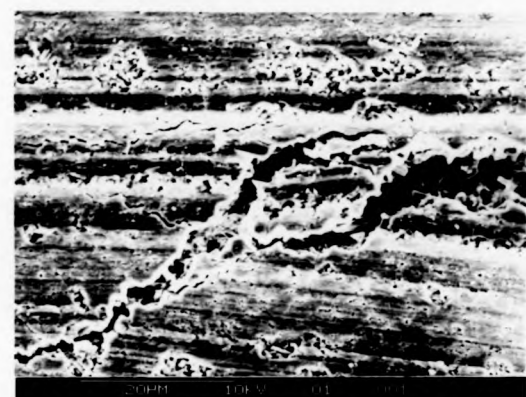
- a) S.E.M. micrograph of notch tip showing crack branching.
- b) S.E.M. micrograph showing extensive multiple crack growth.
- c) Light zone (representing creep) extending from notch on the tensile side which corresponds to the reduced section groove of the specimen's other side (d).

Growth Direction →

notch



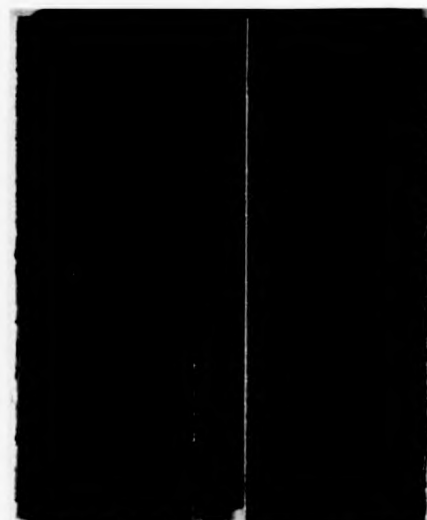
a]



b]



c]



d]

Figure 7.11

Material SO at 1300° C.

- a) S.E.M. micrograph of notch tip showing crack branching.
- b) S.E.M. micrograph showing extensive multiple crack growth.
- c) Light zone (representing creep) extending from notch on the tensile side which corresponds to the reduced section groove of the specimen's other side (d).

primary crack (Fig 7.11b). These features illustrate the increasing loss of g.b. cohesion and a creep mechanism whose extent is illustrated by a wide band, the length of the K_I -V specimen (Fig 7.11c), which represents the creep zone.

In alloys SOC and S13C, with crystalline matrices, intergranular fracture still occurred although at 1300°C, instead of severe crack branching, a single primary crack grew with a characteristic "square-wave"-like shape (Fig 7.12a). The short range growth steps were more linear than for SO and were always perpendicular to the applied load.

Examination of the crack tip shows cavitation still occurring in the very small triple junction glass which is residual to the matrix crystallisation. Grain boundary sliding and cavitation is still concluded to be the growth mechanism, supported by the similar mechanism in Hot-Pressed materials which now have similar volumes of glass. The linear portion of the "square-wave" crack path is thought due to the reduced material plasticity accompanying matrix crystallisation. The stress is then more highly concentrated with cavitation tending to occur only directly in front of the crack rather than in a process zone. The crack path discontinuities are most probably due to spacial variations in the degree of matrix crystallisation, noted in Chapter 5. On entering a region of near-complete matrix crystallinity, viscous phase cavitation will not occur. The subsequent stress build-up at the arrested crack tip will then induce cavitation at a favourable glass junction in the vicinity, whereby the crack will initiate and regrow.

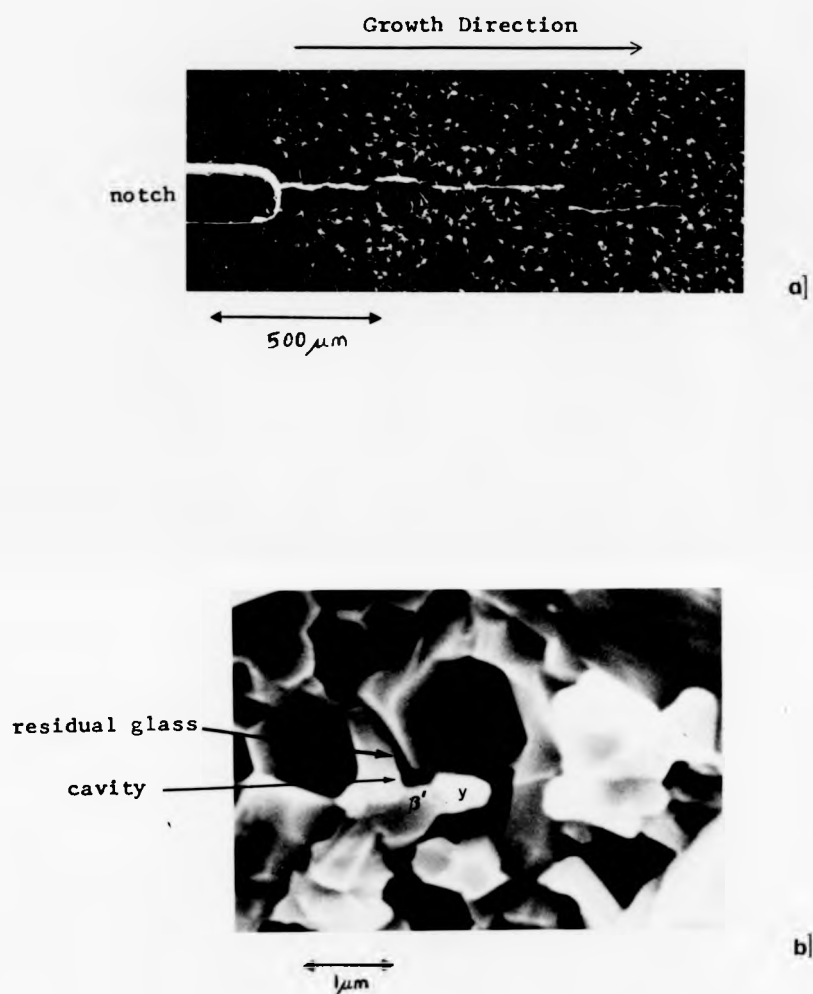


Figure 7.12

- a) S.E.M. of section across crack path of alloy SOC at 1300°C showing "square wave"-like shape.
- b) High mag. S.E.M. micrograph of crack tip region in S13C at 1300°C showing cavity formation in glassy region residual to matrix crystallisation to YAG (Y).

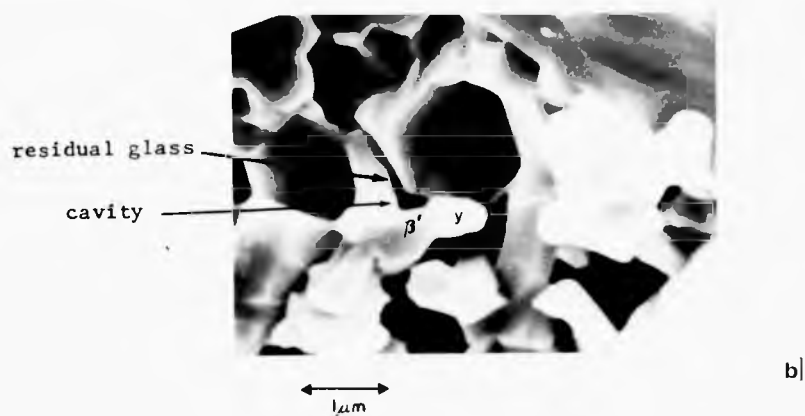
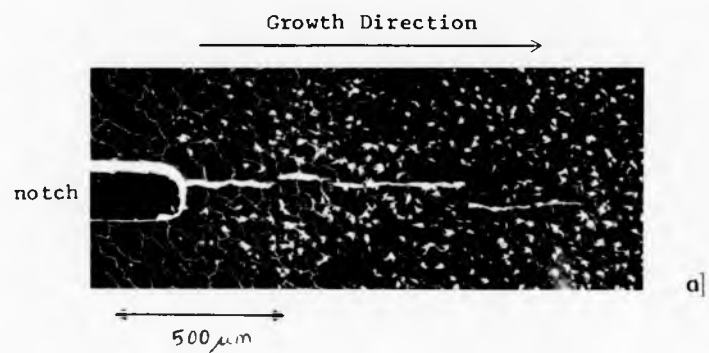


Figure 7.12

- a) S.E.M. of section across crack path of alloy SOC at 1300°C showing "square wave"-like shape.
- b) High mag. S.E.M. micrograph of crack tip region in S13C at 1300°C showing cavity formation in glassy region residual to matrix crystallisation to YAG (Y).

7.4 DISCUSSION AND CONCLUSIONS

It has been shown that the level of K_{IC} can be enhanced by microstructural modifications that correlate with a fibre pull-out model (Eqn. 7.2). Based on this, further K_{IC} improvement could be possible in the Y-Si-Al-O-N system by optimisation of the following features. 1) Reducing grain size, which will increase substantially the g.b. area per unit volume. 2) Increasing β' aspect ratio, which allows for a more tortuous crack path and increased L value. 3) Increased interfacial shear strength. Here, an increased matrix nitrogen level would be expected to improve not only the glass' properties but may directly provide primary Si-N bonding at the interface. Too stronger bonding could be deleterious as fracture will then favour a transgranular mode.

An increased nitrogen level should aid then all these three features and also, therefore, the K_{IC} level. However, previous work has shown (145) there to be a limit to nitrogen solubility in these glasses of $\sim 18\%$, so further improvements in this respect may be limited. A reduction in the matrix's impurity levels should offer, however, similar levels of improvements.

The s.c.g. mechanisms and 'exponent' values at 1200°C are broadly similar to HPSN, which is well documented and understood and hence requires little comment here. What is significant is that the glassy phase is greatly increased in volume here, without any property detriment. The critical feature controlling high temperature s.c.g. is therefore concluded to be the glass' viscosity and its improvement (by compositional changes) rather than volume reduction (via H.I.P.ing, H.P.ing, low additive levels, etc.) will be most beneficial. Further improvements require the complete elimination of glass by matrix crystallisation. The present work identifies the requirement

for tight control over impurity types and levels. Further, crystal type requires consideration for suitability in various environments, highlighted by the YAG-oxide instability, which is considered in Chapter 9.

The conclusions of this work are therefore :

- 1) Within the present range of sintered Y-Si-Al-O-Ns a level of $8 \text{ MPa}\cdot\text{m}^{-3/2}$ for room temperature K_{IC} has been obtained which is higher than previous Si-Al-O-Ns (hot-pressed or sintered) and most Si_3N_4 -based material.
- 2) The K_{IC} level can be significantly enhanced by increasing the 21R additive content. The improvement is readily explained by the large microstructural differences.
- 3) Slow crack growth occurs during K_{IC} determinations above $\sim 1150^\circ\text{C}$ by a mechanism of grain boundary sliding, cavitation, and cavity linkage. S.C.G. effectively increases the K_{IC} level at these temperatures.
- 4) The onset temperature for s.c.g. in glass-matrix alloys is controlled by the glass' softening temperature. An increased glass nitrogen content is found to increase the onset temperature by 150°C , explained by the nitrogen tightening up the glass network structure.
- 5) The attainment of the potential 1500°C s.c.g. threshold temperature upon annealing is critically dependent on complete matrix crystallisation and therefore upon initial impurity levels.
- 6) K_I -V data taken at 1200°C show a variation for glass-matrix materials. The difference is most readily explained by variations in crack growth mechanisms rather than microstructural differences.

- 7) At low K_I levels the s.c.g. in low 21R glass matrix alloys is not by the usual single crack extension but the linkage of independent microcracks formed in a large process zone. The crack branching, blunting and deviation observed are plastic components which give an effective threshold K_I for s.c.g.
- 8) Matrix crystallisation does not alter the s.c.g. mechanism or s.c.g. resistance unless it can be taken to completion.

CHAPTER EIGHT

LASER INDUCED STRUCTURAL DAMAGE

In this chapter, the microstructural stability of the high-Nitrogen bi-phase materials at ultra high temperatures (facilitated by laser irradiation) is studied. Comparison is made with single-phase β' materials, also irradiated. The potential for laser machining of Si-Al-O-N ceramics is explored.

8.1 INTRODUCTION

A novel way of assessing the ultra-high temperature stability of the present ceramics is to subject them to laser irradiation. The rapid heating and cooling may "freeze" high temperature reactions and lead to a better understanding of dominant mechanisms. In addition, a tolerance of high intensity laser irradiation is becoming an important property (as materials are being used as military armour and radomes) and HPSN has been found the most resistant (160) of the current structural ceramics. The microstructural damage mechanism however has not been investigated for these ceramics.

The material loss mechanism during laser irradiation has been developed to allow laser machining, where clean, accurate cutting is performed quickly and inexpensively on difficult materials such as glass (161), concrete, plastic (162) and ceramics. A new application for the present ceramics, that of fine jet nozzles, could result from laser machining. Current use of these nozzles is in high pressure (4.2 Kbars) water-jet cutting, where sapphire with nozzle diameters of

0.076 mm - 0.178 mm are used in conjunction with a water intensifier to produce a jet with a velocity of ~660 m/s. The fine drilling of these nozzles is restricted with conventional equipment to the diamond-tip erosion process, which limits the bore diameter and produces many critical flaws. Laser piercing has been successfully applied (163) to diamond and alumina where the advantages of fine drilling and a material removal mechanism via total evaporation are utilised.

The dominance of β' - Si_3N_4 crystal dissociation in preference to melting and excellent mechanical properties (including thermal shock resistance) suggest that the present Si-Al-O-N ceramics would be suitable for laser machining and the nozzle role. The presence of the g.b. matrix phase (which will be subject to melting/resolidification) is expected to complicate the erosion mechanism. To determine the contribution of the residual phase on the overall performance, nominally single phase Si-Al-O-N materials were also studied.

8.2 MATERIALS AND EXPERIMENTATION

The two-phase materials were a fully crystallised, morphologically stabilised β' + YAG ceramic and its β' + glass pre-anneal parent, described in Chapter 9 and Chapter 5 respectively. A range of nominally single phase hot-pressed Si-Al-O-Ns were also used. Their microstructures consist essentially of equiaxed β' grains ($\sim 1 \mu\text{m}$) with impurity elements segregated along grain boundaries in one material and an Mg, Mn containing phase just detectable at triple grain junctions in the other (127). In addition, sections of the above materials were heat-treated in air at 1430°C for 1000 h to reduce the grain-boundary impurity level (47) via an oxidative extraction mechanism. This last material represents an almost "pure" β' Si-Al-O-N and its behaviour during laser irradiation can also represent the β' contribution in a two-phase material's behaviour.

Small slabs (1 cm x 1 cm) of various thickness (3-10 mm) were drilled using an industrial Nd-YAG laser welding machine (performed by J K Laser Ltd., Rugby, England) for a range of pulse energies (1-10 joules), number of pulses (1-1000) and pulse length (70-30 μ secs).

The drilled specimens were examined in SEM in their as-pulsed condition (Fig 8.1a) and also in a longitudinal fractured state (Fig 8.1b). Electron transparent sections of the bore surface zone proved difficult to obtain using conventional methods of ion-beam thinning of a 100 μ m section containing a circular cross-section of the pulsed hole. The difficulty arose from the layer's relative softness (which allows preferred erosion) and, especially with the hot-pressed materials, the limited thickness (~ 1 μ m) of this layer. The problem was overcome using the technique outlined in fig 8.2. A 0.2 mm thick section was obtained using a high-speed diamond annular saw from a region containing the bore surface. This section was ground from the bulk material side to ~ 150 μ m thickness on silicon carbide papers prior to ion beam thinning, again from the bulk side only. This method ensures an undamaged reconstituted surface layer critical for fine surface microstructural analysis. Remarkably, electron transparent sections of a 1 μ m thick zone and also overlying surface debris could be obtained with sufficient care. In an effort to confirm the crystalline phases present, the reconstituted layer was ground off, crushed and analysed with a Phillips X-ray Diffraction Camera.

8.3 MICROSTRUCTURE OF THE RECONSTITUTED SURFACE LAYER

8.3.1 Two-Phase Ceramics

The macroscopic features of the pulsed hole surface in both two-phase single-pulsed materials are illustrated via SEM in Fig 8.1a, b. They consist of a heavily crazed surface glaze covered with

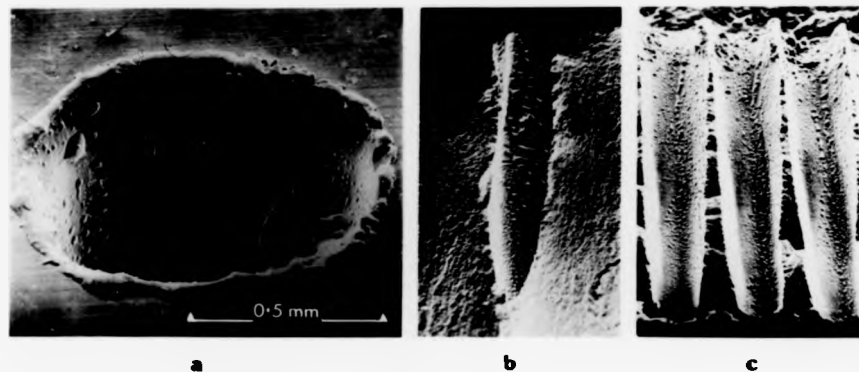


Fig 8.1 Macroscopic view of laser pulsed holes in SEM (a) Hole entrance of 2-phase material, with debris, globules and layer crazing evident. (b) Longitudinal section of 2-phase material. (c) Longitudinal section of single phase, multiple pulsed material.

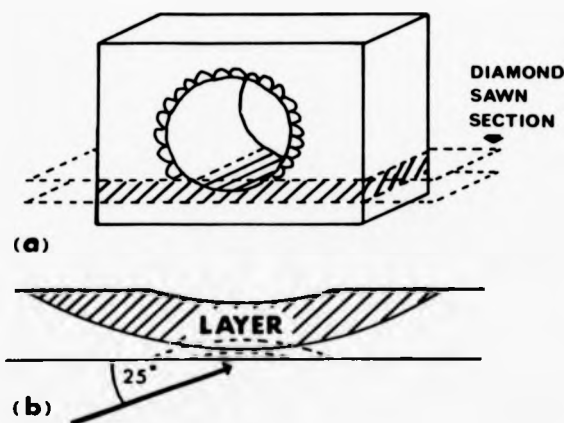


Fig 8.2 Schematic representation of technique used to produce electron transparent sections of the reconstituted layer lining the hole. (a) Sectioning, (b) subsequent ion-beam thinning from one side.

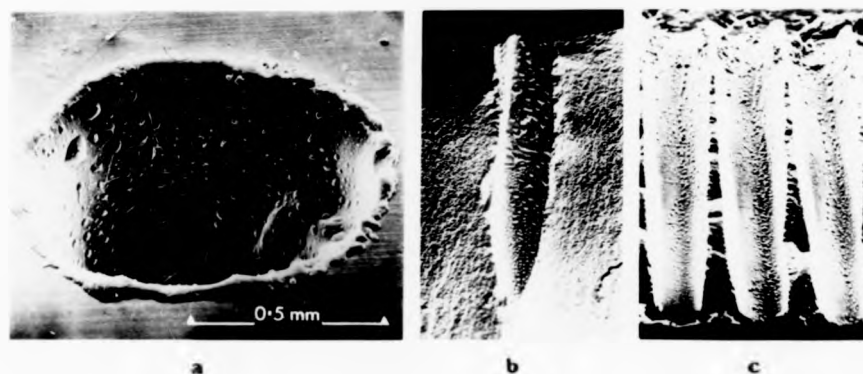


Fig 8.1 Macroscopic view of laser pulsed holes in SEM (a) Hole entrance of 2-phase material, with debris, globules and layer crazing evident. (b) Longitudinal section of 2-phase material. (c) Longitudinal section of single phase, multiple pulsed material.

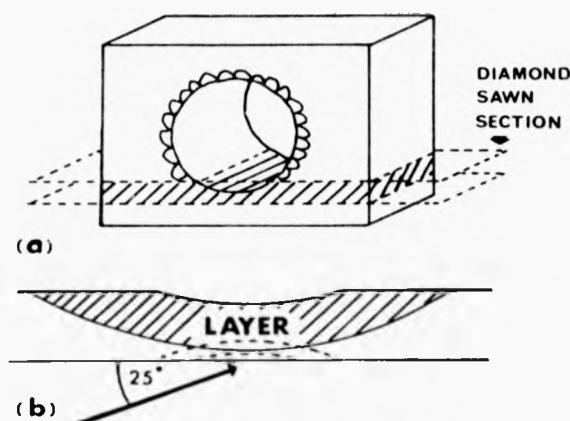


Fig 8.2 Schematic representation of technique used to produce electron transparent sections of the reconstituted layer lining the hole. (a) Sectioning, (b) subsequent ion-beam thinning from one side.

globules, together with additional debris at the hole entrance. The craze pattern is typical of that due to tensile stresses. These will develop during cooling (due to thermal shock and also differences in expansion coefficients) to a level above the glaze's tensile strength. The cracks are not associated with the fine microstructural features in the reconstituted layer and thus the critical expansion coefficient difference is between the layer and the underlying β' /matrix. Imaging in a back-scattered electron mode reveals the globule's internal dendritic structure and also the underlying multi-crystallinity of the reconstituted layer (Fig 8.3a). When viewed in section (longitudinal fractured) as in Fig 8.3b and again imaged via b.s.e., the layer thickness ($\sim 2 \mu\text{m}$) and its recent history can be readily established. The observation of the meniscus-like formation (arrowed) of the layer when in contact with the periphery of the globule indicates that the layer solidifies directly from a liquid layer. It is likely that the globule and layer come into contact whilst both are molten, the globule's shape and wetting characteristics verifying its previously liquid form. The atomic number contrast in Fig 8.3b shows the layer's large concentration of heavy elements which have rapidly increased in volume fraction on traversing into the layer from the bulk.

The finer microstructural detail of the above features was determined using the TEM. Fig 8.4a illustrates a typical region of the reconstituted layer. The matrix is essentially a Y, Al-rich silicate glass, this being ascertained from E.D.A.X. (Fig 8.4d) and its lack of diffraction contrast. Within the matrix there is a fine dispersion of crystallites including spherical regions with polycrystalline internal structures (marked S in Fig 8.4a). These features imply an initial liquid phase separation and subsequent recrystallisation process. The polycrystalline is tentatively identified via selected

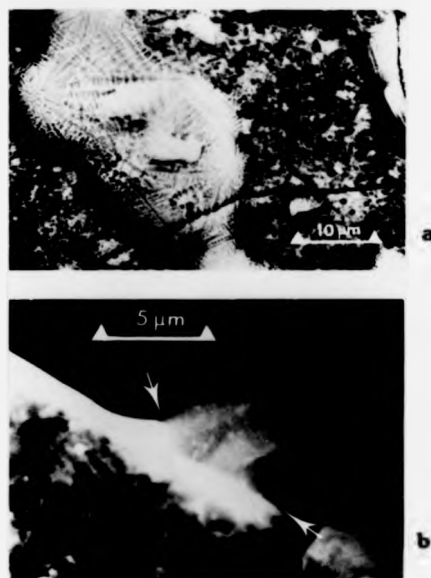


Fig 8.3

SEM Micrographs of the reconstituted layer in 2-phase materials. (a) Backscattered electron image of globule (with interdendritic structure) overlaying a polycrystalline layer. (b) Section of globule, layer (light region) and bulk. Arrows indicate the globule/layer interface and the meniscus effect feature.

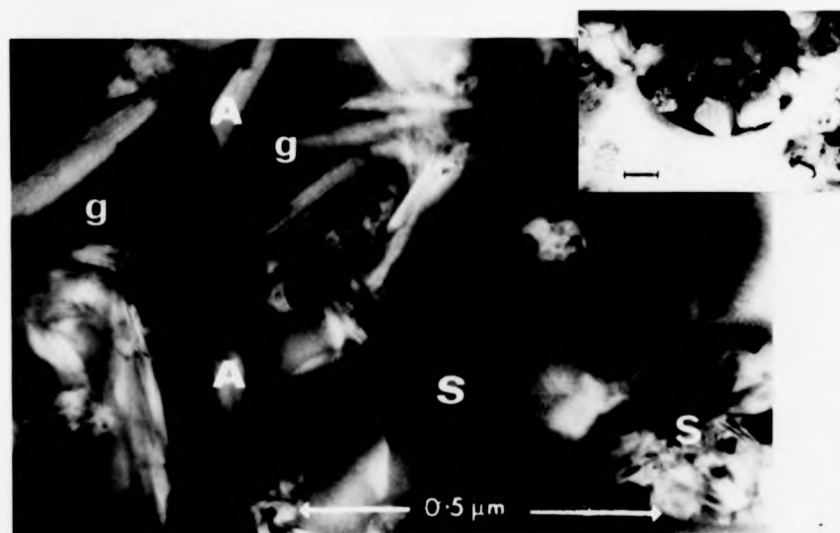
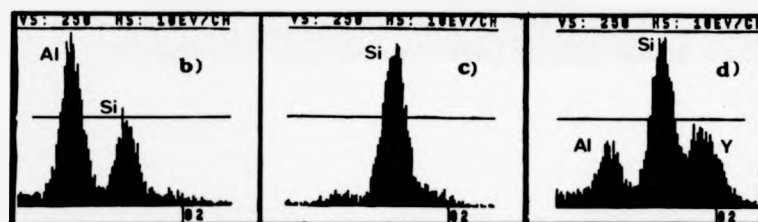


Fig 8.4 TEM micrograph of the 2-phase reconstituted layer microstructure with EDAX spectra of the various features. In the centre, a multicrystalline silicate (S) can be seen to have its growth restricted by the flanking aluminosilicate laths (A). The matrix is glassy (g). Figs b, c, d correspond to the phases, A, S, g respectively. Insert: Multicrystalline silicate, bar=0.1 μm



Fig 8.3

SEM Micrographs of the reconstituted layer in 2-phase materials. (a) Backscattered electron image of globule (with interdendritic structure) overlaying a polycrystalline layer. (b) Section of globule, layer (light region) and bulk. Arrows indicate the globule/layer interface and the meniscus effect feature.

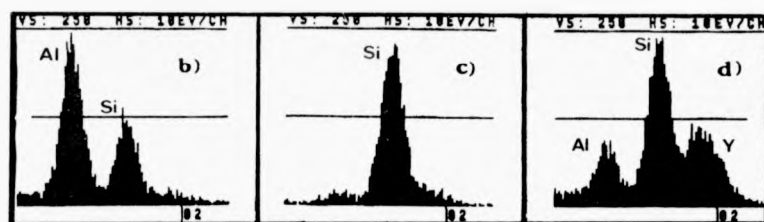


Fig 8.4 TEM micrograph of the 2-phase reconstituted layer microstructure with EDAX spectra of the various features. In the centre, a multicrystalline silicate (S) can be seen to have its growth restricted by the flanking aluminosilicate laths (A). The matrix is glassy (g). Figs b, c, d correspond to the phases, A, S, g respectively. Insert: Multicrystalline silicate, bar=0.1 μm

area diffraction (S.A.D) ring patterns and E.D.A.X. (Fig 8.4c) as an SiO_2 polymorph. This composition is consistent with its origin as a phase-separated globule as there exists a metastable immiscibility dome (between 16-65 wt.% Al_2O_3) in the SiO_2 - Al_2O_3 phase diagram (164). In some of these areas there appears an electron-absorbing, intergranular phase which account for the Al and Y peaks observed in the E.D.A.X. (Fig 8.4c). Also present within the reconstituted layer are fine heavily-faulted lath-like crystals. Their small size limits the use of S.A.D. but the qualitative E.D.A.X. (Figs 8.4b) suggests the alumino-silicate Mullite ($3\text{Al}_2\text{O}_3 \cdot 2\text{SiO}_2$). In studies (15) of the crystallisation of SiO_2 - Al_2O_3 melts rod-like crystals of mullite are found under moderate quenching rates. Mullite is also a product of the devitrification of the glassy oxide (similar composition to this layer's glass) of these materials (54). A T.E.M. study of the interface between the original and reconstituted material (Fig 8.5) reveals the absence of any abrupt microstructural features. Those β' grains closest to the reconstituted layer appear to be "dissolving" in the matrix and the layer is essentially the matrix enhanced in volume. A large area E.D.A.X. probe of the layer (taking in mullite, SiO_2 and glass) shows it to be chemically similar to the original matrix but with an increased silicon level.

The microstructural features of this layer are similar in the as-sintered (glass matrix) and heat-treated ("YAG" matrix) materials. Differences lie only in relative quantities of crystallites and the previously "YAG" matrix retains a higher volume fraction of glass matrix after irradiation.

The globules sitting on the reconstituted layer surface have a dendritic internal structure (Fig 8.6a) with the dendrite arms identified by S.A.D. (Fig 8.6b) and E.D.A.X. in the T.E.M. as twinned

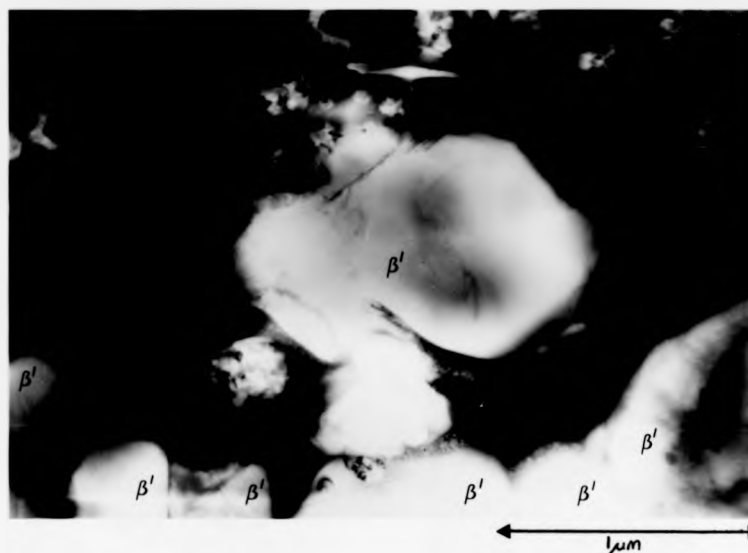
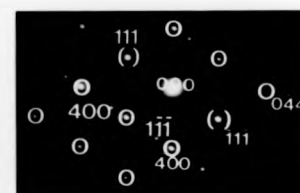
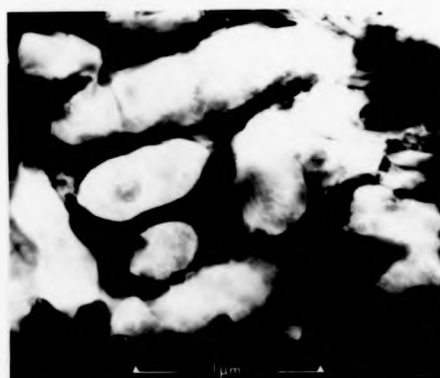


Fig 8.5 TEM Micrograph of interface between original and reconstituted material in bi-phase alloy.



b



c

Fig 8.6 (a) TEM micrograph of dendritic globule in 2-phase material showing crystalline interdendritic phase. (b) Selected area electron diffraction pattern from the dendrite imaged in (a), identifying it as twinned silicon. The component patterns from the twin related Si crystals are identified by different numeral sizes in indexing and by encircling the spots from one pattern. The electron beam direction for both twin-related crystals is $[01\bar{1}]$. The component patterns share a common pair of spots formed by diffraction from (111) and $(\bar{1}\bar{1}\bar{1})$ planes. The interdendritic phase is tentatively identified by (c) and EDAX as the cubic Y-Al phase.

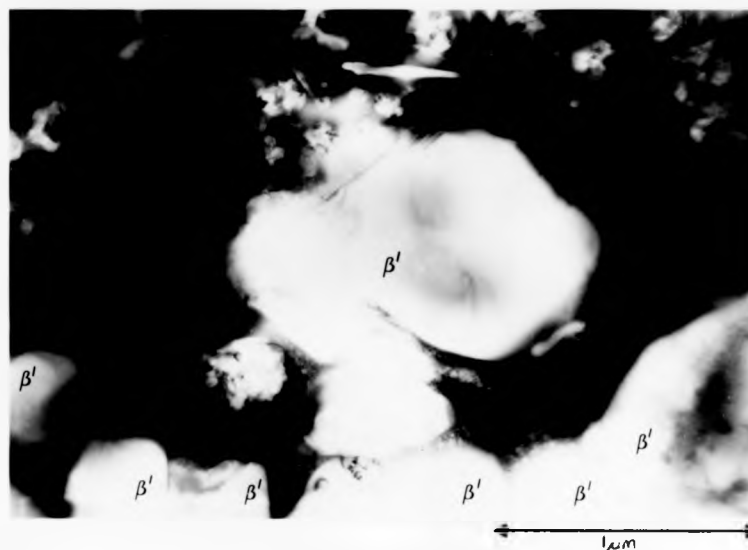
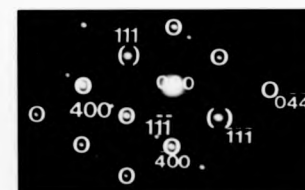
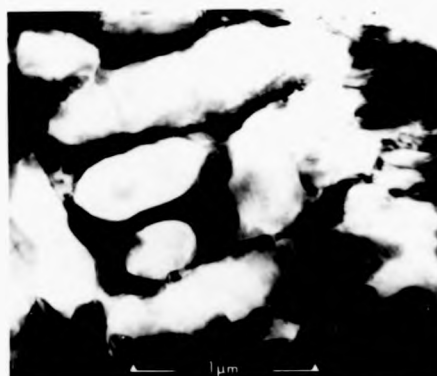
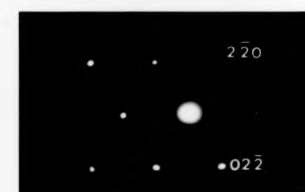


Fig 8.5 TEM Micrograph of interface between original and reconstituted material in bi-phase alloy.



b



c

Fig 8.6 (a) TEM micrograph of dendritic globule in 2-phase material showing crystalline interdendritic phase. (b) Selected area electron diffraction pattern from the dendrite imaged in (a), identifying it as twinned silicon. The component patterns from the twin related Si crystals are identified by different numeral sizes in indexing and by encircling the spots from one pattern. The electron beam direction for both twin-related crystals is $[011]$. The component patterns share a common pair of spots formed by diffraction from (111) and $(\bar{1}\bar{1}\bar{1})$ planes. The interdendritic phase is tentatively identified by (c) and EDAX as the cubic Y-Al phase.

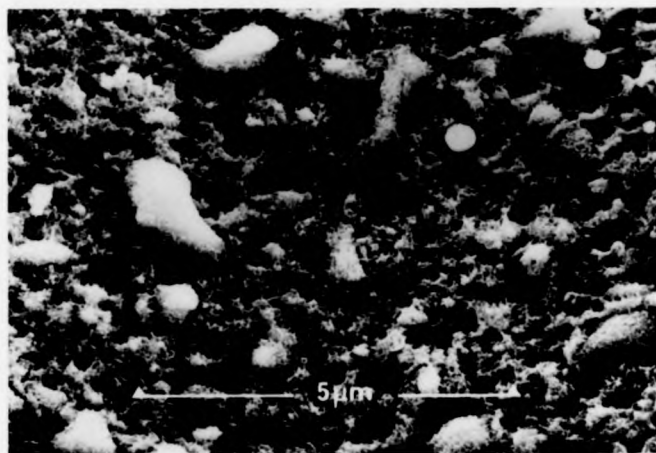
silicon. The dendrite growth kinetics are assisted by a re-entrant edge mechanism in a $\langle 211 \rangle$ direction, typical of a diamond cubic structure, where ease of twinning allows appreciable growth with smaller liquid under-cooling than the normal $\langle 100 \rangle$ rod-form growth. The interdendritic material consists of Al and Y-rich crystals (E.D.S.) of various compositions. Amongst these, from the symmetry and spacing of S.A.D. patterns and E.D.A.X., the cubic intermetallic "Y-Al" phase and Melilite ($Y_2O_3 \cdot Si_3N_4$), are tentatively identified. The small residual glass pockets indicate the growth of these phases into an interdendritic liquid which contains the rejected elements from the Si crystallisation. Melilite has also been found to grow in intergranular β' residual glass (36). These phases have average atomic numbers greater than silicon and hence exhibit relatively strong electron absorption (Fig. 8.6) and back-scattering (Fig. 8.3).

Debris, overlying the above features, is prevalent at the pulsed hole entrance (Fig. 8.1a) and E.D.A.X. shows it to be mainly Y and Al-rich.

8.3.2 Single-Phase Ceramics

All initial examinations of the effects of laser pulsing on single-phase ceramics were concentrated on the heat-treated hot-pressed material. The philosophy underlying this material's selection is that it represents the purest single-phase β' ceramic available and hence enables the determination of a mechanism of material loss and damage from which the effects of various grain-boundary impurity residues can be assessed.

Examination via S.E.M. shows the bore to be macroscopically clean, but finely pitted, with a covering of small lath-like grains approximately 0.5 μm in length (Fig 8.7a). Overlying this is a liquid

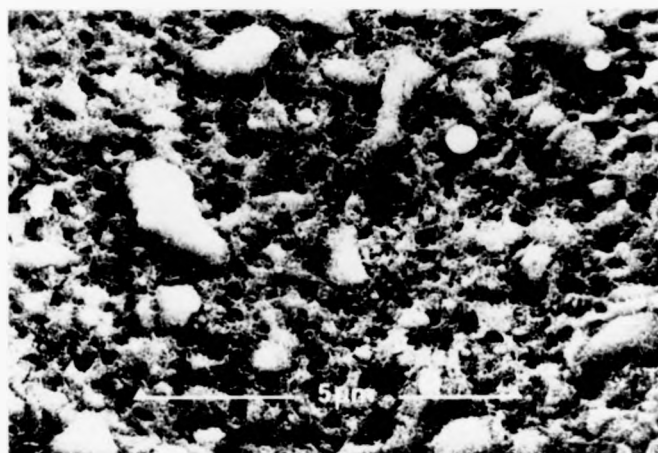


a



b

Fig 8.7 (a) SEM micrograph of the layer surface in single phase material near the bore entrance, showing fine covering of silicon. At the hole exit (b), the sparser silicon covering reveals the initial layer of platelike crystals of β ; and AlN "polytypes".



a



b

Fig 8.7 (a) SEM micrograph of the layer surface in single phase material near the bore entrance, showing fine covering of silicon. At the hole exit (b), the sparser silicon covering reveals the initial layer of platelike crystals of β and AlN "polytypes".

deposited material (Fig 8.1c) which is most prevalent at the bore entrance where vapour is condensed first on its rapid ($\sim 10^3$ m/s) exit. The initial lathy layer can be observed uncovered near the bore exit (Fig 8.7b). This layer is identified in T.E.M. (fig 8.8a) via S.A.D. and E.D.A.X. (fig 8.8b,c) as a composite of high z -value β^0 grains ($z = 2$ to 3) and a range of AlN based "polytypoids" including 15R, 21R and 27R phases (Ramsden notation, 37). The polytypoids were identified by their characteristic streaked $\langle 010 \rangle$ zone axis diffraction patterns (fig 8.8d,e) and by lattice fringe measurement. Fig 8.8f is the lattice fringe image for 15R, identified from its fringe spacing of ~ 14 Å obtained by dark field imaging using 2 diffraction spots from the systematic row of (001) reflections (fig. 8.8d). The lath-like morphology and heavy faulting are typical features of these crystals (165). The faulting arises from long range periodicity fluctuations (illustrated in Fig. 8.8a) that are possible in its "wurtzite" crystal structure. All these phases are highly covalent and under normal conditions do not undergo sequential vapour/liquid/ solid transformations. Hence vapour to solid growth of these crystals is thought to be the most likely deposition mechanism, this being supported by observations of intercrystalline cavities and the lack of residual glass. Evidence for grain-boundary preferred erosion during pulsing is found in T.E.M. at the bulk/layer interface and in S.E.M. via the pitted surface topography (Fig 8.7).

The effect of multiple pulsing is to produce larger droplets that are streaked along the bore length (Fig 8.1c). There is indirect evidence, from a reduction in the wetting angle of the globule (whose composition is unchanged), that the Si level of the layer is also increased with multiple pulsing.

Comparisons of laser damage in hot-pressed Si-Al-O-Ns with and without (that studied above) a detectable second phase (present mainly at triple-grain boundaries) reveals the major difference to be the presence of large, initially liquid, droplets that crystallise with a

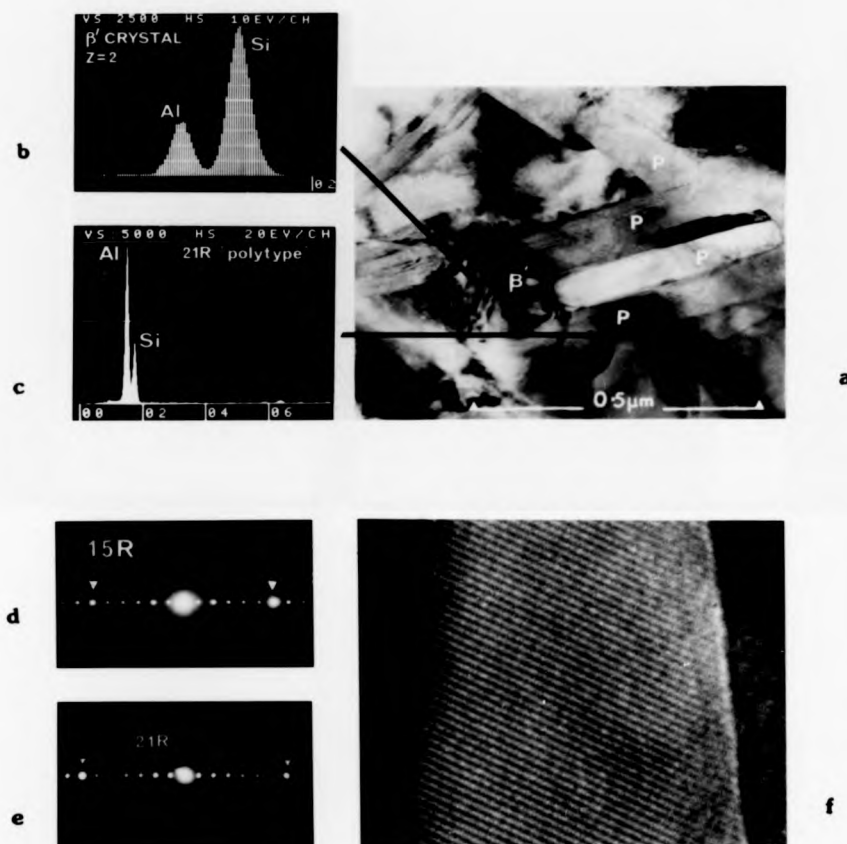


Fig 8.8 TEM section of reconstituted layer in single phase alloys (a) Typical microstructure consisting of high Al content β' grains (EDAX in (b)) and the faulted laths of AlN polytypes (EDAX in (c)). Characteristic rows of (001) reflections identify the 15R (d) and 21R (e) phases. The lattice image spacing of $\sim 14\text{\AA}$ identifies the 15R crystal phase (f).

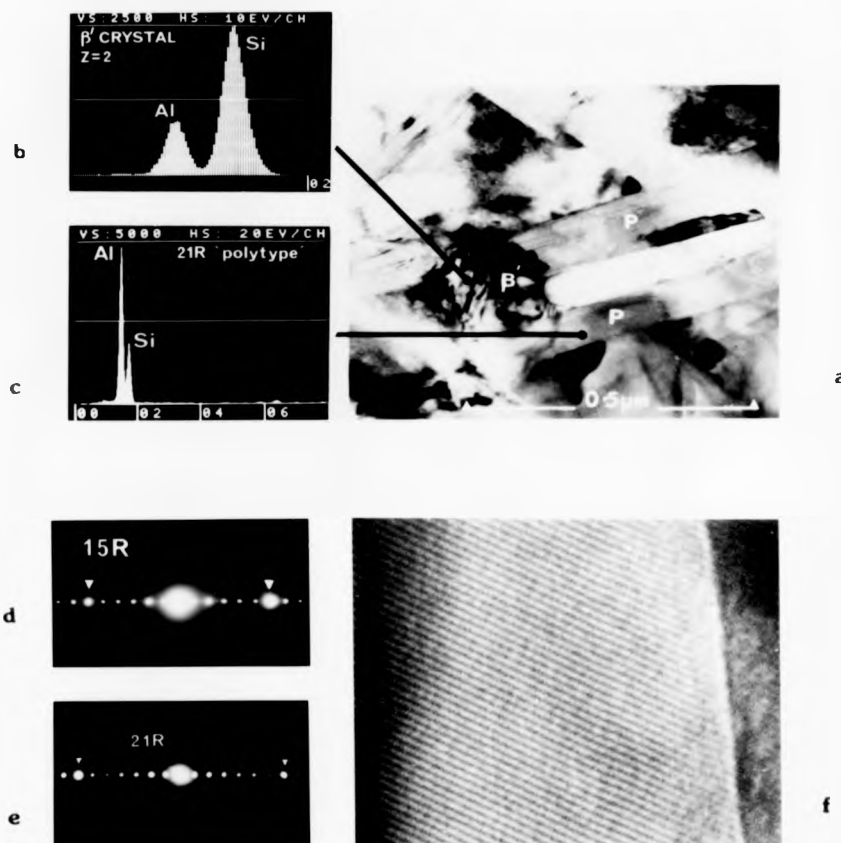


Fig 8.8 TEM section of reconstituted layer in single phase alloys
 (a) Typical microstructure consisting of high Al content β' grains (EDAX in (b)) and the faulted laths of AlN polytypes (EDAX in (c)). Characteristic rows of (001) reflections identify the 15R (d) and 21R (e) phases. The lattice image spacing of $\sim 14\text{\AA}$ identifies the 15R crystal phase (f).

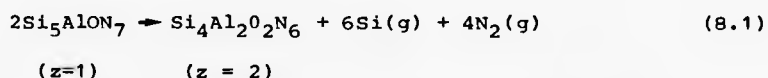
dendritic internal structure (fig 8.9a). The dendrites are of twinned silicon (from S.A.D and E.D.A.X. in fig. 8.9a) similar to the two-phase material but with an interdendritic alloy rich in Fe and Mn (Fig. 8.8c). The Fe is an accidental impurity and Mn is derived from the sintering additive.

8.4 MATERIAL LOSS AND RECONSTITUTION MECHANISMS

In an attempt to unify the material-loss mechanism during laser pulsing, the range of ceramics studied here will be regarded as modifications of the heat-treated, hot-pressed single-phase material.

A mechanism for general material loss from laser drilling has been proposed (163) where material in all three states (gas, liquid, solid) is explosively removed, with the subsequent melting and evaporation of the remaining material. In single-phase Si-Al-O-N there is no evidence for melting (due to the crystal's high covalency) and a grain-boundary preferred dissociation and evaporation is undergone during irradiation. At the termination of the laser pulse there appears to be a condensation of initially high-Al phases, followed by a range of successively lower Al content phases and finally silicon. The following reactions are expected to take place in these materials at these temperatures and ambient atmospheres and can be followed on the Equivalence Diagram of Fig 8.10.

1. Thermal Decomposition, which occurs at above ~4500°C and can be represented approximately by:-



This effectively takes the β' composition along the β' line (ie, increases in z value). The essentially unchanged equiaxed morphology of the highly substituted β' grains suggests the above solid-state transformation rather than a derivation from the vapour phase (which results in a whisker morphology). Upon

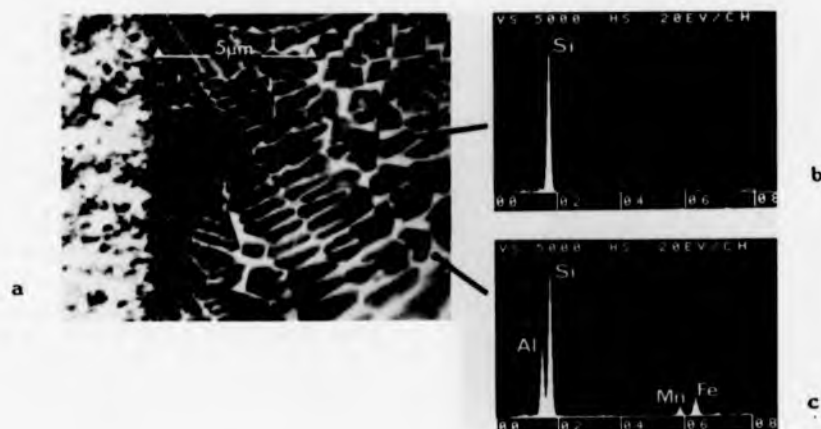


Fig 8.9 (a) SEM micrograph imaged with b.s.e.s showing portion of globule overlying the layer in the single phase material with a detectable second phase.(b) EDAX of dendrite (c) EDAX of interdendritic material.

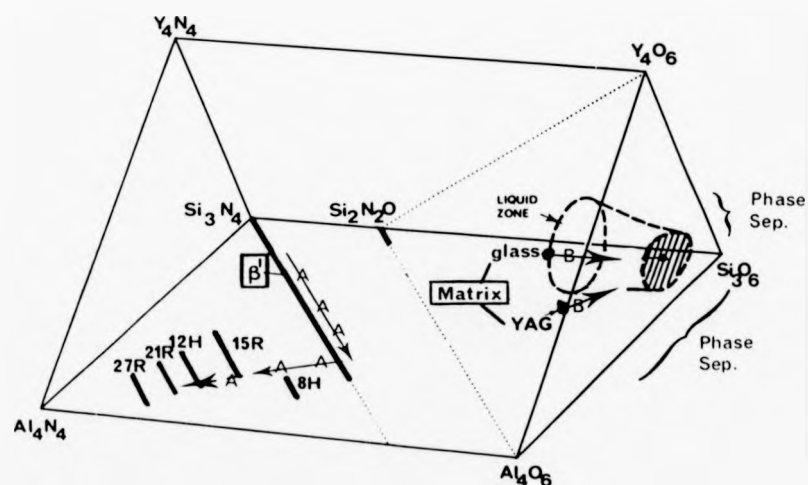


Fig 8.10 Equivalence prism for Y-Si-Al-O-N system (after 37). The arrows A show the compositional modifications to the β' phase during pulsing due to active oxidation and decomposition reactions as occurring in the single phase materials. The compositional variations of the matrix phase (glass and YAG) in the 2-phase materials (arrows B) show a general movement towards the SiO_2 corner entering into the phase separation territory.

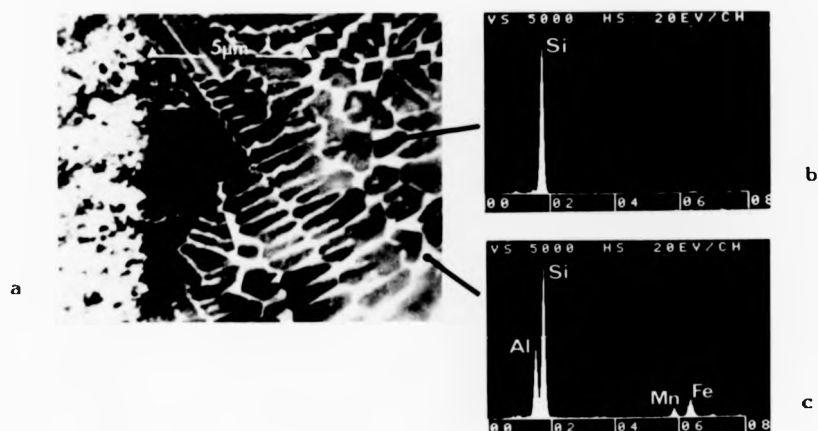


Fig 8.9 (a) SEM micrograph imaged with b.s.e.s showing portion of globule overlying the layer in the single phase material with a detectable second phase. (b) EDAX of dendrite (c) EDAX of interdendritic material.

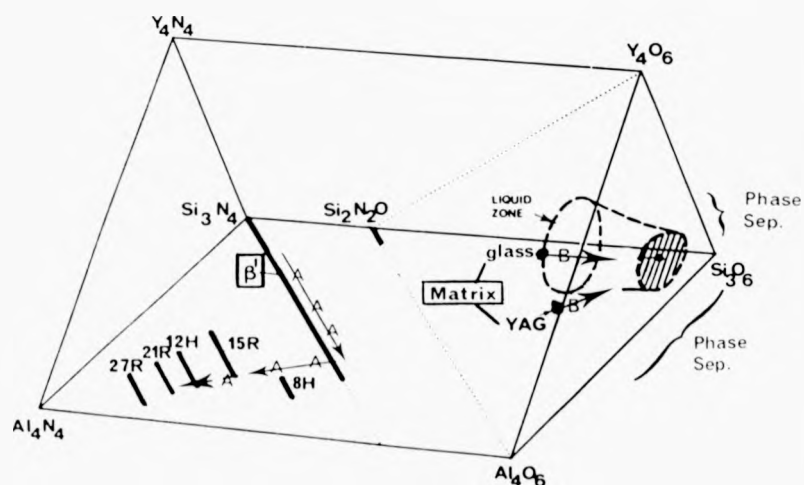
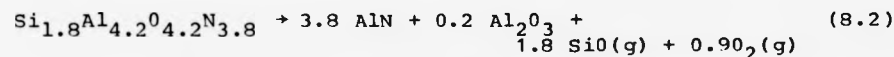


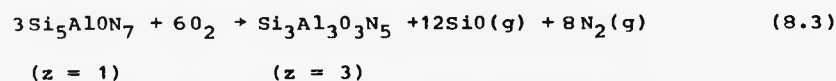
Fig 8.10 Equivalence prism for Y-Si-Al-O-N system (after 37). The arrows A show the compositional modifications to the B' phase during pulsing due to active oxidation and decomposition reactions as occurring in the single phase materials. The compositional variations of the matrix phase (glass and YAG) in the 2-phase materials (arrows B) show a general movement towards the SiO_2 corner entering into the phase separation territory.

reaching the maximum Al, O substitution in the β' framework ($z = 4.2$), the presence of a range of "polytypoids" suggests the composition subsequently moves towards the AlN corner. A decomposition reaction would be:-



where Al_2O_3 and AlN react further to form the various AlN "polytypoids". Mitomo et al. (166) found via XRD and chemical analysis that the thermal decomposition products of a Hot-pressed Si-Al-O-N ($z = 2$) were 15R and also Si and the overall shift in composition was towards the AlN corner, due to the Si and O losses. Goursat (167) also found β' decomposed to 15R and with continued Si, N, O volatile species loss (at 1700°C in Ar) to 12H and AlN.

2. The O_2 species derived from the above reactions coupled with the presence of any atmospheric O_2 in the vicinity of the reaction zone, could allow an ACTIVE OXIDATION reaction of the β' crystal to occur throughout a wide range of temperatures; the oxygen partial pressure considered to be low enough in this instant to negate passive oxidation. A typical reaction is:-



These reactions operating in conjunction readily account for the construction of reconstituted layer found for these single-phase materials. A schematic representation of the loss/reconstitution mechanism and microstructural changes that characterise the single-phase material is given in Fig 8.11. The sequence of deposition of phases will be due to whichever reaction is dominant as the temperature rapidly falls at the termination of the laser pulse and also to vapour pressure differences of the elements/compounds that exist in the vapour plume at that instant.

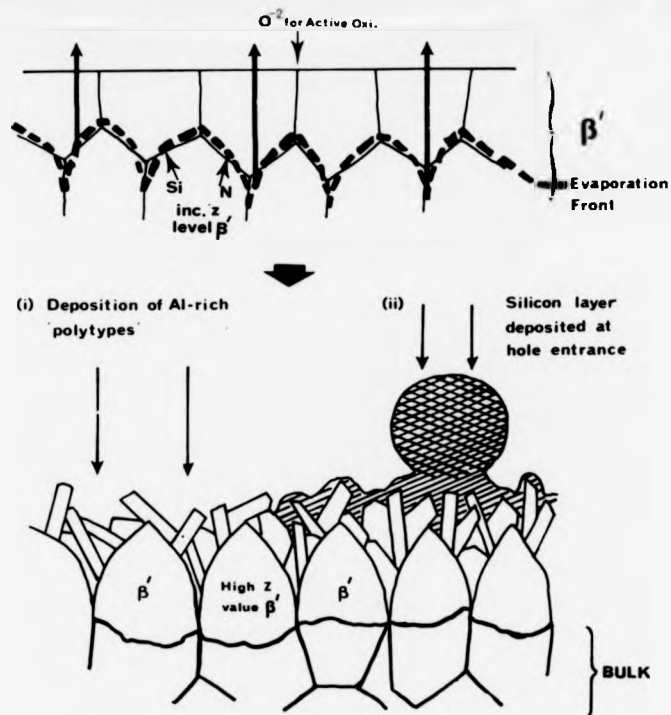


Fig 8.11 Diagrammatic representation of material loss/redeposition mechanism in single phase hot-pressed materials due to laser irradiation.

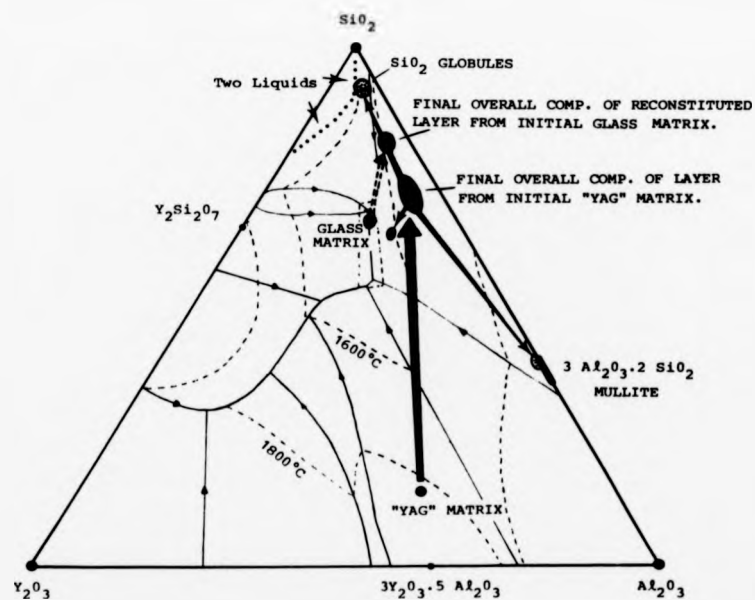
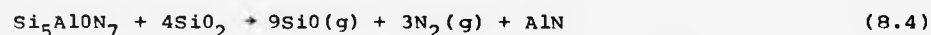


Fig 8.12 Y_2O_3 - Al_2O_3 - SiO_2 ternary phase diagram representing the shifts in composition of the matrix phase in sintered materials during laser irradiation.

With a small residual second phase present in the hot-pressed materials, the impurity elements act as seeds to the silicon vapour with the consequence that larger silicon droplets are condensed, with the impurities re-appearing as an inter-dendritic phase. The pitting, dominant in these materials, could be due to a variety of mechanisms. The impurity-rich SiO_2 g.b. phase could be reacting with β' via an active oxidation mechanism such as:-



which represents a greater loss mechanism than β' grain decomposition. Another, more likely, explanation is simply g.b. thermal etching, where the elevated temperature allows sufficient atomic mobility or vapour phase material transfer for equilibrium between g.b. energy and the surface energy.

The presence of larger volume fractions of second phase (i.e. in the sintered materials) which have an established solid-liquid transition, produce a molten covering during irradiation which is derived from the matrix phase.

If the case of as-sintered material with a "YAG" matrix is considered first, E.D.A.X. shows the overall composition of the final covering (including crystallites) to have shifted (from the initial "YAG" composition) in an increasing-Si direction. This shift is plotted on a Y_2O_3 - SiO_2 - Al_2O_3 oxide phase diagram (Ref168) which can approximate the changes that take place in the second phase (Fig 8.12). It can be seen that an enrichment of the matrix with Si would take the "YAG" into the new SiO_2 - $3\text{Al}_2\text{O}_3$. 2SiO_2 -Eutectic trough phase field where, upon cooling, SiO_2 , Mullite and a eutectic glass are expected. This is exactly the situation within the layer - further evidence for the belief that this layer is an enhanced volume matrix.

The sequence for layer formation upon irradiation is therefore believed to be as follows. As previously determined in Section 6.4.4, "YAG" in the presence of β' transforms to liquid above 1500°C. At slightly higher temperatures the surrounding β' grains will be undergoing thermal decomposition with Si, N₂ and SiO losses. These Si species then dissolve into this molten "matrix" and take its composition towards the SiO₂ corner. The lack of nitrogen containing phases produced on cooling and the known limited N accommodation in any Y, Al containing silica-rich residual glass (145), suggests a rapid loss of evolved nitrogen from the liquid. This is supported by the nucleation of SiO₂ very close to the decomposing β' (Fig 8.5). Nitrogen in the melt is therefore rapidly lost to the atmosphere, probably by ionic diffusion, as no molecular N₂ gas bubbles were observed. The presence of the reactive silicate liquid will dictate that another major β' material erosion mechanism will be that of β' solution, occurring similarly to that in the sub-oxide zone (Section 6.4.2). The melt composition is shifted due to Si and Al enrichment (derived from β') and on cooling the mullite laths are first to crystallise out (as shown in Fig 8.4). The subsequent liquid composition is pulled further towards the liquid immiscibility region, with the SiO₂-rich liquid forming as globules in which a SiO₂ polymorph subsequently crystallises along with a minor Y-rich phase (probably Y₂Si₂O₇). The rejected species from these crystallisations push the remaining matrix towards a ternary eutectic composition which cools to a glass.

In the case of irradiation of β' /glass matrix materials, the matrix will be reactive at a lower temperature and together with its initially higher Si concentration will dictate a layer with an overall composition even closer to the SiO₂ corner in Fig 8.12. This

produces, on cooling, a layer similar in phase content to that of the β' /YAG materials but with a greater amount of SiO_2 globules and Mullite laths and a very small volume of high SiO_2 -content glass. A schematic representation of the material loss mechanism for two-phase ($\beta' +$ matrix) ceramics is given in Fig 8.13.

8.5 POTENTIAL FOR PRECISION LASER MACHINING OF SIALON CERAMICS

The large heavily crazed layer and surface debris that are characteristic of the surface finish on laser irradiated 2-phase ($\beta' +$ matrix) sintered ceramics will present problems if this material is required to be precision machined by lasers. In the pierced state, the material would have a limited life if used as a high-pressure nozzle due to the high critical flaw density of the surface and also the relative softness of the reconstituted layer, which acts as the bore lining. Boyd et al. (169) have shown that liquid formation during pulsing of single crystals of sapphire can be reached by optimisation of the laser pulse spikes. However, there will always be liquid present in 2-phase materials due to the continual matrix enhancement (via β' solution) that will occur just back from the material volatilization surface. Any reconstituted material remaining would suffer from thermal expansion coefficient mismatch and thermal shock that would lead to crazing of the layer on rapid cooling.

The single-phase hot-pressed materials show the greatest promise due to the dominance of solid to vapour transitions during irradiation. A cleaner, less flawed, surface is produced (free from any liquid layer) and in the pierced state, have hole profiles with a greater linearity than those of the sintered materials. The major drawbacks of the single-phase material's irradiated surface are the presence of enlarged grain boundaries (which could act as critical flaws) and the fine lathy crystals which would be susceptible to fracture in the nozzle role. The use of a vapour extraction technique at the termination of the laser

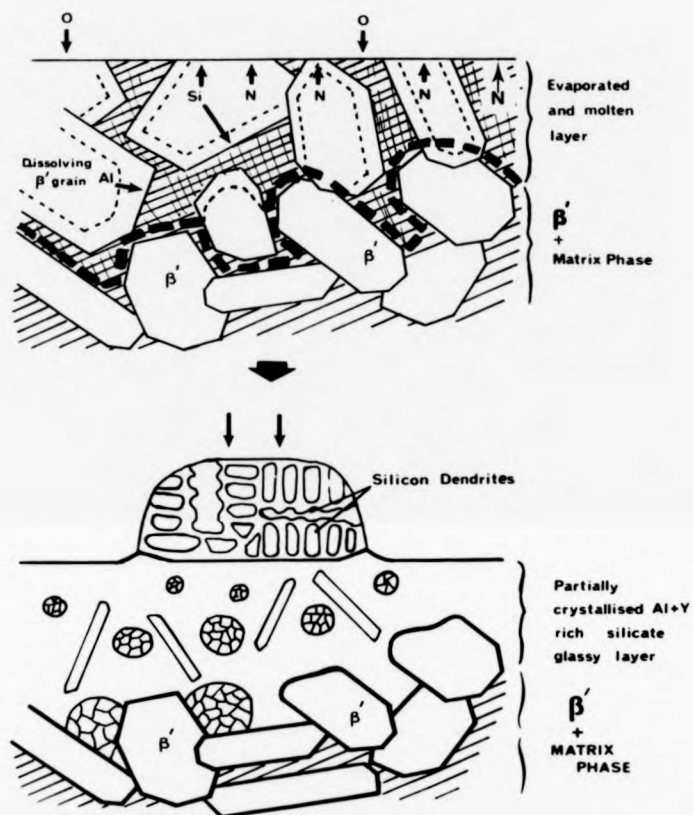


Fig 8.13 Diagrammatic representation of material loss and reconstitution mechanisms in two-phase sintered materials due to laser machining. The heavy broken line represents the melting/evaporation front.

pulse could reduce the amount of vapour deposited material considerably. The surface could then retain its pre-condensation microstructure and utilise the intrinsic β' Si_3N_4 properties with any condensed matter being deposited preferentially at the enlarged grain boundaries (due to their high surface free energy), thus healing the potential critical flaw population.

To maintain this superior surface finish it is essential to keep impurities in these hot-pressed materials to a minimum and control the amount of grain-boundary residual phase by careful "balancing" of sintering components. Small quantities of impurity act as oxygen sources for preferential grain-boundary attack via oxidative reactions during decomposition and can then act as seeds in the vapour plume for large Si droplets that spoil the surface finish.

CHAPTER NINE

OVERVIEW AND FUTURE WORK

The first part of this chapter draws together the main conclusions of this thesis and provides an overview of the present understanding of the high temperature microstructural stability of bi-phase Si-Al-O-N ceramics. The microstructural modifications discovered during this thesis are assessed in terms of improving bi-phase material properties and overcoming the highlighted problems. Finally, the future material property developments suggested by this work, and initial findings from other workers based on this work, are discussed.

9.1 OVERVIEW

The overall aim of the work in this thesis is towards a greater understanding of microstructural stability in various environments with a view to material improvement to meet the requirements of a high temperature engineering ceramic (eg for G.T.E. components). The themes of this thesis are therefore; 1) ceramic fabrication, identifying those variables that significantly influence final microstructures, 2) subsequent microstructure modifications in various environments and 3) high temperature mechanical properties. The properties studied; oxidation resistance, fracture, ultra-high temperature stability and new routes for component shaping (ie laser) are also all pertinent to the G.T.E. component development. The conclusions of these themes shall now be discussed.

a) In as-sintered ceramics having glass matrices, it has been established directly by E.E.L.S. and indirectly by crystallisation phenomena, that Nitrogen can be introduced into this glass. The level of Nitrogen can be controlled by the initial chemical composition ie by the 21R polytypoid addition. It is believed that this Nitrogen

rather than the other glass matrix components gives rise to significant variations in properties over the range of bi-phase alloys studied.

This is supported by external studies of properties of similar composition bulk glasses. The microstructure of as-sintered alloys is significantly altered by Nitrogen's presence in the reactive sintering liquid. This increases its viscosity, thereby reducing β' reprecipitation rate, to provide a finer grained and more interlocked microstructure. This modification dramatically increases the overall level of the alloy's fracture toughness (over the range of temperatures). Further, a high glass Nitrogen level raises the glass transition temperature thereby also raising the temperature for onset of slow crack growth of the bi-phase alloys.

b) The other significant effect of initial composition is on the determination of phase type when crystallising the glass matrix during annealing. Again the glass' Nitrogen content appears most influential, with low N content favouring $\alpha - Y_2Si_2O_7$ crystallisation whilst high N content gives "YAG" crystals. Recent studies on the crystallisation behaviour of similar composition bulk glasses (varying N/O ratio) support these findings(148). The level of Nitrogen also controls the degree of glass matrix crystallisation. In addition, impurities associated with various $\alpha - Si_3N_4$ source materials are critical to full matrix crystallisation. If crystallisation is only partial then bi-phase material properties (K_{IC} , oxidation, slow crack growth) do not show any significant improvement over their glass matrix parent. However, the attainment of complete matrix devitrification gives dramatic improvements in material performance.

By matrix conversion to $\alpha - Y_2S$, grain boundary Y^{3+} ion mobility is stifled which dramatically reduces oxidation kinetics to levels similar to H.P. mono-phase Si-Al-O-Ns. The removal of viscous grain boundary components by devitrification to YAG has been previously

shown to suppress g.b. sliding and cavitation mechanisms during high temperature fracture. The present work highlights the sensitivity of this failure mechanism to exceedingly small glass volumes, residual from incomplete matrix devitrification. However, matrix crystallisation does present some problems. The α - Y2S crystallisation produces substantial matrix porosity which degraded mechanical properties and could not be significantly reduced. Crystallisation to YAG overcame this porosity limitation but produced an environmental instability.

c) In oxidising environments above 1300°C the YAG matrix reacts with the SiO_2 oxide film to revert the matrix to eutectic liquid. This subsequently increases, catastrophically, the oxidation kinetics and mechanical failure of the bulk ensues. During sub-oxide studies of the bulk, Silicon Oxynitride (O') was identified in the matrix as a by-product of this reaction and after a supplementary study its formation mechanism was understood. By suitable annealing in an oxidising atmosphere, sufficient O' developed to form bi-phase ($\text{O}' + \beta'$) sub-oxide regions which were wholly crystalline, and therefore protective.

d) Higher temperature microstructural stability (up to 1450°C) was studied in a variety of atmospheres. In inert atmospheres a phase morphology modification was identified. Mainly increased oxide kinetics resulted in oxidising environments.

An ultra-high temperature range may occur accidentally in service or may be utilised as a component shaping mechanism. Laser irradiation provides the ultra-high temperature environment and also represents a novel way of accurately machining these difficult materials. The irradiated zone undergoes complex phase changes in both the β' and matrix phases. The β' grains when studied in isolation (facilitated by an H.P. Si-Al-O-N material) undergo solid-state transformation to a more highly substituted β' structure.

Subsequently grain boundary preferred dissociation occurs with vapour deposition of AlN based "polytypoid" phases. This modification represents an overall loss in Si and N. Any matrix phase present acts as a sink for the dissociated β' species. Both YAG and glass matrices are liquids at the evaporation temperature and are enhanced in volume (due to the dissolved β' components) producing a thick liquid layer on the component's surface. The liquid cools to a partially crystalline glassy layer, the crystal types revealing that N is lost to atmosphere and Si enriches the liquid.

These ultra high temperature mechanisms can be translated to reactions, for instance, during the sintering process and also at the tip of in-service cutting tools, where even limited studies have been shown to support the present findings (157). Easier component fabrication and processing are important to successful deployment of these ceramics and this work is believed the first to show the capability of laser machining. It also highlights single-phase Si-Al-O-N as a most promising laser machinable ceramic in terms of accuracy and surface finish.

9.2 MICROSTRUCTURALLY MODIFIED β' + YAG ALLOY

9.2.1 The Significance of the YAG Instability Phenomena.

In non-oxidising environments or below 1300°C, β' + YAG material possesses many unique properties. It can be fully crystallised without the porosity development problems associated with α -Y2S. In addition, supplementary K_{IC} tests on the latest (L) source materials (fully crystalline) towards the end of this programme showed excellent resistance to s.c.g. up to a previously unobtainable temperature of 1500°C together with a very high fracture toughness. This only occurs in vacuum however. Bhatti's work on similar fully

crystalline β' + YAG supports these findings (44). This material represents a significant advance in engineering ceramics being easily shaped by its pressureless sintering route, yet having properties superior in many respects to the H.P. Si-Al-O-N "reference" materials. However its critical drawback is the deleterious YAG matrix reversion in oxidizing environments.

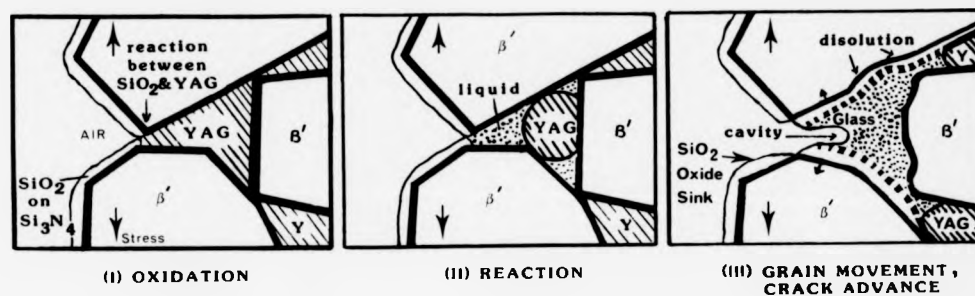
The present work demonstrates the serious effect YAG-reversion has on oxidation resistance, and previous work (45) has shown catastrophic creep behaviour.

The present study also suggests YAG-reversion could lead to a unique s.c.g. mechanism, which is now briefly outlined. Figure 9.1a illustrates YAG-reversion at the crack tip, which would not only enhance g.b. sliding and cavitation, but more significantly, drastically reduce local g.b. cohesion. A K_I -V relationship for this s.c.g. mechanism can be predicted which would include a stress independent regime (fig 9.1b) where the crack velocity would be expected to be controlled by the rate of diffusion of oxygen to the reaction interface. Verification was not possible during this thesis, due to unavailability of fully crystalline material.

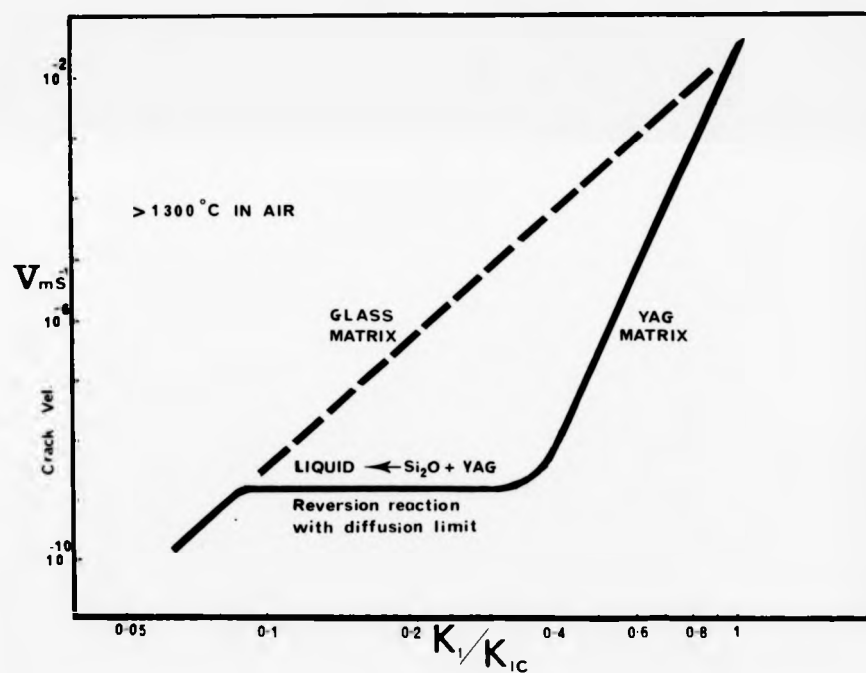
The reduction or total arrest of YAG-reversion, and its deleterious effects on mechanical properties, is obviously a development objective for these otherwise excellent materials. The microstructural modifications during oxidation explained in Chapter 6 were believed to be a possible answer to this problem. Further study and optimisation of modification kinetics were indeed found to provide a range of solutions and are now presented.

The basic philosophy is to produce an effective thin coating of modified microstructure that will protect the unmodified bulk.

9.2.2 Solutions to YAG-Reversion via Microstructural Modification.



a,



b,

Figure 9.1 a) SCHEMATIC OF SLOW CRACK GROWTH MECHANISM POSSIBLE BY YAG REVERSION AT THE CRACK TIP

b) PREDICTED K_I -V RELATIONSHIP FOR SLOW CRACK GROWTH MECHANISM VIA CRACK TIP YAG REVERSION

The YAG instability is so catastrophic primarily because it is able to proceed deep within the bulk and therefore involve large amounts of matrix phase in its reaction. This is facilitated by the semi-continuous nature of the matrix. One solution could be reducing the degree of matrix interlinking. This can be done by reducing matrix volume or transforming the YAG into its more isolated form.

Chapter 6 demonstrated that a range of modifications to YAG morphology and distribution occurred during anneals in various atmospheres. In air, sub-oxide material could be greatly enhanced by YAG-reversion and θ' formation. All these modifications were subsequently found to increase resistance to in-service YAG reversion although to differing degrees as described below.

9.2.2a Isolated YAG

Matrix volume reduction is facilitated by increasing 21R content for the range of Norton based alloys, N4, N6 and N8 as described in Chapter 5. The rate of YAG reversion can be indicated by the depth of the sub-oxide zone after ~1000 hrs at 1320°C and figure 9.2 shows a rate decrease with increased 21R content. However even for high 21R alloys, the matrix is still semi-continuous and gives a substantial sub-oxide zone.

As described in section 6.4.4, one effect of YAG "morphological stabilisation" is to transform the interconnected YAG into isolated pockets. Samples of this modified material and its parent were oxidised at 1350°C for 90 hrs. YAG reversion was still occurring although the zone growth rate was reduced by approximately 40%. T.E.M. sections showed that the reactive liquid was able to proceed along β'/β' g.b.s (to link the isolated YAG pockets), via the β' dissolution mechanism. The slower kinetics of dissolution compared to YAG reversion account for the overall reduction in zone growth.

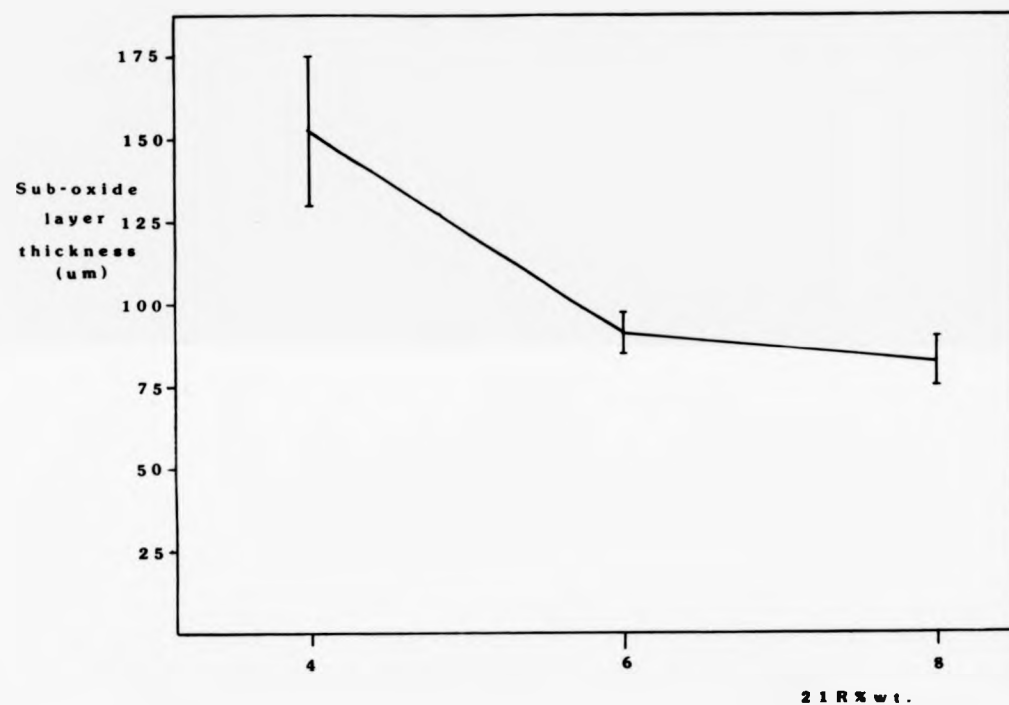


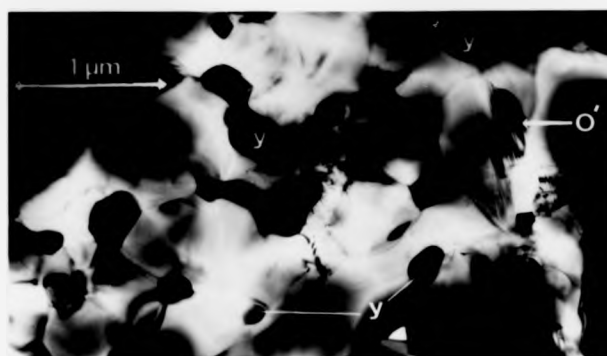
Figure 9.2 SUBOXIDE LAYER DEPTH AFTER 1000 HRS AT 1320°C FOR β' + YAG ALLOYS WITH INCREASING 21R CONTENT

9.2.2b Isolated YAG + O'.

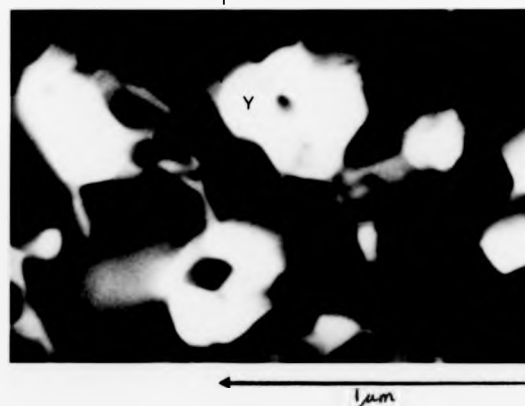
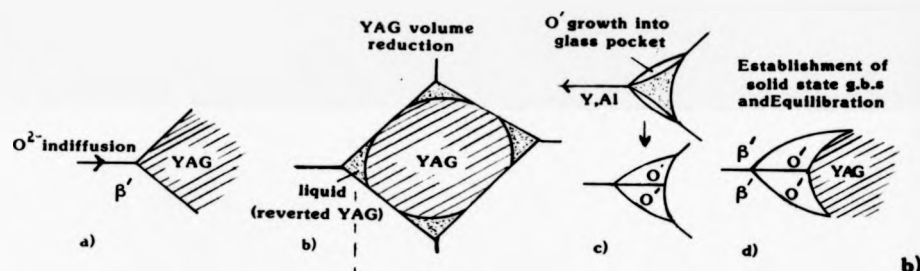
A volume reduction of reactive liquid available and increase in effective mean free path between YAG grains should improve the situation further. A suitable microstructure having reduced YAG volume and increased YAG isolation was produced (fig 9.3a) by long time annealing (1000 hrs) at a temperature slightly below that used to produce the microstructure in section 6.6.1 (ie 1320°C).

A mechanism for this microstructural modification is given in figure 9.3b. Due to the lower temperature only partial YAG reversion occurs. It attempts to attain a minimum surface area spherical morphology, which reduces its volume considerably. There is supporting evidence for this stage (fig 9.3c) from an S.E.M. section showing many YAG grains with this morphology. Subsequently O' nucleates and grows into the liquid volume. Once a solid-state O'/YAG boundary exists, the spherical morphology is lost due to equilibration of surface tensions and the characteristic YAG shape in figure 9.3a is produced. Direct O' detection at these triple junctions was difficult but there is evidence from a) an identified O' grain in the vicinity, b) the fact that the equilibration mechanism requires a crystalline matrix.

Oxidation of this layer at 1350°C (fig 9.4) showed a rate decrease that represents a considerable improvement over the material in section 9.2.2a and is of the same order of magnitude as that reported for H.P. Si-Al-O-N ($Z=1.4$). The oxide is mainly glassy with β -Y₂S crystals (similar to oxide product of β' + α -Y₂S material). However, sub-oxide zone growth again occurs albeit at a rate of ~20% of that of the original β' + YAG material. T.E.M. revealed only limited YAG reversion and β' dissolution. Although a considerably improved material, these features will still weaken the microstructure.

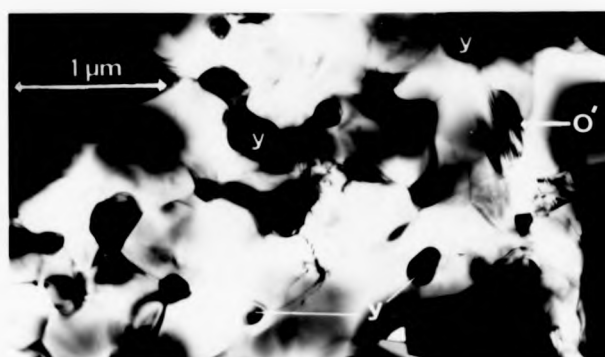


a)

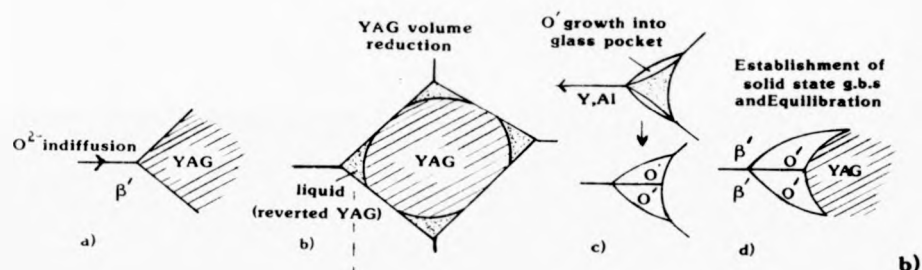


c)

Figure 9.3. a) T.E.M. section of sub-oxide zone showing isolated and reduced volume YAG phase with a large intergranular, heavily faulted O' grain nearby. b) Schematic of mechanism of YAG volume reduction and 'isolation' in the presence of an oxidising environment. c) High mag. S.E.M. (bse) section identifying transition stage, with partial YAG dissolution and consequential rounding and volume reduction.



a)



b)



c)

Figure 9. 3. a) T.E.M. section of sub-oxide zone showing isolated and reduced volume YAG phase with a large intergranular, heavily faulted O' grain nearby. b) Schematic of mechanism of YAG volume reduction and 'isolation' in the presence of an oxidising environment. c) High mag. S.E.M. (bse) section identifying transition stage, with partial YAG dissolution and consequential rounding and volume reduction.

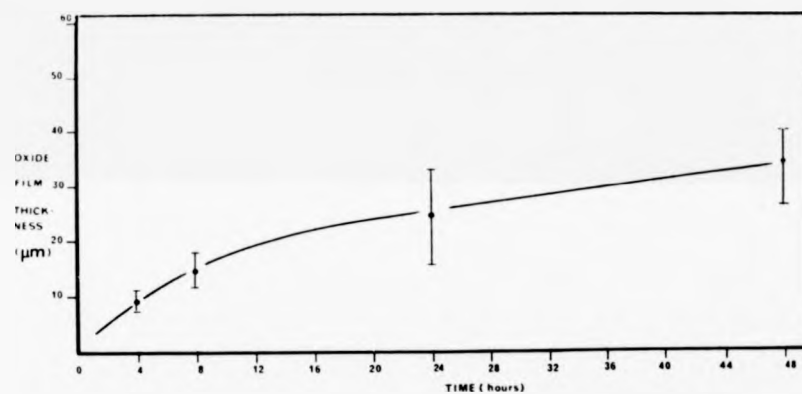


Figure 9.4. Oxide thickness with time for material with "isolated" Y₂G and O' matrix at 1350° C.

It becomes obvious that the most protective zone would be one denuded of YAG, ie solely of β' and O' .

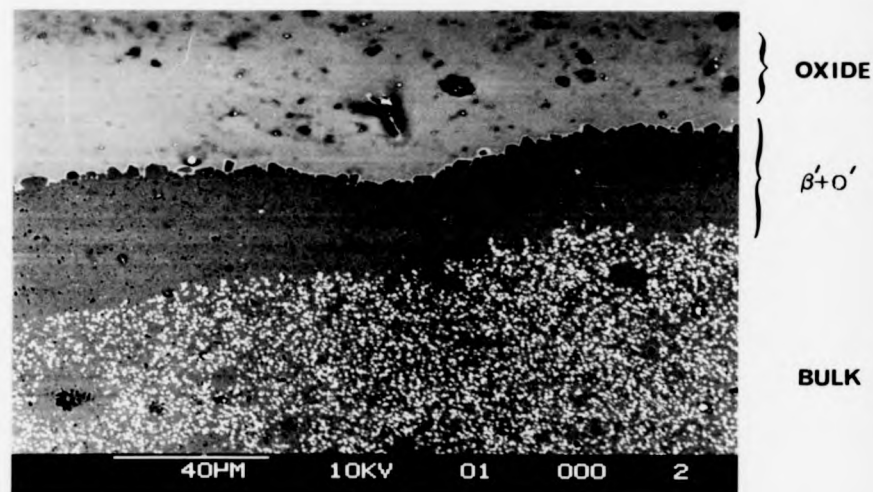
9.2.2c $O' + \beta'$ Zone.

Large zones of $O' + \beta'$ exist in the protective layer described above, although zones of YAG matrix are always present. Presumably this is due to these regions statistically not having a continuous matrix to the oxide. If all YAG could be accessed in the anneal stage, a solely $O' + \beta'$ layer should be possible. Raising the anneal temperature will increase YAG reversion and β' dissolution rates and open up g.b.s to access previously unconnected YAG. However, at too high a temperature ($\sim 1350^\circ\text{C}$) the excessive oxidation will counter zone growth by effective material loss. 1335°C was identified as optimal and after 1000 hrs a YAG denuded $\beta' + O'$ layer of thickness $\sim 300\text{--}400\mu\text{m}$ was produced (fig 9.5a).

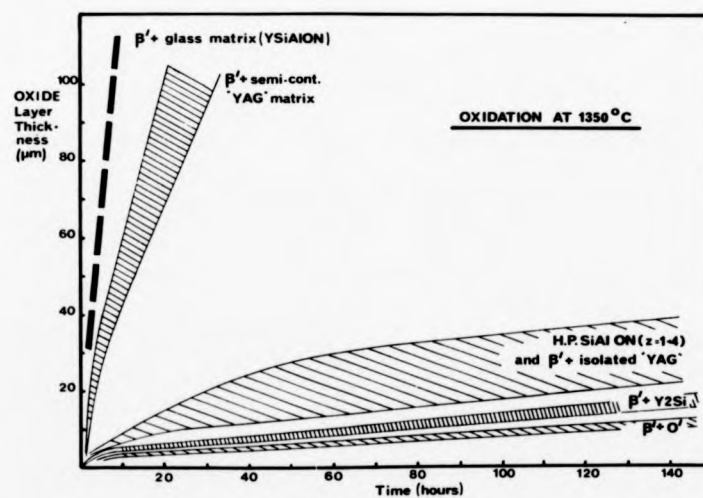
The oxide from the anneal was ground off and the $O' + \beta'$ coated material re-oxidised at 1350°C for 150 hrs. The oxide was totally glassy, of fairly uniform thickness ($9\mu\text{m} \pm 1\mu\text{m}$) with a low Y content. This rate of oxidation is extremely small, assuming parabolic kinetics, the rate constant is approximately $0.01\text{mg}^2\text{cm}^{-4}\text{h}^{-1}$, which betters all currently available H.P. Si_3N_4 or Si-Al-O-N. In T.E.M. the YAG containing area adjacent to the $O' + \beta'$ layer was found to consist of morphologically stabilised YAG with a large proportion of g.b. O' present. No glass was observed.

9.2.3 Conclusions on Microstructural Modifications.

A comparison of oxidation rates for the range of Y-Si-Al-O-Ns at 1350°C is given schematically in figure 9.5b. It demonstrates the dramatic improvements over as-sintered material possible by microstructural modification, the most important being the $O' + \beta'$ protective coating. In addition to its excellent oxidation resistance, it should share the advantages of the $\beta' + \text{YAG}$ core



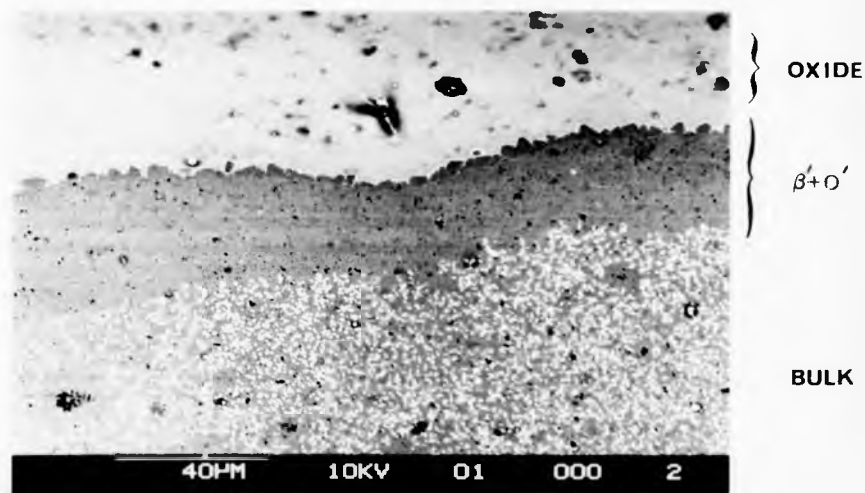
a)



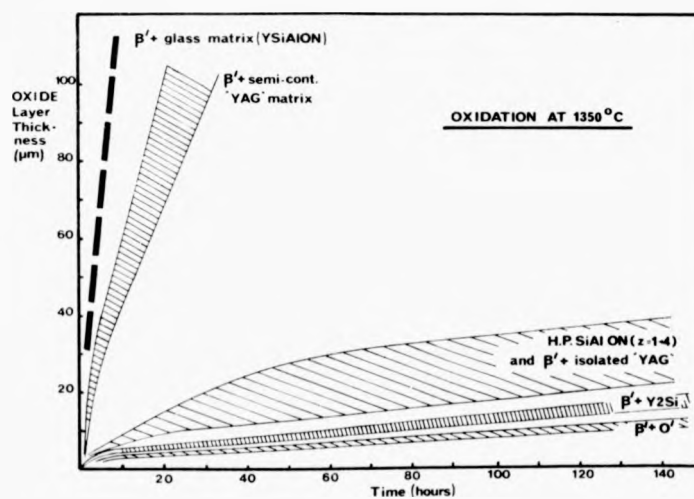
b)

Figure 9.5.a) S.E.M. section of β' + YAG material oxidised for 1,000 hours at 1350°C to produce a β' + O' layer.

b) Comparison of oxidation rates for the range of Si-Al-O-Ns at 1350°C .



a)



b)

Figure 9.5.a) S.E.M. section of β' + YAG material oxidised for 1,000 hours at 1350°C to produce a β' + O' layer.

b) Comparison of oxidation rates for the range of Si-Al-O-Ns at 1350°C .

material i.e. high fracture toughness and creep resistance (45). It will also have the flexibility of the pressureless sintering route as the surface modification is performed on the shaped component.

The morphological stabilisation of YAG, its volume reduction and protection by g.b. O' are valuable routes producing substantial improvements in oxidation behaviour. Although inferior to $O' + \beta'$ coated material, they have advantages in a) production controllability, b) having a greater modification depth (important if in-service surface abrasion/damage is likely) and c) having a less well-defined interface which is potentially stronger and less liable to spalling.

To the authors' knowledge these oxidation induced microstructural modifications are a new route to improving the properties of pressureless sintered materials and could represent a major solution to current problems.

9.3 Future Work

From the findings of this thesis, certain predictions for material developments and properties can be made. These can be supported by supplementary studies.

1) The dependence of impurity level and type upon full matrix crystallisation to YAG was identified. Additional study is required to quantify these effects further. The inability to fully crystallise results in mechanical properties only slightly superior to the parent $\beta' + \text{glass}$ materials. The reduction and loss of certain impurities obtained by utilising alternative source materials, i.e. the latest grades, demonstrates the dramatic improvement and the attainment of s.c.g. resistance up to 1500°C in vacuum. It is therefore felt that additional study is required to further quantify the effects of impurities.

2) With the availability of fully crystalline alloys, the proposed s.c.g. mechanism outlined in section 9.2.1 should be studied in depth via the Double Torsion technique. Not only is it of scientific

interest as a new mechanism, but as a low stress effect could be a lifetime determining factor for G.T.E. components. A simulated G.T.E. gaseous environment should be experimented with to determine its effect on this s.c.g. mechanism.

3) The stifling of the YAG-reversion process (and therefore material degradation) by the α' + β' coating is an important modification and the properties of these materials should be studied in depth. Above 1300°C, in oxidising environments, replication of β' + YAG mechanical properties in vacuum would be expected i.e. resistance to high temperature s.c.g., retention of high K_{IC} values. Further, creep behaviour would be expected to be superior to that previously found (fig 2.1) (45). Initial follow-up work on surface modified alloys at 1350°C (157) confirms this.

4) An optimal production route for the desirable α' + β' layer has been determined, but due to the low anneal temperature is probably uneconomic as it required a long anneal time. This could be reduced using higher temperatures but then the excessive oxidation degrades the surface and uniformity of the α' + β' layer. As the major role of the oxide is just as a source of viscous SiO_2 , this effect could be more efficiently produced by a slab of pure SiO_2 in contact with the β' + YAG material. A proposed route would then be to Hot Isostatically Press components i.e. high temperature anneal of components in an SiO_2 viscous envelope, pressurised (3 atmospheres) in an inert environment. Direct environmental oxidation of β' (which causes surface degradation) is avoided and the pressure and higher temperature should increase the rate considerably. The success for this route is supported by observations of surface modifications to a α' + β' layer in the sintered skin of pressureless sintered billets. These had an SiO_2 -rich slurry applied prior to sintering (Chapter 5). The promising results from the microstructural study of laser irradiated alloys should be supplemented by mechanical tests to determine the effect of the various surface finishes on the alloy's strength.

Appendix 1.1

DEVELOPMENT OF EQUIVALENCE DIAGRAM REPRESENTATION FOR Y-Si-Al-O-N SYSTEM

The adoption by many workers of the Equivalence Diagram representation of the often complex M-Si-Al-O-N system (presented by Jack, 37) has eased interpretation and comparison of experimental data and is explained below.

THE 4-COMPONENT SYSTEM

Initially the Si-Al-O-N system can be represented as a regular tetrahedron with each vertice an atom of one element (Fig. A1.1.a). Assuming the elements retain their accepted valencies Si(+4), Al(+3), O(-2), N(-3), then all equilibrium compounds within the tetrahedron will only exist in an irregular quadrilateral plane (Fig. A.1.1b) joining Si_3N_4 , AlN , Al_2O_3 and SiO_2 (the binary compounds located along the metal/non-metal joins). This treatment of compounds in ionic terms (even though interatomic bonding is predominantly covalent) reduces the system to a pseudo-ternary one. This representation is further simplified by now expressing concentrations in equivalents, as is common with reciprocal salt systems. Any composition can be characterised by two quantities

$$\frac{[\text{Al}].3}{[\text{Si}].4 + [\text{Al}].3} \quad \text{and} \quad \frac{[\text{O}].2}{[\text{N}].3 + [\text{O}].2}$$

and using Si_3N_4 as the base, a convenient square diagram with other end members 4AlN , $2\text{Al}_2\text{O}_3$, 3SiO_2 is produced (Fig. A.1.1c).

The x and y axes represent equivalent % O and equivalent % Al respectively and lines parallel to these axes represent constant metal (Al/Si) or non-metal (N/O) atomic ratios. Any composition point within the square is made up of a constant combination of 12+ve and 12-ve valencies even though the number of atoms may change.

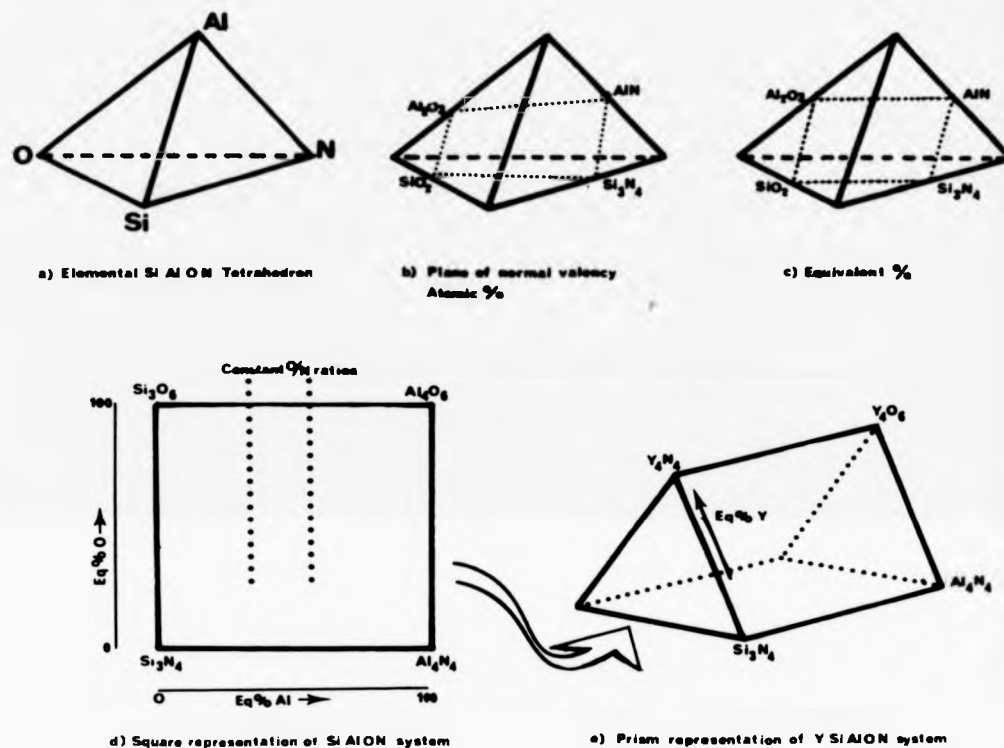


Fig.A11 Development of Si-Al-O-N and Y-Si-Al-O-N Equivalence Diagrams.

FIVE COMPONENT SYSTEM

The addition of Y_2O_3 sintering aid gives a 5-component Y-Si-Al-O-N system which can be regarded as a pseudo-quaternary reciprocal salt system, again assuming all phases have fixed valency. The system is commonly represented by a regular triangular prism (where all edges are equal) based on the Si_3N_4 - Al_4N_4 - Al_4O_6 - Si_3O_6 square diagram, with Y in equivalent units along a third dimension (Fig. A.1.1d). Each square side represents one of 3 pseudo-quaternary systems and the 2 triangular sides represent the oxide and nitride ternary systems. Subsolidus phase relations, represented by these faces and also sectional planes through the prism, are continually being determined in an effort to fill-in the details within the prism volume.

APPENDIX 4.1

K_{IC} SPECIMEN DIMENSION VARIATIONS

Although Eqn.4.1 accounts for various w:b:d ratios and gave similar K_{IC} levels with varying $(\frac{b}{w})$ ratio for Refel SiC specimens (126), K_{IC} constancy was not found during trials with the present materials aimed at reducing bar dimensions. The trials involved dimensional variations of the type (1) reduction in total size but keeping the w:b:d ratio constant ($6 \times 3 \times 25 \text{ mm} \rightarrow 4.8 \times 2.4 \times 20 \text{ mm}$) and (2) altering the b/w ratio ($6 \times 3 \times 25 \text{ mm} \rightarrow 5 \times 3 \times 25 \text{ mm}$ and $4.8 \times 2.4 \times 20 \text{ mm} \rightarrow 4 \times 2.4 \times 20 \text{ mm}$). The materials to be subsequently studied were all cut to the above dimensions and each tested at temperatures of 750°C, 950°C, 1150°C and 1200°C in the two K_{IC} jigs. Using the $6 \times 3 \times 25 \text{ mm}$ bar as a reference a consistent relationship existed for the dimensional variations. The $\frac{b}{w}$ reduction gave an

increased K_{IC} level ($\sim 1 \text{ MPa}\cdot\text{m}^{1/2}$) which rose to $2.5 \text{ MPa}\cdot\text{m}^{1/2}$ at 1200°C . The reduced size, constant $w:d:L$ ratio specimens all yielded similar K_{IC} values (within the typical experimental scatter even at 1200°C) and were then subsequently used for K_{IC} determinations. The high temperature discrepancy probably arises from the inclusion of the s.c.g. zone in the calculated notch depth and a non-linear relationship between specimen dimensions and the s.c.g. zone size. The specimen size difference can effectively alter the applied strain rate (as found during strength tests (109)) and a plastically induced s.c.g. zone would be expected to be strain rate dependent.

Appendix 4.2

RELAXATION TEST PROCEDURE

The Equation.4.3 only holds if, (1) the relaxation of the loading components can be accurately measured; (2) all specimen deformation is due to crack opening. $\frac{dP_m}{dt}$ was determined from auxiliary relaxation tests at temperatures and loads corresponding to the major test. To ensure minimum contribution from specimen deformation an ungrooved, thicker (4 mm) DT specimen of HP Si-Al-O-N (which is known (127) to be particularly resistant to s.c.g and creep at the temperatures of interest) was used here. At various temperatures (1100°C , 1200°C , 1300°C , 1350°C) loading to a range of P_1 gave a family of relaxation curves (shown schematically in Fig.44.1a). At any given temperature $\frac{dP_m}{dt}$ is determined by instantaneous load (P) and time (t) after the onset of relaxation. The relationship between these parameters is best represented (127) by taking the $\frac{dP_m}{dt}$ for a specific 't' for the family of curves (Fig.A4.1.b) and plotting it against its corresponding P (Fig.A4.1c). The actual results for the above

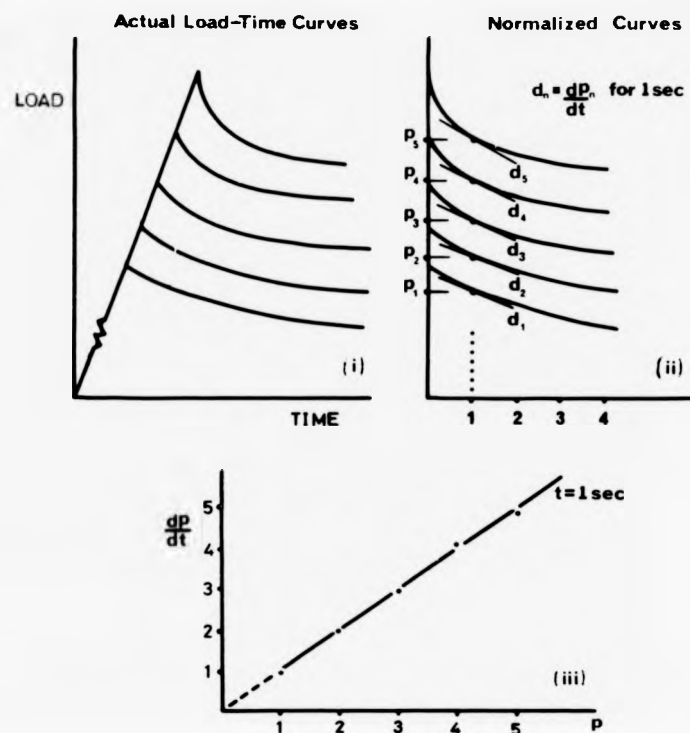


Figure A4-1 Schematic route for determining the machine relaxation using an ungrooved, thick, H.P.Si-Al-O-N tablet.

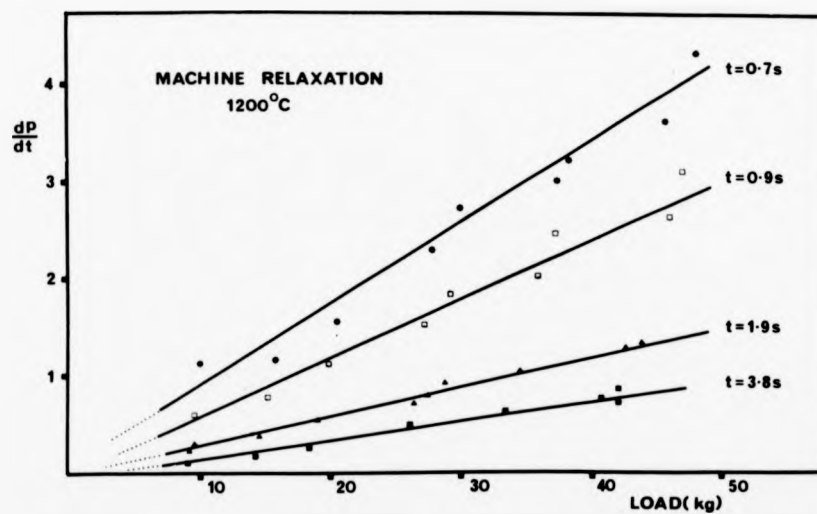


Figure A4-2 Actual Machine Relaxation Relationships $\left[\frac{dp_m}{dt} \right]$ at 1200°C.

temperatures and a variety of t values all show a near linear relationship (Fig.A4.2 is representative and is for 1200°C) with the straight lines passing through the origin showing a correct zero relaxation rate at $P = 0$.

To obtain the specimen relaxation rate $\frac{dp_s}{dt}$ from an actual DT test, the total relaxation rate $\frac{dp_m}{dt}$ and corresponding P are measured after specific times t (say 3 seconds). $\frac{dp_m}{dt}$ for this P value is then given from the $t = 3$ secs. plot (Fig.A4.2), which by subtraction gives the $\frac{dp_s}{dt}$ required for velocity determination.

Appendix 4.3

YOUNG'S MODULUS-TEMPERATURE RELATIONSHIP

The temperature variability of Young's Modulus (E) and Shear Modulus (G) could not be directly determined. However it could be extrapolated from the load/deflection rate of specimens (3 x 6 x 20 mm) subjected to 4 point loading (at a standard crosshead speed of 0.005 cm/min) via the K_{IC} determination apparatus, at various temperatures. The room temperature load/deflection rate for material (SO) is directly proportional to the sonically obtained E value. Therefore by comparison of load/deflection rates, the E for any material and at any temperature can be extrapolated. Compression of machine and jig components influences the total load/deflection rate and was accounted for by auxiliary testing on a thick, low compliance specimen.

The rapid matrix crystallisation of these materials tested (detailed in Chapters 5 and 6) resulted in anomalies in E /temperature relation, as crystallisation was occurring during furnace warm-up. More representative E values required rapid heating to the testing temperature. Since a separate specimen is therefore required for each

temperature only one run was performed. The E-temperature relations are therefore only approximate (complicated further by high temperature strain rate and partial crystallisation effects) but are given in Fig A 4.3.

APPENDIX 4.4

DETERMINATION OF K_I -V RELATIONSHIP FROM COMPLIANCE CHANGE

The compliance of a bend bar as a function of crack length can be derived from the strain energy release rate G_I :

$$G_I = (P^2/2bw) \frac{dC(x)}{dx} \quad (A4.1)$$

where P = total load, C is the compliance, which is a function of x , the normalised crack length = a/w . It is known that

$$K_I = \frac{3P(L-1)}{2bw^{3/2}} \times Y(x) \quad (A4.2)$$

where K_I is the plane strain stress intensity factor. L , l , b , w are as in Fig 4.3b is also a function of Y , a geometric factor, itself a function of crack length. Squaring Eqn. A4.2, substituting into Eqn 3.8 and equating to Eqn A4.1 gives.

$$xY^2 = \frac{2bw^2E}{9(L-1)^2(1-\nu^2)} \frac{dC(x)}{dx}$$

This equation may be integrated to obtain the compliance for any particular crack length.

$$I(x) = \int_0^x x'Y^2 dx' = \frac{3bw^2E}{9(L-1)^2(1-\nu^2)} \int_0^x dC(x)$$

$$I(x) = \frac{wbw^2E}{9(L-1)^2(1-\nu^2)} (C(x) - C_0)$$

where C_0 is the compliance of an unnotched bar. $I(x)$ was evaluated using Tada's formulation for $Y(x)$ (170).

$$Y(x) = \left(\frac{2 \tan \frac{\pi x}{2}}{x} \right)^{1/2} \frac{0.923 + 0.199 \left[1 - \sin \frac{\pi x}{2} \right]^4}{\cos \frac{x}{2}} \quad (A4.4)$$

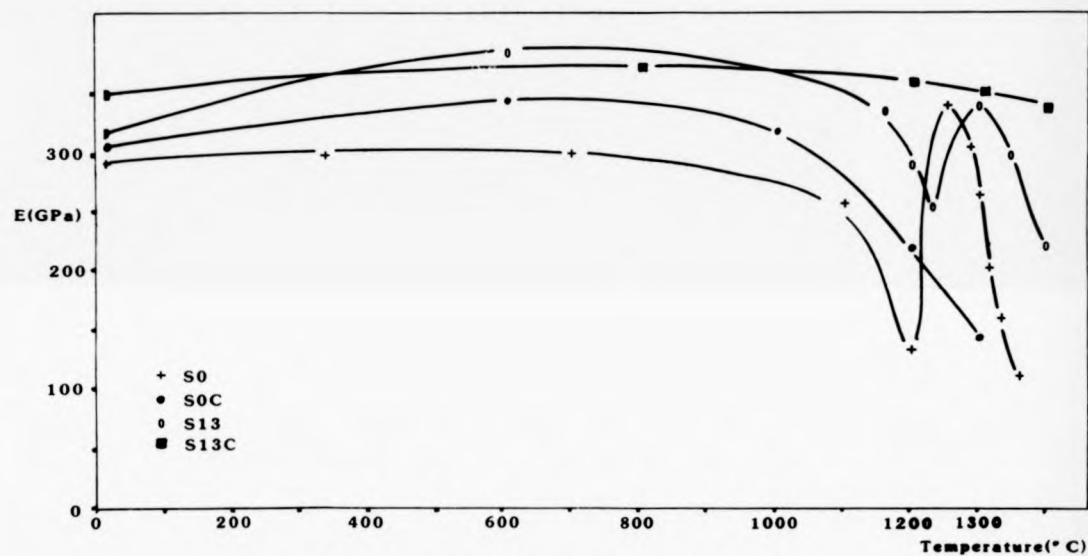


Figure A4-3 Young's Modulus Variation with Temperature for the Various Alloys. Tests in vacuum.

which is valid for $x = 0$ to 1. This numerical integration results in Fig 4.7
By substitution of C_{xf} and C_{x0} and rearrangement of Eqn. A4.3. the value
of $I(x)$ for any crack length is

$$I(x) = I(x_0) + \frac{I(x_f) - I(x_0)}{C(x_f) - C(x_0)} (C(x) - C(x_0)) \quad (A4.5.)$$

Determination of K_I -V data from K_{IC} load displacement curve Fig 4.7a
involves the following steps:-

Step 1: Determine Cx_0 , Cx_f and corresponding times from 0 and
instantaneous load P. Measure $\frac{a}{w} \left(\frac{\text{notch depth}}{\text{specimen width}} \right)$ and also $\frac{a + \text{s.c.g.}}{2}$
where s.c.g. = the discernable zone on the fracture surface.

Step 2: From Graph 1 (which is the compliance integration as a function
of crack length determined by (170) from Tada formula) (a/w) and
 $\left(\frac{a + \text{s.c.g.}}{w} \right)$ give Ix_0 and Ix_f .

Step 3: Substitution of values of $I(x_0)$, $I(x_f)$ and Cx_f and Cx_0
into eqn. A4.5.

$$I(x) = I(x_0) + \frac{Ix_f - Ix_0}{Cx_f - Cx_0} [C(x) - C(x_0)]$$

Gives the simplified

$$I_x = X + Y[Cx - Cx_0] \quad (A4.6.)$$

Step 4: Sub. values of C_x into Eqn A4.6. The range of I_x are converted to $\frac{a}{w}$
from Graph 1.

Step 5: A set of $\frac{a}{w}$ values exists and these given corresponding times
(seconds) (zeroed at the point 0) determined by the loading rate.

Step 6: A graph of $\frac{a}{w}$ against time (Fig.4.7f) is produced and the slope of various tangents to this line $\frac{d(a/w)}{dt}$ gives the crack velocity. A plot of calculated velocity against time is produced, Fig 4.7d.

Step 7: From the values of $\frac{a}{w} = x$, K_I is determined from

$$K_I = \frac{3P}{2bw} \frac{[L-1]^{3/2}}{x^{1/2}} Y(x)$$

where

$$Y(x) = \left[\frac{2}{x} \tan \frac{\pi x}{2} \right]^{1/2} \frac{0.923 + 0.199 \left[1 - \sin \frac{\pi x}{2} \right]^4}{\cos \frac{\pi x}{2}} \quad (A4.7.)$$

L, l, w, b are dimensions given in Fig 4.3b and P is the load at any point x on the curve.

The determined K_I is plotted against time (t) as in Fig 4.7

Step 8: Graph of Fig.4.7d and Fig.4.7e are combined to eliminate time (t) and give the K_I - V diagram.

REFERENCES

1. Probst H B. Amer. Ceram. Soc. Bulletin, 59, 206 (1980).
2. Moulson A J. J Mat. Sci., 14 1017 (1979).
3. Katz R N. "Science" 208 p841 May 1980.
4. Kenney G B and Bowen H F. Amer. Ceram. Soc. Bulletin 62, No 5, 590 (1983).
5. Mueller J I. Amer. Ceram. Soc. Bulletin, 61, No 5, 588 (1982).
6. McLean A F. Amer. Ceram. Soc. Bulletin, 61, No 8, 861 (1982).
7. Giachello A, and Popper P. Ceramurgia Int. 5, 110 (1979).
8. Knoch H, Gazza G E and Katz R N. Energy and Ceramics, Vincencini - ed., Elsevict, Amsterdam (1980).
9. Knoch H and Ziegler G. Science of Ceramics, 9, 494 (1977).
10. Larsen D C, Adams J W, Ruh R. "Progress in Nitrogen Ceramics" Ed. F L Riley, Martinus, Nijhoff P.695 (1983).
11. Swain M V, Hannink R H, Garvie R C. "Fracture Mechanics of Ceramics-Vol 6". Eds. R C Bradt, A G Evans, D P H Hasselman and F F Lange, Plenum Press, New York. P339 (1983).
12. Brysik W. DOE Conf 801182, 269-272 (1983).
13. Robb S. Amer. Ceram. Soc. Bulletin, 62, No 5, 556 (1983).
14. Lumby R J, Butler E and Lewis M H. "Progress in Nitrogen Ceramics", ed. F L Riley, Martinus, Nijhoff P, p683 (1983).
15. Risbud S H and Pask J A. J. Amer, Ceram. Soc., 61, (1-2) 63-7 (1978).
16. Lange F F. J. Amer. Ceram. Soc., 56, (10), 518 (1973).
17. Schwier G. "Progress in Nitrogen Ceramics", ed F L Riley, Martinus, Nijhoff, p157 (1983).
18. Buljau S T and Stermer F E. US Pat. No 4, 073, 845, (1978).
19. Yamada T, Kawahito T and Iwai T. J. Mat. Sci. Letts, 2, No 6 275 (1983).
20. Komeya K, Inque H, Ohta T. German Pat. No 2, 642, 554, (1977).
21. Mori W, Inque H, Ochiai T. "Progress in Nitrogen Ceramics", ed F L Riley, Martinus, Nijhoff, p149 (1983).
22. Shimada M, Koizumi M, Tanaka A and Yamada T. Commun of the Amer. Ceram. Soc. C-48 (1982).
23. Greskovich C and Rosolowski H H. J. Amer. Ceram. Soc., 59, 337 (1976).

24. Deely G G, Herbert J M and Moore N C. Powder Met. No 8, p145 (1961).
25. Lumby R J, North B and Taylor A J. "Special Ceramics 6", ed. P Popper, pp 283-298 (Stoke on Trent 1974).
26. Jack K H and Wilson W I. Nature Physical Science, 238, 28 (1972).
27. Rice R W and McDonough W J. J. Amer. Cer. Soc., 58 264 (1975).
28. Lewis M H, Heath G R, Winder S M, Lumby R J. "Deformation of Ceramics II", eds. R E Tressler and R C Bradt, Plenum Press, p605 (1984).
29. Greskovich C, "Progress in Nitrogen Ceramics". Ed. F L Riley, p283 (1983).
30. Pompe R, Carlsson R. "Progress in Nitrogen Ceramics". Ed. F L Riley, Martinus, Nijhoff, p219 (1983).
31. Quackenbush C L, Smith J T, Neil J T, French K W. "Progress in Nitrogen Ceramics" ed. F L Riley, Martinus, Nijhoff, p699 (1983).
32. Oda, I, Matsui M and Soma T. "Progress in Nitrogen Ceramics", Ed. F L Riley, Martinus, Nijhoff, p501 (1983).
33. Popper P, "Progress in Nitrogen Ceramics". ed F L Riley, p187-210 (1983).
34. Larker H T, "Progress in Nitrogen Ceramics". Ed F L Riley, Martinus, Nijhoff, p717 (1983).
35. Clarke D R, Thomas G. J. Amer. Ceram. Soc. 61 p114 (1978).
36. Ahn C C, Thomas G. J. Amer. Ceram. Soc. 66 p14 (1983).
37. Jack K H. J. Mat. Sci. 11, p1135 (1976).
38. Lange F F, Singhal S C, Kuznicki R C. J. Amer. Ceram. Soc. 60 p249 (1977).
39. Oyama Y and Kamigaito O, Japan J. Appl. Physics, 10, 1937 (1971).
40. Drew P. and Lewis M H. J. Mat. Sci. 4 (11) 1833 (1974).
41. Lewis M H, Powell B D and Drew P. J. Mat. Sci. 12, 61-74 (1977).
42. Lewis M H, Bhatti A R, Lumby R J and North B. J. Mat. Sci. 15, 438-442 (1980).
43. Lewis M H, Bhatti A R, Lumby R J and North B. J. Mat. Sci., 19, 103-111 (1980).
44. Bhatti A R. M. Phil. Thesis, Dept of Physics, University of Warwick (1979).
45. Lewis M H, Karunaratne B S B, Meredith J, Pickering C. "Creep and Fracture of Engineering Materials and Structures" ed. Wilshire and Owen p365 (1981).
46. Lange F F, Davis B I, Metcalf M G. J. Mat. Sci. 18, p1497 (1983).

47. Karunaratne B S B and Lewis M H. J. Mat. Sci. 15, 1781 (1980).
48. Wagner C. Z. Phys. Chem. 21B, 25 (1933).
49. Singhal S. J. Mat. Sci. p500 (1976).
50. Billy M. "Progress in Nitrogen Ceramics", ed. F L Riley, Martinus, Nijhoff, p403 (1983).
51. Barrer R M. J. Chem. Soc. 89 p378 (1934).
52. Singhal S C. pp 697-712 in "Properties of High Temperature Alloys", Eds. Z A Foroulis and F S Pettit, The Electrochemical Society, Princeton NJ (1976).
53. Cubicciotti D and Lau K H. J. Amer. Ceram. Soc, 61 No 11-12, 512 (1978).
54. Lewis M H and Barnard P. J. Mat. Sci. 15, 443 (1980).
55. Clarke D R and Lange F F. J. Amer. Ceram. Soc. 63 No 9 p586 (1980).
56. Lange F F. J. Amer. Ceram. Soc., 61 53 (1978).
57. Wu C C, McKinney K R, Rice R W, McDonough W J and Freiman S W. J. Mat. Soc. 16, 3099 (1981).
58. Babini G N and Vincenzini P. "Progress in Nitrogen Ceramics", Ed. F L Riley, Martinus, Nijhoff, p427 (1983).
59. Babini G N, Bellosi A and Vincenzini P. J. Mat. Sci. 18 No 1, 231 (1983).
60. Arias A. NASA Technical Paper 1246.
61. Drew R A L, Hampshire S, Jack K H. "Special Ceramics 7", Eds. D Taylor and P Popper, Proc. Brit. Cera. Soc. 31, 119 (1981).
62. Hampshire S and Jack K H. "Special Ceramics 7". Eds. D Taylor and P Popper, British Ceramic Society, Stoke-on-Trent, p37, (1981).
63. Ball R K, Private Communication.
64. Hench L L and Freiman S W. J. Mat. Sci. 16, 2767 (1981).
65. Singhal S C and Lange F F. J. Amer. Ceram. Soc. 60, 1-2, 190-191 (1977).
66. Galasso F J, Veltri R D. Comm. of the Amer. Ceram. Soc. C15 (1981).
67. Karunaratne B S B and Lewis M H. J. Mat. Sci, 15 449 (1980).
68. Lange F F. Int. Met. Rev. 25, 1-20 (1980).
69. Sharp J V, J. Mat. Sci. p1755 (1973).
70. Evans A G and Davidge R W. J. Mat. Sci. 5 314 (1970).
71. Cubicciotto D and Lau K H. J Electrochem. Soc. 126, 1723 (1979).

72. Griffith A A. Phil. Trans. Roy. Soc. London, 211A, 163 (1920).
73. Inglis C E. Trans. Inst. Naval Archit. 55, p219 (1913).
74. Orowan E. Rep. Progr. Phys. 12, 185 (1949).
75. Irwin G R. Jou. Welding, 31, 450 (1952).
76. Paris P C and Sih G C. ASTM Special Tech. Pub. 1, No 381 (1965).
77. Henshall J L, Rowcliffe D J and Edington J W. J. Amer. Ceram. Soc. 62, 36 (1979).
78. Edington J W, Rowcliffe D J and Henshall J L. Powder Metallurgy International, Vol 7, No 3, p136. (1975).
79. Fields R J, Chuang T J, Fuller E R, Tighe N J. "Progress in Nitrogen Ceramics", Ed. F L Riley, Martinus, Nijhoff, p507 (1983).
80. Kříž K. "Progress in Nitrogen Ceramics". Ed F L Riley, Martinus, Nijhoff, p523 (1983).
81. Orange G, Chavez D, Dubois J and Fantozzi G. Proc. Int. Conf. on Fracture (ICF 5), Pub. Advances in Fracture Research, Vol 4, pp 1551. (1975).
82. Lewis M H, Smith G. "Proc. of 4th Int. Conf. on Fracture" ed. D Taplin p867 (1977).
83. Fields R J, Tighe N J and Fuller E R. "Progress in Nitrogen Ceramics", Ed. F L Riley, Martinus, Nijhoff, p507 (1983).
84. Becher P F. J. Amer. Ceram. Soc. 66, p485 (1983).
85. Pabst R F and Popp G. "Fracture Mechanics of Ceramics, Vol 5", Eds. Bradt, Evans, Hasselman, Lange, Plenum Press, NY, p305 (1983).
86. Henshall J L, Rowcliffe D T and Edington J W. J. Mat. Sci. Letts, 9, 1559-1561 (1974).
87. Petrovic J J, Jacobson L A. J. Amer. Ceram. Soc. 59 p34 (1976).
88. Lange F F, J Amer. Ceram. Soc, 62 p222 (1979).
89. Cheeseman C, Ph.D. Thesis, Oxford University (1984).
90. Evans A G and Johnson H. J. Mat. Sci, 10 214-222 (1975).
91. Wiederhorn S M and Ritter J R. "Fracture Mechanics Applied to Brittle Materials", ASTM STP 678, Ed. S W Freiman (Am. Soc. for Testing and Materials, Philadelphia, R A 1978) pp202-14.
92. Weiderhorn S M, Fuller E R and Thomson R, Metal. Sci. 14, 8-9, p450-8 (1980).
93. Weiderhorn S M. Int. J. Fract. Mech. 4 171 (1968).
94. Evans A G and Linzer M. J. Amer. Ceram. Soc., 53 543 (1973).
95. Charles R J. J. Appl. Physics, 29 (12) 1657-62 (1958).
96. Evans A G. J. Mat. Sci., 7 1137-1146 (1972).

97. Minnear W P and Bradt C. J. Amer. Ceram. Soc., 58, 245 (1975).
98. Stevens R N and Dutton R. Mater. Sci. Eng., 8, 220 (1971).
99. Dutta S. J. Amer. Ceram. Soc., 65 (1) C2 (1982).
100. Chuang T T, US Atomic Energy Commission, Contract No AT (11-1) - 3084, Technical Report No 32 (1974).
101. Chuang T J, Hagawa K I, Rice J R and Sills L B. Acta. Met., 27, 265-284 (1979).
102. Greenwood J N, Miller D R, Svitter J W. Acta. Met., 2, 250 (1954).
102. Evans A G. "Ceramics for High-Performance Applications", Eds. J J Burke, A E Giorun, N Katz, p373-397 (1974).
104. Evans A G and Longdon T G. "Progress in Material Science" (Pergamon Press) 21, p171 (1976).
105. Khuri-Yakub B T, Evans A G and Kino G S. J. Amer. Ceram. Soc., 63, 65-71 (1980).
106. Davidge R W, McLaren J R and Tappin G. J. Mat. Sci., 8, 1966-1705 (1973).
107. Ritter J E and Sherburne C L. J. Amer. Ceram. Soc., 54 601-05 (1971).
108. Katz R N, Quinn G D, "Progress in Nitrogen Ceramics", Ed. F L Riley, Martinus, Nijhoff p491 (1983).
109. Ritter J E and Jakus K. J. Amer. Ceram. Soc., 60, No. 3-4, 192 (1977).
110. Freiman S W. "Fracture Mechanics of Ceramics - Vol 6" Eds. R C Bradt, A G Evans, D P H Hasselman and F F Lange, Plenum Press, New York, p27 (1983).
111. Baker L M. Eng. Fract. Mech., 9 361-369 (1977).
112. Govila R K, Kinsmann K R, and Beardmore P. J. Mat. Sci., 13, 2081 (1978).
113. Siebels J E. "Progress in Nitrogen Ceramics", Ed. F Riley, Martinus, Nijhoff, p529 (1983).
114. Fields R J, Fuller E R, Chuang T J, Chuck L and Kobayashi K. "Fracture Mechanics of Ceramics - Vol 6" Eds. R C Bradt, A G Evans, D P H Hasselman and F F Lange; Plenum Press, New York. p463 (1983).
115. Steigorwald E A and Hanna G L. Proceed. Amer. Sci. for Testing and Materials, 62, 885-913 (1962).
116. Krell A, J. Mat. Sci. 17, p1649 (1982).
117. Evans A G, Linzer M and Russell L R, Mater. Sci. Eng. 15, 253 (1974).
118. Singhal S C. J. Amer. Ceram. Soc. 59, (1-2) 81-82 (1976).
119. Tripp W C and Graham H C, J. Amer. Ceram. Soc. 59, 399 (1976).
120. Lindberg L J, Richerson D W, Carruthers W D and Gresch H M. Amer. Ceram. Soc. Bulletin, 61, No 5, 574 (1982).

121. Timoshenko S "Strength of Matrials" (Von Nostrand Reinhold, New York) Pt II, p57 (1958).
122. Claussen N, Pabst R and Lahmann C P, Brit. Ceram. Soc. p139.-149 (1975).
123. Henshall J L, Ph.D. Thesis, Department of Metallurgy and Materials Science, University of Cambridge (1975).
124. Hodge J D, Lessing P A and Gordon R S. J. Mat. Sci. 12, 1598-1604 (1977).
125. Srawley J E and Brown B F, ASTM Special Tech. Pub. 410, 8-16 (1969).
126. Smith H R and Piper D E, in "Stress Corrosion Cracking in High Strength Steels and in Titanium and Aluminium alloys:", Ed B F Brown (Naval Research Laboratory, Washington 1972) p17.
127. Karunaratne B S B, Ph.D. Thesis, Department of Physics, University of Warwick (1980).
128. Kies J A and Clark A B. Proc. 2nd Int. Conf. on Fracture, Ed P L Pratt, Chapman and Hall Ltd. p482 (1969).
129. Williams D P and Evans A G, Journal of Testing and Evaluation, p264-270 (1973).
130. Ferber M K and Brown S D. J. Amer. Ceram. Soc. 63, 424 (1980).
131. Evans A G, Russel L R and Richerson D W, Metallurgical Transactions A, 6A, 707-715 (1975).
132. Spinner S and Teft W E. Proc. Am. Soc. Test. Mater. 61, 1121-38 (1961).
133. Clarke D R. J. Appl. Phys. 49, (1978).
134. Clarke D R and Thomas G. J. Amer. Ceram. Soc. 60, No 11-12, 491-495 (1977).
135. Clarke D R. Ultramicroscopy, 4 33 (1979).
136. Clarke D R. "Progress in Nitrogen Ceramics: ed. F L Riley, Martinus, Nijhoff, p341 (1983).
137. Raj R. Report No. 4092 issued by the Mat. Sci. Centre, Cornell Uni. (1979).
138. Russ J C. In "Microprobe Analysis Applied to Cells and Tissues", Eds. Hall, Echlin and Kaufman.
139. Zeigler G and Knoch H. "Special Ceramics 7", Eds. Taylor and Popper, Proc. Brit. Ceram. Soc. 31, p145 (1981).
140. Loezman R E. J. Non-Cryst. Solids, 42, (1-3) 433-46 (1980).
141. Clarke D R, Zaluzec N J and Carpenter R W. J. Amer. Ceram. Soc. 65, No 8, C132 (1982).
142. Thomas G, Ahn C and Weiss J. Commun. of the Amer. Ceram. Soc. C-185 (1982).

143. Winder S M and Lewis M H. J. Mat. Sci. Letters, Vol 4, No 2, p241 (1985).
144. Messier D R and Broz A. Commun. of the Amer. Ceram. Soc. C-123 (1982).
145. Drew R A L, Hampshire S and Jack K H. "Progress in Nitrogen Ceramics", Ed. F L Riley, Martinus, Nijhoff, p323 (1983).
146. Keith M L and Roy R. Amer. Mineral, 39, 1 (1954).
147. McMillan P W. "Glass Ceramics", Academic Press, London (1979).
148. Ramsey M. Unpublished work.
149. Clarke D R. Commun. of the Amer. Ceram. Soc. C-21 (1982).
150. Evans J R G. J. Mat. Sci. Letts. 2, 19-21 (1983).
151. Jack K H, Private Communication (1984).
152. Warshaw I, Roy R. J. Amer. Ceram. Soc. 42, p434 (1959).
153. Hirai T, Niihara K and Goto T. J. Amer. Ceram. Soc., 63, No 7, 419, (1980).
154. McDonough W J, Wu C C and Morgan P E D, J. Amer. Ceram. Soc., 63, C-45, (1981).
155. Lewis M H, Reed K, Butler N D. To be published.
156. Cottrell A H. Proc. Roy. Soc., 282A, 2, (1964).
157. Mason S. Internal Report, Dept. of Physics, University of Warwick, (1985).
158. Mulfinger H O. J. Amer. Ceram. Soc., 49, 462, (1966).
159. Quinn G D and Quinn J B. "Fracture Mechanics of Ceramics-Vol 6". Eds. R C Bradt, A G Evans, D P H Hasselman and F F Lange, Plenum Press, New York. (1983).
160. Veltri R and Galasso F. Commun. of the Amer. Ceram. Soc, C-53 p107 (1982).
161. Chui G K. Amer. Ceram. Soc. Bull. 514, (1975).
162. Mohaupt U H and Burns D J Exp. Mech. 14, 152 (1974).
163. Paer U C and Gagliano F D, I.E.E.E., JQE, Vol. QE-8, No 2 p112 (1972).
164. Toropov N A and Bondar I A. Izvest. Akad. Nauk. SSSR. Otdelenie Khim Nauk, 544-550, (1960).
165. Clarke D R. J. Amer. Ceram. Soc., 63, 208, (1980).
166. Mitomo M, Yajima Y and Kuramoto N. J. Amer. Ceram. Soc. 62, No 5-, 316 (1979).
167. Goursat P. "Nitrogen Ceramics", Ed. F L Riley (Noordhoff (1977)) p81-86.
168. Bondar I A and Galakhov F Ya. Izvest. Akad. Nauk. SSSR. Ser. Khim, 7, 1325, (1963).
169. Boyd D and Garden J P. I.E.E.E. JQE, Vol 8, p120 (1972)
170. Tada H, Paris P and Irwin G. "The Stress Analysis of Cracks Handbook" Del Research Corp. Hellerton PA (1973)